# GROWTH AND CHARACTERIZATION OF SOME OF THE ORGANIC SINGLE CRYSTALS



Thesis submitted to the Bharathidasan University,

Tiruchirappalli in partial fulfilment of the requirement
for the award of the degree of

DOCTOR OF PHILOSOPHY IN PHYSICS

# By Mrs G. AMUDHA

(Ref. No. 40119 / Ph.D.K2 / Physics / Part-Time /January 2017 / Date: 28.12.2016)

Research advisor

Dr. R. SANTHAKUMARI

ASSISTANT PROFESSOR OF PHYSICS



# PG AND RESEARCH DEPARTMENT OF PHYSICS GOVERNMENT ARTS COLLEGE FOR WOMEN (Autonomous)

(Re-accredited with B\*\* Grade by NAAC)

(Affiliated to Bharathidasan University, Tiruchirappalli-24)

PUDUKKOTTAI - 622 001

TAMIL NADU, INDIA

**MARCH 2022** 

# Dr. R. SANTHAKUMARI

Assistant Professor & Research Advisor Department of Physics Government Arts College for Women (Autonomous) Pudukkottai - 622 001

Tamil Nadu, India

Tel.: +91 4322 236020.

**E-mail:** santhasrinithi@yahoo.co.in



# **CERTIFICATE**

This is to certify that the thesis entitled "Growth and characterization of some of the organic single crystals" submitted by Mrs. G. AMUDHA is a bonafide record of research work done by her during the period of study 2017 – 2021 under my supervision in the Department of Physics, Government Arts College for Women (Autonomous), Pudukkottai - 622001, Tamil Nadu, India and that the thesis has not previously formed the basis for the award of any Degree, Diploma, Associateship, Fellowship or any other similar title. The thesis represents the independent work on the part of the candidate.

Pudukkottai

(R. SANTHAKUMARI)

**March 2022** 

RESEARCH SUPERVISOR

Dr. R. SANTHAKUMARI

Assistant Professor & Research Advisor

Department of Physics

Government Arts College for Women (Autonomous)

Pudukkottai - 622 001

Tamil Nadu, India

Tel.: +91 4322 236020.

**E-mail:** santhasrinithi@yahoo.co.in



# **DECLARATION**

I hereby declare that the work presented in the thesis entitled "Growth and characterization of some of the organic single crystals" has been originally carried out by me independently under the guidance and supervision of Dr. R. Santhakumari, Assistant Professor & Research Advisor, Department of Physics, Government Arts College for Women (Autonomous), Pudukkottai-622001, Tamil Nadu, India. This work has not been submitted either in whole or in part for any other Degree or Diploma at any University or Research Institute.

Pudukkottai (G. AMUDHA)

**March 2022** 

# Dr. R. Santhakumari,

Assistant Professor and Research Advisor
PG & Research Department of Physics
Government Arts College for Women (Autonomous)
Pudukkottai – 622 001.

To

The Director - Research, Bharathidasan University, Tiruchirappalli.

# **CERTIFICATE**

Sir,

This is to certify that the Ph.D Research Work in Physics carried out by Mrs. G. AMUDHA (Ref: No. 40119 / Ph.D.K2 / Physics / Part-Time / January 2017 / Date:28.12.2016) titled "Growth and characterization of some of the organic single crystals" is the original independent work of the Researcher. As per the new regulations of our university, plagiarism check has been made using Ouriginal software and it is found that the significance level is 05% (Introduction & Review) & 05% (Remaining Chapters).

Hence, I recommend that the thesis may kindly be accepted and considered for evaluation.

Thanking you,

Yours faithfully,

(Dr. R. Santhakumari)



# **Document Information**

Analyzed document Mrs G. AMUDHA - Intro & Review.pdf (D129487672)

**Submitted** 2022-03-05T07:28:00.0000000

**Submitted by** Dr.S.Vanitha

Submitter email vanitha@bdu.ac.in

Similarity 5%

Analysis address navitha.bdu@analysis.urkund.com

# Sources included in the report

SA	Prof. KK Thesis Chapter 1.doc  Document Prof. KK Thesis Chapter 1.doc (D41093604)	88	1
SA	Kannadhasan-Physics_SVMASC.pdf Document Kannadhasan-Physics_SVMASC.pdf (D110350868)	88	1
W	URL: http://lib.buet.ac.bd:8080/xmlui/bitstream/handle/123456789/1898/Full%20%20Thesis%20%20.pdf?sequence=1&isAllowed=y Fetched: 2022-03-05T07:29:26.6070000	88	1
SA	CHAPTER I FINAL.pdf Document CHAPTER I FINAL.pdf (D52879467)		2
SA	Chapter 1_V3_Plagcheck.docx Document Chapter 1_V3_Plagcheck.docx (D107349533)	88	1
W	URL: https://www.science.gov/topicpages/n/nlo+single+crystal Fetched: 2020-08-28T11:23:09.0500000		1
SA	MANUSCRIPT OVERVIEW.docx Document MANUSCRIPT OVERVIEW.docx (D19914904)		1
SA	<b>chapter 1.docx</b> Document chapter 1.docx (D20916903)		1
SA	Bharathidasan University, Tiruchirappally / The crystals have fascinated man with their charming colors.docx  Document The crystals have fascinated man with their charming colors.docx (D53829585)  Submitted by: library@andavancollege.ac.in  Receiver: library.bdu@analysis.urkund.com		1



# **Document Information**

**Analyzed document** Mrs G. AMUDHA - Remaining Chapters.pdf (D129487673)

**Submitted** 2022-03-05T07:28:00.0000000

**Submitted by** Dr.S.Vanitha

**Submitter email** vanitha@bdu.ac.in

Similarity 5%

Analysis address navitha.bdu@analysis.urkund.com

# Sources included in the report

our	ces included in the report		_
W	URL: https://coek.info/pdf-crystal-growth-structural-optical-vibrational-analysis-hirshfeld-surface-and-qua.html Fetched: 2021-07-17T07:58:58.4370000	88	:
SA	3AP4NP - Growth, Characterization and DFT manuscript sent to Urkund on 4-11-2016 - [For publication in JMSME].docx  Document 3AP4NP - Growth, Characterization and DFT manuscript sent to Urkund on 4-11-2016 - [For publication in JMSME].docx (D23012897)		
N	URL: https://www.researchgate.net/publication/262569310_Synthesis_experimental_and_theoretica l_Studies_of_8-hydroxyquinolinium_35-dinitrobenzoate_single_crystal Fetched: 2021-07-01T07:11:08.5730000	88	
A	PAPER_edit_25Jan_GINO.docx  Document PAPER_edit_25Jan_GINO.docx (D126046607)	88	
V	URL: http://www.acrhem.org/download/195.pdf Fetched: 2021-06-24T05:35:08.3430000		
V	URL: https://www.researchgate.net/publication/316563240_Synthesis_structure_combined_with_c onformational_analysis_biological_activities_and_docking_studies_of_bis_benzylidene_cyclohexan one_derivatives Fetched: 2020-02-11T15:03:56.7670000		
A	Manuscript.docx Document Manuscript.docx (D42008615)		
V	URL: http://ijream.org/papers/IJREAMV05I0351122.pdf Fetched: 2022-01-20T11:28:44.2430000		
V	URL: https://link.springer.com/article/10.1007/s00894-012-1578-x/tables/1 Fetched: 2022-03-05T07:29:37.1800000		
V	URL: http://www.rsc.org/suppdata/d0/cp/d0cp04354k/d0cp04354k1.pdf Fetched: 2022-03-05T07:28:34.7970000		
N	URL: https://www.researchgate.net/publication/307438123_Growth_and_Characterization_of_an_ Organic_Crystal_and_DFT_Studies_of_2-Amino_5-Methyl_Pyridinium_Salicylate Fetched: 2020-08-03T06:24:54.2000000	88	



Dedicated to beloved

Matha, Pitha, Guru, Deivam

#### ACKNOWLEDGEMENT

\_\_\_\_\_\_

First and foremost, I would like to thank **GOD** Almighty for giving me the strength, knowledge, ability and opportunity to undertake this research study and to persevere and complete it satisfactorily. Without His blessings, this achievement would not have been possible.

I would like to express my special thanks to our Principal **Dr. B. BUVANESWARI,** Government Arts College for Women (Autonomous), Pudukkottai, for her tremendous guidance and support during this research work.

I am highly thankful to **Dr. K. RENUKA DEVI**, Associate Professor, Head and Department of Physics, Government Arts College for Women (Autonomous), Pudukkottai.

It is with immense pleasure that I thank **Dr. R. SANTHAKUMARI**, Assistant Professor & Research Advisor, Department of Physics and Government Arts College for Women (Autonomous), Pudukkottai for her guidance and constant encouragement in carrying out my research successfully. It was a memorable academic journey for me. I am so privileged and feel proud of being a ward to such a dedicated scholar. I sincerely thank her for allowing me to utilize the facilities available in the Department.

I gratefully acknowledge my doctoral committee members **Dr. R. MANIMEKALAI**, Associate Professor, Department of Physics, AVVM Sri Pushpam College, Poondi, Thanjavur and **Dr. A. JANAKI**, Assistant Professor, Department of Physics, Government Arts College for Women (Autonomous), Pudukkottai for their valuable advice.

I greatly acknowledge **Dr. C. Usha, Dr. R. Jayasree, Mrs S. Mugeshini, D. Chandrika and N. Rajeswari** for their advice, co-operation, and fruitful discussion, which made a backbone of this research and so to this thesis. Her involvement with this work has triggered and nourished my intellectual maturity that I will benefit from, for a long time to come.

This thesis would not have been possible without the guidance and the help of several individuals who in one way of another contributed and extended their valuable assistance in the preparation and completion of this study.

Finally, a deepest personal acknowledgement to **my Family members** for their constant encouragement. I extend my sincere thanks to colleagues and other friends for their consistent help and encouragement.

G. AMUDHA

#### **PREFACE**

Organic material has been sought for a variety of applications in recent years, including photonics, electro optic systems, color display optical switching, and frequency doubling. Organic crystal has been synthesized in recent years in order to improve chemical stability, laser damage threshold, and nonlinear optical characteristics. Density functional theory simulations are an excellent option for designing NLO molecules because they allow for the prediction of features such as molecular dipole moments, polarizabilities, and hyperpolarizabilities.

On the grown crystals, single crystal X-ray diffraction was performed to confirm the cell parameters. The crystalline planes were identified using powder X-ray diffraction analysis. FT-IR and FT-Raman spectroscopic techniques were performed to determine the vibrational modes of functional groups of the grown crystal. UV-vis-NIR spectrum and fluorescence analyses were used to establish its optical properties. The thermal stability of grown crystal was studied using thermo gravimetric and differential thermal analysis (TG/DTA). The mechanical property of grown crystals was determined using a Vickers microhardness test. Density functional theory (DFT) calculations with B3LYP different basis sets was used to find out optimization molecular geometries, vibrational frequencies, Frontier molecular orbitals (FMOs), Mulliken atomic charges, molecular electrostatic potentials, first order hyperpolarizability, thermodynamic properties natural bond orbital (NBO) analysis and Hirshfeld surface analysis were highlighted.

**Chapter-1** provides the introduction to crystal growth methods on solution growth technique and discusses about the organic nonlinear optical materials.

**Chapter-2** presents the characterization techniques adopted to analyze the properties of the grown crystals. Single crystal XRD, Powder XRD, FT-IR, FT-Raman, UV-vis-NIR, Photoluminescence, Thermal analysis, Microhardness, DFT and Hiresfeld surface analysis.

Chapter-3 presents the characterization of single crystals of 4-amino-N-carbamothioylbenzene sulfonamide (ACBS) have been grown at room temperature using slow evaporation solution growth method. The cell parameters of the grown crystals were calculated through X-ray diffraction analysis. The ACBS crystal belongs to the monoclinic crystal system with P2<sub>1</sub> space group. The crystalline planes were identified by powder X-ray diffraction analysis. The presents of various functional groups in the grown crystal were obtained by Fourier Transform Infrared (FT-IR) spectral analysis. UV-vis-NIR, thermal analysis, fluorescence analysis, spectral analysis was carried out in order to study the optical properties of the grown crystal. The molecular structure, mechanical strength and the surface morphology were analysed through <sup>1</sup>H NMR, Vickers microhardness and SEM techniques respectively.

Chapter-4 describes the pyrazolemethoxy benzaldehyde (PMB) was synthesized and crystals were grown by slow evaporation solution growth method. PMB crystal was crystallized in a monoclinic crystal system with a centrosymmetric C2/c space group, according to single crystal X-ray diffraction analysis. The crystalline planes were identified using powder X-ray diffraction analysis. FT-IR, FT-Raman spectroscopic techniques were performed to determine the vibrational modes of functional groups for the grown crystal. UV-visible spectral analysis and photoluminescence studies were taken to investigate the linear optical properties of the grown crystal. Thermogravimetric and differential thermal analysis (TG/DTA) were used to determine the thermal stability of the PMB crystal. In addition to this density functional theory (DFT) calculations such as Frontier molecular orbitals (FMOs), Global chemical reactivity parameters, hyperpolarizability, natural bond orbital (NBO) analysis, Mullikan atomic charge distribution, and molecular electrostatic potential map analysis were carried out in gaseous phase using B3LYP/6-311G\* basis set.

**Chapter-5** is devoted to organic single crystal pyridine urea (PYUA) was synthesized using the slow evaporation solution growth method at room temperature.

Structural characteristics of the crystal were studied through crystal X-ray diffraction, Fourier transform infrared (FT-IR), and UV-vis-NIR spectral analysis. The thermogravimetric analysis (TGA) and differential thermal analysis (DTA) techniques was used to investigate the thermal stability of the PYUA crystal. The Vickers hardness study confirmed the PYUA as a soft crystal constructed by H-bonds and  $\pi...\pi$  interactions of average strength. The DFT calculations with the B3LYP method and Gaussian 09 software were used to perform computational analyses in a gaseous state. Hiresfeld investigations reveal H--H interactions, demonstrating the largest contribution in the molecular packing.

Chapter-6 illustrates the synthesis and characterization of aminopyridinium chloronicotinate (APCN) single crystal were grown using a slow evaporation solution growth method. The APCN crystal belongs to the monoclinic P2<sub>1</sub>/c crystal system with a centrosymmetric space group, according to X-ray diffraction analysis of a single crystal. Powder X-ray diffraction analysis was used to determine crystallinity nature of grown crystals. Various functional groups in the grown crystal were identified using Fourier transform infrared (FT-IR) spectroscopy. The optical transmittance, energy bandgap of the crystal, are analyzed through UV-vis-NIR spectroscopy. The thermal stability of APCN crystal was studied by thermogravimetric and differential thermal analysis (TG/DTA). The mechanical property of the grown crystal was determined by the Vickers microhardness test. The density functional theory (DFT) method at B3LYP 6-31+G (d, p) basis set was used to perform the theoretical investigations in order to get the information regarding the HOMO-LUMO, Global chemical reactivity descriptors (GCRD), natural bond orbital (NBO), Mulliken atomic charges, molecular electrostatic potential (MEP), and thermodynamical properties of the molecule in the gaseous state.

**Chapter-7** provides the highlight of the work presented in the thesis and the scope for future work.

# **CONTENTS**

1	Intro	duction to Crystal Growth Technique	1 - 18
1.1	Introd	luction	1
1.2	Nucle	ation	2
	1.2.1	Primary Nucleation	3
	1.2.2	Secondary Nucleation	4
1.3	Metho	ods of crystal growth	4
1.4	Soluti	on Growth method	5
	1.4.1	High Temperature Solution Growth	5
	1.4.2	Hydrothermal growth	5
	1.4.3	Flux growth	6
1.5	Low t	emperature solution growth	6
	1.5.1	Slow evaporation method	7
	1.5.2	Slow Cooling method	8
	1.5.3	Temperature gradient method	9
1.6	Soluti	on, Solubility, and Supersaturation	10
	1.6.1	Solution	10
	1.6.2	Solubility	11
	1.6.3	Supersaturation	13
1.7	Nonli	near optical materials	13
1.8	Classi	ification of materials	14
	1.8.1	Organic materials	14
	1.8.2	Inorganic materials	15
	1.8.3	Semi organic materials	16
1.9	Densi	ty functional theory (DFT) method	16
1.10	Scope	of the present work	17

2	Characterization Techniques	19 - 42
2. 1	Introduction	19
2.2	Single Crystal X-ray diffraction	20
	2.2.1 X-ray Powder diffractometer	21
2.3	FT-IR spectral analysis	23
	2.3.1 Instrumentation FT-Raman	26
2.4	UV spectral analysis	28
2.5	Microhardness analysis	30
2.6	Thermal analysis	33
	2.6.1 Thermogravimetric analysis	33
	2.6.2 Differential thermal analysis	34
2.7	Photoluminescence study	36
2.8	Nuclear Magnetic Resonance (NMR) Spectroscopy	37
2.9	Scanning electron microscope analysis	39
2.10	Computational details	40
	2.10.1 Frontier molecular orbital analysis	40
	2.10.2 Mulliken atomic charge analysis	41
	2.10.3 Molecular electrostatic potential map analysis	41
	2.10.4 Hirshfeld surface analysis	42
3	Growth and characterization of 4-amino-N-carbamothioylbenzene Sulphonamide: A nonlinear optical single crystal	43 - 56
3.1	Introduction	43
3.2	Experimental procedure	44
	3.2.1 Synthesis	44
	3.2.2 Crystal growth	44

3.3	Instrumentation	45
3.4	Results and discussions	46
	3.4.1 Single crystal X-ray diffraction analysis	46
	3.4.2 Powder X-ray diffraction analysis	46
3.5	Vibrational analysis	47
3.6	UV-Vis-NIR spectral analysis	49
3.7	Thermal analysis	50
3.8	Fluorescence studies	51
3.9	<sup>1</sup> H NMR Spectral analysis	52
3.10	Microhardness analysis	53
3.11	SEM analysis	55
4	Synthesis, growth, dft, and HOMO-LUMO studies on	57 - 80
	pyrazolemethoxy benzaldehyde single crystals	
4.1	pyrazolemethoxy benzaldehyde single crystals Introduction	57
4.1 4.2		57 58
	Introduction	
	Introduction  Material and Methods	58
4.2	Introduction  Material and Methods  4.2.1 Synthesis and crystal growth	58 58
4.2	Introduction  Material and Methods  4.2.1 Synthesis and crystal growth  Results and discussions	58 58 60
4.2	Introduction  Material and Methods  4.2.1 Synthesis and crystal growth  Results and discussions  4.3.1 Single X-ray diffraction studies	58 58 60 60
4.2	Introduction  Material and Methods  4.2.1 Synthesis and crystal growth  Results and discussions  4.3.1 Single X-ray diffraction studies  4.3.2 Powder X-ray diffraction analysis	58 58 60 60
4.2 4.3 4.4	Introduction  Material and Methods  4.2.1 Synthesis and crystal growth  Results and discussions  4.3.1 Single X-ray diffraction studies  4.3.2 Powder X-ray diffraction analysis  FT-IR, FT-Raman spectral analysis	58 58 60 60 60 61
4.2 4.3 4.4 4.5	Introduction  Material and Methods  4.2.1 Synthesis and crystal growth  Results and discussions  4.3.1 Single X-ray diffraction studies  4.3.2 Powder X-ray diffraction analysis  FT-IR, FT-Raman spectral analysis  UV-vis-NIR spectral analysis	58 58 60 60 60 61 64
4.2 4.3 4.4 4.5 4.6	Introduction  Material and Methods  4.2.1 Synthesis and crystal growth  Results and discussions  4.3.1 Single X-ray diffraction studies  4.3.2 Powder X-ray diffraction analysis  FT-IR, FT-Raman spectral analysis  UV-vis-NIR spectral analysis  Photoluminescence studies	58 58 60 60 60 61 64 65
4.2 4.3 4.4 4.5 4.6 4.7	Introduction  Material and Methods  4.2.1 Synthesis and crystal growth  Results and discussions  4.3.1 Single X-ray diffraction studies  4.3.2 Powder X-ray diffraction analysis  FT-IR, FT-Raman spectral analysis  UV-vis-NIR spectral analysis  Photoluminescence studies  Thermal analysis	58 58 60 60 60 61 64 65 66

	4.8.3	Global Chemical Reactivity Analysis	73	
	4.8.4	Hyperpolarizability studies	74	
	4.8.5	NBO analysis	76	
	4.8.6	Mulliken atomic charges	77	
	4.8.7	Molecular Electrostatic Potential analysis	79	
_	-			
5		th, Spectroscopic and Hirshfeld surface analysis on ine urea single crystal	81 - 100	
5.1	Introd	uction	81	
5.2	Exper	imental Procedure	82	
	5.2.1	Crystal growth	82	
5.3	Result	s and discussion	83	
	5.3.1	Single crystal and powder X-ray diffraction studies	83	
5.4	FT-IR	spectral analysis	85	
5.5	UV-vi	is-NIR spectral analysis	87	
5.6	Therm	nal studies	88	
5.7	Micro	hardness studies	89	
5.8	Comp	utational analyses	90	
	5.8.1	Molecular geometry optimization	90	
	5.8.2	HOMO-LOMO analysis	91	
	5.8.3	Global reactivity descriptors	93	
	5.8.4	Mulliken and Natural population analysis	94	
	5.8.5	Molecular electrostatic potential (MEP) map analysis	96	
	5.8.6	NBO Analysis	96	
	5.8.7	Thermodynamic properties	97	
5.9	Hirshf	Feld Surface analysis	99	

6	Synthesis, growth, physicochemical characterization, and computational studies on aminopyridinium chloronicotinate single crystal	101 - 122
6.1	Introduction	101
6.2	Experimental Procedure	102
	6.2.1 Synthesis and crystal growth	102
6.3	Computational details	103
6.4	Results and Discussion	104
	6.4.1 Single and Powder X-ray diffraction analysis	104
6.5	FTIR spectral analysis	105
6.6	UV-vis-NIR spectral studies	108
6.7	Thermal Studies	108
6.8	Microhardness studies	109
6.9	Theoretical investigations	111
	6.9.1 Molecular geometry	111
	6.9.2 HOMO - LUMO analysis	113
	6.9.3 Global chemical reactivity descriptors	115
	6.9.4 NBO analysis	116
	6.9.5 Mulliken atomic charge analysis	118
	6.9.6 Molecular electrostatic potential (MEP) map analysis	120
	6.9.7 Thermodynamical Properties	121
7	Summary and suggestions for future work	123 - 126
	References	127 - 136
	List of Publications in International Journals	137
	List of conferences attended	138

# LIST OF FIGURES

Figure No.	Title	Page No.
1.1	Classifications of nucleation	3
1.2	Classification of crystal growth	4
1.3	Slow evaporation method	8
1.4	Slow cooling method	9
1.5	Temperature gradient method	10
1.6	Meirs solubility diagram	12
1.7	Scheme of an electron acceptor and donor bridge	15
2.1	Photograph of single crystal X-ray diffractometer	21
2.2	Single crystal X-ray diffractometer	21
2.3	Bragg's Law	22
2.4	Powder X-ray diffraction technique	23
2.5	Perkin Elmer FT-IR spectrometer	25
2.6	Schematic diagram of FT-IR	25
2.7	Optical arrangement of a FT-Raman instrument	27
2.8	Raman scattering phenomenon	27
2.9	Bruker RFS 27 FT-Raman spectrometer	28
2.10	Block diagram of UV-vis spectrometer	29
2.11	UV-visible spectrometer	30
2.12	Schematic diagram of Vickers diamond pyramid indenter	31
2.13	Schematic diagram of TGA	34
2.14	A Schematic diagram of differential thermal analysis	35
2.15	Photograph of photoluminescence spectrometer	37
2.16	Photograph of NMR spectrometer	38
2.17	Block diagram of scanning electron microscope	39

3.1	As grown single crystal of ACBS	45
3.2	Powder XRD pattern of ACBS	47
3.3	FTIR spectrum of ACBS	48
3.4	UV – Vis – NIR transmission spectrum of ACBS	49
3.5	Plot of (αhν) <sup>2</sup> vs. hv of ACBS crystal	50
3.6	TGA / DTA curve of ACBS crystal	51
3.7	Fluorescence spectrum of ACBS single crystal	52
3.8	<sup>1</sup> H NMR spectrum of ACBS single crystal	53
3.9	Hardness H <sub>v</sub> versus load (P) for ACBS crystal	54
3.10	Log P and Log d for ACBS crystal	55
3.11	(a) and (b) SEM pictures of ACBS crystal	56
4.1	Reaction scheme of PMB crystal	58
4.2	Solubility curve of PMB	59
4.3	As grown crystal of PMB crystal	60
4.4	Powder XRD spectrum of PMB crystal	61
4.5	(a-b) FT-IR spectrum of experimental and theoretical PMB crystal	62
4.6	(a-b) FT-Raman spectrum of experimental and theoretical PMB crystal	63
4.7	UV-visible absorption spectrum PMB crystal	65
4.8	Photoluminescence of the PMB crystal	66
4.9	TGA/DTA thermogram of PMB crystal	67
4.10	Optimized molecular structure of PMB crystal	69
4.11	Frontier molecular orbital of PMB crystal	72
4.12	The Mulliken atomic charge distribution of PMB crystal	79
4.13	Plot of Mulliken atomic charges of PMB crystal	79
4.14	Molecular electrostatic potential (MEP) map of PMB crystal	80
5.1	The photograph of PYUA crystal	83

5.2	(a) Experimental and (b) Simulated Powder XRD spectrum of PYUA crystal	84
5.3	FT-IR spectra of PYUA (a) Experimental (b) Simulated	86
5.4	(a) Experimental UV-vis –NIR spectrum of PYUA crystal (b) Theoretical UV-vis spectrum of PYUA	87
5.5	TGA/DTA plot of PYUA crystal	88
5.6	(a) Plot of load (P) versus hardness (Hv) of PYUA crystal (b) Plot of log d versus of log P of PYUA crystal	89
5.7	HOMO-LUMO energy gap of PYUA	92
5.8	(a) The plot of Mulliken and Natural Atomic Charges of PYUA crystal (b) Molecular electrostatic potential map ranges from -7.992e <sup>-2</sup> to 7.99e <sup>-2</sup> of PYUA crystal	95
5.9	(a) Hiresfeld surfaces mapped with (a) d <sub>norm</sub> (b) shape index (c) curvednesss (b) Hiresfeld surfaces mapped with transparent view (a) d <sub>norm</sub> (b) shape index (c) curvednesss (c) 2D Fingerprint plots	99
6.1	As grown crystals of APCN	103
6.2	Powder X-rd spectrum APCN crystal	105
6.3	FTIR spectrum of APCN crystal	106
6.4	UV-vis-NIR spectrum of APCN crystal	108
6.5	TGA/DTA curves of APCN crystal	109
6.6	Plot of load (P) Vs Hv	110
6.7	Plot of Log (d) Vs Log P	111
6.8	Optimized molecular structure of APCN crystal	112
6.9	HOMO and LUMO molecular orbital of APCN	114
6.10	Plot of Mulliken atomic charges of APCN crystal	120
6.11	MEP surface of APCN crystal	121

# LIST OF TABLES

Table No.	Title	Page No.
3.1	Comparison of crystal data of ACBS crystal	46
3.2	Assignments of vibrational wavenumber (cm <sup>-1</sup> ) of TU, SA and ACBS single crystals	48
4.1	FT-IR, FT-Raman and DFT frequencies with their assignments of PMB crystal	64
4.2	Experimental and optimized geometry parameters of PMB crystal computed by B3LYP/6311G* basis set	69
4.3	E <sub>HOMO</sub> , E <sub>LUMO</sub> and energy gap values of PMB crystal	72
4.4	Calculated quantum parameters and electronic properties of PMB crystal	74
4.5	The dipole moment $(\mu)$ , polarizability $(\alpha)$ hyperpolarizability $(\beta)$ of the PMB crystal	75
4.6	The significant second order perturbation theory analysis of the PMB crystal	77
4.7	Mulliken atomic charges of PMB crystal	78
5.1	Experimental and simulated (DFT) FT-IR spectral assignments of PYUA crystal	86
5.2	Experimental and geometrical parameters of PYUA crystal calculated by B3LYP/6- 31+G(d,p) basis set	91
5.3	Global chemical reactivity descriptors parameters of PYUA	93
5.4	Mulliken atomic charges and Natural population analysis	95
5.5	NBO analysis of PYUA crystal	97
5.6	Theoretically computed thermodynamic parameters of PYUA	98

6.1	Single X-rd data of APCN crystal	104
6.2	Observed IR bands of APCN crystal	107
6.3	Selected bond length, bond angles of APCN crystal obtained from theoretical and experimental data	113
6.4	GCRD Parameters of APCN crystal	115
6.5	Second-order perturbation theory analysis of the APCN in NBO basis including the stabilization energies using DFT at B3LYP 6-31+G (d, p) level	117
6.6	Mulliken atomic charges of APCN crystal	119
6.7	Thermodynamic parameters of APCN calculated by DFT/B3LYP method	122

\_\_\_\_\_

# INTRODUCTION TO CRYSTAL GROWTH TECHNIQUE

# 1.1 Introduction

Crystal growth is a fascinating area that includes materials science, optoelectronics, photonics, metallurgy, chemistry and other fields. Crystal growth has been a major research area for the past few decades, as the demand for high quality crystals has expanded to meet technological demands [1]. Modern technology cannot progress without single crystals. Crystals have evolved into modern technology's pillars, occupying a key position in the field's ever expanding scope. To fully benefit from the applications for which the crystals are employed, high quality crystals are required at this time. Crystals are divided into two categories: single crystals and polycrystals. A polycrystal is a crystal that has atoms ordered in a regular pattern over a short distance. In all three dimensions, a single crystal is a regular arrangement of atoms. Single crystal growth is definitely more difficult than polycrystalline growth (Laudise 1970).

Every day, new crystals form and new technology emerge from these crystals. In recent decades, crystal growth researchers have been piqued by the potential applications of nonlinear optical (NLO) single crystals in various photonic technologies such as optical switching, image processing, optical sensors, optoelectronics, optical data storage, optical telecommunication and others [2]. The requirement for non linear optical (NLO) single crystals is increasing every day as the variety of NLO device applications develops.

Crystal formation continues to play an essential role in both theoretical and practical research areas, as well as in applications (Jagannathan et al. 2007, James et al. 1975,

Ravindra et al. 2008). Given the increased need for materials in technological applications, higher-quality crystals are a herculean effort to achieve and this can be accomplished using theories developed in the late nineteenth century in the disciplines of crystal formation, nucleation and thermodynamics.

It takes skill to grow a crystal with the proper shape, clarity and size for a given use. Growing crystals is getting more popular among materials scientists as the size of the crystals grows larger. In the production of crystals for device applications, growing crystals free of defects and contaminants is a critical stage (Shimura 2017). Organic crystals have good optical characteristics and nonlinearity, making them interesting among the many forms of crystals. In organic crystals, delocalized π-electrons move between the electron donor and acceptor groups. It results in charge transfer between molecules, resulting in complex formation.

# 1.2 Nucleation

The first and most important phase in the crystal formation process is nucleation (Sangwal et al. 1987). Growing a crystal can be done using both simple and complicated procedures. Nucleation is defined as the set of atomic or molecular events in which atoms or molecules of a reactant phase rearrange into a cluster of the product phase large enough to grow irreversibly to a macroscopically larger size and this cluster is known as a nucleus or crucial nucleus [3]. Figure 1.1 depicts a block diagram that can be used to describe the many types of nucleation. Primary nucleation refers to both types of nucleation that occur in the absence of crystalline materials. Secondary nucleation occurs when nucleation occurs in the proximity of crystals in a supersaturated solution. The supersaturated state condition must be met by any crystallisation procedure. A series of bimolecular collisions is assumed to initiate primary nucleation, resulting in an aggregate of a few dissolved material

molecules. Secondary nucleation occurs when nucleation is aided by the presence of crystals of the same substance [4-6].

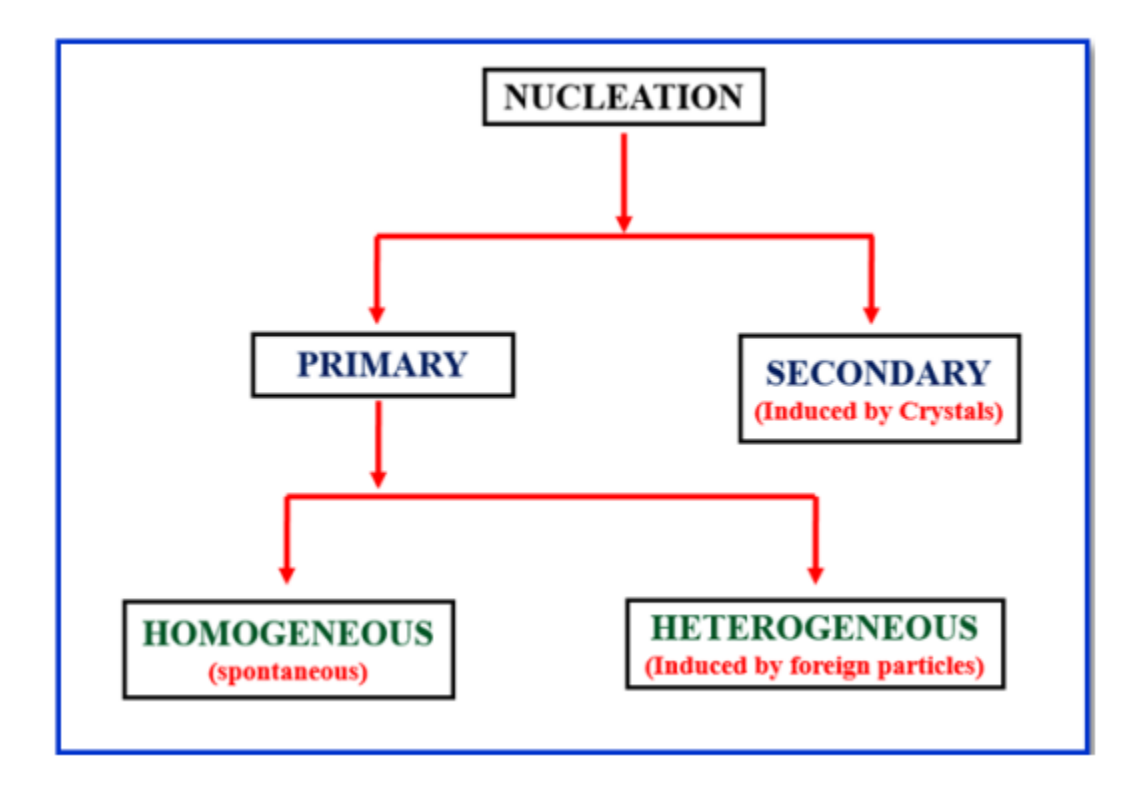


Figure 1.1 Classifications of nucleation

# 1.2.1 Primary Nucleation

Primary nucleation happens in the first step of crystallisation and is classified into two types: homogeneous and heterogeneous nucleation. In homogeneous nucleation, nuclei are formed without any external provocation, but in heterogeneous nucleation, foreign particles are induced.

# (a) Homogeneous Nucleation

When the nucleation process occurs spontaneously in the interior of the parent phase, it is referred to as homogeneous nucleation.

# (b) Heterogeneous Nucleation

Heterogeneous nucleation occurs when a nucleation process is purposefully created.

# 1.2.2 Secondary Nucleation

When new crystals develop in the presence of existing crystals in the same solution, this is known as secondary nucleation.

# 1.3 Methods of crystal growth

The intention of crystal growth is to build a massive single crystal using the optimum approach for a specific material. Crystal growth is the process of converting polycrystalline materials into a single crystal with no grain boundaries (Mullin et al. 1961). In today's era of rapid technological and scientific innovation, where crystal applications know no bounds, single crystal development plays a critical role. Crystal formation methods are widely characterised as shown in Figure 1.2. The solution growth strategy is the most popular because of its adaptability and simplicity.

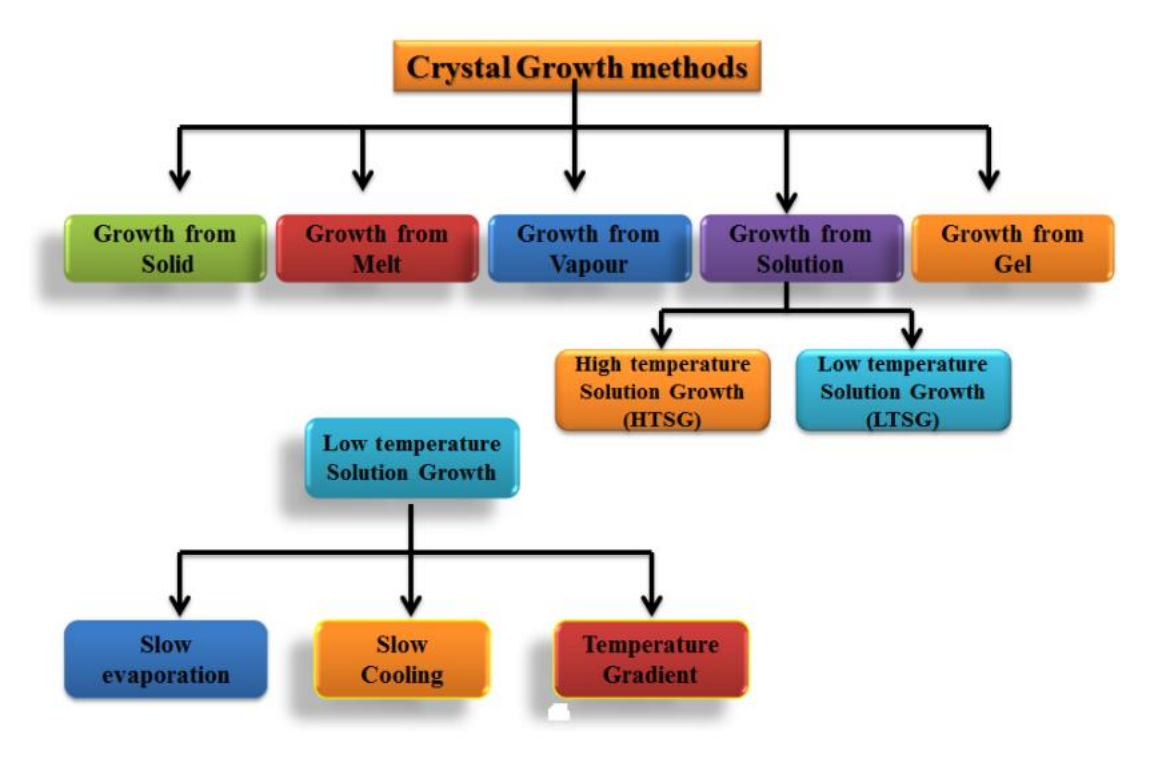


Figure 1.2 Classification of crystal growth

# 1.4 Solution Growth method

The solution growth technique is widely utilised and has been used for decades to produce a wide range of organic and inorganic crystals for various technological applications. The solution growth method is widely used to generate outstanding ferroelectric crystals, nonlinear, transparent and other materials, depending on the solvent and solubility of the solute. Crystal growth from an aqueous solution is one of the most important methods for creating high quality single crystals. Solution growth is one of the most popular ways for generating single crystal due to its versatility and simplicity. Low temperature solution growth might take weeks, months, or even years to produce crystals. There are two mechanisms for solution growth, depending on the solvents and solubility of the solute

- ➤ High temperature solution growth
- ➤ Low temperature solution growth

# 1.4.1 High Temperature Solution Growth

Single crystals are formed from materials that are not soluble at lower temperatures using this high temperature solution growth technique. Crystals are produced from a solution at a higher temperature using this method.

High temperature solution growth can be divided into two categories:

- Hydrothermal growth
- Flux growth.

# 1.4.2 Hydrothermal growth

Hydrothermal conditions are characterised by high pressure and high temperature. At low temperatures and pressures, calcite and quartz are insoluble in water, yet, at high temperatures and pressures, they are soluble. Crystal growth under high temperatures and pressures is known as hydrothermal growth. Temperatures range from 400 to 600 °C, with

a high pressure involved (hundreds or thousands of atmospheres). For growth, steel autoclaves with gold or silver linings are typically utilised. According to their pressure, autoclaves are classed as low, medium, or high pressure autoclaves. The concentration gradient required for growth is created by a temperature difference between the nutrient and growth zones. Because of the great pressure required, only a few high quality crystals with enormous diameters are formed using this procedure. In industry, quartz is a great example of hydrothermal crystallisation. A significant disadvantage of this method is the frequent inclusion of hydroxyl ions in the crystal, which makes them unsuitable for many applications.

# 1.4.3 Flux growth

Crystals of incongruently melting materials are grown using the flux growth method. A saturated material solution is formed in the flux growth procedure and the flux is held at a temperature above saturation. The temperature of the crucible is then lowered to allow crystals to form more easily. Crystals such as emerald and ruby were formed using this method, according to reports.

# 1.5 Low temperature solution growth

In the ancient method of crystal development, the low temperature solution growth method is frequently used. A solution is generated by dissolving a chemical in a liquid solvent at room temperature in this process. It's a lengthy process that can take a week, a month, or even years to complete. By setting moderate to high solubility and altering the temperature range from ambient to 100°C at constant air pressure, materials can be grown utilising the low temperature solution growth technology. In this procedure, the drug is dissolved in a suitable solvent to form a saturated solution, then crystallisation is generated by slow cooling or solvent evaporation. This process produces massive crystalline crystals of industrially significant chemicals [7-11]. After a series of experimental attempts, changes

and refinements, the solution growth procedure produces high quality, unidirectional and bulk crystals for use in technological applications (Sankaranarayanan & Ramasamy 2005). It also enables the production of materials with dimensions ranging from a micrometre to several centimetres.

This method is commonly employed for the following reasons:

- > the growth apparatus is simple and inexpensive; the low temperature imparts fewer thermal stresses into the grown crystals than melt-grown crystals.
- Researchers can analyse the crystal formation processes because emerging crystals usually have well developed surfaces (growth behaviour).

The three types of low temperature solution growth methods are as follows:

- i. Slow evaporation method
- ii. Slow cooling method
- iii. Temperature gradient method

# 1.5.1 Slow evaporation method

One of the most fundamental methods for generating crystals is the slow evaporation method. Materials that are moderately and highly soluble at room temperature are good candidates for crystal formation utilising the slow evaporation process. With non-toxic solvents like water, allowing evaporation into the atmosphere is legal. Typical growing conditions include temperature stabilisation at around ±0.005°C and evaporation rates of a few ml/hr. By evaporating extra solvent at a constant temperature, this method achieved the required supersaturation (Brice 1973). As a result, the solvent evaporates faster and the particles in the solution lose their supersaturation. It is covered with perforated aluminium foil (or) paper (or) plastic sheet. As a result, evaporation is kept under control. Transparent crystals emerged at the end. Figure 1.3 shows the creation of crystals using the slow evaporation process.

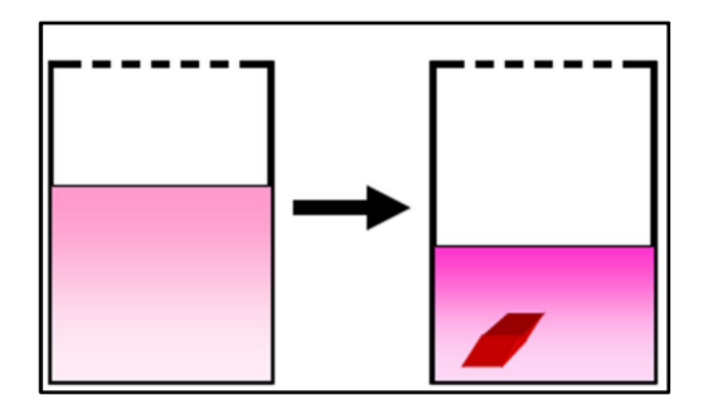


Figure 1.3 Slow evaporation method

The advantages of the slow evaporation method are as follows:

- i) Ease of use
- ii) It is less costly
- iii) Materials with a low coefficient of solubility at low temperatures are suitable.
- iv) This method can produce crystals with a wide range of morphologies and polymorphic structures.

# 1.5.2 Slow Cooling method

A gradual cooling procedure is the best way to make single crystals utilising the solution growth process. The nature of the material's solubility in the chosen solvent determines the rate at which the temperature drops. The uniform saturated solution is poured into the crystallizer and heated a few degrees above saturation temperature to avoid spontaneous nucleation. To remove dust and contaminants, the crystal growing substance is dissolved in a suitable solvent and then filtered. The solution is kept in a large water bath to increase temperature stability. It calls for the usage of a pre-programmed temperature controller. At a pace of 0.1°C/day, the temperature is dropping. For better crystallisation results, a wide range of crystallisation temperatures is not required. The method has a high success rate despite its complexity, which demands programmable temperature control. The

temperature range for such crystallisation is generally 45-75 °C, with room temperature being the lower limit of cooling [12]. Slow cooling method is depicted in Figure 1.4.

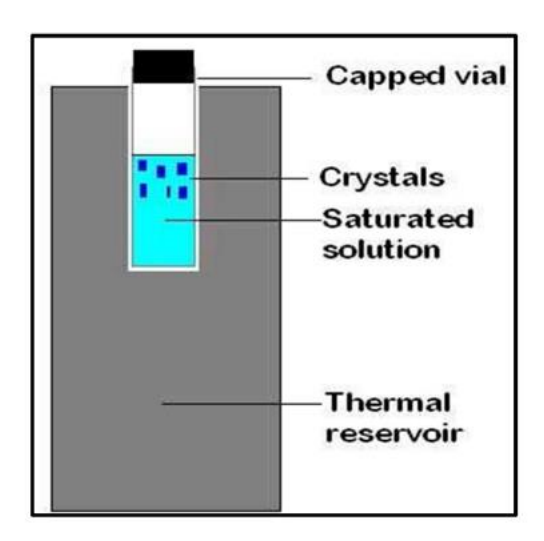


Figure 1.4 Slow cooling method

# 1.5.3 Temperature gradient method

The temperature gradient method involves two zones. Figure 1.5 illustrates this. One is a heated region that houses the source material, while the other is a cold region where crystallisation takes place. To tackle this problem, crystallizers with a three-vessel growth system consisting of a crystallizer vessel, a saturator vessel and a superheater vessel are used.

The saturator vessel has a temperature difference of 10 °C from the crystallizer vessel. The temperature of the solution in the superheater vessel will be significantly greater than the temperature in the saturator vessel. Supersaturation and crystal development occur when a saturated solution is transferred from the hot zone to the cold zone.

The following are the technique's key advantages:

- Crystals grow at a specific temperature and if both the source and the growing crystal are changed at the same time, this method is unaffected by temperature fluctuations.
- > The solvent and solute economy.

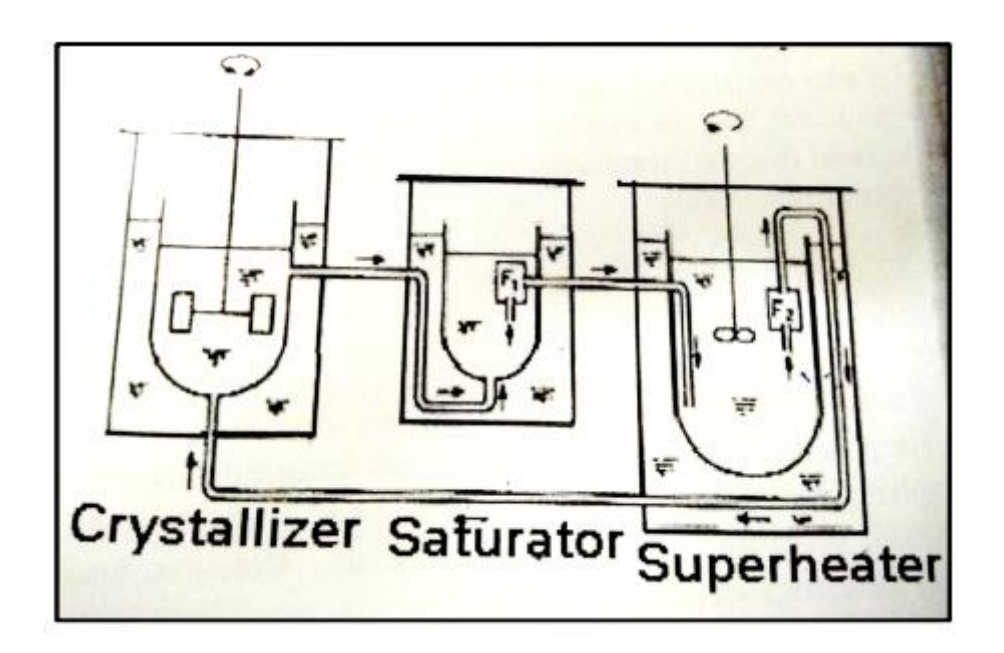


Figure 1.5 Temperature gradient method

# 1.6 Solution, Solubility and Supersaturation

# 1.6.1 Solution

A solution is a mixture of a solute and a solvent that is homogeneous in composition (Pamplin, 1979). The solute is the component that dissolves in the solution but is present in smaller amounts. More dissolved solids are found in supersaturated solutions than in equilibrium saturated fluids. For all crystallisation conditions, this is a prerequisite. For a particular solute, there may be multiple solvents. The following features of the solvent must be considered when generating crystals from the solution. For the given solute, a high amount of solute solubility.

- It has a lower density than the bulk solute and has a good solute solubility temperature coefficient.
- It has a low viscosity and a high degree of volatility.
- It is less corrosive and non-toxic.
- The size and pace of growth of the crystals are restricted by their solubility.

  The solute's solubility in the chosen solvent must be determined before the growth process can begin. The solubility gradient is another important factor that influences the development process.

# 1.6.2 Solubility

The solubility of a substance in a solvent determines the quantity of material available for crystal formation, as well as the ultimate size limit. It is difficult to generate bulk single crystals due to the high solubility and the size and development rate of the crystals are limited. Another significant component that determines the growth process is the solubility gradient. As a result, a lower viscosity solvent is preferable (Ohara & Reid 1973). Measuring a solution's solubility at various temperatures is the most popular method for assessing its saturation. Most materials' solubility increases as the temperature rises. To achieve saturation, slow evaporation processes might be applied. As a result, the solubility of the material in the chosen solvent at various temperatures must be evaluated before initiating the crystal formation process. The link between supersaturation and spontaneous crystallisation was thoroughly investigated by Meirs and Isaac (Meirs & Isaac 1987) and the results are shown in Figure 1.6. The saturated solution line separates the entire concentration temperature field into two regions: unsaturated and supersaturated states, as seen in this typical solubility diagram. As the temperature rises, so does the solubility of most compounds (the temperature coefficient of the solubility is positive). Crystals can only form in supersaturated solutions, which have more solute than the equilibrium value. The supersaturated solution region separates the metastable (stable) and labile (unstable) zones.

Nucleation will occur on its own in the labile zone. The metastable zone is the level of supersaturation in which seed crystals are required to stimulate the growth process without spontaneous nucleation.

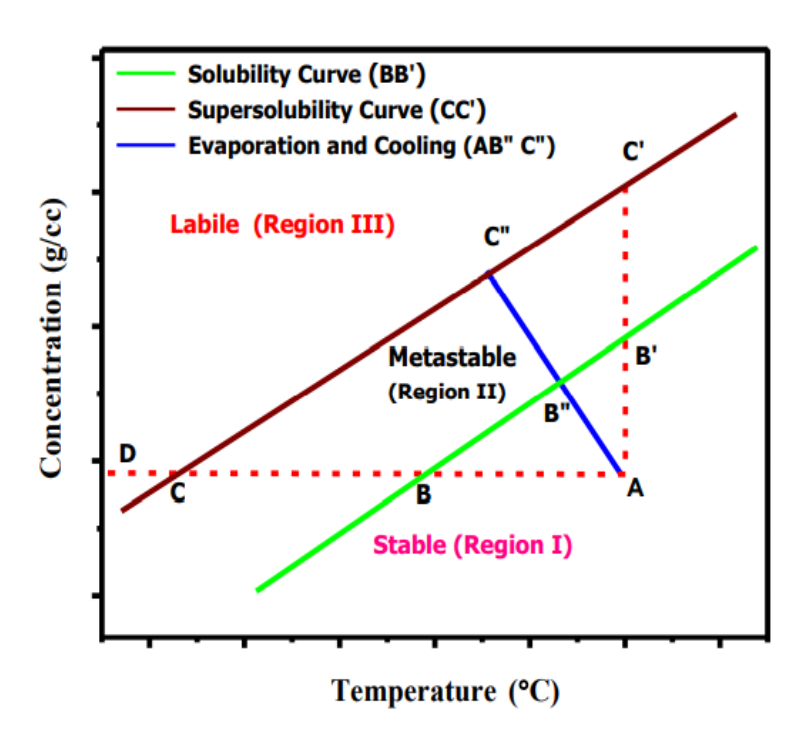


Figure 1.6 Meirs solubility diagram

The following zones are explained using the solubility diagram.

- 1. *The stable (unsaturated) zone* Crystallization is impossible above the unsaturated zone.
- 2. **The metastable (saturated) zone -** Crystallization is phenomenal in the saturated zone between the solubility (I) and super solubility (II) curves. Spontaneous crystallisation is not conceivable in this environment. The growth will be substantially enhanced if a seed crystal is placed at this stage.
- 3. The supersaturated (labile) zone where spontaneous crystallisation is possible.

#### 1.6.3 Supersaturation

**Saturated solution:** At a specific temperature, a saturated solution is one in which the required amount of solute is completely dissolved in the specified amount of solvent.

**Supersaturated solution:** For the solution growth process, supersaturation is a crucial characteristic. A solution is considered to be supersaturated when it contains more solute than the solute can dissolve at a given temperature.

**Undersaturated solution:** When a little amount of solute is dissolved in a given amount of solvent at a specific temperature, an undersaturated solution is created.

# 1.7 Nonlinear optical materials

Nonlinear optics is the maximum typically located fabric phenomenon in nonlinear media including crystals (Eaton 1991). This could be very essential in NLOs and has a large effect on records era and commercial applications. The goal is to create materials that have substantial nonlinearities while still having a fast optical reaction, a large transparency window, a high laser damage threshold, flexibility, phase matching ability and the capacity to interface with other crystals (Boyd 1989). The effort to find the best suited NLO material is ongoing, as the technological value and uses of NLO materials continue to grow. Because of their versatility, organic compounds with NLO properties are widely employed. Organic compounds are attractive because of their simple synthesis technique, which allows for the development of a wide range of new NLO materials at a low cost. Crystalline materials offer unique optical and electrical properties that are often superior to those of randomly formed materials. Many organic and inorganic materials are highly polarizable, making them ideal for NLO research. Inorganic and organic materials each have their own set of advantages and disadvantages [13], but the goal of semi organic materials is to combine the benefits of both.

# 1.8 Classification of materials

In nonlinear optical (NLO) crystals, the active medium for nonlinear processes.

These NLO crystals can be classified into three groups based on the materials used in their formation.

- Organic materials
- Inorganic materials and
- Semiorganic materials

# 1.8.1 Organic materials

Organic materials are made up of a variety of chemical changes that can be "molecularly manipulated" to acquire specific optical properties. In the manufacturing of organic crystals, nonlinear susceptibilities are high and less expensive. The NLO characteristics of large organic molecules have been the subject of much theoretical and experimental research during the last two decades (Bappalige 2012).

It has the following advantages:

- ❖ The high degree of nonlinearity
- high laser resistance (high LDT value)
- better optical responsiveness
- wide transmittance window
- fast optical response
- high thermal and mechanical stability
- high laser damage.

Many modern technologies require high speed data processing and organic materials have the ability to double or treble the frequency of laser light. Because NLO material is in such high demand in technical applications, a unique material for NLO applications is necessary, as well as phase matching capabilities. Organic compounds with both conjugated

bonds and an acceptor group on one side and a donor group on the other side are known as nonlinear optical (NLO) materials [14]. Organic materials have stronger nonlinearity than inorganic materials because organic molecules include  $\pi$  - electrons [15-16]. Figure 1.7 depicts the electron acceptor and donor bridge arrangement. The following is an example of a typical active molecule:



Fig. 1.7 Scheme of an electron acceptor and donor bridge

The optical nonlinearity of organic molecules can be improved by adding strong electron donating and withdrawing entities, as well as controlling the distance between donor and acceptor. This produces a highly polarizable charge transfer molecule with an asymmetric electron distribution.

#### 1.8.2 Inorganic materials

A quartz crystal was the first solid to exhibit second-order NLO capabilities and research of nonlinear optical effects were initially focused on pure inorganic systems. For diverse NLO applications, many effective inorganic materials have been investigated. Ammonium dihydrogen phosphate (ADP), potassium dihydrogen phosphate (KDP), potassium titanyl phosphate (KTP), lithium niobate (LiNbO<sub>3</sub>), lithium triborate (LBO) and potassium niobate are examples of these compounds (KNB). Because of their good physicochemical properties and importance in several NLO applications, materials researchers investigated LiNbO3 and KDP in the aforementioned list [17,18]. The physicochemical properties of certain inorganic crystals generated were investigated by a number of material scientists. High melting points, chemical inertness, increased

mechanical strength and susceptibility are all desirable properties of inorganic materials. However, it has a number of flaws, including a low laser damage threshold value, visible spectrum absorption, minor nonlinearity and low optical transmittance [19]. Ionically bonded inorganic crystals are the most common, because manufacturing inorganic materials is always easier. Chemically inert and with a high melting point, these are often used. Many of these materials have been successfully employed in commercial frequency doublers, mixers and parametric generators to produce coherent laser light in a new spectrum region not accessible by nonlinear crystal standard sources.

#### 1.8.3 Semi organic materials

Inorganic and organic materials are rapidly being replaced by semi-organic materials. They have both organic and inorganic properties [20]. Metal complexes of organic molecules have recently gained a lot of attention due to their strong non-linearity. Semi organic NLO crystals are projected to help both organic and inorganic materials. The materials' varied range of electrical characteristics, thermal stability and mechanical hardness, as well as facile organic processing, structural range and strong polarizability, all contribute to the advantages. In this type of crystal, organic components connect metals together to form indefinitely lengthy structures. Because it possesses both inorganic and organic characteristics, it has attracted and projected attention. They additionally function a excessive harm threshold, deliquescence, sturdy nonlinear coefficients and an extensive transparency range, making them best for tool construction.

#### 1.9 Density functional theory (DFT) method

Quantum chemical methods for computing the nonlinear optical properties of molecules have also advanced significantly, yielding numerous important insights into the optimal molecular structures and identifying a number of structure property relationships. Conjugated organic systems are especially suited for use in electro-optic modulators, optical

switches and other electronic devices due to their fast response time, nearly limitless structural modification possibilities, high NLO susceptibility and simplicity of processability. As a result, NLO materials research has centred on the development of first principles based methodologies for predicting structure property correlations in organic materials. As a result, the NLO characteristics have recently been investigated using density functional theory (DFT). They provide a physical description of the event as well as the material attributes needed for technological applications. As a result, computational materials research has a wide range of applications, ranging from providing complete knowledge of the physics underlying a technologically important event to identifying systems with relevant device properties. The use of quantum mechanics to investigate and predict molecule properties in chemical problems is known as Molecular Quantum Mechanics. To calculate solutions for many electron systems, two strong approaches, ab initio and density functional theory (DFT), were developed. Both of these theories are entirely dependent on quantum mechanical equations and their computations do not require any experimental factors. These theories can be used to compute a variety of molecular properties in addition to ground state energy and structures. Density functional theory (DFT) is the most prevalent theoretical method for investigating ground state molecule properties.

# 1.10 Scope of the present work

Organic materials outperform inorganic and semi organic materials, according to a thorough analysis of literature studies. In recent years, there has been a lot of interest in finding new organic materials that can be used in nonlinear optical (NLO) applications. The organic crystal is required for the creation of highly sensitive optoelectronic devices due to its nonlinear optical property. The classification of crystal growth processes as well as the history of crystal growth have been studied. Various crystal growth methods have been thoroughly presented, with a focus on the fundamental and experimental features of the low temperature solution growth technique. As a result, an attempt has been made to synthesis

novel organic single crystals at room temperature using the solution growth technique. In solid state and photonic device applications, the development of pyridinium based single crystals is particularly popular. As a result, the present work focuses on the synthesis, growth and thermal, mechanical, physicochemical vibrational and nonlinear optical properties of the following organic crystals,

- ➤ 4-amino-N-carbamothioyllbenzene sulfonomide (ACBS)
- Pyrazole methoxy benzaldehyde (PMB)
- > Pyridine urea (PYUA)
- ➤ Aminopyridinium chloronicotinate (APCN)

In this study, a single crystal was studied. The characterisation data were analysed and reported in this thesis utilising scientific approaches. The structure and lattice characteristics of the grown crystals were confirmed using single crystal and powder X-ray diffraction methods. To investigate functional groups and optical properties, FT-IR, FT-Raman and UV-vis spectroscopy were used. The thermal stability of the grown crystals was determined using TG/DTA analysis. The mechanical properties of the grown crystals were estimated using microhardness tests. Quantum chemistry computations utilising Density Functional Theory (DFT) were used to explore molecular polarizability, HOMO-LUMO energy gap, Mulliken charge distribution, Molecular electrostatic potential, NBO and Hirshfeld surface analysis.

#### \_\_\_\_\_\_

# **CHARACTERIZATION TECHNIQUES**

#### 2.1 Introduction

In this chapter, the working principle and instrumentation of various techniques used for sample characterization are briefly reviewed. The structural, chemical composition, physicochemical and optical properties of the grown crystal were investigated using a variety of characterization techniques. The crystal and powder samples were treated with care since the results are dependent on the purity and quality of the sample. Single crystal XRD, Powder XRD, FT-IR, FT-Raman, UV-vis-NIR, Photoluminescence, TGA/DTA investigations, Microhardness and SEM examination are among the techniques used to investigate various aspects of the grown crystals. The four important criteria that impact the properties of single crystals are purity, composition, crystallographic structure and crystal defects. The basic ideas and operation of characterization techniques used to analyze various properties of grown crystals are covered in this chapter.

Different characterizations and grown crystals are as follows,

- ❖ An X-ray diffractometer were used to confirm the structure of the grown crystals and collect the unit cell parameters.
- The various functional groups present in the molecule were confirmed using FT-IR and FT-Raman studies.
- ❖ Linear optical studies by using UV-vis-NIR spectrophotometer
- ❖ TGA/DTA analysis was used to determine the thermal stability of the grown crystals.

- The mechanical behavior of the grown crystals is investigated using Vicker's hardness test.
- ❖ A scanning electron microscope is used to examine the surface morphology of the produced crystals (SEM).

#### 2.2 Single Crystal X-ray diffraction

The crystal structure of all the grown crystals was examined using single crystal X-ray diffraction (SXRD). The size of unit cells and the positions of atoms in the crystal sample were determined using the single crystal XRD technique. Atomic positions are directly related to bond lengths and bond angles [21]. By selecting optically acceptable quality crystals, data was obtained using SXRD. Diffraction data were collected at 294 K with molybdenum K as the source (λ=0.71073) using a Bruker Kappa apex II X-ray diffractometer. The data were collected and the structures were solved using SHELXS-97 [22-24]. During the experiment, X-rays were produced using a cathode ray tube and focused at the crystal. Interference is formed when incident x-rays are reflected back and obey Bragg's law (n=2dsinθ). The collimator allows X-rays to flow through and make contact with the crystal (Figures 2.1 and 2.2). Rays can pass through the crystal, be reflected off the surface, or diffracted by the crystal's lattice. Interference occurs when incident x-rays are reflected back. Three goniometers in the diffractometer gather the diffracted X-rays. These goniometers gather the X-rays reflected in all three axes (x, y and z). Rays can pass through the crystal, be reflected off the surface, or diffracted by the crystal's lattice. A beam stop is put in front of the collimator to limit transmitted photons and prevent the detector from blowing up. The sensor does not pick up the reflected light due to the angles involved. The detector subsequently collects diffracted photons in the setup's proper orientation.



Figure 2.1. Photograph of single crystal X-ray diffractometer



Figure 2.2 Single crystal X-ray diffractometer

# 2.2.1 X-ray Powder diffractometer

For measuring unit cell sizes and identifying powdered crystalline material, it is the most basic analytical procedure. X-ray powder diffraction (XRD) is a rapid analytical technique for determining unit cell dimensions and is used to detect crystalline material phases [25]. The crystallinity of the crystals generated in this analysis were determined by powder X-ray diffraction analysis. X-ray powder diffraction were used to analyze the

structure, composition and condition of polycrystalline materials. A correctly produced sample of a powdered solid will present a completely random selection of all possible crystal faces at the powder interface and diffraction of this surface will show all possible atomic spacings in the crystal surface.

When X-rays are passed through a sample, electrons from atoms existing in the substance scatter them in the original direction. Because Bragg's law was satisfied, the scattered waves constructively interfered. In Figure.2.3, an X-ray beam is reflected from two parallel lattice plates at the same time. We can more easily determine the size and shape of the unit cell for any compound by using the diffraction of the X-ray path difference between two waves:

$$2 \times \text{wavelength}(\lambda) = 2\text{dsin}\theta$$
 (2.1)

This leads to the Bragg equation

$$n \lambda = 2 d \sin \theta$$

 $\lambda$  = wavelength of the incident beam, d = distance between the planes in crystal,  $\theta$  = angle of beam diffraction. The reflected X-rays will be in phase when the relationship is satisfied and this process is termed as constructive interference.

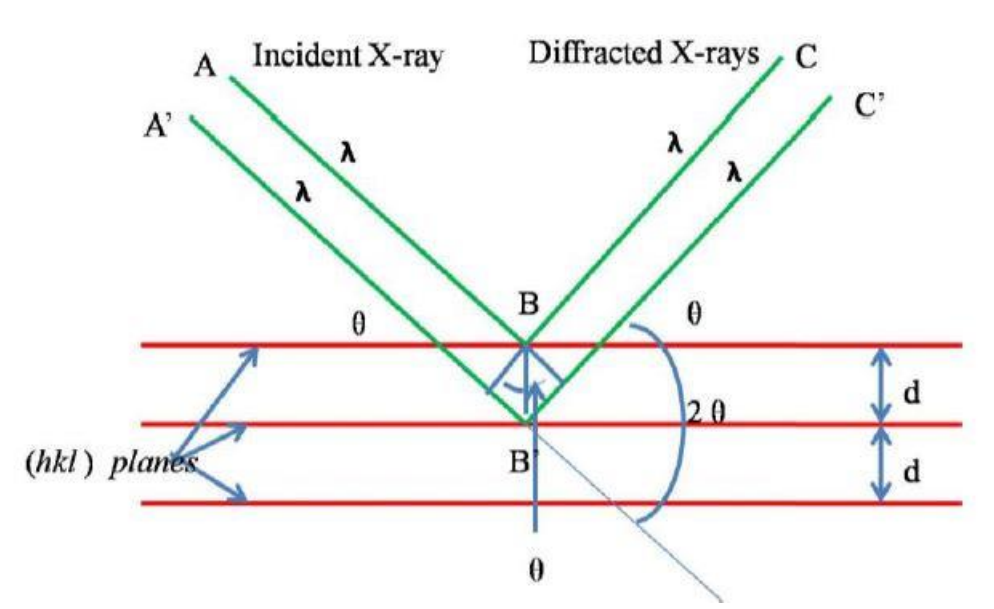


Figure 2.3 Bragg's Law

Figure 2.4 depicts a powder X-ray diffractometer schematically. For common powder patterns found in the X-ray scan, data is collected at two angles ranging from  $10^{\circ}$  to  $80^{\circ}$ . A Bruker Nonius Kappa Apex II, CCD diffractometer system with Cu  $K_{\alpha}$  ( $\lambda$ = 1.5418) radiation were used to investigate powder X-ray diffraction on finely crushed crystal powder. The sample was scanned at a rate of one per minute. The diffraction peaks created by d-spacing may be used to identify the material because each material has its own set of d-spacing. To achieve this, the d-spacing is compared to several common reference patterns. To acquire the crystal structure, Redfield refinement is employed and this process may also be used to determine sample purity. All conceivable diffraction lattice planes must be examined for a full characterization of the material.

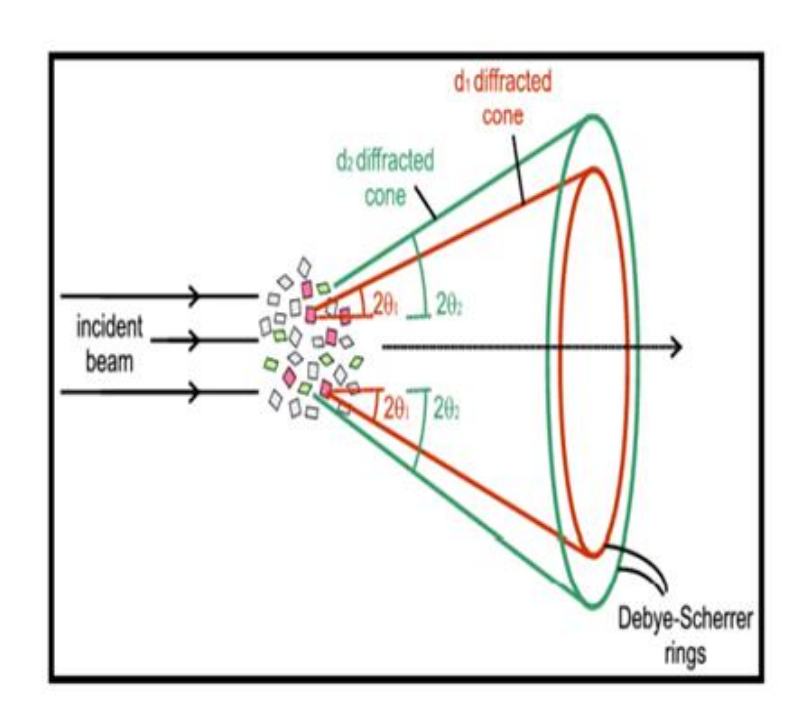


Figure 2.4 Powder X-ray diffraction technique

#### 2.3 FT-IR spectral analysis

It is one of the most commonly used methods for determining the functional groups contained in a grown crystal. The Fourier transform interferometer employed in this study passes light from an acceptable infrared (IR) source. The background emission spectra of

the IR source are recorded first, followed by the emission spectrum of the IR source with the sample in position. The absorption spectrum of the sample is proportional to the sample spectrum to background spectrum ratio. The absorption spectrum produced by the natural vibration frequencies of chemical bonds and functional groups in the sample demonstrates that the sample has a variety of chemical bonds and functional groups. The frequency range of 4000 to 1500 cm<sup>-1</sup> is classified as the functional group zone. The peaks in this region represent the functional groups of the molecule. A fingerprint region is defined as the frequency range between 1500 and 600 cm<sup>-1</sup>. The mid-IR range is used in a wide range of analytical applications. It gives the molecules a distinct fingerprint that can be differentiated from the absorption patterns of other vibrations. In this investigation, the IR spectra of the grown crystals were recorded using the KBr pellet method. As shown in Figure 2.5, the FT-IR spectra were obtained using a Perkin Elmer FT-IR spectrometer. All of the samples were made with KBr pellets and the IR spectra were captured in the 4000-400 cm<sup>-1</sup> region. The schematic diagram of FT-IR is shown in Figure 2.6. The incident radiation is split into two beams by a beam splitter in the FTIR spectrometer. One beam is permitted to pass via a stationary mirror and is reflected back to the beam splitter. A second beam is directed at a moving mirror and reflected back to the beam splitter.

After passing through the sample, the resulting beam is focused on the detector. When the two beams meet at the beam splitter, there are both constructive and destructive interferences. Depending on the type of the connection and binding strength, the molecules' vibrations were observed at different wavenumbers. After passing this combined laser over the sample, the spectrum produced were recorded. Theoretically, measuring wide band radiation travelling through the material should result in a broad infrared spectrum [26].



Figure 2.5 Perkin-Elmer FT-IR spectrometer

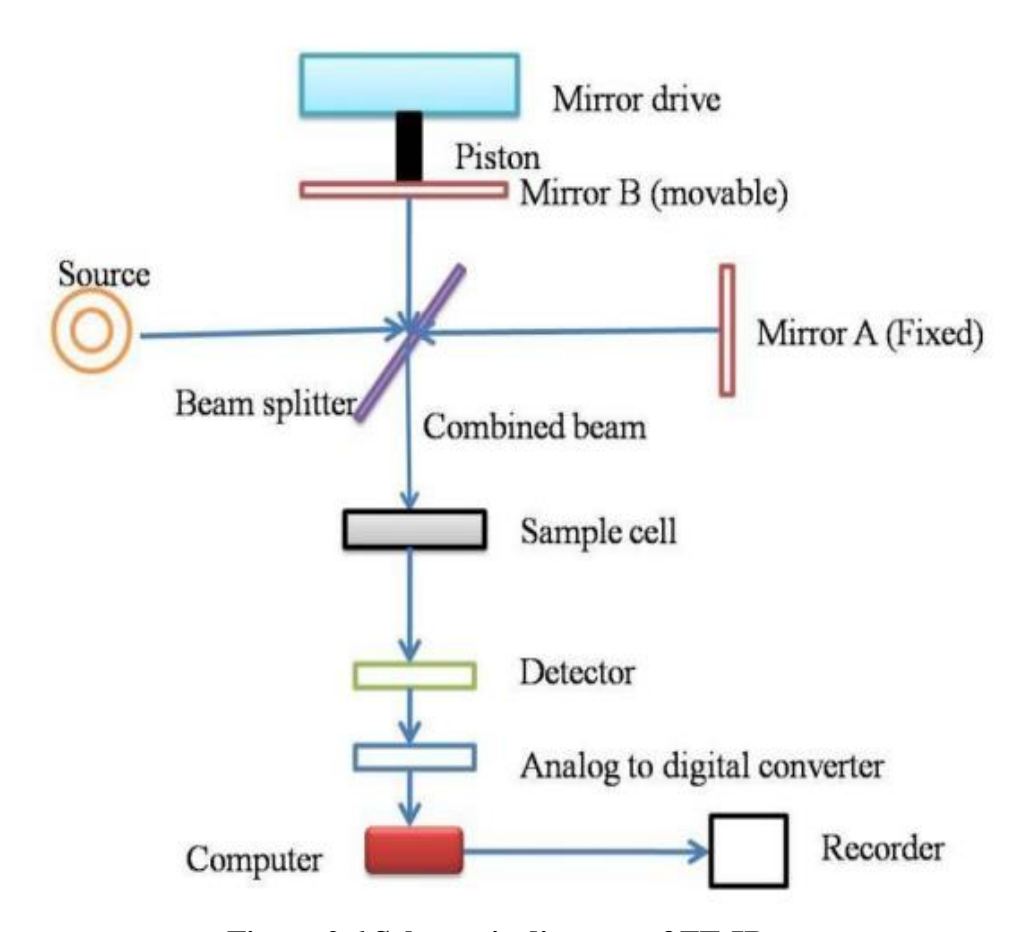


Figure 2.6 Schematic diagram of FT-IR

#### 2.3.1 Instrumentation FT-Raman

The FT-Raman spectrum is a complement to the infrared IR spectrum and it's likely to be useful for detecting certain compounds. The Raman band is intense, similar to IR bands and its location is influenced by the kind of replacement and group geometry. It's commonly used to investigate both qualitatively and quantitatively covalently bonded chemical molecules. Raman spectroscopy provides vibrational information that is specific to chemical bonding and symmetry in molecules [27].

The Fourier transformation Raman spectroscopy, as opposed to absorption, is concerned with the scattering of radiation by the material. It works on the basis of inelastic photon scattering by molecules. The vibrational, rotational and other low-frequency modes in the system are studied using the FT-Raman spectroscopy method. The FT-Raman spectrometer is depicted schematically in Figure 2.7. With a wavelength of 1064 nm, the laser source is an Nd: YAG laser. The light from the spot is captured using a lens and allowed to travel through a monochromator.

Due to elastic Rayleigh scattering, wavelengths closer to the laser line are filtered out. The remaining light is distributed onto a detector. When a molecule relaxes, it emits a photon before returning to a different rotational or vibrational state. A frequency shift in the released photon is caused by the energy difference between the original and new states. Raman scattering is a phenomena that may be observed in Figure 2.8. The FT-Raman spectrum acquired for the sample using a Bruker RFS 27 standalone FT-Raman spectrometer in the range 4000 - 50 cm<sup>-1</sup> is shown in Figure 2.9.

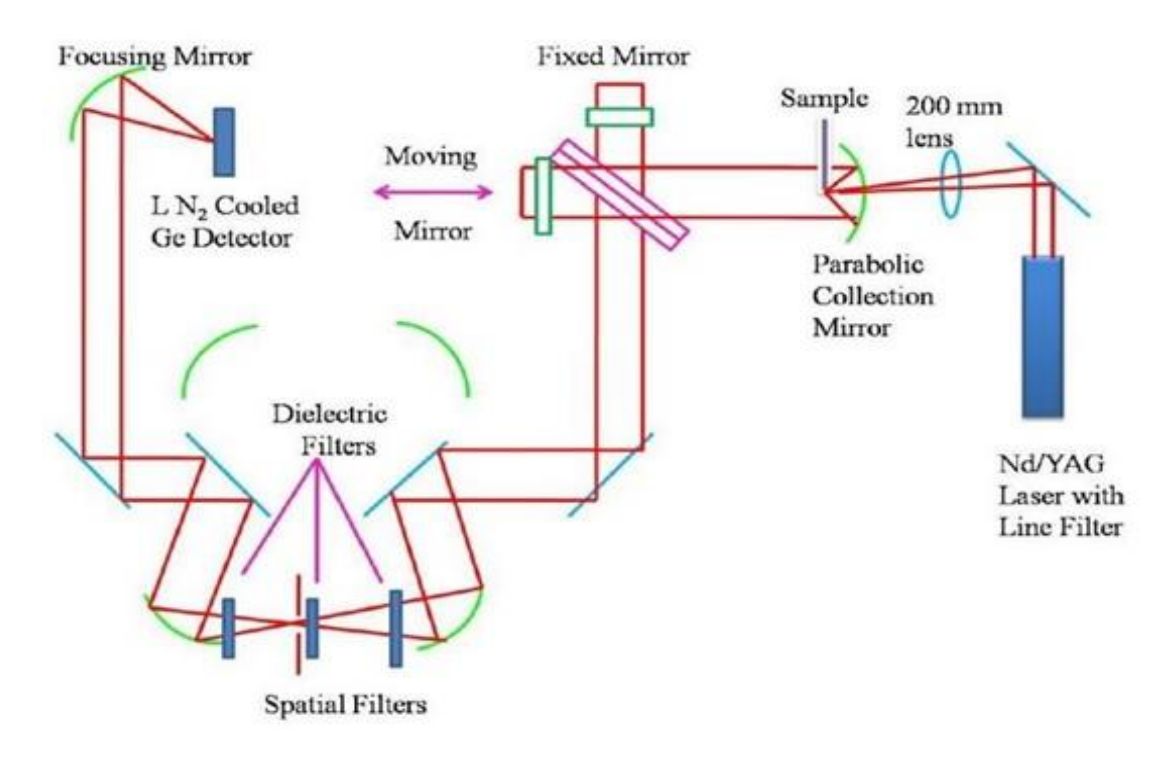


Figure 2.7 Optical arrangement of a FT-Raman instrument

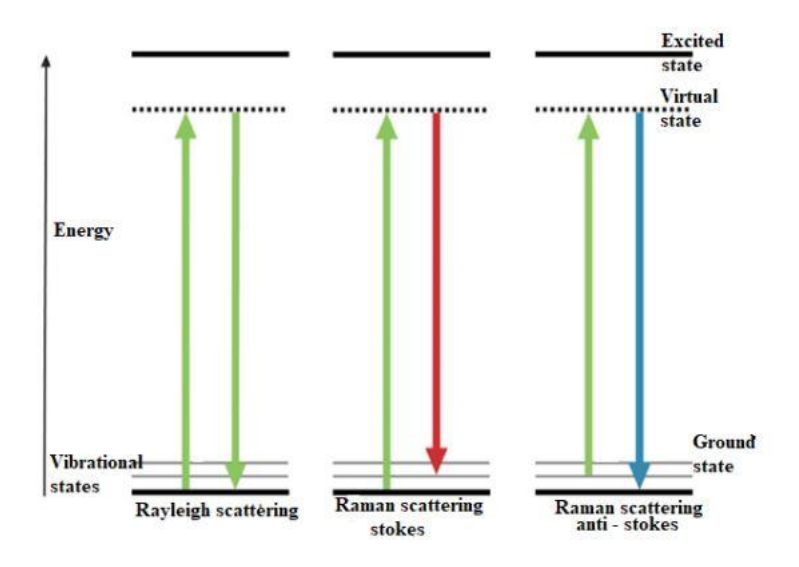


Figure 2.8 Raman scattering phenomenon



Figure 2.9 Bruker RFS 27 FT-Raman spectrometer

It differs from fluorescence, which involves the molecule being excited to a definite (rather than virtual) energy level. The energy shift reveals which phonon modes are present in the system.

#### 2.4 UV spectral analysis

Using a SHIMADZU 1800 UV-Vis spectrophotometer, the crystal's UV-Visible spectrum was recorded in the wavelength range of 190 to 900 nm. A light source, a monochromator that separates the wavelengths of radiation, a sample compartment and a detector that detects the quantity of light transmitted by the sample comprise the spectrophotometer (Figure 2.10). A small bandwidth was chosen with the use of bandpass filters. The intensity differences between the two beams were then measured electronically after the two rays were combined. The radiation used had a wavelength of 190 to 900 nm and the sources were a deuterium lamp and a tungsten lamp.

Following that, the radiation was passed alternately through the crystal and the solvent. This approach uses two beams to eliminate the intensity changes caused by radiation scattering and solvent effects. The intensity differences between the two beams

were measured electronically since they were combined. The monochromator and recorder movements were synced and modified so that the record shows the right radiation intensity. In the transmission investigation, the intensity was assessed in terms of transmittance in percentage along the y-axis and wavelength along the x-axis.

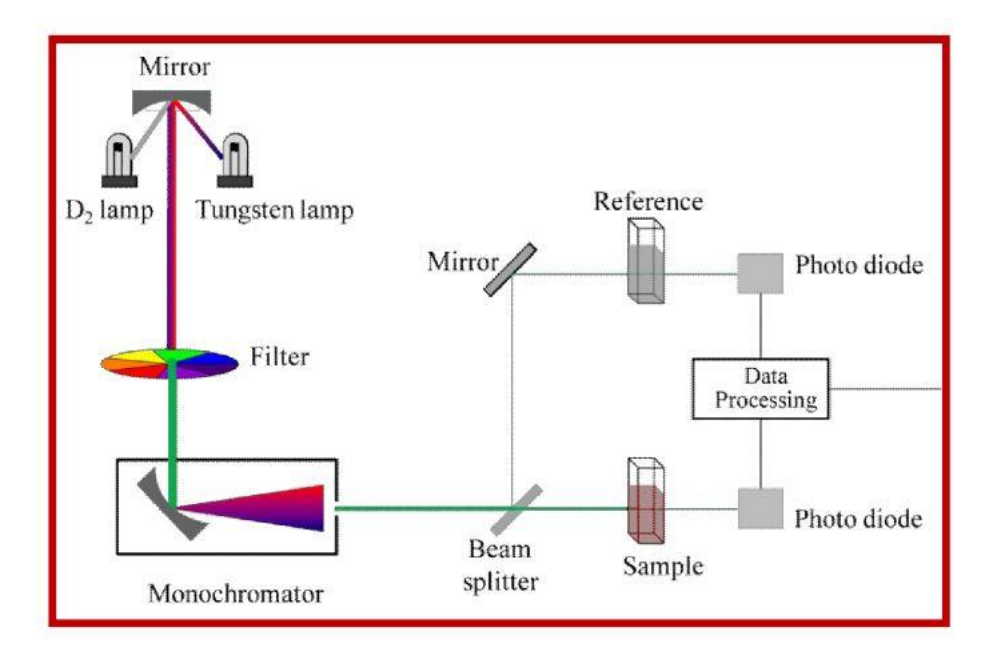


Figure 2.10 Block diagram of UV-vis spectrometer

The optical transmittance spectrum was acquired for the wavelength range of 200 to 1100 nm and provides information on the crystal's optical cut-off value. Depending on the bandgap of the material, energy is absorbed in a specific wavelength while passing through light radiation. The relation may be used to get the optical an of any crystal

$$\alpha = \frac{2.303 \log(\frac{1}{T})}{t} \tag{2.2}$$

T stands for optical transmittance and t stands for crystal thickness. Additionally, the optical is provided by

$$\alpha = \frac{A(h\nu - E_g)^{1/2}}{h\nu} \tag{2.3}$$

A is a proportionality constant and Eg is the photon's energy. Furthermore, by using T to show the photograph of the UV-Visible spectrometer (Figure 2.11), the bandgap value of the crystal may be derived from the observed transmittance data.



Figure 2.11 UV-visible spectrometer

#### 2.5 Microhardness Analysis

Microhardness investigations of the grown crystal are crucial in establishing the material's mechanical stability. In device manufacture, a crystal's hardness value is significant, because it's linked to laser damage and bond strength. Hardness tests are often used to determine a material's mechanical strength and they are related to other mechanical parameters such as elastic constants, brittleness index and yield strength. This measurement can be classified as a macro, micro, or nano by applying force to the crystal and displacement is obtained.

A procedure in which a crystal is subjected to relatively high pressure in a limited location is known as hardness. Hardness tests on all crystalline materials may be easily performed under a variety of temperature and pressure conditions by using the right indenter material and very simple equipment construction. Because the deformation is limited, multiple trials can be performed on a single small specimen and the results can be replicated by keeping the specimen indenter orientation connection. Brinell, Vickers and Rockwell are the three main standard test methods for expressing the relationship between hardness and impression size. The Vickers hardness test method is the most frequent and reliable of these hardness assessment procedures. A diamond indenter is used to make a micro indentation on the surface of a specimen in this method (Figure 2.12).

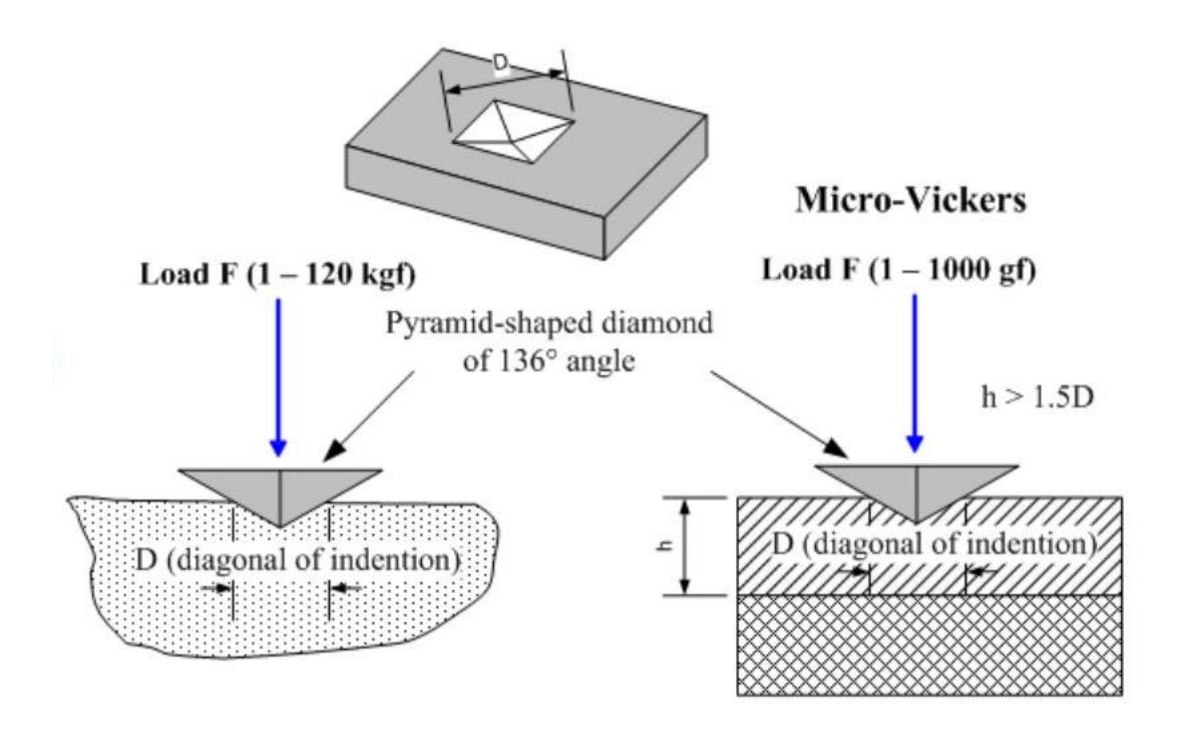


Fig. 2.12 Schematic diagram of Vickers diamond pyramid indenter

A pyramid may be used in place of a ball to offer geometrical similation under varying loads [28]. The Vickers pyramid indenter, which has an angle ( $\alpha = 136^{\circ}$ ) on opposite

faces, is the most frequently approved pyramid indenter. The following two factors make a pyramid ideal for hardness tests.

- A pyramid indenter's contact pressure is independent of the size of the indent.
- > Pyramid indenters are less impacted by elastic release than other indenters.

The ratio of the load applied to the indentation's surface area is commonly referred to as hardness. The Vickers hardness number, often known as the Diamond Pyramid Number (DPN) is given by

$$H_{v} = (2 \text{ P} \sin \alpha/2) / d^2 \text{ kg/mm}^2$$
 (2.4)

where  $\alpha$  is the indenter's apex angle = 136°. As a result, the Vickers hardness number is computed using the formula

$$H_v = 1.8544 \text{ P} / d^2 \text{ kg/mm}^2$$
 (2.5)

Here, *P* is the applied load in kg, d denotes the average diagonal length of the indentation portion in mm and Hv denotes the Vickers hardness number.

The size of the impression left after a loaded indenter has penetrated and been removed from the surface is used to calculate hardness values. As a result, the reported hardness behavior in the final measurement of the residual impression is the total of several processes involved in the material's reaction to indentation pressure during loading [29].

Microhardness measurements were taken with a Vickers microhardness indentor in this investigation (Leitz Weitzier hardness tester). The work hardening coefficient (n) is calculated by plotting log P versus log d and calculating the slope of the plot. Hardness testing gives useful information on the strength and deformation characteristics of materials [30]. Microhardness is a measure of mechanical property.

# 2.6 Thermal analysis

Thermogravimetric (TG) analysis provides information on the sample's thermal stability and various stages of decomposition as the temperature rises. A thermo-balance is used in this analysis to determine the mass changes that occur throughout a temperature range and the data can be shown as a plot of mass loss vs temperature. Thermal analysis is a material science subject that investigates how temperature influences the thermophysical and kinetic properties of materials [31]. Furthermore, thermo gravimetric and differential thermal analyses are frequently employed in conjunction because any one of the studies alone will not provide enough data to investigate the physicochemical changes in the sample during heating. The rate of change of mass with respect to time and temperature is plotted in a derivative thermogravimetric (DTG) analysis.

#### 2.6.1 Thermogravimetric analysis

This is a method of observing the change in weight of a substance as a function of temperature over time. Temperature is gradually increased for a known initial weight of a substance and weight variations are carefully recorded at various stages. A thermogram or thermogravimetric curve is a graph that shows the relationship between a substance's weight and temperature. This method is used to determine the amount of inorganic and organic components in materials, as well as solvent residues, degradation temperatures, explosive decomposition points and absorbed moisture content. Figure. 2.13 shows a schematic diagram of the TGA.

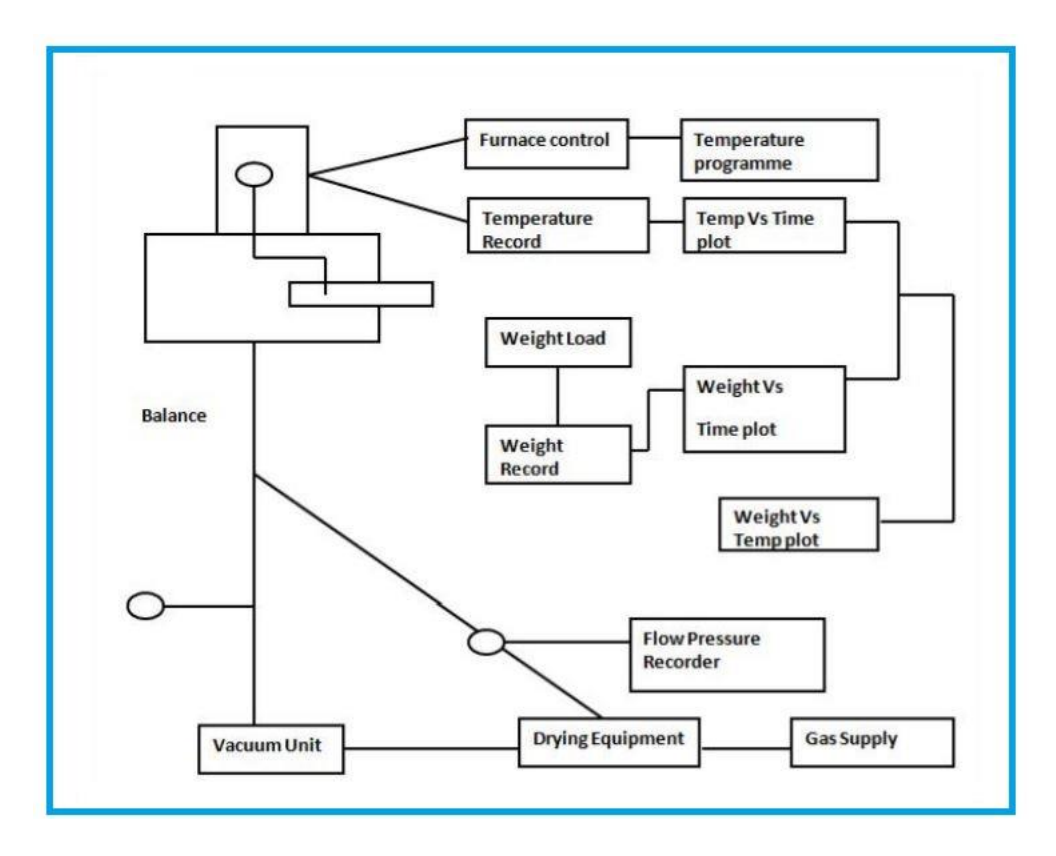


Figure 2.13 schematic diagram of TGA

- A furnace can be heated in such a way that the temperature rises in a linear fashion overtime.
- A thermobalance with high precision.
- > TGA devices that are very advanced electronic based and pricey are now available.

#### 2.6.2 Differential thermal analysis

Differential thermal analysis (DTA), which is frequently thought of as a supplement to TG is, in fact, more adaptable and produces data of a far more fundamental nature. Because both the sample and the inert reference materials are subjected to identical thermal regimes, the procedure is simple. It entails measuring the temperature differential between the sample and the inert reference materials in a heated or cooled environment at a constant pace. The energy difference between the products and the reagents, or between the two phases of a substance, is the source of the temperature differential in the sample. Enthalpy

changes, both exothermic and endothermic, show this energy differential. Figure 2.14 shows a schematic representation of a current differential thermal analysis.

DTA determines these qualities by comparing the sample's temperature to that of a reference material that is inert in similar conditions. This temperature difference is calculated as a function of time or temperature in a controlled environment and it offers information not only about the transition temperature but also about its thermodynamics and kinetics [32,33].

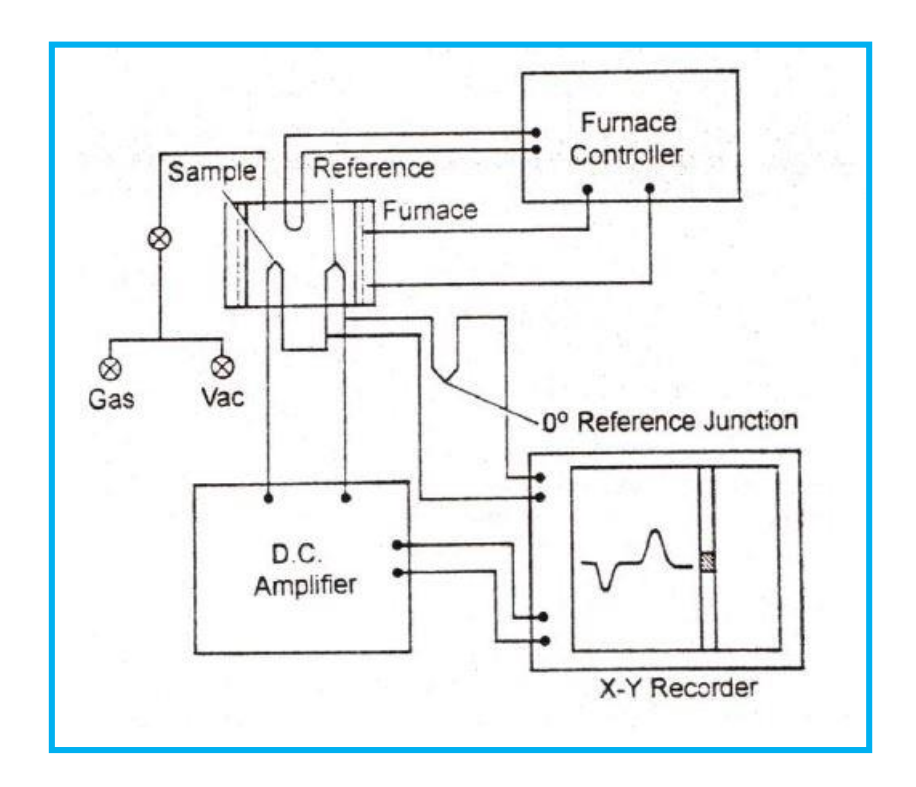


Figure 2.14 A Schematic diagram of differential thermal analysis

Until the sample's physical or chemical condition changes, the differential thermal curve will be parallel to the temperature axis (time). However, after the sample has achieved the temperature of this transition of state, the additional heat flow reaching the sample will not increase the sample's temperature at the same rate as the reference, resulting in a peak in the differential signal. Only after the sample's change in status is complete and the

temperature is the same as the reference material would the differential signal return to the baseline.

The thermal impacts are visible as peaks whose sequence (on the temperature scale), sign (endothermic or exothermic), amplitude and form reflect the physical or chemical changes that take place. The DTA method is applicable to all of the studies listed for TG, as well as phase transformations such as polymerization, phase balance and chemical reactions because any change in the chemical or physical state of a substance is accompanied by energy changes that manifest themselves in the form of heat changes.

#### 2.7 Photoluminescence study

Photoluminescence (PL) is an electromagnetic spectroscopy technique that examines a sample's fluorescence. It entails utilizing a beam of light, typically ultraviolet light, to excite the electrons in specific compounds' molecules, causing them to emit lower-energy light. In photoluminescence, light absorption causes a transition from the ground state to an excited state of an atom or molecule, after which the system undergoes non-radioactive internal relaxation and the excited electron moves to a more stable excited level; the electronic system then returns to the ground state after a characteristic lifetime in the excited state. The energy is released in the form of light and photoluminescence is used to detect this emitted light. The sample compartment module, which includes a Xenon bulb, uses 450 watts.

Because it delivers a constant output from 200 nm to 800 nm, this high pressure Xenon lamp is commonly employed in instrumentation. The spectral dependence of the intensity of the photoluminescence spectrum can reveal information about the material's qualities. The PL emission including defect level transitions may also be used to assess the existence of defects in materials, allowing the quality of materials to be determined. The photo of the Photoluminescence spectrophotometer is shown in Figure 2.15.



Figure 2.15 Photograph of photoluminescence spectrometer

An emission spectrum is a plot of emission against wavelength for all possible excitation wavelengths. The excitation spectrum is the result of changing the excitation wavelength and plotting the emission from the sample versus the wavelength of stimulating light. The luminescence attribute of a material is determined by its emission spectrum. The photoluminescence signal's intensity provides crucial information about the materials' purity and crystalline quality.

#### 2.8 Nuclear Magnetic Resonance (NMR) Spectroscopy

In general, <sup>1</sup>H NMR spectra were used to determine the position of hydrogen atoms in organic materials. The proton (<sup>1</sup>H) NMR is the most researched nucleus and the technique is known as proton NMR spectroscopy. Proton NMR confirms the number of hydrogen atoms present in the molecule. Proton NMR provides information on the many types of protons in a molecule. The number of protons of each kind and the ratio of different types of protons in the molecule can also be determined using <sup>1</sup>H NMR spectra. The absorption process involves the nuclei of the atoms. The change in magnetic dipole moment between the permissible spin states causes the absorption. NMR spectra are said to provide a molecule's "fingerprint" and may also reveal information about functional groups present in the substance. It's also excellent for resolving very close peaks in 2D spectra or compounds

with a small number of protons [34, 35]. The <sup>1</sup>H is used to indicate where hydrogen atoms in a molecule are located. It's one of the most effective methods for figuring out the structure of biological compounds. A 400 MHz Bruker NMR spectrometer was used to record the <sup>1</sup>H NMR of the samples. The powdered crystal samples were dissolved in deuterated chloroform and then subjected to analysis. The prepared sample was held under a strong magnetic field. The nucleus is oriented to the magnetic field direction at higher magnetic fields. The sample is then bombarded with radio waves, which the nucleus absorbs and reemits depending on its environment. The positions of hydrogen and carbon present in the sample were ascribed to the corresponding peaks detected. Figure 2.16 depicts an image of the NMR spectrometer.



Figure 2.16 Photograph of NMR spectrometer

# 2.9 Scanning electron microscope analysis

The scanning electron microscope (SEM) is a device that can measure features as small as nm. Fully automated and semi-automated SEMs are used in the technology sector and other high tech manufacturing. In a scanning electron microscope, an image is formed and shown by a very fine electron beam focused on the surface of an object. The surface morphology was examined to use a JEOL JSM 5610 LV scanning electron microscope with a resolution of 3.0 nm and an acceleration voltage of 0.3 to 30 kV with a maximum magnification of 3,00,000 times (Figure 2.17). The scanning electron microscope (SEM) is a fantastic tool for uncovering the hidden world of micro space. It can display extremely detailed three dimensional images at a considerably higher magnification than an optical microscope can. A high energy electron beam is emitted by an electron gun (at the top). This beam descends via a succession of magnetic lenses that focus the electrons into a very small area. Secondary electrons are knocked loose from the sample's surface as the electron beam hits each area. These electrons are counted by a detector, which transfers the signals to an amplifier. The number of electrons emitted from each place on the sample is used to create the final image.



Figure 2.17 Block diagram of scanning electron microscope

# 2.10 Computational details

Quantum chemical calculations provide information on the molecule's electrical charge, energy and dipole moment. Density Functional Theory (DFT) was used to perform all of the quantum chemistry calculations for all of the molecules at the B3LYP level, using the Gaussian 09 software package. The optimized bond angle, bond length and dihedral angles were noted and compared to the experimental values after the molecules were optimized using the CIF file of the molecule. Additional molecular properties were investigated, including the Frontier molecular orbital (FMO), Global chemical reactivity descriptive attributes, Mulliken atomic charge analysis and the molecular electrostatic potential (MEP) map.

#### 2.10.1 Frontier molecular orbital analysis

The FMO study reveals the molecule's chemical reactivity in the  $\pi$ -conjugated electron system [36]. The chemical reactivity, kinetic stability, chemical hardness and softness of a molecule are all determined by the energy gap between the HOMO and LUMO orbitals. Furthermore, the energy value has a significant impact on molecular charge transport properties.

By using the energy values of HOMO and LUMO, some of the properties of the molecule were calculated such as chemical hardness ( $\eta$ ), electronegativity ( $\chi$ ) and electrophilicity index ( $\omega$ ). The chemical hardness value of the compound determines the chemical stability. The chemical hardness is given by the relation,

$$H = (E_{LUMO} - E_{HOMO}) / 2 \tag{2.6}$$

The electronegativity value is the ability of an atom to attract an electron and is determined by the relationship,

 $E_{\text{HOMO}}$  and  $E_{\text{LUMO}}$  are the energy values of the HOMO and LUMO orbitals, respectively. The global electrophilic index is calculated as follows:

$$\omega = \frac{\mu^2}{2\eta} \tag{2.7}$$

Where  $\mu$  is the chemical potential.

The relationship between ionization potential and electron affinity is:

Ionization potential  $(I) = -E_{HOMO}$ 

Electron affinity  $(A) = -E_{LUMO}$ 

The molecule's HOMO and LUMO energies are E<sub>HOMO</sub> and E<sub>LUMO</sub>, respectively.

#### 2.10.2 Mulliken atomic charge analysis

It depicts the molecule's charge distribution and net charge in the simplest way possible [37]. The Mulliken atomic charge study of a molecule reveals the total charge of the molecule [38]. The atomic population of a group of atoms is calculated by adding all of their atomic orbitals. The DFT technique was used to study the Mulliken charge analysis of all the compounds and the results were depicted as a bar diagram and discussed in the appropriate chapters.

#### 2.10.3 Molecular electrostatic potential map analysis

The electrophilic and nucleophilic sites of a molecule can be identified using molecular electrostatic potential (MEP). The MEP of all molecules was produced using the Gauss view 5.0 programme. In MEP mapping, the various electrostatic potentials of the surface are represented by different colours. The nucleophilic sites have the most positive charge, which is represented by the blue colour in the MEP. Similarly, the electrophilic sites are shown by the surface's negative charge, which is shown in red. In the order red < orange < yellow < blue, the potential increases from negative to positive.

#### 2.10.4 Hirshfeld surface analysis

A well known and efficient method for studying and evaluating a molecule's strength and intermolecular interactions is Hirshfeld surface analysis [39]. The 3-dimensional Hirshfeld surface and 2-dimensional fingerprint map of the molecules were generated using Crystal Explorer 3.1. The molecule's 3D surface was calculated using d<sub>norm</sub> (normalized contact distance), curvedness and shape index. Three colours represent the created d<sub>norm</sub> surface white, blue and red. The negative and positive values of d<sub>norm</sub> are represented by the three different colors on the surface. The value of d<sub>norm</sub> is displayed in red if it is bigger than the Van der Waals radii. Similarly, the d<sub>norm</sub> is displayed in blue if it is smaller than the Van der Waals radii. When d<sub>norm</sub> equals Van der Waals radii, it's displayed in white.

The normalized contact distance is calculated as follows:

$$d_{\text{norm}} = \frac{d_i - r_i^{\text{vdw}}}{r_i^{\text{vdw}}} + \frac{d_e - r_e^{\text{vdw}}}{r_e^{\text{vdw}}}$$
(2.8)

Where  $d_e$  is the distance between the outside of the nearest nuclei's surface and the point on the surface,  $d_i$  is the distance between the interior of the nearest nuclei's surface and vdW is the atom's Van der Waals radii.

\_\_\_\_\_

# GROWTH AND CHARACTERIZATION OF 4-AMINO-N-CARBAMOTHIOYLBENZENE SULFONAMIDE: NONLINEAR OPTICAL SINGLE CRYSTAL

\_\_\_\_\_

#### 3.1 Introduction

Nonlinear Optical (NLO) materials are a scientifically important class of materials which find applications in the area of fiber optic communication, laser technology, optical switching and optical signal processing [40]. Organic materials of the are exquisite interest within the synthesis of materials with NLO properties and they additionally provide a chance to use theoretical modeling [41, 42]. In the past decades, considerable research work has shown the organic materials can exhibit NLO efficiencies which can be two orders of value more than the counterpart inorganic crystals [43, 44]. From the device factor of view, the NLO materials are usually used within the shape single crystals they must satisfy kind of material necessities for optical usage [45]. The organic crystals exhibit excellent nonlinear properties due to their electronic structure  $\pi$ -conjugated structures among donors and acceptors [46, 47]. This is because of non - centrosymmetry nature which leading to large NLO performance, showed by way of organic crystals of the order of 10 to 100 times of large than that of inorganic crystals through the macroscopic second order nonlinear reaction [48]. Thiourea (TU) is an organosulfur compound with the chemical formula CH<sub>4</sub>N<sub>2</sub>S which belongs to an orthorhombic crystal system, with centrosymmetric, P<sub>nma</sub> space group with the capability of forming an extensive network of hydrogen bonds because of its big dipole moment [49-52]. Sulphanilic acid (SA) is an interesting and important compound with the formula of (NH<sub>3</sub><sup>+</sup>C<sub>6</sub>H<sub>4</sub>SO<sub>3</sub><sup>-</sup>), which find a variety of applications including nonlinear optics and crystallized in orthorhombic crystal system with Pca2<sub>1</sub> space group [53-55]. The inductive zwitterionic structure of sulphanilic acid has dosimetric part and anionic part [56]. With this literature, a survey attempt has been made to grow new NLO crystal 4-amino-N-carbamothioylbenzenesulfonamide from the aqueous solution by slow evaporation method and the physical and chemical properties were discussed.

# 3.2 Experimental procedure

#### 3.2.1 Synthesis

Thiourea and Sulphanilic acid were separately taken in 2:1 molar ratio. The estimated amount of thiourea was dissolved in triple distilled water at room temperature. The sulphanilic acid was then slowly added to the solution with constant stirring. The resultant solution was continuously stirred for 3 hours. The reaction mechanism for the growth of 4-amino-N-carbamothioylbenzenesulfonamide is depicted in scheme 3.1.

Scheme 3.1 Reaction mechanism of 4-amino-N-carbamothioylbenzenesulfonamide

# 3.2.2 Crystal growth

The fully dissolved solution was filtered using a whatmann filter paper. Then the solution was optimally tightly closed by using a perforated polythene paper and stored in undisturbed situations. The resultant final solution was allowed to dry at room temperature. After three weeks, good quality of ACBS crystal of size 13 x 8 x 7 mm<sup>3</sup> was obtained and is shown in Figure 3.1.



Figure 3.1 As grown single crystal of ACBS

#### 3.3 Instrumentation

The single crystal X-ray diffraction (XRD) analysis on ACBS was executed employing Bruker Apex CCD diffractometer the usage of MoKα monochromated radiation  $(\lambda=0.7107 \text{ Å})$  device. The powder X-ray diffraction study of the grown crystal was performed using Rigaku X-ray diffractometer using CuK $\alpha$  radiation ( $\lambda = 1.5406$  Å). The sample was scanned in the 2θ range starting from 10° to 70°. The FT-IR spectrum was recorded by using KBr pellet technique ranging from 400 cm<sup>-1</sup> to 4000 cm<sup>-1</sup>. Optical transmission spectrum also has been recorded in the range of 200 nm - 800 nm using Perkin Elmer Lambda 35 Model UV-vis-NIR spectrophotometer. Thermogravimetric and differential thermal analysis (DTA) were carried out by using a SDT Q600 V20.9 alumina thermal analyzer within the temperature vary from 20 °C to 650 °C at a heating rate of 20 °C within the nitrogen atmosphere. The Photoluminescence (PL) spectrum was recorded using a Varian Carry Eclipse Fluorescence spectrometer. The proton <sup>1</sup>H NMR spectra experiments were performed for the ACBS crystal and spectral data were recorded in a magnetic field of 11.75 tesla using Bruker AVANCE III 500 MHz (AV 500) Fourier Transform NMR spectrometer (For 500 MHz <sup>1</sup>H NMR) for analyzing the molecular structure. The microhardness studies of the ACBS crystal have been characterized by Leitz wetzler Vickers microhardness technique. The surface analysis of the grown crystal was performed with CAREL ZEISS EVO 18 High resolution scanning electron microscope.

#### 3.4 Results and discussions

# 3.4.1 Single crystal X-ray diffraction analysis

The crystalline nature and the lattice parameters have been determined using X-ray diffraction studies. It is observed that the ACBS crystal crystallizes in monoclinic system of P2<sub>1</sub> space group. The determined values of the lattice parameters are a=6.45Å, b=18.32 Å, c=6.78Å,  $\alpha$ = $\gamma$ =90°,  $\beta$ =93° with the cell volume of V=801Å<sup>3</sup>. The single crystal data of ACBS is compared with the reported value and are depicted in Table 3.1.

Table 3.1 Comparison of crystal data of ACBS crystal

Lattice	TU	SA	ACBS
Parameters	Reported work [50]	Reported work [55]	<b>Present Work</b>
a(Å)	7.8585	7.5113	6.45
b(Å)	8.4850	7.2791	18.32
c(Å)	5.485	13.898	6.78
$\alpha=\beta=\gamma$ (°)	90	90	α=γ=90; β=93
$Volume(\mathring{A}^3)$	380.8926	-	801
System	Orthorhombic	Orthorhombic	Monoclinic
Space group	Pnma	Pca2 <sub>1</sub>	P2 <sub>1</sub>

From the table, it was found that the structure of ACBS crystal belongs to the monoclinic system differs from those of thiourea and sulphanilic acid system of reported values with changes in a, b and c cell parameters values.

# 3.4.2 Powder X-ray diffraction analysis

The indexed powder x-ray diffraction pattern of ACBS single crystal is shown in Figure 3.2. Due to large difference in intensity of the peaks, the diffraction pattern is splitted

into two part and the indexed patterns are shown in inset. It is found that a sharp high intense present at 19.94°. The XRD pattern also indicates many different peaks and the presence of sharp peaks shows that the material is in good crystalline nature. The properly described Bragg's peaks at specified  $2\theta$  angles suggest the high crystallinity of the grown crystals.

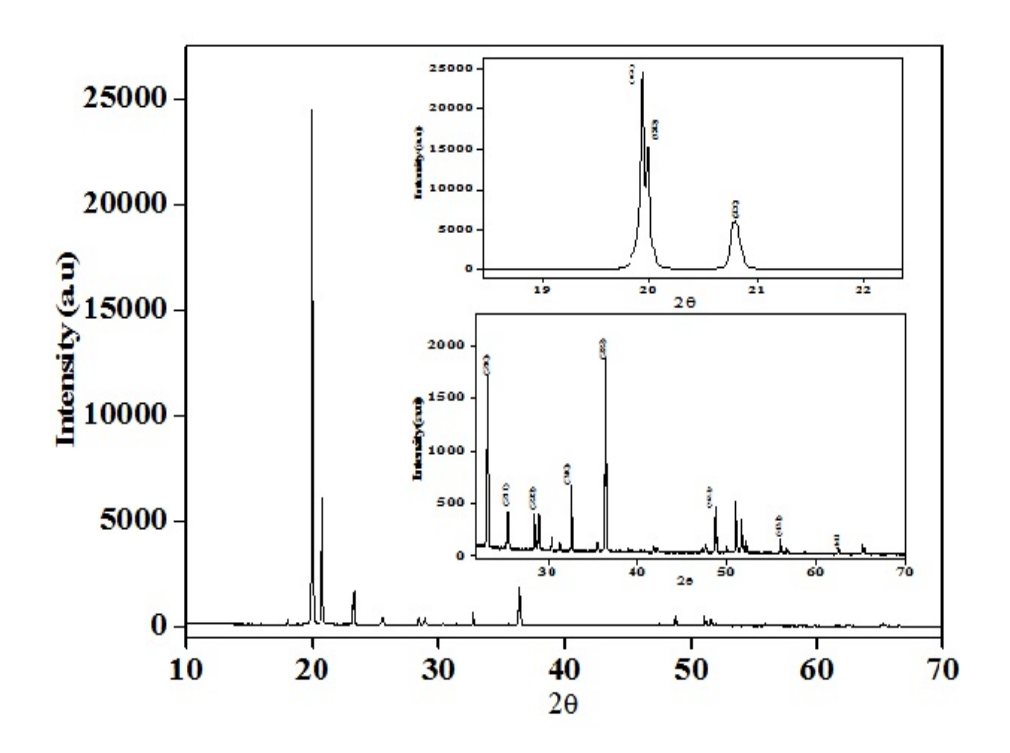


Figure 3.2 Powder XRD pattern of ACBS

#### 3.5 Vibrational analysis

The FTIR spectra of grown ACBS single crystal are shown in Figure 3.3. The functional groups present in the ACBS crystals are identified and compared with thiourea (TU), Sulphanilic acid (SA) as stacked in Table 3.2. In the present work, the sharp high intense peaks at 3382 cm<sup>-1</sup> and 3178 cm<sup>-1</sup> are attributed to asymmetric and symmetric stretching modes of NH<sub>2</sub> group. The C=S asymmetric and symmetric stretching frequencies show a shift towards higher wave numbers when compared to thiourea and sulphanilic acid. The metal – sulfur bond is assumed to be responsible for the shifting of vibration at 1471 cm<sup>-1</sup> and 834 cm<sup>-1</sup> to high wavenumber in each material. The peak observed at 1415 cm<sup>-1</sup> and 1008 cm<sup>-1</sup> are the symmetric and asymmetric frequency of SO<sub>2</sub> group

respectively. The stretching and bending vibrations of N-C-N and C-N-C were positioned at  $684~\rm{cm^{-1}}$  and  $487~\rm{cm^{-1}}$  respectively.

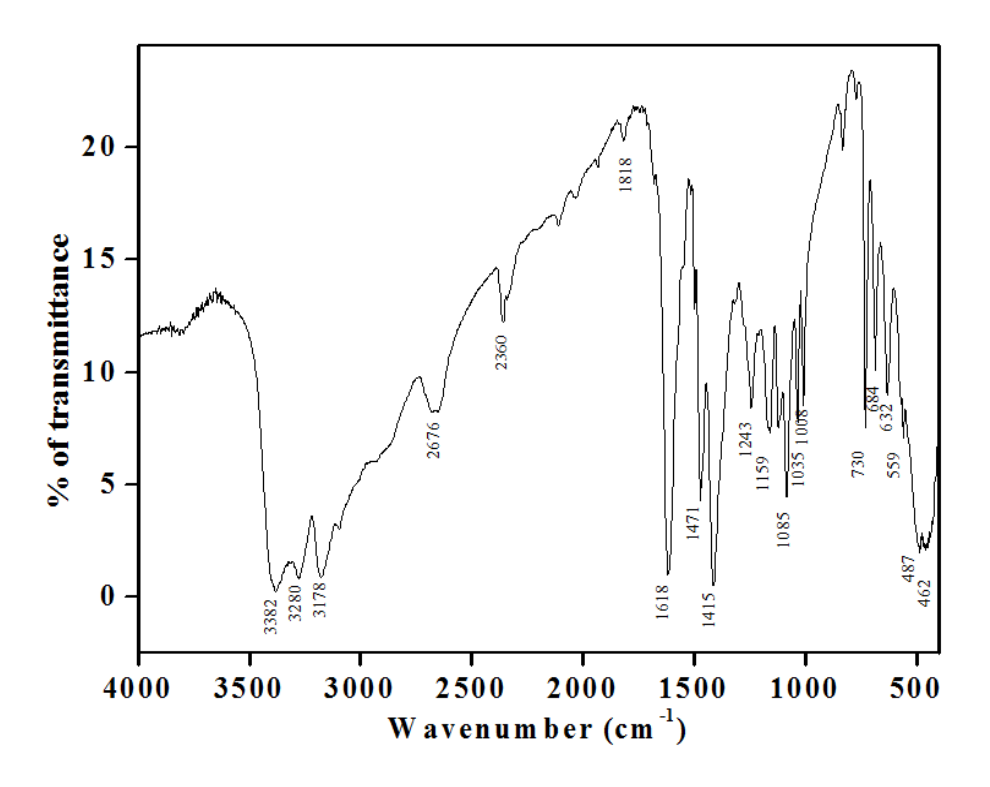


Figure 3.3 FTIR spectrum of ACBS

Table 3.2 Assignments of vibrational wavenumber (cm<sup>-1</sup>) of TU, SA and ACBS single crystals

Wavenumber (cm <sup>-1</sup> )			
		ACBS Present	
TU [50]	SA [55]	work	Assignments
3347	3371	3382	NH <sub>2</sub> asymmetric stretching
3167	3051	3178	NH <sub>2</sub> symmetric stretching
2350	2400	2360	C-H stretching
1464	1431	1471	C=S asymmetric stretching
1387	1349	1415	asymmetric SO <sub>2</sub> vibration
1091	1271	1085	C-N symmetric stretching
-	1025	1008	symmetric SO <sub>2</sub> vibration
731	782	834	C=S symmetric stretching
627	694	684	N-C-N symmetric stretching
491	511	487	C-N-C bending

# 3.6 UV-Vis-NIR spectral analysis

The UV spectra of ACBS single crystal is shown in Figure 3.4. From the UV spectra it is seen that the UV transparency cut off wavelength for ACBS crystal happens at 344 nm and transparency ~95% in the visible regions 416 nm - 800 nm which makes the ACBS crystal is potential candidate for second harmonic generations (SHG). Since it is seen that the absence of absorption in the visible region, the grown crystal is an appropriate candidate for optoelectronic applications [57]. The Tauc's plot variation of  $(\alpha hv)^2$  vs. the photon energy (hv) is estimated as proven in Figure 3.5. The optical band gap (Eg) for the ACBS crystal was predicted using the relation,

$$\alpha = \frac{A (hv - E_g)^2}{(hv)}$$

Where  $\alpha$  is the absorption coefficient, A is the proportional constant. The  $E_g$  is measured by using the extrapolation of the linear part and the band gap of the ACBS crystal was become found to be 2.69 eV.

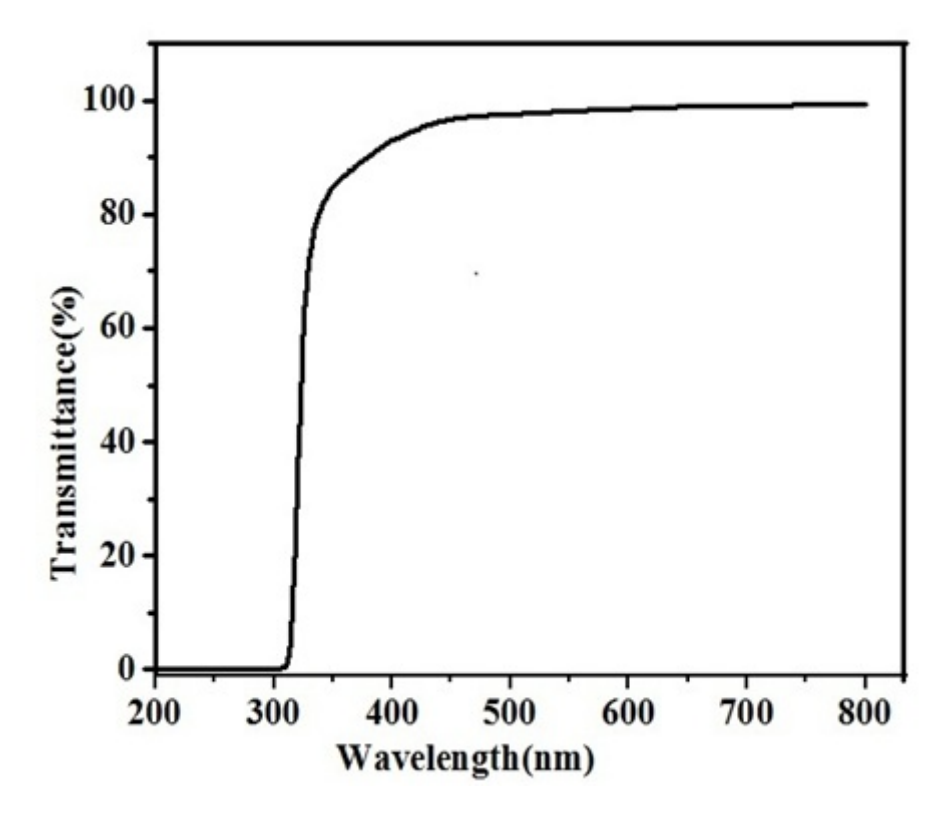


Figure 3.4 UV – Vis – NIR transmission spectrum of ACBS

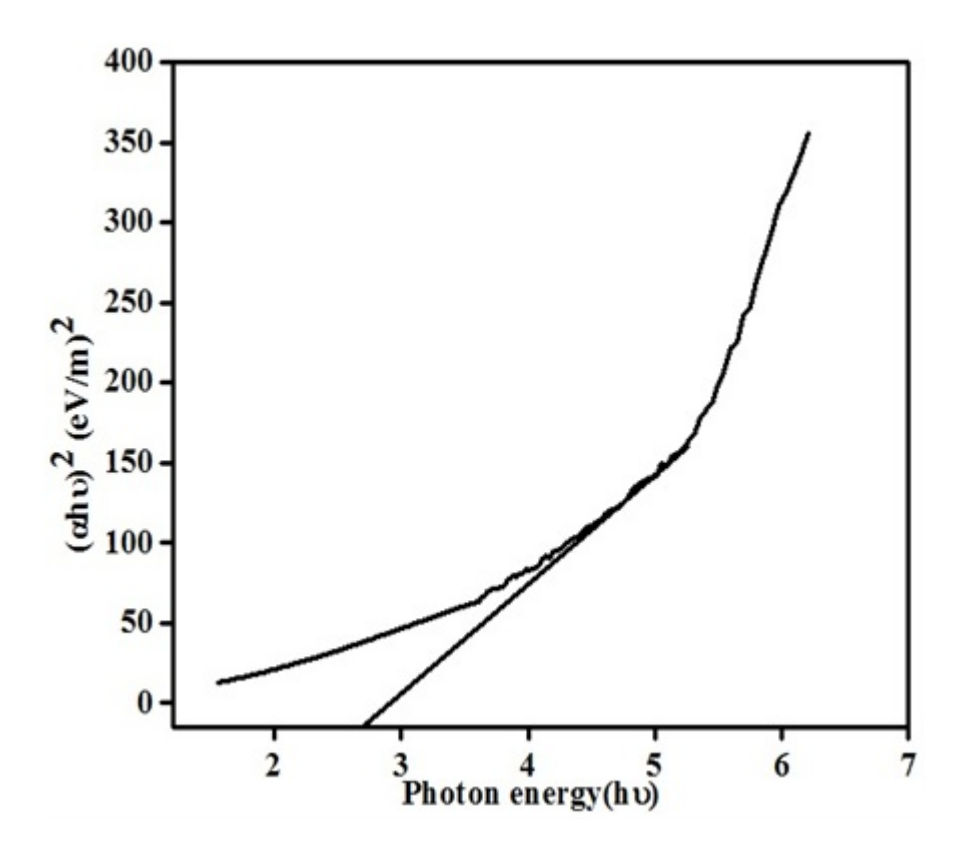


Figure 3.5 Plot of (αhv) <sup>2</sup> vs. hv of ACBS crystal

# 3.7 Thermal analysis

Thermal stability, melting point, endothermic or exothermic reactions have been analyzed using thermal studies. The thermal analysis curves are shown in Figure 3.6. Because there is no endothermic or exothermic transition below 175 °C and as a result of the material is strong up to this temperature. Within the differential thermal analysis curve, endothermic reactions are found at 184 °C and 253 °C. The endothermic peak placed at 184 °C suggests the begin of decomposition and the material is completely decomposed at 253 °C and consequently the trace in TGA at 175 °C in TGA shows the melting point of the crystal. The sharp endothermic peak indicates the good crystalline of the ACBS crystal. On the same time the melting point of ACBS crystal is determined to be more than that of reported value 173 °C of pure sulphanilic acid crystal [58].

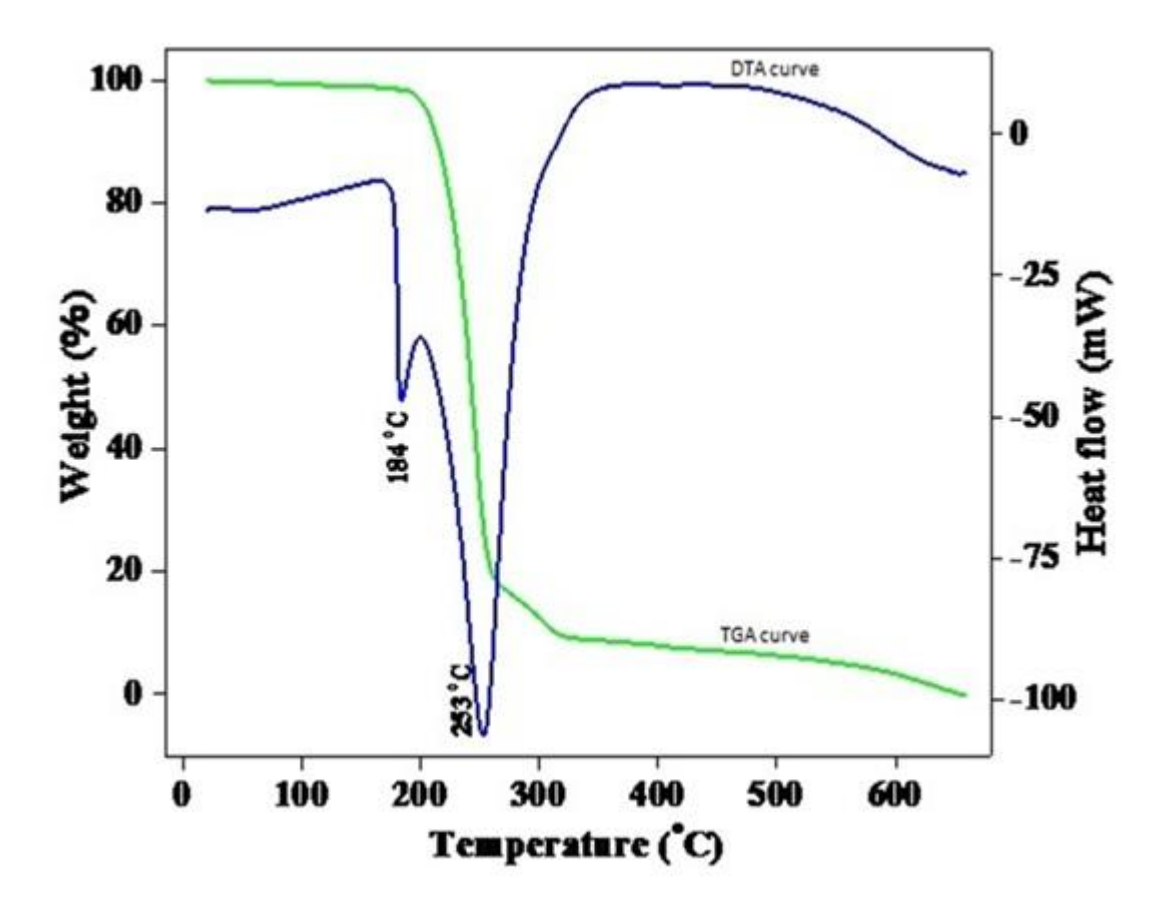


Figure 3.6 TGA / DTA curve of ACBS crystal

### 3.8 Fluorescence studies

The fluorescence spectra of ACBS single crystal is shown in Figure 3.7. The photoluminescence spectrum of ACBS crystal gives information of various energy states available among valance band and conduction band answerable for radiative recombination. The ACBS was excited at 297.8 nm and the spectra were recorded in the range from 200 nm to 800 nm. From the figure is observed the high intense peak at 416.2 nm. The usage of the conversion wavelength to energy relation  $E_g = (1.24 / \lambda)$  eV, the band gap value calculated and  $\lambda$  is the wavelength of fluorescence. The fluorescence band gap of the ACBS single crystal is  $E_g$  located to be 2.97 eV. This indicates that the ACBS crystal is a violet light emitting material. Either different low intensity peaks can be intrinsic defects of the crystal.

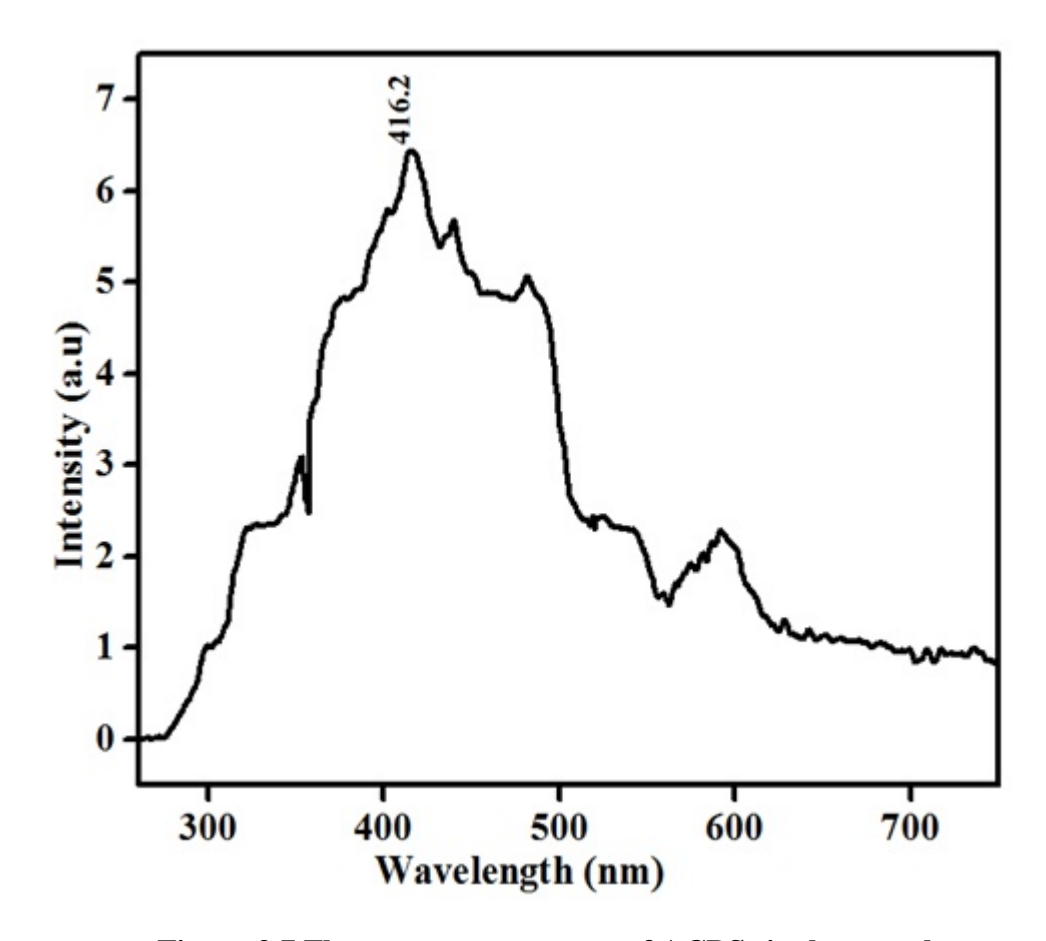


Figure 3.7 Fluorescence spectrum of ACBS single crystal

# 3.9 <sup>1</sup>H NMR Spectral analysis

The Proton NMR spectrum of ACBS single crystal is shown in Figure 3.8. It is seen that the  $^1H$  Proton NMR spectra affirms the nearness of eleven protons in ACBS compound which incorporate interchangeable protons also. In the spectrum, a singlet signal appearing at  $\delta = 2.110$  ppm is due to the protons of carboxylic acid connected sulphanilic acid moiety. The doublet signals appearing at  $\delta = 3.404$  and  $\delta = 3.389$  ppm attributed to the presence of -CH group of sulphanilic acid. The solvent  $D_2O$  sharp peak  $\delta = 4.69$  ppm is merged with the protons of  $-NH_2$  and  $HSO_3$  groups. Due to that the peak intensity is very high [59]. The doublet signal at  $\delta = 6.761$  and  $\delta = 6.734$  are assigned to phenyl protons which are present in orthoposition amino group. The doublet peaks observed at  $\delta = 7.483$  and  $\delta = 7.455$  are assigned to the proton of  $NH_2$  group of thiourea.

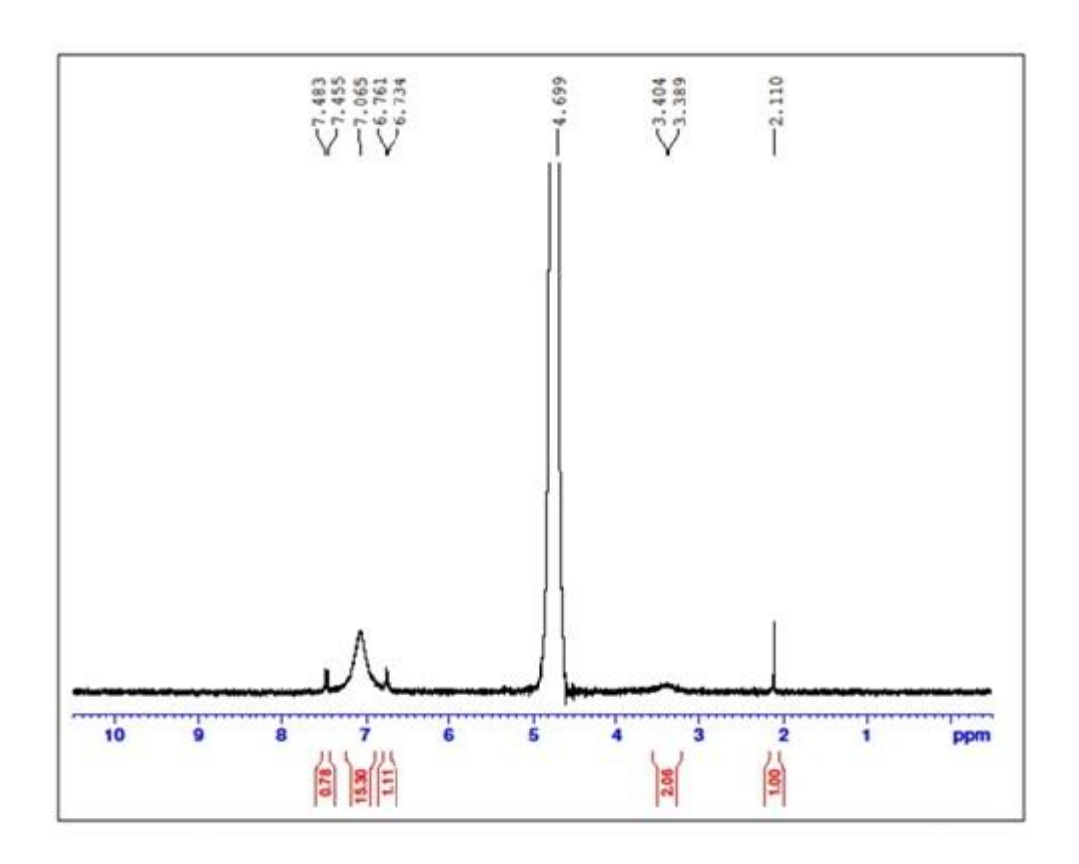


Figure 3.8 <sup>1</sup>H NMR spectrum of ACBS single crystal

# 3.10 Microhardness analysis

The microhardness analysis of the ACBS crystal was carried out by a Leitz Wetzler tester with a Vickers diamond pyramidal indenter. Hardness is a measure of a materials resistance to the nearby deformation resulting from indentation. It plays a key role in device fabrication [60]. The indentation hardness is generally defined as the ratio of the implemented load to the surface area of the indentation. The time of indentation became stored constituent at 10s for all trials and therefore the microhardness activity became taken between the implemented load (P) varying from 25 g to 100 g. The micro hardness number (Hv) was calculated using the formula [61]. Hv =  $1.8544 \text{ P} / \text{d}^2 \text{ (kg / mm}^2 \text{)}$ , where P is the applied load in kg and d is the average diagonal length of the indentation in mm. The hardness value H<sub>v</sub> with load P for ACBS as shown in Figure 3.9. It is concluded that Hv increases with increases in P which is known as reverse indentation size effect. For an indentation load of 100g, cracks had been located on the crystal surface across the indent

and it is far because of the discharge of internal pressure domestically initiated through indentation. The index number 'n' is predicted as 2.81 from the graph drawn between log P versus log d from Figure 3.10. According to Hanneman [62] and Onitsch [63] the values of 'n' lies between 1 and 1.6 for difficult materials and it is more than 1.6 for soft materials. For this reason, from Mayer's index number, it is far clean that ACBS belongs to soft material category.

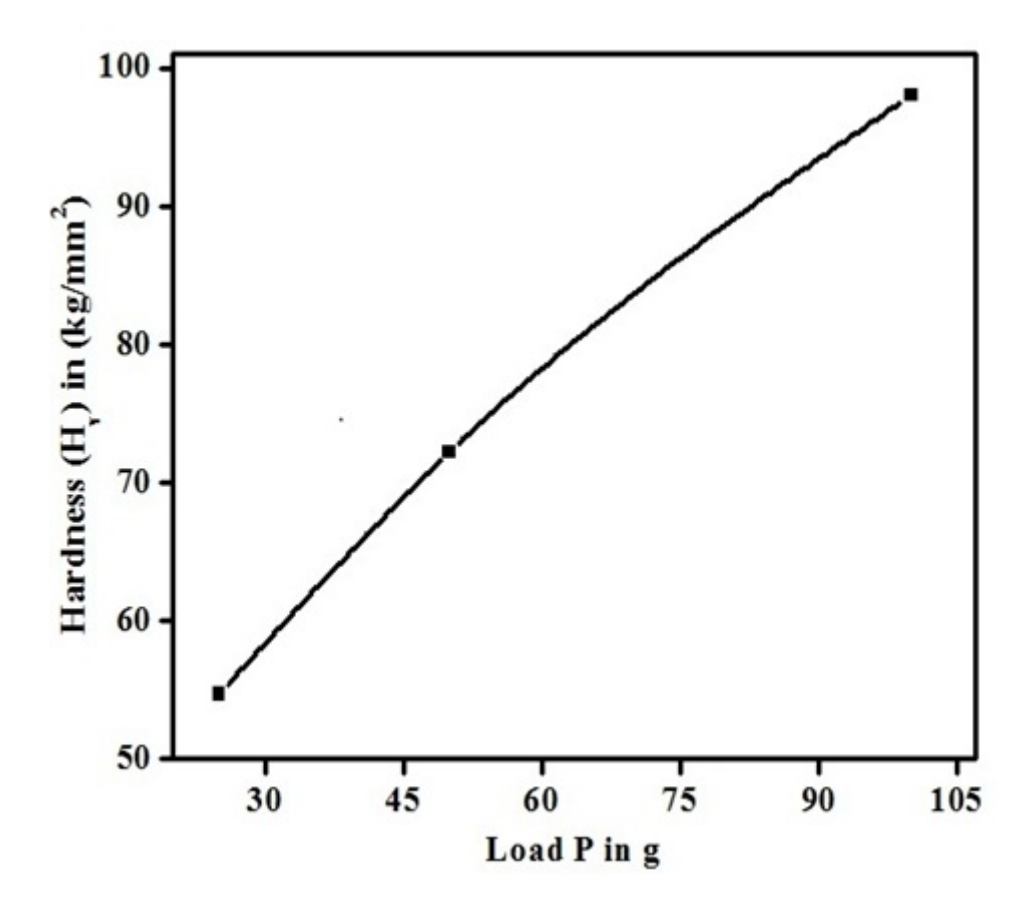


Figure 3.9 Hardness (H<sub>v</sub>) verses load (P) for ACBS crystal

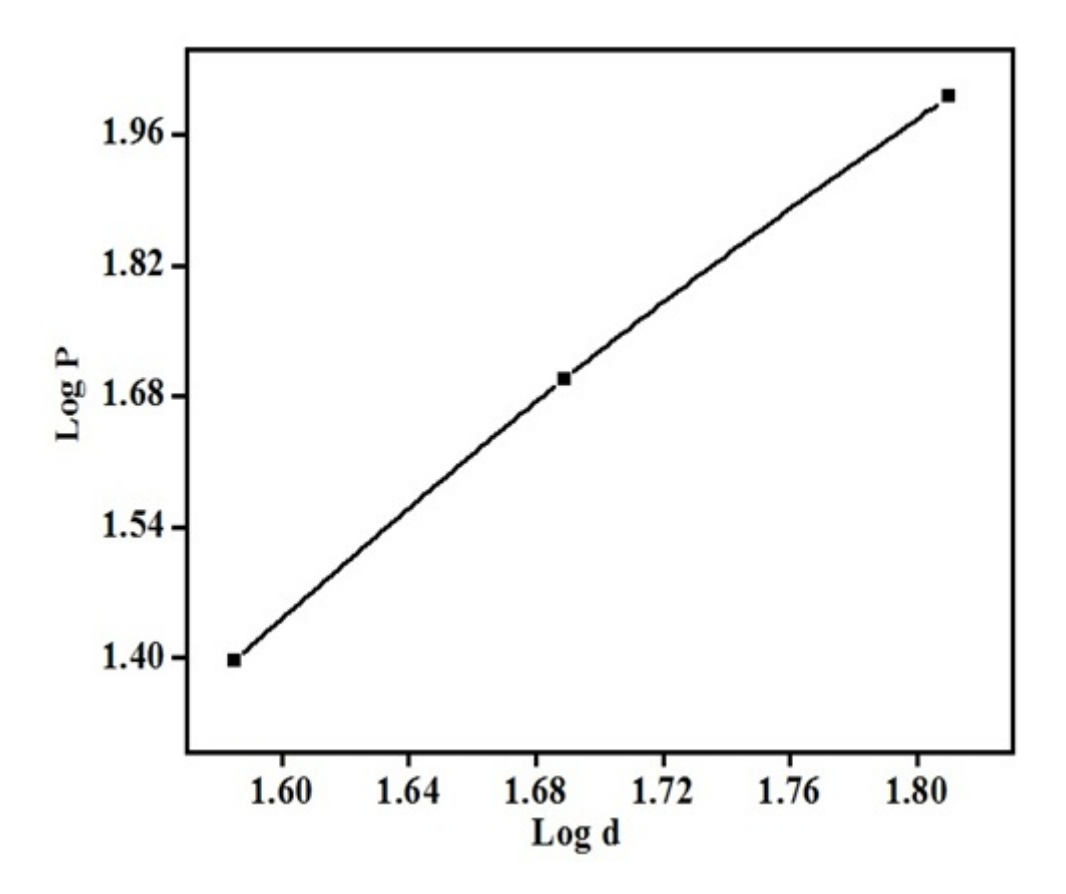


Figure 3.10 Log P and Log d for ACBS crystal

# 3.11 SEM analysis

Surface morphology of ACBS crystal was carried out using high resolution scanning electron microscope. Figure 3.11(a) and (b) show the SEM pictures of ACBS crystal surface with magnification of 10 µm and 20 µm respectively. The scanning electron microscope studies give the information regarding the nature, morphology, composition variations and also it is mainly used to check surface imperfections. Because the organic materials are nonconducting in nature, gold carbon coating ought to be done before subjecting the crystal surface to electron beam. It is observed from the SEM image it is clear that the surface of the crystal appears smooth through it has pots and microcrystal on the surface. Overall, the surface was very smooth, fine grain boundaries and few vale regions are determined [64].

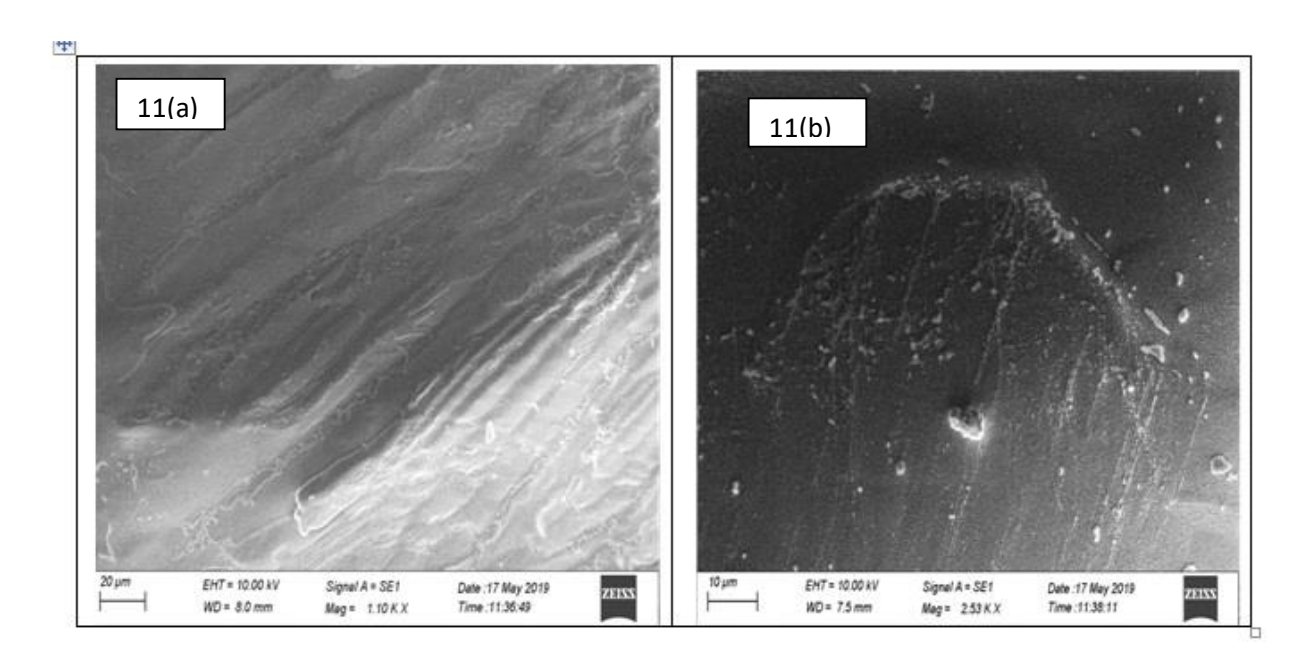


Figure 3.11 (a) and (b) SEM pictures of ACBS crystal

\_\_\_\_\_

# SYNTHESIS, GROWTH, DFT AND HOMO-LUMO STUDIES ON PYRAZOLEMETHOXY BENZALDEHYDE SINGLE CRYSTALS

#### 4.1 Introduction

Organic material has been sought for a variety of applications in recent years, particularly photonics, electro-optic systems, color display optical optoelectronics and frequency doubling [65-67]. As a result, several research groups are interested in developing new organic crystals with strong nonlinear optical properties. Organic crystals usually outperform inorganic and semi-organic materials, with substantial optical nonlinearity due to  $\pi$ -electron delocalization, low dielectric constant at higher frequencies and a high damage threshold value [68-69]. 2-Methoxybenzaldehyde is an organic material containing a benzene ring that has been replaced with an aldehyde and a methoxy group. It appears in three varieties, ortho, meta and para in which the two functional groups (methoxy and aldehyde) are alpha, beta and a comma to each other. Benzaldehyde and its derivatives have vibrational spectra which can be used to study biological processes and analyze comparatively complex structures. It is used to make pharmaceuticals, plastic cleaners, agrochemicals and dyes among other things. It is very important in the intermediate processing of performs and flavoring elements [70]. Pyrazole is an aromatic organic material. A five-membered lactam ring structure of three carbon atoms and two nitrogen atoms in adjacent locations distinguishes it from other heterocyclic sequences. Antifungal and pesticide properties are found in pyrazole derivatives and crystals with the hydrazine moiety are a common class of organic molecules in medicinal and pharmaceutical chemistry [71-76]. The methyl and amino groups are frequently referred to as electron donation substituents in aromatic ring structures. Hyper conjugation of the methyl group with the adjacent  $\pi$ -system causes electronic delocalization, which the molecular orbital technique takes into consideration [77, 78]. In the present study,

experimental and theoretical investigations of Pyrazolemethoxy benzaldehyde (PMB) are reported. The PMB crystals were investigated by powder X-ray diffraction, Fourier transforms infrared analysis, FT-Raman, UV-vis-NIR studies, photoluminescence and thermogravimetric differential thermal analysis. Computational studies such as optimized molecular structure, Frontier molecular orbital, Global chemical reactivity descriptors, natural bond orbital, Mullikan atomic charge and molecular electrostatic potential analysis are performed and discussed its results.

#### 4.2 Material and Methods

#### 4.2.1 Synthesis and crystal growth

The PMB compound was synthesized using commercially available AR grade 4-acetyl-3-methyl-1-phenyl-5-hydroxy pyrazole (4A5P) and 2-methoxybenzaldehyde (2MB) in a 1:1 molar ratio in acetone. The prepared solution was continually stirred with a magnetic stirrer and the solution becomes turbid, hence, ethanol was added and gradually warmed until a clear solution was obtained. The clear homogeneous solution was filtered using Whattman filter paper to eliminate impurities. The prepared homogeneous solution was transferred to a beaker and covered with a perforated sheet to manipulate the evaporation. It was kept in an undisturbed condition. Yellow-colored PMP powder was obtained according to the chemical reaction process depicted in Figure 4.1.

Figure 4.1 Reaction scheme of PMB crystal

As a first step towards the crystal growth process, the solubility of PMB compounds in different solvents like ethanol and methanol is performed at various temperatures. From Figure 4.2 it is concluded that the PMB has a high solubility in ethanol compared to methanol. Hence ethanol has been taken as a solvent to grow PMB crystals. The synthesized material was further purified by repeating the recrystallization process two times in ethanol. The purified salt dissolved in ethanol solution provides high quality PMB crystal, which was collected over 4 weeks period. The photographs of as grown PMB crystals are shown in Figure 4.3.

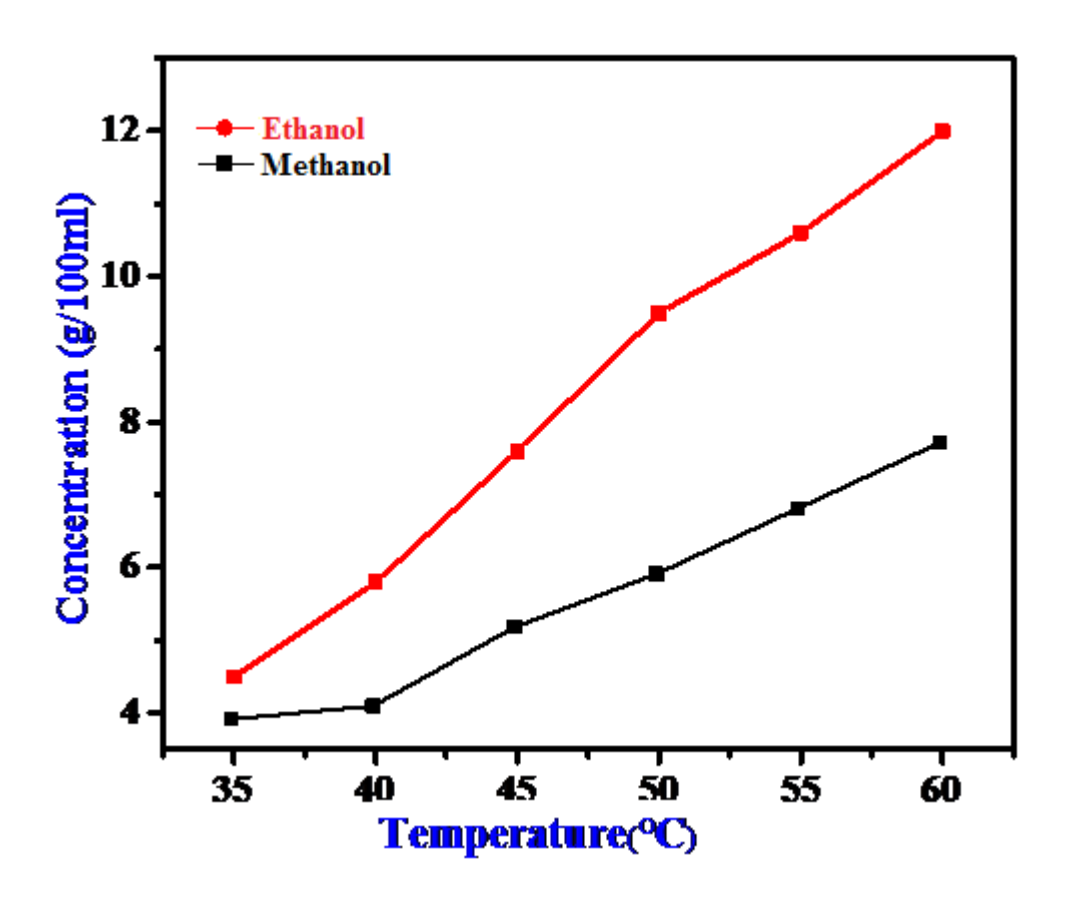


Figure 4.2 Solubility curve of PMB

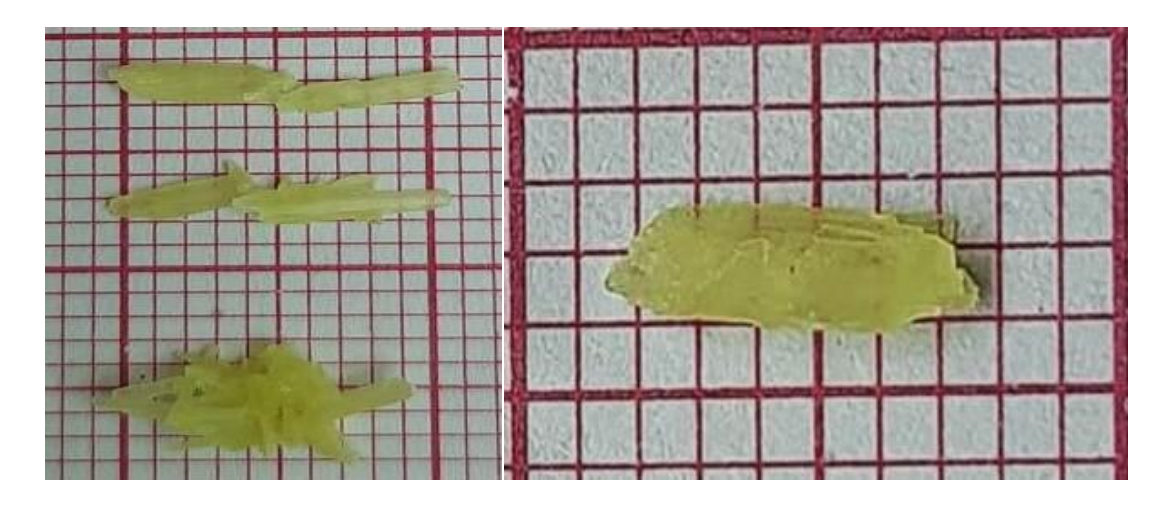


Figure 4.3 As grown crystal of PMB crystal

#### 4.3 Results and discussions

#### 4.3.1 Single X-ray diffraction studies

The single crystal X-ray diffraction studies revealed that PMB crystal belongs to the monoclinic system with centrosymmetric space group C2/c, with lattice parameters of a = 28.179 Å, b = 4.71108 Å and C = 23.819 Å and a cell volume of 3157.7 Å<sup>3</sup>. The lattice parameters are in good agreement with the reported values [79].

# 4.3.2 Powder X-ray diffraction Analysis

The powder X-ray diffraction pattern of the grown crystal was recorded using a powder X-ray diffractometer with ( $\lambda = 1.5408$ ) CuK $\alpha$  radiation. The grown crystal was scanned at 2 $\theta$  values ranging from 10° - 80°. The indexed powder X-ray diffractogram of the PMB crystal is shown in Figure 4.4. The XRD results also show a variety of peaks and the presence of sharp peaks suggests that the material is in good crystalline nature. The clearly defined Bragg's peaks at 2 $\theta$  angles indicate that the grown crystal has high crystallinity.

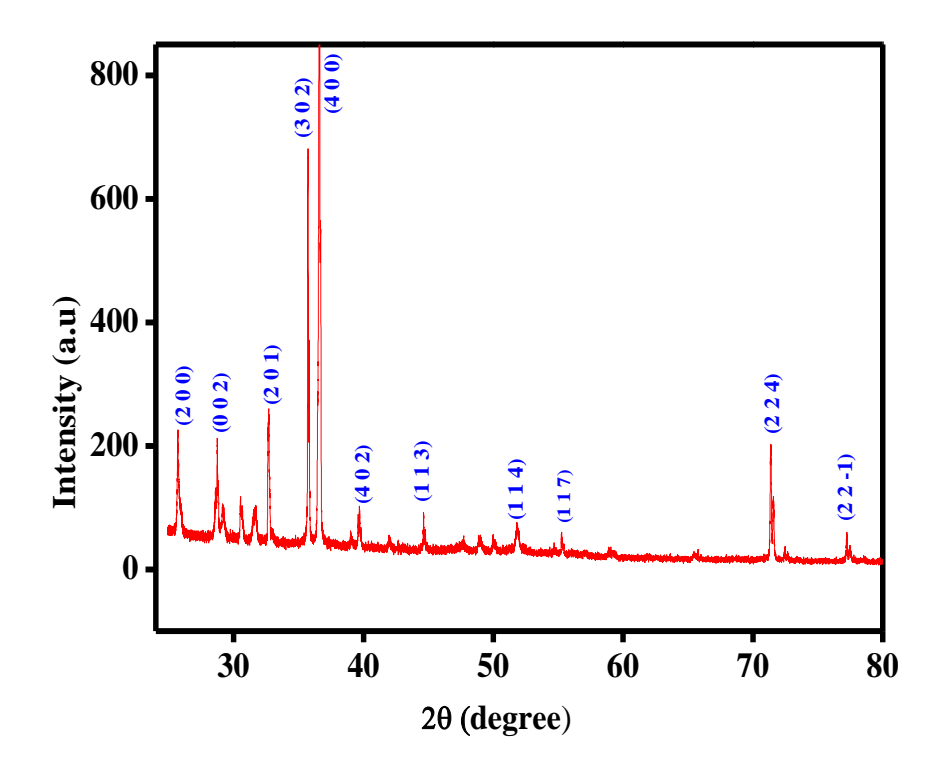
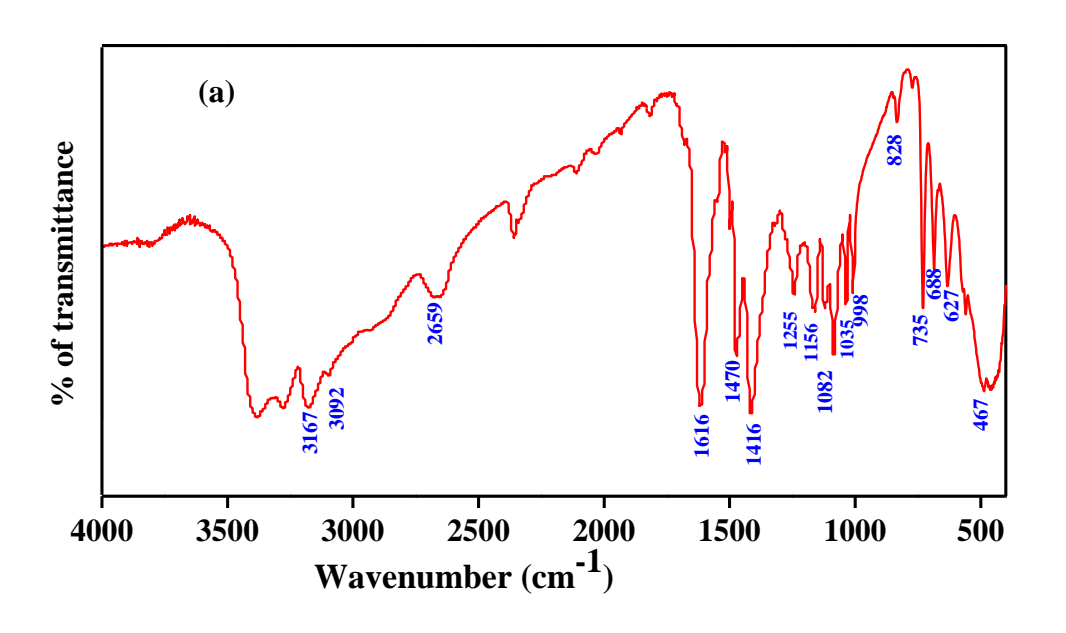


Figure 4.4 Powder XRD spectrum of PMB crystal

# 4.4 FT-IR, FT-Raman spectral analysis

The FT-IR spectrum was obtained on a JASCO FTIR 460 plus spectrometer in the wavelength range of 4000-400 cm<sup>-1</sup> at room temperature using the KBr pellet technique with a scanning speed of 2 mms<sup>-1</sup>. A Bruker RFS 100/s spectrometer was analyzed to examine the FT-Raman spectrum at room temperature. Figure 4.5 (a-b) and Figure 4.6 (a-b) show the experimental, theoretical FT-IR and FT-Raman spectrum respectively. The various frequencies of functional groups in PMB crystal were calculated by the DFT/B3LYP method using 6-311G\* level and compared with the experimental values. The vibrational frequency assignments are listed in Table 4.1. Aromatic ring C-H stretching vibrations are assigned in the range of 3200-3000 cm<sup>-1</sup> [80-82]. The C-H stretching vibrations were observed experimentally at 3167 cm<sup>-1</sup> in the FT-IR spectrum and 3053 cm<sup>-1</sup> in the FT-Raman spectrum in the present work. The asymmetric stretching modes of CH<sub>3</sub> groups belonging to methoxy groups are assigned to the absorption bands at 3092 cm<sup>-1</sup> in FT-IR and 2968 cm<sup>-1</sup> in FT-Raman. In particular, the bands at 1616 cm<sup>-1</sup> and 1590 cm<sup>-1</sup> observed in

FT-IR and FT-Raman spectra corresponds to C=O stretching vibrations in the methyl group with the pyrazole ring. In the crystal, the phenyl ring C=C stretching band is observed experimentally at 1416 cm<sup>-1</sup> in the FT-IR spectrum and 1450 cm<sup>-1</sup> in the FT-Raman spectrum. The N-N stretching mode is 1082 cm<sup>-1</sup> and 1096 cm<sup>-1</sup> observed by IR and Raman spectrum, respectively. In the IR and Raman spectra, the benzene ring exhibits C-H out-of-plane bending, with peaks at 467 cm<sup>-1</sup> and 476 cm<sup>-1</sup> respectively.



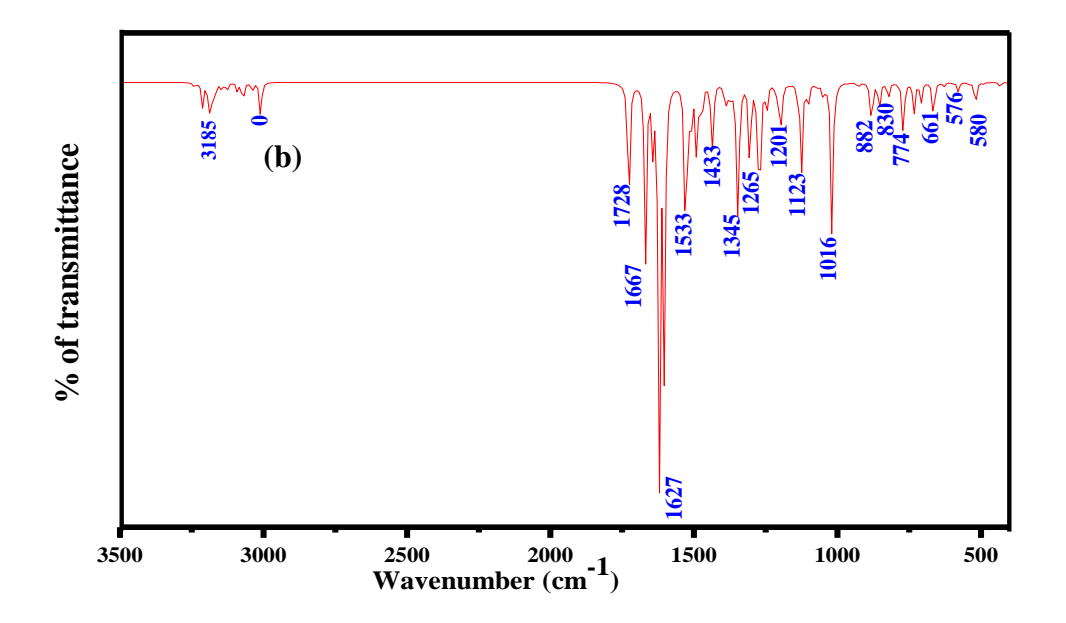
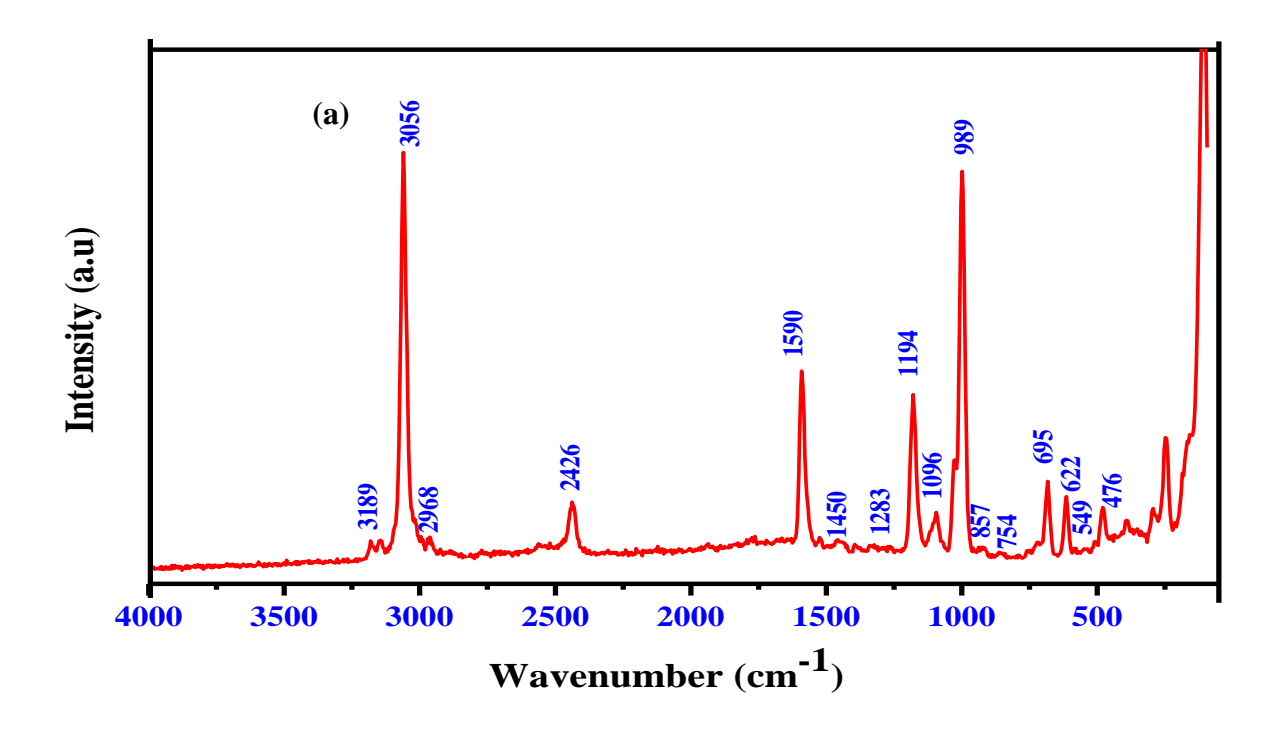


Figure 4.5 (a-b) FT-IR spectrum of experimental and theoretical PMB crystal



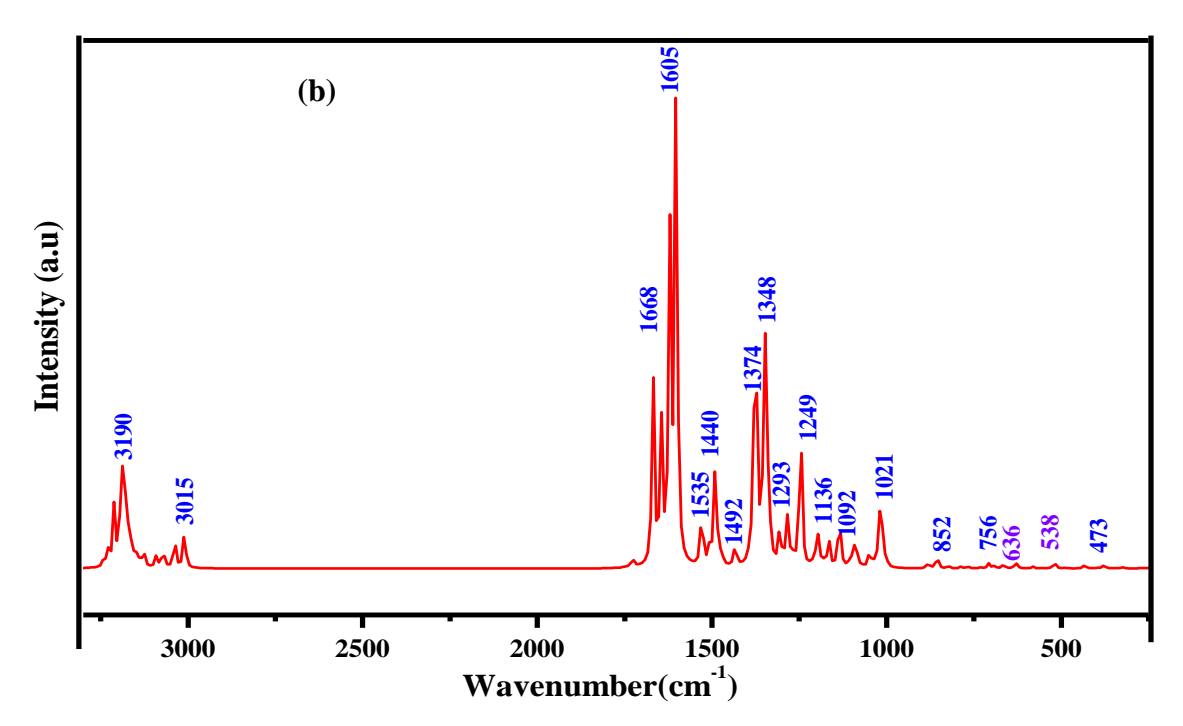


Figure 4.6 (a-b) FT-Raman spectrum of experimental and theoretical PMB crystal

Table 4.1 FT-IR, FT-Raman and DFT frequencies with their assignments of PMB crystal

FT-IR			FT-I	Raman
Experimental	Theoretical	Experimental	Theoretical	Assignments
3167	3185	3056	3190	C-H stretching
3092	3010	2968	2968	CH3 asymmetric stretching
1616	1627	1590	1605	C=O stretching
1416	1433	1450	1440	C=C stretching
1255	1265	1283	1249	C-H stretching
1156	1123	1194	1136	C-N stretching
1082	1016	1096	1092	N-N stretching
828	882	857	852	C-H bending
735	744	695	756	C-H twisting
627	661	622	636	Skeleton deformation
467	465	476	473	C=O out of plane bending

# 4.5 UV-vis-NIR spectral analysis

The UV-visible absorbance spectrum of the grown crystal was recorded using a PerkinElmer Lamda 35 UV-vis-NIR spectrometer in the range of 200 nm - 1100 nm and is given in Figure 4.7. The optical absorption spectrum of PMB crystal shows low absorption across the visible range, with no absorbance from 290 nm to 1100 nm. The cut-off wavelength of the grown crystal was discovered to be 235 nm. Excitation in the aromatic ring and the C=O group would be responsible for the observed absorption. The advantages of this method for NLO applications are the high transparency of the grown crystal in the UV-visible region [83].

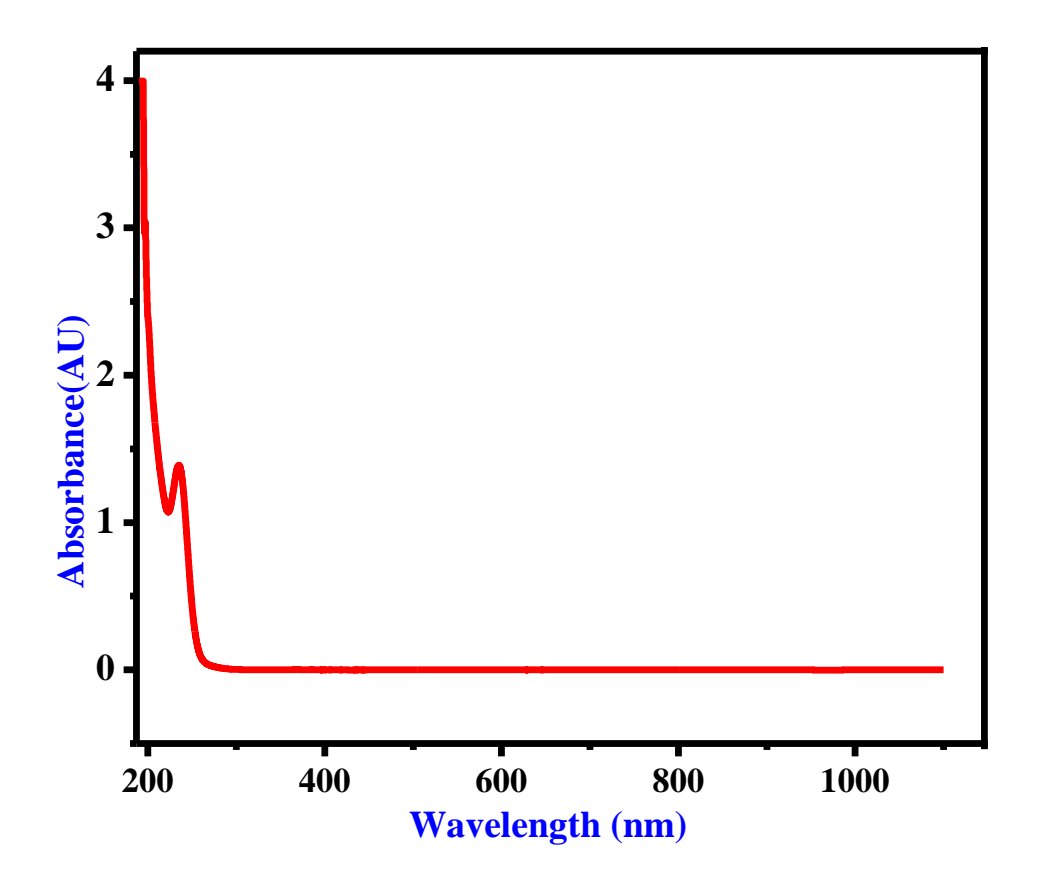


Figure 4.7 UV-visible absorption spectrum PMB crystal

#### 4.6 Photoluminescence studies

The photoluminescence (PL) emission spectrum of PMB crystal was analyzed on a Varian Cary Eclipse fluorescence spectrometer from 200 nm to 800 nm, as shown in Figure 4.8. The PL emission spectrum is a mechanism that emits light when photons are excited from their ground state and it provides information about molecular electronic transitions, defects and some imperfections in grown crystal [84, 85]. The grown crystal was excited at 250 nm and the emission was measured from 250 nm to 800 nm. The two emission peaks are shown in the same figure at 415 nm and 484 nm. The violet light emission is visible in the first emission peak at 415 nm. The second blue emission at 484 nm was caused by the  $\pi$ - $\pi$ \* transition [86]. These results demonstrated that the PMB crystal had violet and blue emission properties, making it suitable for usage in light emitting devices [87].

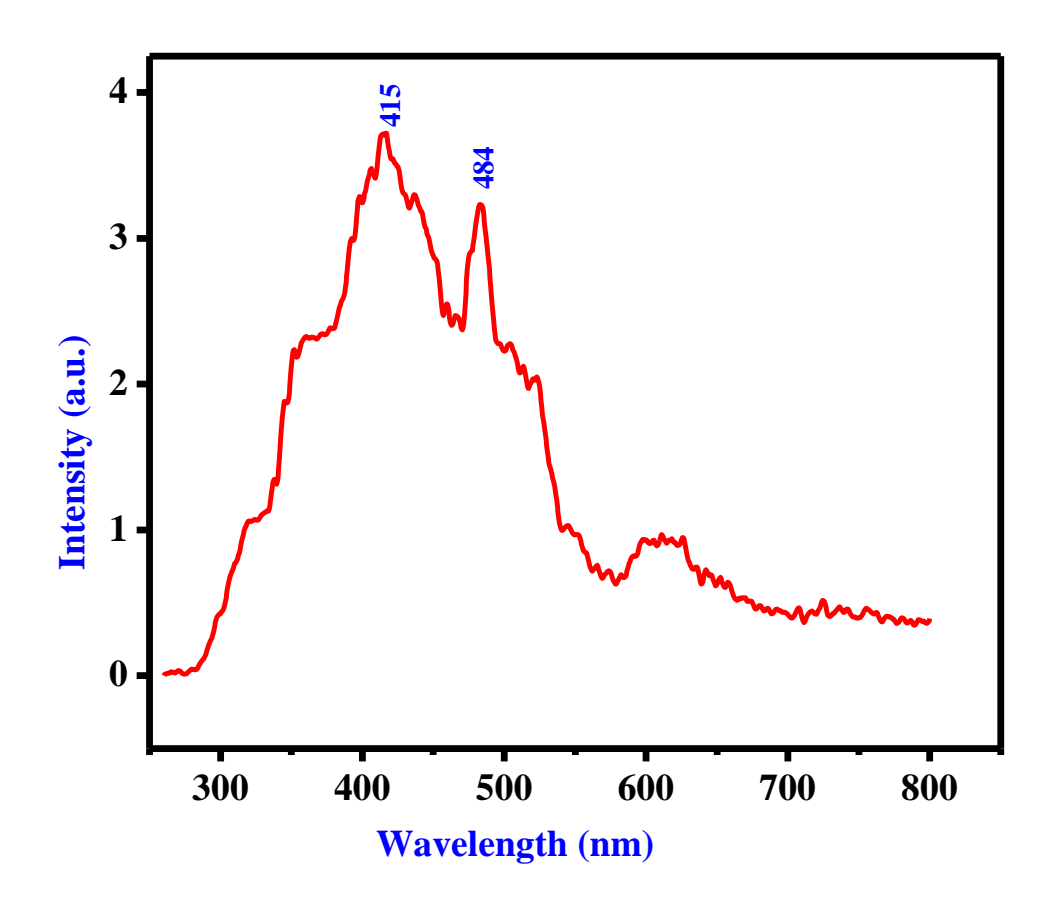


Figure 4.8 Photoluminescence of the PMB crystal

# 4.7 Thermal analysis

The thermal analysis was performed on the PMB crystal using SDT Q600 V20.9 Build 20 in the temperature range of 30°C – 700°C under an N2 atmosphere at a rate of 10 °C/min. Thermogravimetric (TG) and differential thermal analysis (DTA) were used to measure the thermal stability of the grown crystal. Figure 4.9 shows the TG/DTA thermogram of the grown crystal. Two transitions can be seen in the TGA curve. The first and second transitions occur between 185°C to 263°C and 263°C to 315°C, respectively, due to the melting point of the substance. The TGA curve shows that the material is stable up to 183°C. Two endothermic peaks were found on the DTA curve. The sharp endothermic peak suggests that the material has good crystallinity and purity. The DTA curve indicates that the PMB crystal has a first endothermic peak at 184°C, which is attributed to the material's melting point. The second endothermic peak was recorded at 250°C, equivalent

to significant material weight loss. At a temperature of 183°C, the material starts to decompose slowly, with the majority of the material evaporating and the substance becoming volatile. The absence of endothermic or exothermic peaks before the melting point of a substance indicates thermal stability [88].

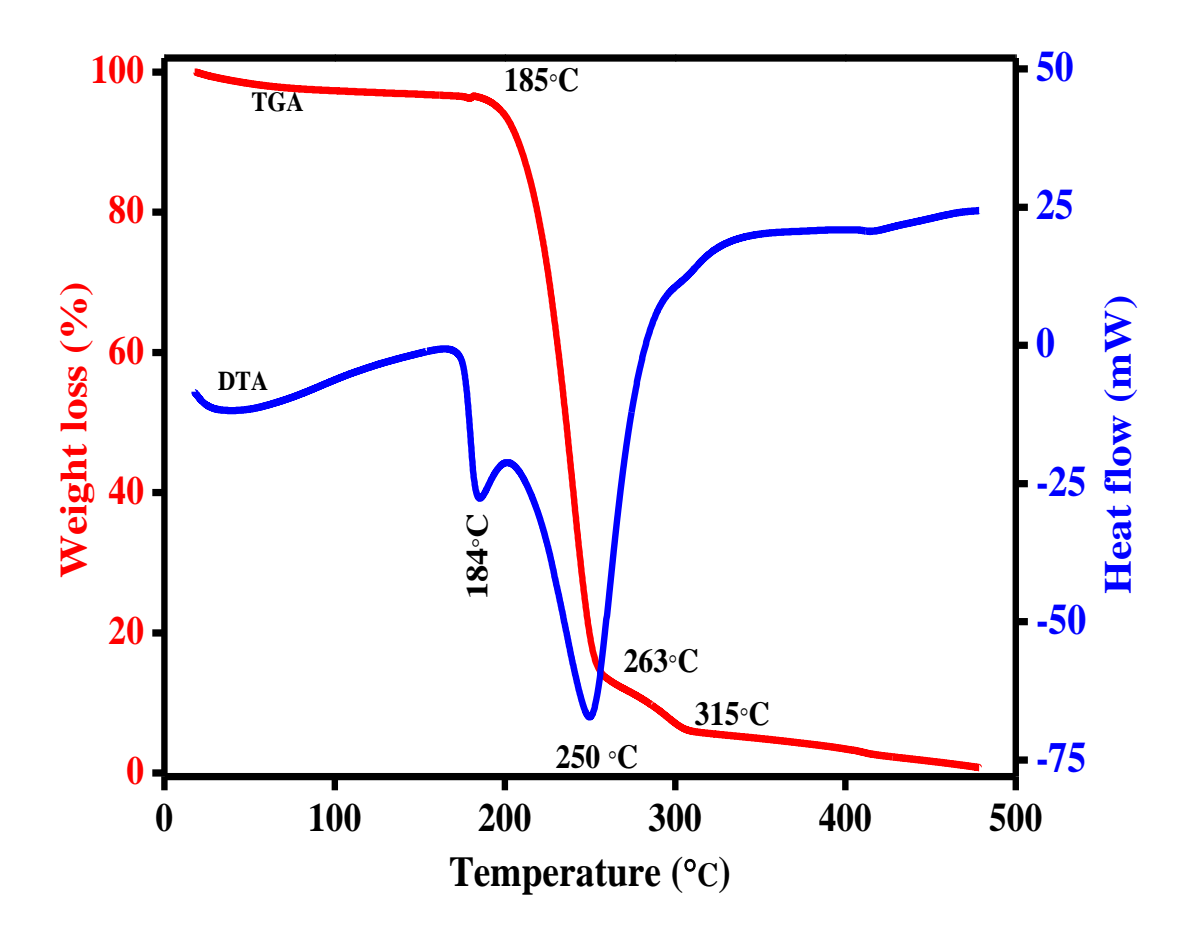


Figure 4.9 TGA/DTA thermogram of PMB crystal

# 4.8 Computational Details

The molecular structure, energies and other properties of a crystal can be calculated using DFT analysis through *ab initio* computational calculation. The geometry of PMB has been optimized at the B3LYP level of theory and the 6-311G\* basis set was utilized to describe the atoms of the molecule. Vibrational frequency calculations are performed on the optimized structure to confirm their stationary points. Natural bond orbital (NBO) is estimated using the same level of theory and basis sets. Quantum chemical computational

calculations through DFT have been effective in predicting the vibrational spectra of chemical crystals. All these computational procedures have been used as per the Gaussian-09 package [89-91] guidelines. The molecular structure, electronic properties and vibrational spectra were visualized and rendered from the output data of DFT calculations.

# 4.8.1 Molecular geometry optimization

The structure of PMB was optimized to produce a precise molecular geometry of the molecule, as shown in Figure 4.10. PMB contains 41 atoms, 174 electrons and is neutral in charge with spin at singlet. From the calculation, the global minimum energy or self-consistent field (SCF) energy of PMB at B3LYP level with the basic set of 6-311G is -1107.1823 a.u; with a dipole moment of 8.8811 Debye. The single and double bonds are highlighted and the van Der Walls radii of each atom are represented in the same figure.

The Optimized geometrical parameters derived by the B3LYP (Becke three parameter Lee-yang-parr) method using 6-311G\* basis sets are more similar to the experimental values listed in Table 4.2. The C-C bond lengths vary from 1.367Å to1.493Å for XRDs values and from 1.353 Å to 1.495 Å for B3LYP values. The C-H bond length was measured in the range of 0.930 Å - 0.960 Å in XRD and 1.080 Å-1.095 Å in B3LYP and found to be similar. The experimental bond distances of C17-C18, C18-C-19, N5-C19, N4-N5 and N4-C1 atoms in the pyrazolone ring, XRD values of 1.462, 1.438, 1.305, 1.405 and 1.389 respectively, were found to be similar to theoretical DFT values of 1.477, 1.448, 1.299, 1.392 and 1.397 Å. The bond lengths in X-ray data were much shorter than observed theoretical values, which might be explained by packing interactions in the solid-state molecule, whereas estimated bond distances for free molecules in the gaseous state were achieved. The O3-C38 (1.424 Å) bond length is longer than the other C-O bond lengths, due to oxygen atom commitment in carbon bond interactions, while the O1-C17 (1.230 Å) bond length is shorter. The calculated N-C bond length value in B3LYP was between 1.299Å

1.416Å with the equivalent XRD value between 1.305 Å - 1.419 Å. The N-N bond length is 1.392 Å for the B3LYP/6-311G\* method and 1.392 Å for XRD. The DFT/B3LYP/6-311G\* estimated bond angles of PMB were found to be in extremely good agreement with the XRD values, with a few small deviations. Because of the presence of the methyl group, the bond angles of C6-N4-C17 are greater than other bond angles, with a value of 129.2°.

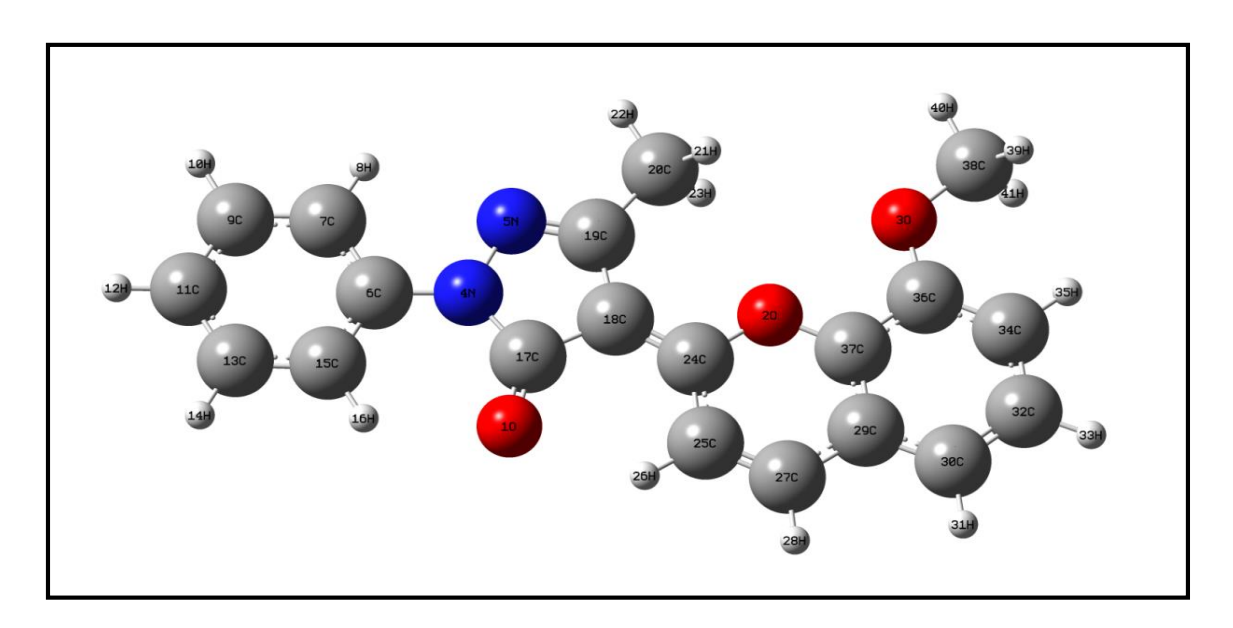


Figure 4.10 Optimized molecular structure of PMB crystal

Table 4.2 Experimental and optimized geometry parameters of PMB crystal computed by B3LYP/6311G\* basis set

Bond length(Å)			Bond angles(°)		
Parameters	EXP*	B3LYP/ 6311G*	Parameters	EXP*	B3LYP/ 6-311G*
O1-C17	1.230	1.226	C24-O2-C37	121.4	121.9
O2-C24	1.358	1.364	C36-O3-C38	117.1	118.3
O2-C37	1.377	1.365	N5-N4-C6	118.4	118.9
O3-C36	1.358	1.355	N5-N4-C17	112.4	112.2
O3-C38	1.424	1.424	C6-N4-C17	129.2	128.9
N4-N5	1.405	1.392	N4-C6-C7	119.6	119.1
N4-C6	1.419	1.416	N4-C6-C15	121.6	121.3
N4-C17	1.389	1.397	С6-С7-Н8	119.4	119.0
N5-C19	1.305	1.299	C6-C7-C9	119.2	119.9

C6-C7	1.401	1.402	C7-C9-C11	120.9	120.8
C6-C15	1.404	1.402	C9-C11-H12	120.5	120.5
С7-Н8	0.930	1.080	C9-C11-C13	119.2	119.0
C7-C9	1.390	1.390	H12-C11-C13	120.5	120.5
C9-H10	0.960	1.085	C11-C13-H14	120.0	120.0
C9-C11	1.390	1.393	C11-C13-C15	121.2	121.2
C13-C15	1.391	1.392	C6-C15-H16	119.6	119.6
C17-C18	1.462	1.477	O1-C17-N4	125.9	126.7
C18-C19	1.438	1.448	O1-C17-C18	130.8	130.0
C18-C24	1.372	1.373	N4-C17-C18	103.7	103.2
C19-C20	1.493	1.495	C17-C18-C19	105.5	105.3
C20-H21	0.960	1.093	C17-C18-C24	125.0	124.5
C24-C25	1.438	1.436	C19-C18-C24	129.6	130.2
C25-C27	1.367	1.353	N5-C19-C18	111.9	111.1
C27-C29	1.433	1.442	N5-C19-C20	119.6	120.3
C29-C30	1.404	1.407	C18-C19-C20	128.5	128.6
C29-C37	1.390	1.399	C19-C20-H21	109.5	111.3
C30-C32	1.382	1.382	C19-C20-H22	109.5	109.0
C32-C34	1.404	1.402	H21-C20-H22	109.5	109.4
C34-C36	1.391	1.393	O2-C24-C18	116.3	116.8
C36-C37	1.404	1.408	O2-C24-C25	118.1	118.3
С38-Н39	0.960	1.095	C18-C24-C25	124.5	124.9
			C24-C25-C27	120.6	120.4
			C25-C27-H28	120.5	120.4
			C25-C27-C29	120.9	120.9
			C27-C29-C30	124.5	124.1
			C27-C29-C37	118.3	116.8
			C30-C29-C37	119.2	119.1
			O3-C36-C34	125.9	125.8
			O3-C36-C37	116.1	116.1
			C34-C36-C37	119.0	118.1
			O2-C37-C29	121.6	121.6
			C29-C37-C36	121.3	121.6

#### 4.8.2 Frontier molecular orbital property

The quantum chemical properties  $E_{HOMO}$ ,  $E_{LUMO}$ ,  $\Delta E$  and related parameters provide valuable information about the reactivity of chemical crystals. The reactivity zone of a molecule is shown by the electron density at the molecule's frontier. The calculation of Frontier electron density can be calculated in many ways. The difference between a neutral system's highest occupied molecular orbital (HOMO) and its lowest unoccupied molecular orbital (LUMO) gives excitation energies. This is also referred to energy gap that reveals the molecular stability. LUMO represents an electron acceptor containing region and HOMO represents electron donator containing region of a molecule. The relative energy of the molecular orbital has been calculated and graphical representations of HOMO and LUMO of PMB are given in Figure 4.11. HOMO<sup>+</sup>, HOMO<sup>2+</sup>, LUMO<sup>-</sup> and LUMO<sup>2-</sup> are also rendered in the same figure. The atoms 6C, 7C, 9C, 11C, 13C, 15C, 4N, 5N, 17C, 18C and 19C of the molecules largely contributed to the HOMO energy. The HOMO<sup>+</sup> energy of the molecule is contributed by most of the atoms of the PMB molecule. HOMO2<sup>+</sup> energy is primarily derived from the 7C, 9C, 13C and 15C atoms of the molecule. The LUMO energy of PMB was from 5N, 17C, 18C, 19C, 24C, 25C, 27C, 37C, 30C, 32C, 34C and 36C atoms. The LUMO energy of the molecule was from almost the same atoms except few in the region. LUMO2<sup>-</sup> energy exhibited from 29C, 30C, 32C, 34C, 36C and 37C atoms of the molecule. The HOMO-LUMO energies were: -5.38839 eV; and -2.5788 eV respectively, while the energy gap,  $\Delta E$  was 2.80959 eV; ( $\Delta E$  reveals the molecule's chemical activity). The energy gap conveys the molecule's small excitation energies. The energy gap of PMB discloses that the molecules possess low reactivity and high kinetic stability. But, adding a reactive molecular region to this base molecule would be valuable to make highly reactive crystals from this molecule. The calculated values of E<sub>HOMO</sub>, E<sub>LUMO</sub> and energy gap are listed in Table 4.3.

Table 4.3 Ehomo, Elumo and energy gap values of PMB crystal

S. No	Property	Value	
1	E (method)	-1107.18233229 a.u.	
2	Dipole Moment	8.8811 Debye	
3	Еномо	-5.38839 eV	
4	E <sub>LUMO</sub>	-2.5788 eV	
5	Energy gap (ΔE)	2.80959 eV	

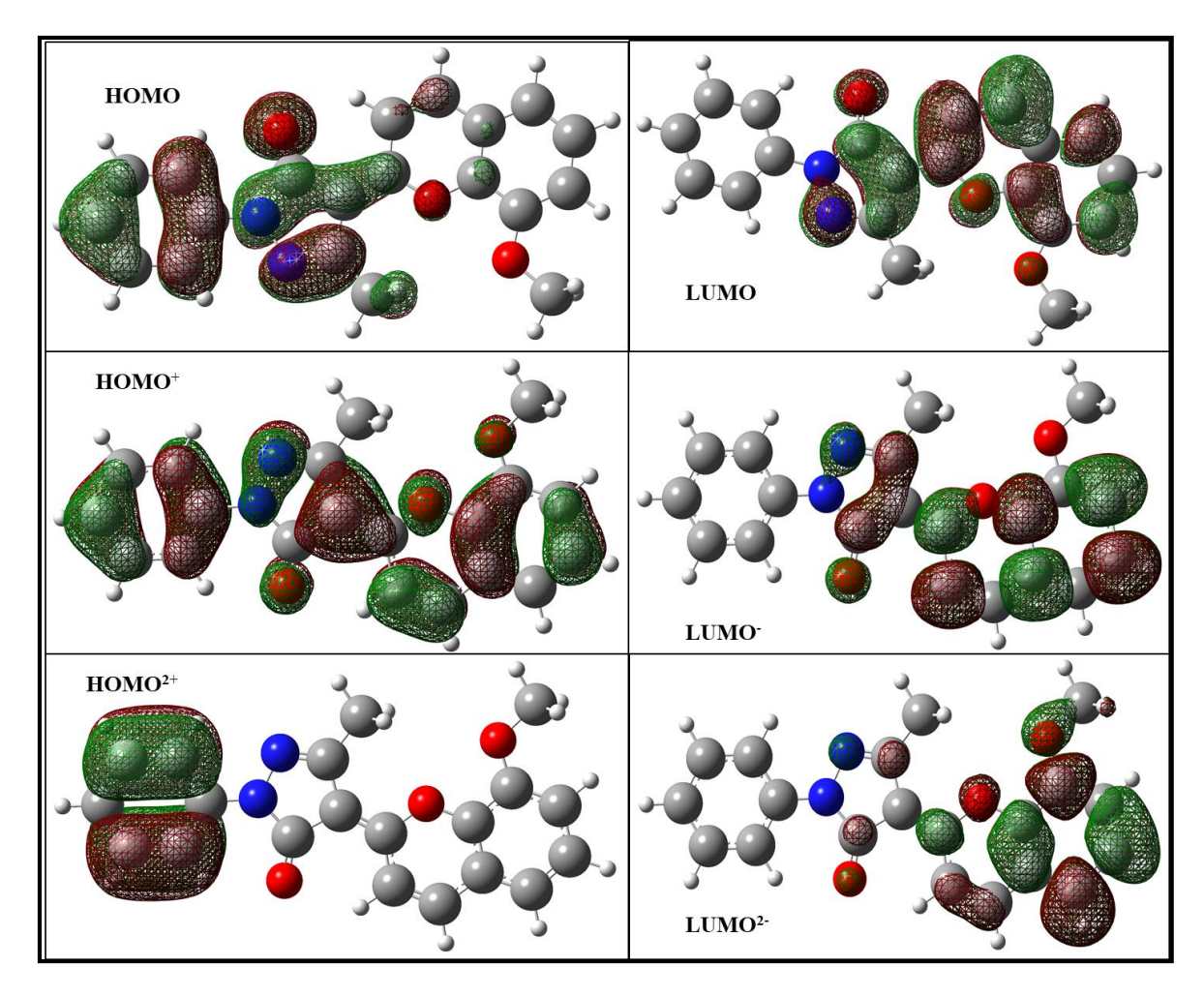


Figure 4.11 Frontier molecular orbital of PMB crystal

#### 4.8.3 Global Chemical Reactivity analysis

The energy gap values obtained from the DFT method have been used to measure the material's total electrochemical reactivity and structural stability [92]. The theorem of Koopmans says HOMO – LUMO energy gap values can determine ionization potential and electron affinity [93]. The ionization potential of the PMB was estimated using the HOMO orbital energy value.

Ionization Potential (I) = 
$$-E_{HOMO}$$
 (4.1)

The LUMO orbital energy was utilized to compute electron affinity because it is determined as the ability to require one electron from a donor.

Electron affinity (A) = 
$$-E_{LUMO}$$
 (4.2)

The chemical reactivity descriptors provided by the electron affinity and ionization potential required by using energy values help in the computation of specific chemical quantities and the characterization of molecular properties [94]. The electronegativity ( $\chi$ ) and global hardness ( $\eta$ ) of PMB were computed using the formulas shown below [95].

The Electronegativity of PMB is calculated as 
$$(\chi) = (I+A)/2$$
 (4.3)

The global hardness is calculated as, 
$$(\eta) = (I-A)/2$$
 (4.4)

The chemical potential is computed as 
$$(\mu) = -(I+A)/2$$
 (4.5)

The softness of the molecule is measured as, 
$$(\sigma) = 1/\eta$$
 (4.6)

The global electrophilicity index of a material is estimated as, 
$$(\omega) = \mu^2/2 \eta$$
 (4.7)

The chemical reactivity descriptors evaluated using HOMO – LUMO energy values display that the crystals have high stability [96], with a hardness value of 1.40475eV. The PMB molecule's chemical potential is negative, indicating strong stability. In the present study, PMB confirmed the material's great chemical potential and good stability, indicating

its suitability for optoelectronic applications. Table 4.4 displays the calculated values for  $E_{\text{HOMO}}$ ,  $E_{\text{LUMO}}$ , energy gap and other global descriptor parameters.

Table 4.4 Calculated quantum parameters and electronic properties of PMB crystal

S. No	Property	B3LYP/6-311G*
1	Еномо (еV)	-5.38839
2	E <sub>LUMO</sub> (eV)	-2.5788
3	Energy gap (eV)	2.80959
4	Ionization potential	5.38839
5	Electron affinity	2.5788
6	Global hardness	1.40475
7	Electronegativity	3.98355
8	Global softness	0.71187
9	Chemical potential	-3.98355
10	Global Electrophilicity Index	5.81288

# 4.8.4 Hyperpolarizability studies

The dipole moment  $(\mu)$ , polarizability  $(\alpha)$  and first hyperpolarizability  $(\beta)$  values each have a significant impact on optical properties [97-101] and are derived from the nonlinear properties of a PMB crystal using x, y and z components are given as follows.

The total electrostatic dipole moment is

$$\mu_{\text{tot}} = (\mu_{\text{X}}^2 + \mu_{\text{Y}}^2 + \mu_{\text{Z}}^2)^{1/2} \tag{4.8}$$

Where  $\mu_X$ ,  $\mu_Y$  and  $\mu_Z$  are diagonal moments along x, y and z directions

The isotropic polarizability is

$$\alpha_{\text{tot}} = \frac{1}{3} (\alpha_{xx} + \alpha_{yy} + \alpha_{zz}) \tag{4.9}$$

Where,  $\alpha_{xx}$ ,  $\alpha_{yy}$  and  $\alpha_{zz}$  are the diagonal components of polarizability tesnor

The mean hyperpolarizability

$$\beta_{\text{tot}} = (\beta^2_x + \beta^2_y + \beta^2_z)^{1/2} \tag{4.10}$$

Where,

$$\beta_{x} = \beta_{xxx} + \beta_{xyy} + \beta_{xzz}$$

$$\beta_{y} = \beta_{yyy} + \beta_{yzz} + \beta_{yxx}$$

$$\beta_{z} = \beta_{zzz} + \beta_{zxx} + \beta_{zyy}$$

The first hyperpolarizability could also be a 3rd rank tensor which can be characterized as a 3 x 3 x 3 matrix, with Kleinman symmetry reducing the 27 elements of the 3D matrix to 10 elements [102]. Since polarizability and hyperpolarizability are measured in atomic units, they are converted to electrostatic units using 1 a.u =  $0.1482 \times 10^{-24}$  esu and the values using 1 a.u =  $8.6393 \times 10^{-33}$  esu, [103, 104]. The theoretically predicted values of  $\mu$ ,  $\alpha$  and  $\beta$  are found to be 8.881D, 19.683 x10<sup>-24</sup>esu and 24.754 x10<sup>-30</sup> esu respectively, for the present molecule. As a result, many molecules start to align in the direction of the supplied electric field. Because of their large dipole moment, organic molecules have large nonlinearities [105, 106]. Table 4.5 displays the tensor values for polarizability and hyperpolarizability.

Table 4.5 The dipole moment ( $\mu$ ), polarizability ( $\alpha$ ), hyperpolarizability ( $\beta$ ) of the PMB crystal

Parameters	Value	Parameter	Value
$\alpha_{xx}$	-118.0839	$\beta_{xxx}$	195.5831
$\alpha_{xy}$	2.6418	$\beta_{xxy}$	37.1705
$\alpha_{yy}$	-130.7497	$\beta_{xyy}$	69.6588
$\alpha_{xz}$	-0.0021	$\beta_{yyy}$	17.5852
$\alpha_{ m yz}$	-0.0007	$\beta_{xxz}$	-0.0353
$\alpha_{zz}$	-149.616	$\beta_{xyz}$	0.0117
$\alpha_{totol}$	-19.683 x10 <sup>-24</sup> esu	$eta_{ m yyz}$	-0.003
$\mu_{x}$	8.8219	$\beta_{xzz}$	14.2906
$\mu_{\mathrm{y}}$	1.0235	$\beta_{yzz}$	8.1743
$\mu_z$	-0.0006	$\beta_{zzz}$	0.0104
$\mu_{tot}$	8.881D	$\beta_{total}$	24.754 x10 <sup>-30</sup> esu

# 4.8.5 NBO analysis

A natural bond orbital (NBO) is a computed bonding orbital having the highest electron density in quantum theory. Computational chemistry calculates bond order, donor and acceptor interactions and hence the electron density between the atoms. The donor – accepter interactions in NBO analysis are evaluated using the version of the NBO 3.1 program as implemented within the Gaussion 09 package at the DFT/B3LYP method using the second order perturbation theory of Fock matrix [107, 108] with 6-311G\* basis set for each donor (i) and acceptor (j), the stabilization energy (E2) associates with the delocalization i-j is estimated as,

$$E(2) = \Delta Ei = qi = \frac{(Fi, j)}{(Ei - Ej)}$$
(4.11)

Where,  $F_{(i, j)}$  is the off diagonal Fock matrix element,  $E_i$ ,  $E_j$  is diagonal elements (orbital energy) and  $q_i$  is the donor orbital occupancy. The different interactions with PMB stabilization energies are listed in Table 4.6. The highest E (2) value provides important information about the donor and acceptor group's relationship. In the present work, the electron donating from the BD (C11-C13), BD (C6-C15), BD (C18-C24), LP(2)O3 and LP(1) N4 to the antibonding acceptor BD\*(C7-C9), BD\*(C11- C13), BD\*(O1-C17), BD\*((C34 – C36), BD\*( (O1 – C17), orbitals and their corresponding energy values are 21.61, 21.70, 22.45, 31.72 and 58.34 KJ/ mol, with the highest stabilization energies of electron delocalization because of the replacement of the molecule.

Table 4.6 The significant second order perturbation theory analysis of the PMB crystal

Donor(i)	Acceptor(j)	E(2)	E(j)-E(i) (a.u)	F(i, j)
		(kcal/mol)		(a.u)
BD(1) N4-N5	BD*(1) C19-C20	4.99	1.23	0.07
BD(1) C36-C37	BD*(1) C29-C37	4.75	1.26	0.069
BD(2) N5-C19	BD*(2) C18-C24	10.94	0.33	0.057
BD(2) C6-C15	BD*(2) C7-C9	18.98	0.29	0.066
BD(2) C6-C15	BD*(2) C11-C13	21.70	0.29	0.071
BD(2) C7-C9	BD*(2) C6-C15	20.94	0.28	0.07
BD(2) C7-C9	BD*(2) C11-C13	18.83	0.28	0.066
BD(2) C11-C13	BD*(2) C6-C15	19.33	0.28	0.067
BD(2) C11-C13	BD*(2) C7-C9	21.61	0.28	0.070
BD(2) C18-C24	BD*(2) O1-C17	22.45	0.30	0.076
BD(2) C18-C24	BD*(2) N5-C19	20.81	0.31	0.072
BD(2) C25-C27	BD*(2) C18-C24	20.06	0.31	0.073
BD(2) C25-C27	BD*(2) C29-C37	13.22	0.29	0.059
BD(2) C29-C37	BD*(2) C25-C27	13.65	0.31	0.061
BD(2) C29-C37	BD*(2) C30-C32	16.60	0.30	0.064
BD(2) C30-C32	BD*(2) C29-C37	20.00	0.28	0.069
BD(2) C30-C32	BD*(2) C34-C36	17.88	0.28	0.064
BD(2) C34-C36	BD*(2) C29-C37	18.26	0.29	0.067
BD(2) C34-C36	BD*(2) C30-C32	19.75	0.30	0.069
LP(2)O1	BD*(2) N4-C17	26.75	0.67	0.121
LP(2)O1	BD*(2) C17-C18	17.88	0.69	0.101
LP(2)O2	BD*(2) C18-C24	30.47	0.38	0.098
LP(2)O2	BD*(2) C29-C37	26.78	0.36	0.092
LP(2)O3	BD*(2) C34-C36	31.72	0.34	0.098
LP(1)N4	BD*(2) O1-C17	58.34	0.27	0.112
LP(1)N4	BD*(2) N5-C19	22.42	0.28	0.073
LP(1)N4	BD*(2) C6-C15	33.09	0.3	0.089

# 4.8.6 Mulliken atomic charges

Mulliken population analysis revealed the atomic electronic charges of PMB crystal. The atomic charges have an impact on electronic structure, properties of molecular systems, dipole moment and molecular polarizability. Furthermore, a molecule's bonding ability is determined by the electronic charge of the chelating atoms. Mulliken population analysis was used to determine the atomic charge values [109]. The Mulliken population analysis of

PMB was calculated using the B3LYP/6311G\* basis set to confirm the reliability of our results. The calculated Mulliken atomic charge values of PMB crystal values are given in Table 4.7. The Mulliken charges of each atom of the molecule are shown in Figure 4.12. Figure 4.13 shows the plot of Mulliken atomic charges on several element atoms of the PMB crystal. The Mulliken atomic charge of all hydrogen carries a positive charge. The atoms C17, C24 and C37 have more positive charges (0.554, 0.208 and 0.238) and these atoms may donate electrons during interactions and atoms 4N, 5N, 1O, 2O and 3O (-0.429, -0,225, -0.403, -0.317 and -0.335) have a more negative charge and these atoms may act as electron acceptors.

Table 4.7 Mulliken Atomic Charges of PMB crystal

S. No	Atom. No	Charges	S. No	Atom. No	Charges
1	O1	-0.403	22	H22	0.118
2	O2	-0.317	23	H23	0.120
3	O3	-0.335	24	C24	0.208
4	N4	-0.429	25	C25	-0.111
5	N5	-0.225	26	H26	0.154
6	C6	0.227	27	C27	0.047
7	C7	-0.096	28	H28	0.107
8	Н8	0.114	29	C29	-0.135
9	C9	-0.101	30	C30	-0.050
10	H10	0.089	31	H31	0.094
11	C11	-0.090	32	C32	-0.098
12	H12	0.085	33	H33	0.108
13	C13	-0.103	34	C34	-0.112
14	H14	0.089	35	H35	0.116
15	C15	-0.118	36	C36	0.143
16	H16	0.135	37	C37	0.238
17	C17	0.554	38	38C	0.135
18	C18	-0.441	39	39H	0.117
19	C19	0.287	40	40H	0.140
20	C20	-0.233	41	41H	0.117

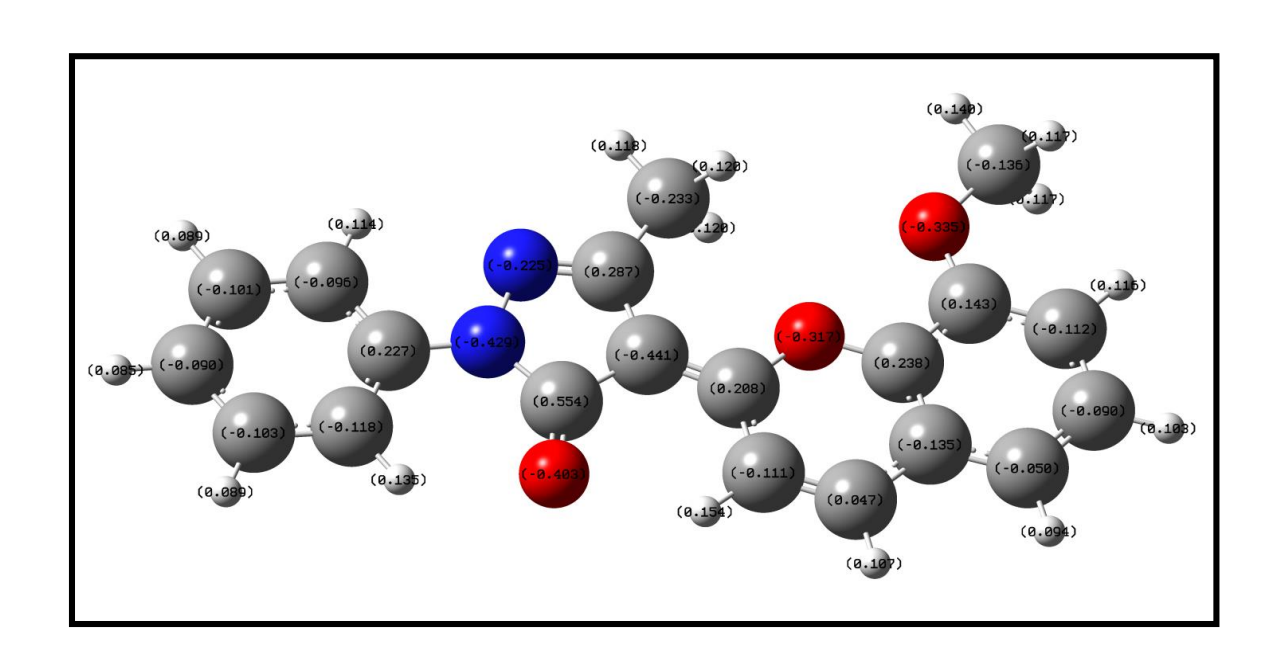


Figure 4.12 The Mulliken atomic charge distribution of PMB crystal

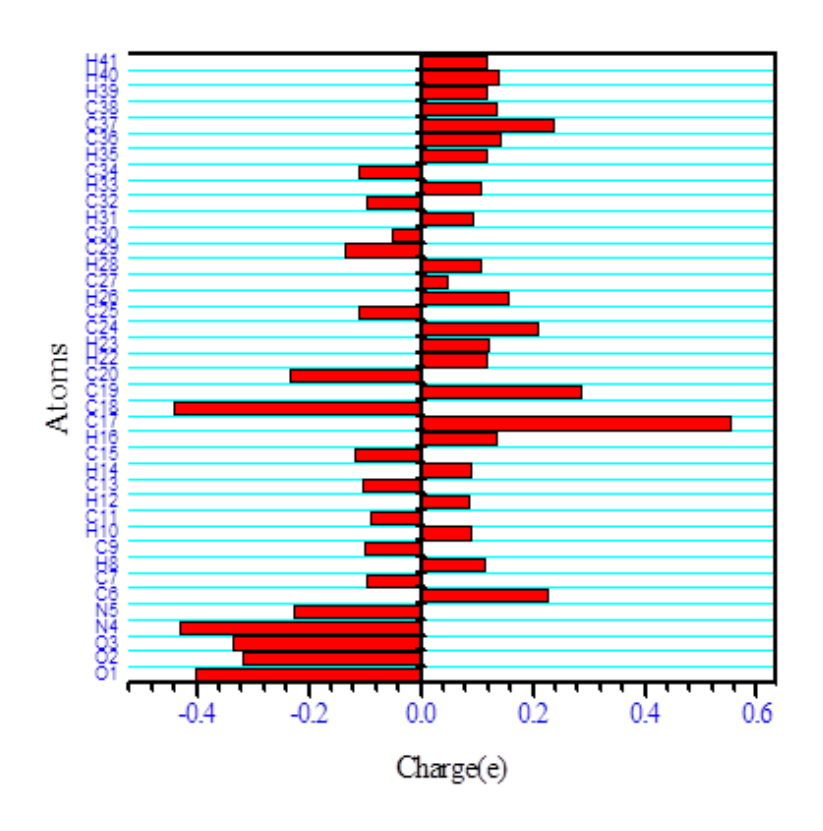


Figure 4.13 Plot of Mulliken atomic charges of PMB crystal

# 4.8.7 Molecular Electrostatic Potential analysis

A molecular electrostatic potential is a useful tool for predicting the reactivity of a variety of chemical systems in electrophillic and nucleophillic reactive sites. Figure 4.14

shows a map of molecular electrostatic potential (MEP). For the PMB material the electrostatic potential map colour coding ranges from -5.098e-2 (deepest red) to +5.098e-2 (deepest blue). The values are most often represented by different colours, with the magnitude increasing as red < orange < yellow < green < blue [110, 111]. The regions of negative electrostatic potential are represented by red, the regions of positive electrostatic potential are represented by blue and the regions of zero potential are represented by green. The negative portions are connected with electrophilic reactivity, whereas the positive portions are connected with nucleophilic reactivity. In the present work, the hydrogen atoms bound to the methyl group represent an electron deficient, partially positive charge in blue colours with a nucleophilic nature. The red colour in oxygen (O1) atoms indicates the negative potential of electrophilic activity, whereas the green colour indicates zero potential.

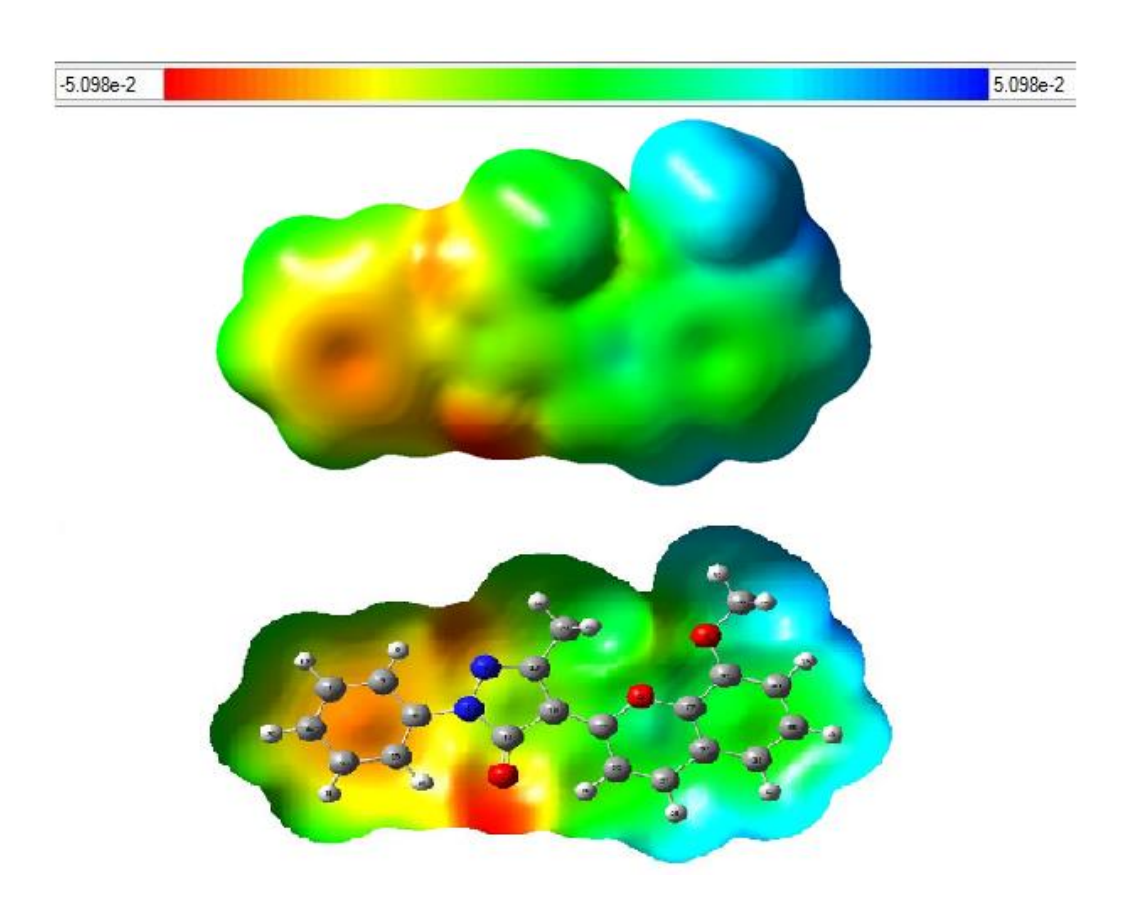


Figure 4.14 Molecular electrostatic potential (MEP) map of PMB crystal

\_\_\_\_\_

# GROWTH, SPECTROSCOPIC AND HIRSHFELD SURFACE ANALYSIS ON PYRIDINE UREA SINGLE CRYSTAL

\_\_\_\_\_

#### 5.1 Introduction

Owing to the recent advances in crystal growth technology, several innovative nonlinear optical (NLO) materials have been developed for various applications like frequency conversion, electronic switching and modification of electro-optical signals [112-114]. An organic compound having nonlinear optical characteristics has stimulated the interest of researchers due to its extensive range of applications, including optical modulation, optical data storage, medical applications and laser remote sensing. Desirable materials are highly sought owing to their strong nonlinear optical susceptibilities, high laser damage thresholds and ultrafast nonlinear reaction times [115,116]. High quality crystals with greater efficiency in nonlinear optical materials are still desired. Organic nonlinear optical devices have faster response times and stronger second-order nonlinear susceptibilities than inorganic NLO crystals. Organic molecules have been proven to be more effective in material tailoring than inorganic molecules. Pyridine and its derived functions are excellent nonlinear materials having a variety of technological and industrial uses, including optical telecommunication, image processing and data processing [117, 118]. The chemical formula for the organic molecule urea, also known as carbamide, is CO(NH<sub>2</sub>)<sub>2</sub>. There are few hydrogens bond sources and acceptors in urea. In this amide, a carbonyl (C=O) functional group connects two -NH2 groups. Urea crystals are organic materials with high optical nonlinear absorption coefficients, great birefringence, but they have hygroscopic qualities, making it difficult to generate laser-sized crystals for various applications [119]. Hydrogen-bonded organic frameworks (HOFs) are a type of porous molecular material that uses hydrogen-bonding interactions to assemble organic building blocks into two-dimensional (2D) and three-dimensional (3D) crystalline networks. The role of H-bonds and  $\pi...\pi$  interactions in the assembly and stabilisation of contemporary soft materials such as hydrogen-bonded organic frameworks (HOFs) [120, 121]. In this study, a crystal of pyridine urea was grown using slow evaporation solution growth method. The PYUA crystal was characterized using XRD, FT-IR, UV-vis-NIR, thermal studies (TGA/DTA), microhardness tests and theoretical calculations. The DFT analysis was carried out by Frontier molecular orbital, Global chemical reactivity descriptors analysis, Mulliken atomic charge, molecular electrostatic potential analysis, NBO analysis, thermodynamic parameters and the results are discussed. In addition to these studies, the intermolecular interaction within the PYUA was obtained from Hirshfeld analysis and a theoretical discussion based on the results has been presented.

# **5.2** Experimental Procedure

### 5.2.1 Crystal growth

Pyridine urea (PYUA) single crystal was synthesized in the 2:1 molar ratio of pyridine (Purity: 99.8% -Aldrich) and urea (Purity 99.5%- Aldrich) and dissolved in acetone and deionized water mixed solvents at room temperature. The synthesized chemical solution was continuously stirred for approximately 7 h to achieve homogeneity and the resulting solution was filtered using petri dish paper to eliminate impurities. The saturated solution was poured into a beaker and a clear polythene paper was used to cover the mouth of the beaker to protect the solution from dust and other impurities. Within two weeks, an optically good, transparent, colorless crystal was obtained. Scheme 5.1 depicts the chemical reaction of the pyridine urea crystal. Figure 5.1 is an image of an as grown crystal of pyridine urea.

Scheme 5.1 The reaction scheme of pyridine urea

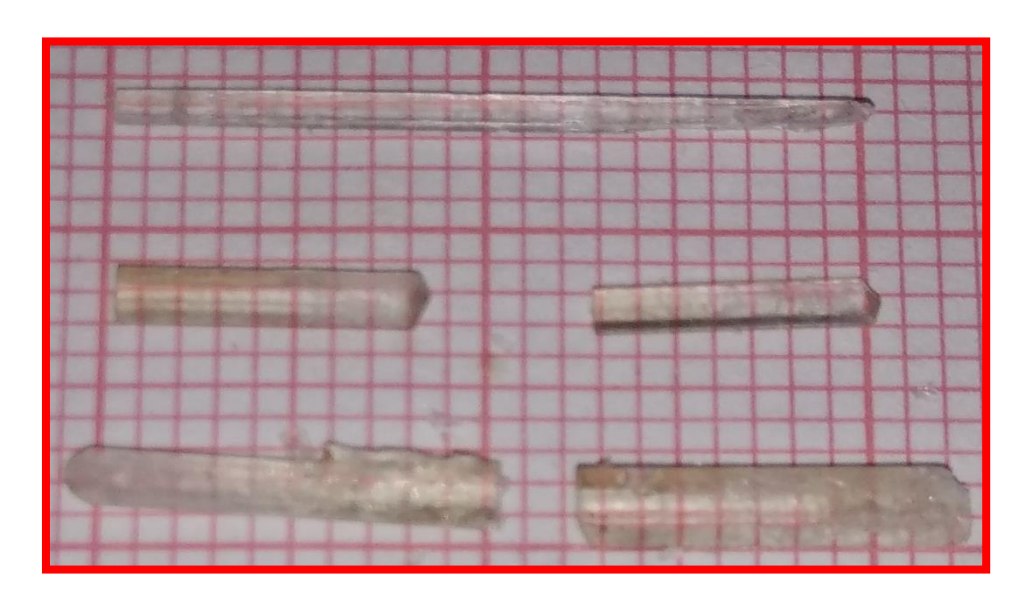


Figure 5.1 The photograph of PYUA crystal

#### 5.3 Results and discussion

# 5.3.1 Single crystal and powder X-ray diffraction studies

To determine lattice parameter values, the XRD data of the PYUA crystal was obtained using the BRUKER KAPPA II CCD X-ray diffractometer with MoK $_{\alpha}$  ( $\lambda$ =0.70173Å) radiation. The PYUA crystal has the centrosymmetric space group P2 $_{1}$ /c and is a monoclinic crystal system. The cell parameters obtained are a = 9.6052(3) Å, b = 10.7195 (2) Å, c = 7.4485(2) Å,  $\alpha$  =  $\gamma$  = 90°,  $\beta$  = 110.615(3)° and cell volume V = 724.57(4) Å $_{3}$ . The observed unit cell parameters are good in agreement with the reported

values [122]. Powder XRD (PXRD) of pyridine urea crystal was measured with an XPERT-PRO diffractometer and  $CuK_{\alpha}(\lambda=1.54056~\text{Å})$  radiation in the  $2\theta$  range from  $10^{\circ}$  to  $50^{\circ}$  and compared with the PXRD simulated spectrum using MERCURY software. The experimental and simulated XRD patterns of the PYUA crystal are compared in Figure 5.2 (a) and (b). The experimental PXRD spectrum matches the simulated PXRD spectrum very closely. The intensity of sharp peaks defining  $2\theta$  angles indicates the good crystalline and purity of PYUA crystal.

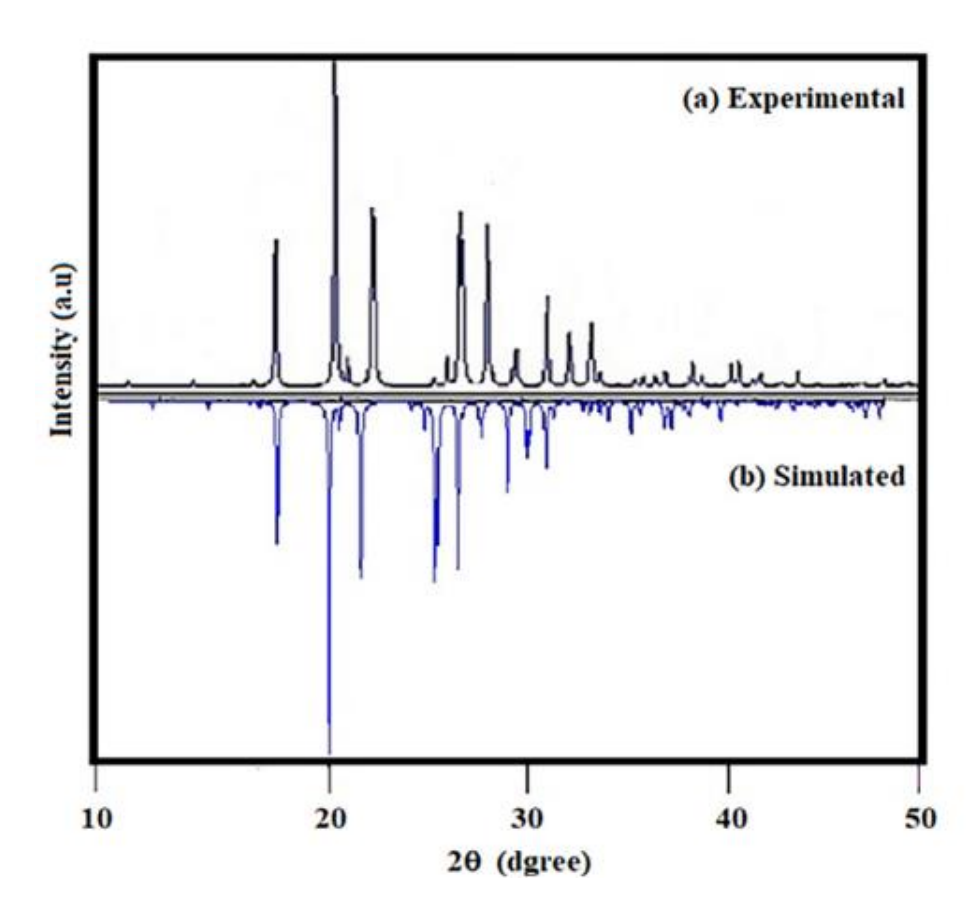


Figure 5.2 (a) Experimental and (b) Simulated Powder XRD spectrum of PYUA crystal

# 5.4 FT-IR spectral analysis

FT-IR analysis was performed on an FT-IR 8000 spectrometer in the range of 4000-400 cm<sup>-1</sup> using the KBr pellet method. Figure 5.3(a) and (b) shows the experimental and simulated FT-IR spectra, respectively. Stretching vibrations of the aromatic ring C-H appear in the range of 3200-3000 cm<sup>-1</sup> [123,124]. The DFT/B3LYP method was used to compute the various frequencies of functional groups in PYUA crystal using the 6-31+G(d,p) level and the results were compared to experimental and reported values. Table 5.1 shows the vibrational frequency assignments. Experimentally at 3182 cm<sup>-1</sup> and in DFT at 3184 cm<sup>-1</sup>, C-H stretching vibrations were identified. The stretching mode of vibration C=O assigned band at 1619 cm<sup>-1</sup> in experimental and 1625 cm<sup>-1</sup> in DFT. In pyridine derivatives, the C-C stretching vibrations range from 1650 to 1400 cm<sup>-1</sup> [125, 126] are getting match for the crystal PYUA in the experimental spectra at 1470 cm<sup>-1</sup>, 1436 cm<sup>-1</sup> and in the DFT spectra at 1428 cm<sup>-1</sup>, 1411cm<sup>-1</sup>, respectively. Experimental and DFT spectra show the N-C-N stretching vibration of the pyridinium ring in the PYUA crystal at 1185 cm<sup>-1</sup> and 1172 cm<sup>-1</sup>. In the experimental and DFT spectra, the C-H in-plane bending modes of vibrations in the PYUA molecule are shown at 1089 cm<sup>-1</sup>, 1035 cm<sup>-1</sup> and 1096 cm<sup>-1</sup>,1040 cm<sup>-1</sup>, respectively. The intense peaks found at 925 cm<sup>-1</sup> and 957 cm<sup>-1</sup>, shows the presence of NH<sub>2</sub> vibration rocking in both the experimental and DFT, respectively. Peaks at 735 cm<sup>-1</sup> in the experimental spectrum and 764 cm<sup>-1</sup> in the DFT spectrum were recognised as NH<sub>2</sub> vibration of wagging. In the experimental and DFT spectrum of the PYUA crystal, NH out-of-plane bending modes of vibration are recorded at 630 cm<sup>-1</sup> and 638 cm<sup>-1</sup>. In the experimental and DFT spectrum of PYUA, which contain amine and carboxylic acid groups, nearly all of the predicted peaks were detected.

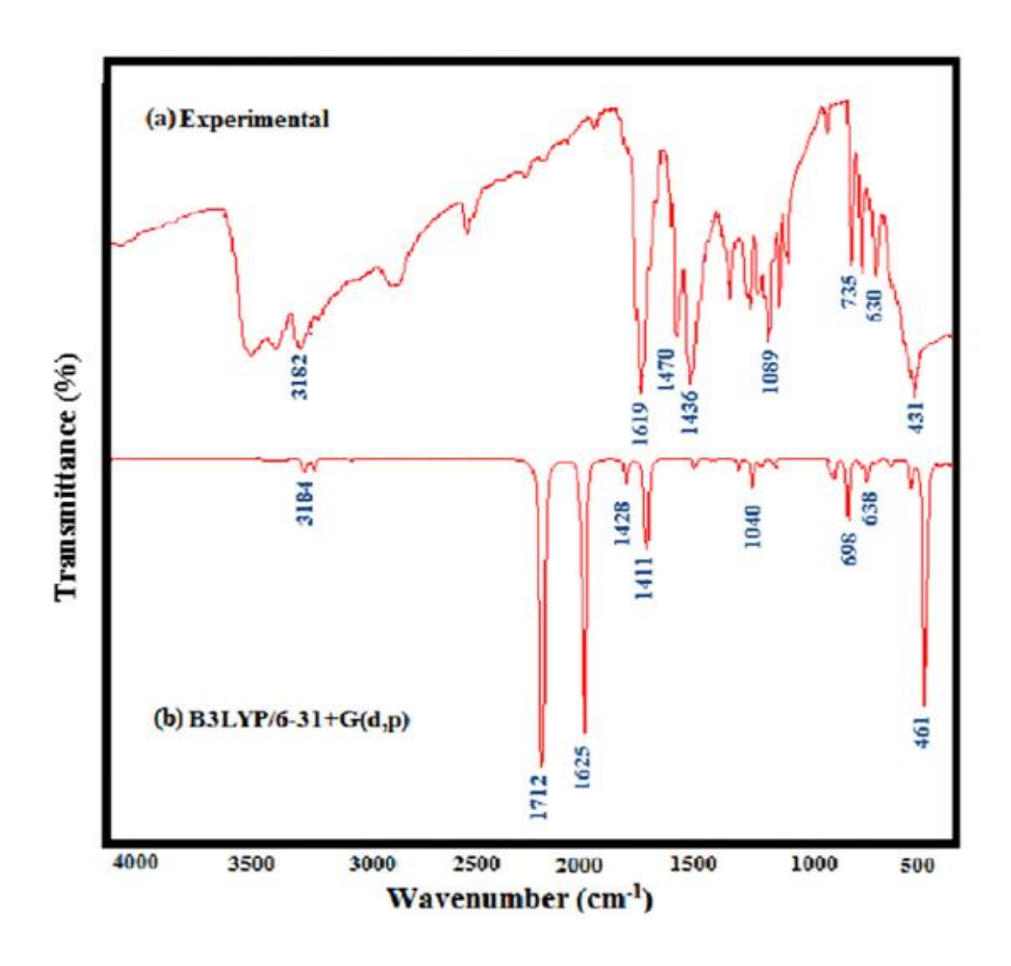


Figure 5.3 FT-IR spectra of PYUA (a) Experimental (b) Simulated

Table 5.1 Experimental and simulated (DFT) FT-IR spectral assignments of PYUA crystal

	Observed Wavenumbers (cm <sup>-1</sup> )					
Pyridine	Urea		DFT/			
[127]	[128]	Experimental	6-31+G(d, p)	Assignments		
-	3196	3182	3184	C-H stretching		
1632	1625	1619	1625	C=O stretching		
1462	1453	1470, 1436	1428, 1411	C-C stretching		
1162	1162	1185	1172	N-C-N stretching		
1078	1053	1089, 1035	1096, 1040	C-H in-plane bending		
929	-	925	957	NH <sub>2</sub> rocking		
746	785	735	764	NH <sub>2</sub> wagging		
725	-	688	698	C-C in-plane bending		
699	587	630	638	N-H out-of plane bending		
464	-	491	461	C-C out-of plane bending		

# 5.5 UV-vis-NIR spectral analysis

Figure 5.4 (a) depicts the ultraviolet spectrum of pyridine urea measured with a Perkin Elmer Lambda-35 UV spectrometer from 200 nm to 800 nm. It specifies the wavelength of absorption in the visible region. Figure 5.4 (b) illustrates the theoretical absorption spectra of PYUA crystal produced using TD-DFT. The oscillator strengths and theoretical electronic excitation energies were estimated using the TD-DFT method with the basis set at 6-31+G(d, p) to support experimental data [129]. The excitation energy in TD-DFT is 281.49 nm, while the oscillator strength f is ~0.0047 experimentally at a wavelength of 245.31nm. The TD-DFT (gaseous) method predicts a value of 281.49 nm and the experimental excitation wavelength is 245.31 nm, which is quite similar to the experimental value.

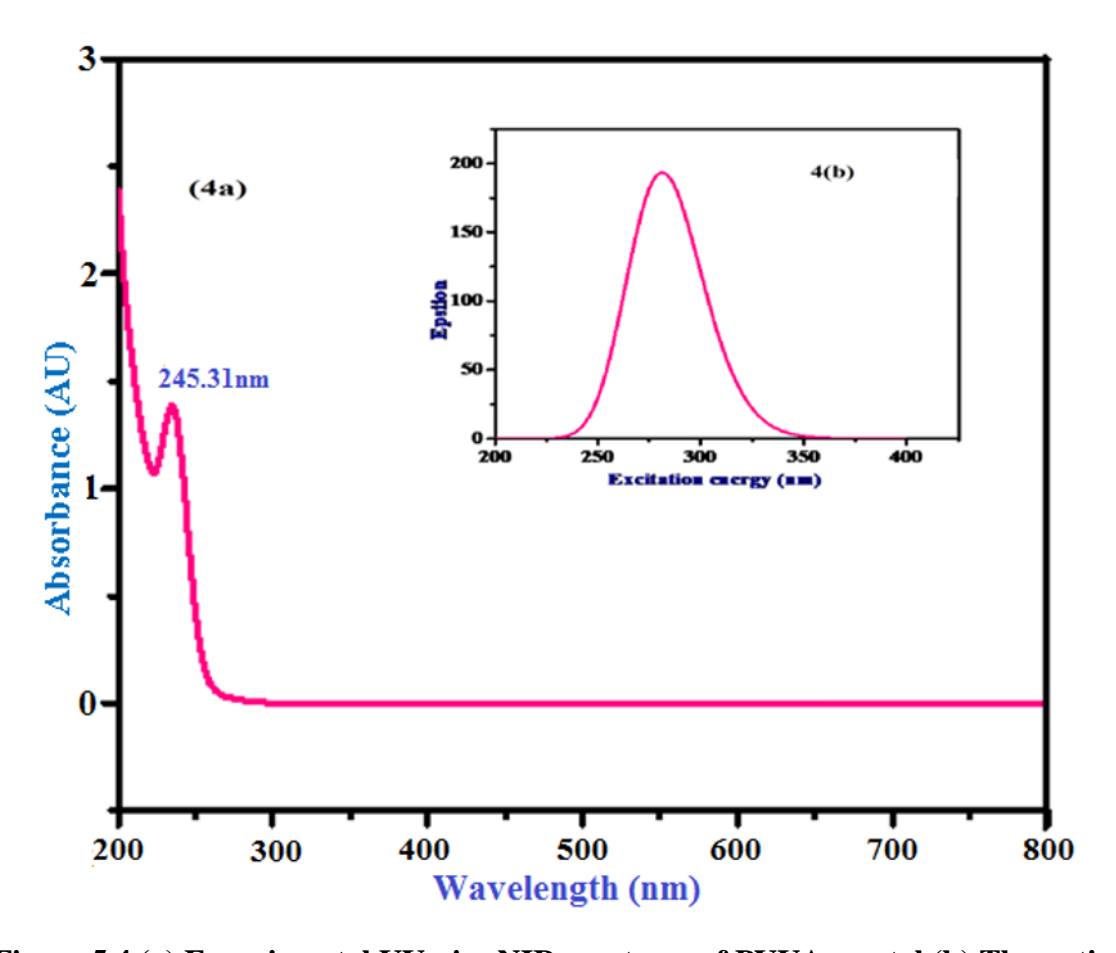


Figure 5.4 (a) Experimental UV-vis –NIR spectrum of PYUA crystal (b) Theoretical UV-vis spectrum of PYUA

# **5.6** Thermal studies

The thermal investigation was carried out in a nitrogen atmosphere, using an SDT Q600 V20.9 alumina thermal analyser maintaining a temperature of 10 °C/min. Thermogravimetric and differential thermal analyses were done on the PYUA crystal and the results are shown in Figure 5.5. The crystal was stable upto 150 °C, which confirms the melting point of the PYUA crystal, since the melting point of the pyridine is found to be 115 °C and urea is 133 °C. The first strong endothermic peak was found in the DTA plot at 162 °C. The second strong endothermic peak accompanied by a substantial weight loss was detected at 237 °C, indicating the decomposition point of the PYUA crystal. The sharpness of the endothermic peak shows the crystalline nature and purity of the material [130]. There were no endothermic or exothermic peaks absorbed before this melting point. This suggests that there is no isomorphic transition.

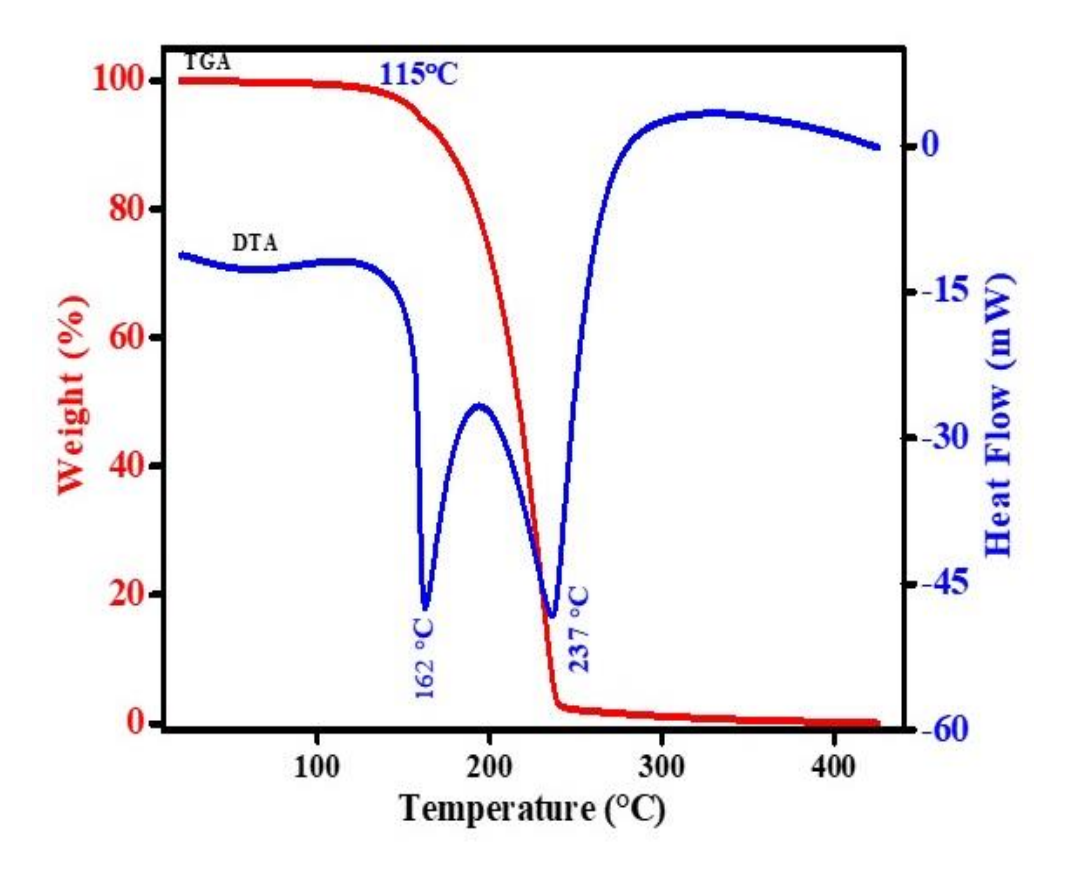


Figure 5.5 TGA/DTA plot of PYUA crystal

#### 5.7 Microhardness studies

Vickers microhardness testing was performed on the PYUA crystal with a diamond pyramidal indenter on a SHIMADZU HMV microhardness tester. Using a Vickers microhardness tester, the grown crystal's mechanical strength was tested. Microhardness is an important mechanical property of the material that plays a significant part in the fabrication of devices. Figure 5.6 (a) depicts a graph of Vickers hardness (Hv) versus load P. The reverse indentation size effect (RISE) is seen to rise when the hardness number (H<sub>v</sub>) increases [131]. For microhardness measurements, a transparent polished crystal with no crakes and a smooth surface was chosen. For indentation durations of 10s, hardness values were obtained for various applied loads (P) ranging from 25 to 100g. There was a crack initiated by indentation with a 100g indentation load. By means of the following equation, the Vickers micro hardness number (H<sub>v</sub>) was determined.

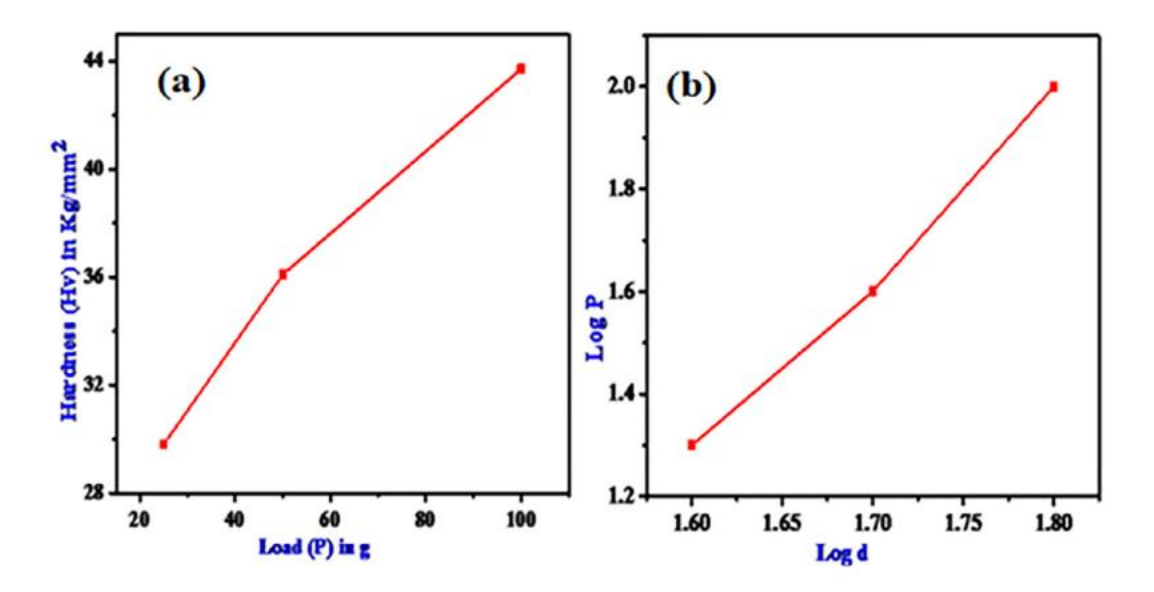


Figure 5.6 (a) Plot of load (P) versus hardness (Hv) of PYUA crystal (b) Plot of log d versus of log P of PYUA crystal

$$H_V = \frac{1.8544P}{d^2} (K g/m m^2)$$

Where P is the applied load in kg, d is the indentation's diagonal length in mm and  $H_v$  is the Vicker's hardness number. The work hardening coefficient (n) was determined by finding the slope of the straight line between log P and log d, as illustrated in Figure 5.6(b). It's PYUA has a work hardening coefficient of 3.2, showing that its PYUA crystal has a work hardening coefficient greater than 1.6, indicating that it is in the soft material group [132, 133].

# 5.8 Computational analyses

The DFT method was also applied at B3LYP, with a 6-31+G (d, p) basis set and the Gaussian 09 programme. The NBO 3.1 programme was used to perform the natural bond orbital study. Crystal Explorer 3.1 was used for the Hirshfeld surface analysis and display of the 2D fingerprint plot [134].

#### 5.8.1 Molecular geometry optimization

PYUA is composed of 19 atoms, 74 electrons and has a singlet spin and is neutral in charge. The global minimum energy of PYUA at B3LYP level with the basis set of 6-31+G(d,P) is -473.6057 a.u, with a dipole moment of 8.3704 Debye, according to the calculations. Table 5.2 compares the geometrical parameters of the PYUA molecule, such as bond lengths, bond angles and dihedral angles, to experimental values. These values have a good agreement between our experimental and calculated results.

Table 5.2 Experimental and geometrical parameters of PYUA crystal calculated by B3LYP/6-31+G(d,p) basis set

Во	Bond length(Å)		Bond A	Bond Angle(°)		) Dihedral angle		
Atoms	DFT	EXP*	Atoms	DFT	EXP*	Atoms	DFT	EXP*
O1-C5	1.229	1.250	O1-C5-N2	122.9	122.0	C18-N9-C10-C12	-0.002	0.160
N2-H3	1.013	0.875	O1-C5-N6	122.9	121.9	C10-N9-C18-C16	-0.001	0.210
N2-H4	1.008	0.872	N2-C5-N6	114.1	116.1	N9-C10-C12-C14	0.002	0.040
N2-C5	1.380	1.336	C5-N6-H7	119.4	118.4	C10-C12-C14-C16	-0.001	-0.590
C5-N6	1.380	1.347	C5-N6-H8	115.4	118.0	C12-C14-C16-C18	-0.001	0.920
N6-H7	1.013	0.866	H7-N6-H8	118.7	120.8	C14-C16-C18-N9	0.002	-0.760
N6-H8	1.008	0.875	C10-N9-C18	117.7	116.1			
N9-C10	1.343	1.345	N9-C10-H11	116.0	118.4			
N9-C18	1.343	1.336	N9-C10-C12	123.3	123.4			
C10-H11	1.088	0.950	C10-C12-H13	120.1	120.6			
C10-C12	1.396	1.385	C10-C12-C14	118.5	118.6			
C12-H13	1.085	0.950	C12-C14-H15	120.7	120.7			
C12-C14	1.396	1.385	C12-C14-C16	118.7	118.8			
C14-H15	1.086	0.950	C14-C16-H17	121.4	120.7			
C14-C16	1.396	1.377	C14-C16-C18	118.5	118.6			
C16-H17	1.085	0.950	N9-C18-C16	123.3	123.4			
C16-C18	1.396	1.379	N9-C18-H19	116.1	118.3			
C18-H19	1.088	0.950	C16-C18-H19	120.6	120.6			

# **5.8.2 HOMO-LOMO analysis**

The ability to donate and accept electrons is represented by the highest occupied molecular orbital (HOMO) and the lowest unoccupied molecular orbital (LUMO). These orbitals are known as frontier molecular orbital's (FMOs). The FMOs are instrumental in determining optical and electrical characteristics and also in evaluating molecular properties [135, 136]. There are 235 molecular orbitals in the PYUA molecule, 37 of which are occupied and 198 of which are unoccupied. The energy band gap value between the PYUA

compound's HOMO-LUMO has been estimated at the Becke-3-Lee-Yang-Parr (B3LYP) level by means of the Gaussian 09W computer software program basis set [137]. The molecule's energy value between HOMO (-9.2268 eV) and LUMO (-4.5056 eV) is roughly 4.7212 eV. The charge carrier interactions inside the molecule are described by the HOMO and LUMO energy gaps. Figure 5.7 depicts the HOMO-LUMO energy levels. The LUMO is located over C-C bond of pyridine and HOMO is located over N-H group of urea.

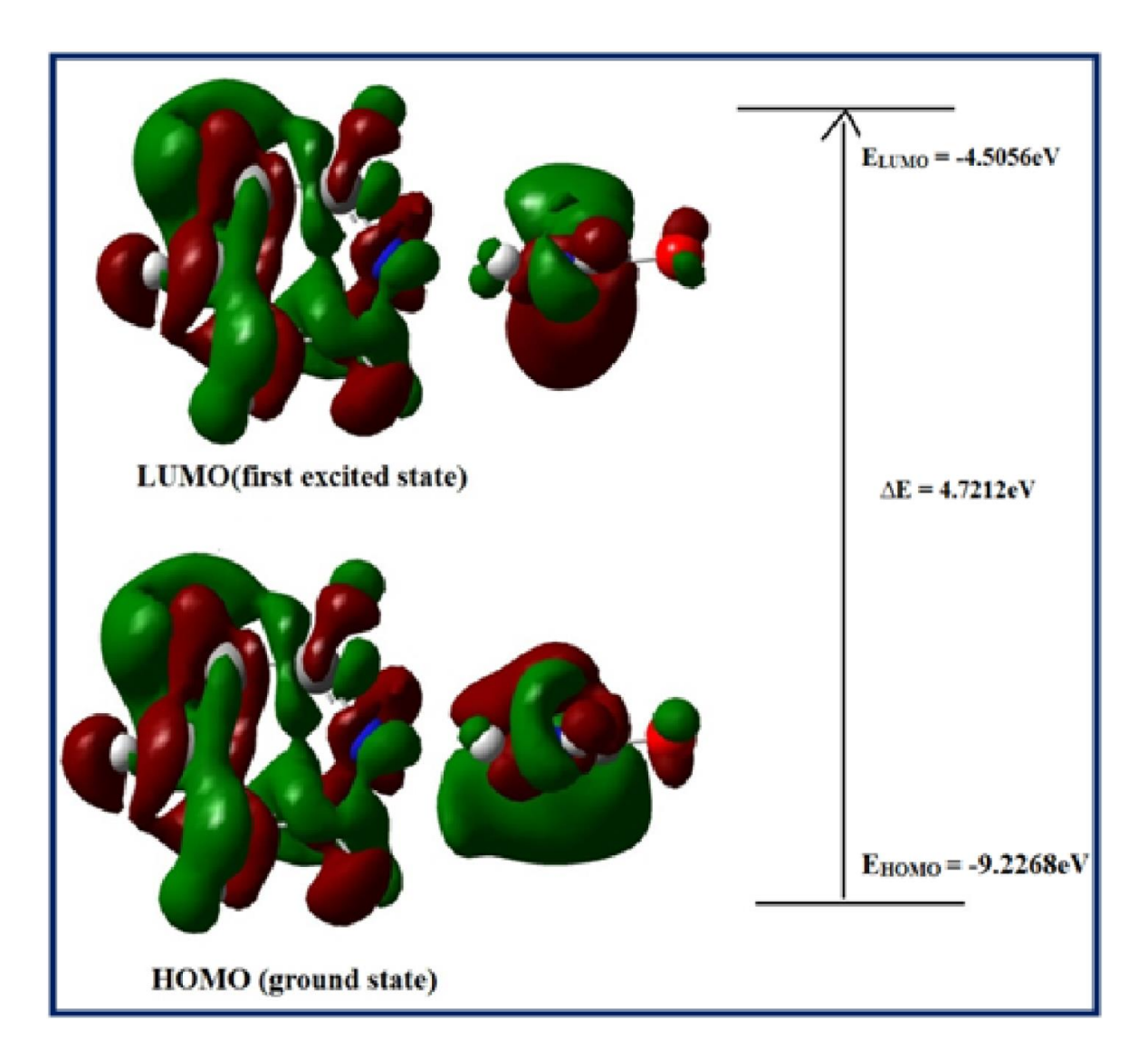


Figure 5.7 HOMO-LUMO energy gap of PYUA

#### **5.8.3** Global reactivity descriptors

The outer most orbital of HOMO has a nucleophilic feature that is primarily caused by electron donation and is directly associated with the ionization potential. However, LUMO is an electrophilic property of the inner most orbital hypothesis that functions as an electron acceptance centre and is closely linked to electron affinity [138]. The energy difference between HOMO and LUMO could be a significant characteristic in defining a molecular system's nonlinear optical properties. The global chemical reactivity characteristics of pyridine urea molecules like electronegativity ( $\chi$ ), electrophilicity index ( $\omega$ ) and chemical potential ( $\mu$ ), softness (s), hardness ( $\eta$ ), of the molecule can be evaluated using HOMO and LUMO energy values for a PYUA molecule [139]. The ionization potential (I) and electron affinity (A) for closed-shell molecules could be stated using Koopmans's theorem [140]  $I = -E_{HOMO}$  and  $A = -E_{LUMO}$ . The DFT B3LYP/6-31+G (d, p) technique was calculated using the ionization potential and electron affinity of pyridine urea. The molecule's electronegativity is  $(\chi) = (I + A) / 2$ ; its chemical hardness  $(\eta) = (I - A) / 2$ ; its chemical potential ( $\mu$ ) =- (I-A) / 2; its softness (S) = 1/2; its electrophilicity index  $(\omega) = \mu^2 / 2\eta$ ; and its energy gap  $(E_g) = E_{LUMO} - E_{HOMO}$ . Table 5.3 presents the estimated values of the global reactivity descriptors parameters.

Table 5.3 Global chemical reactivity descriptors parameters of PYUA

Parameters	DFT/B3LYP
	(e.V)
Еномо	-9.2268
E <sub>LUMO</sub>	-4.5056
Energy gap (E <sub>g</sub> )	4.7212
Ionization potential	9.2268
Electron affinity	4.5056
Elctronegativity	6.8662
Chemical hardness	2.3606
Chemical potential	-6.8662
Electrophilicity index	9.9857
Dipole moment (Debye)	11.4991

The molecule was stabilized by N-H-N, N-H-O and C-H-O hydrogen bonding and characterized by its chemical potential (-6.8662eV). The molecule's hardness (2.3606eV) made it soft, allowing for faster electron transport. The pyridine urea compound had a high electrical attraction power based on electronegativity and electrophilicity values.

# 5.8.4 Mulliken and natural population analysis

Mulliken atomic charges (MAC) and natural population analysis (NPA) could be a great tool for population analysis and determining the charge distribution in each atom of a PYUA molecule. The plot of Mulliken and natural atomic charges on various PYUA molecule element is shown in Figure 5.8(a). Because they influence the electronic structure, molecular polarizability, dipole moment along with other system features, Mulliken atomic charges are significant in the usage of molecular systems for quantum chemical processing [141]. Both negative and positive charges are found on distinct atoms in the PYUA molecule and are given in Table 5.4. According to the charge distribution molecule, all the hydrogen atoms are positively charged. Positive charges were applied to carbon atoms C5, C12 and C16, while negative charges were applied to the other carbon atoms. C5 has the biggest positive charge (0.512015e) and C14 has the most negative charge (-0.39361e). The nitrogen atoms in N2 (-0.5994e), N6 (-0.59931e) and N9 (-0.28757e) are all negative. According to the charge distribution, carbon (C10 and C18) atoms coupled to nitrogen atoms possess negative charges, while carbon (C5) atoms connected to oxygen atoms possess positive charges. As a result, negatively charged carbon atoms are linked to nitrogen atoms, whereas positively charged hydrogen atoms are attached to carbon atoms.

Table 5.4 Mullikan atomic charges and Natural population analysis

Atom No	MAC	NPA
O1	-0.58216	-0.71093
N2	-0.5994	-0.80724
Н3	0.330892	0.38457
H4	0.310982	0.38729
C5	0.512015	0.77528
N6	-0.59931	-0.80807
H7	0.330847	0.37901
H8	0.310954	0.38974
N9	-0.28757	-0.50375
C10	-0.12778	0.04905
H11	0.147413	0.20256
C12	0.111184	0.23882
H13	0.140861	0.21892
C14	-0.39361	-0.16027
H15	0.143793	0.21439
C16	0.112921	0.24143
H17	0.139929	0.21923
C18	-0.14103	0.04941
H19	0.139067	0.20108

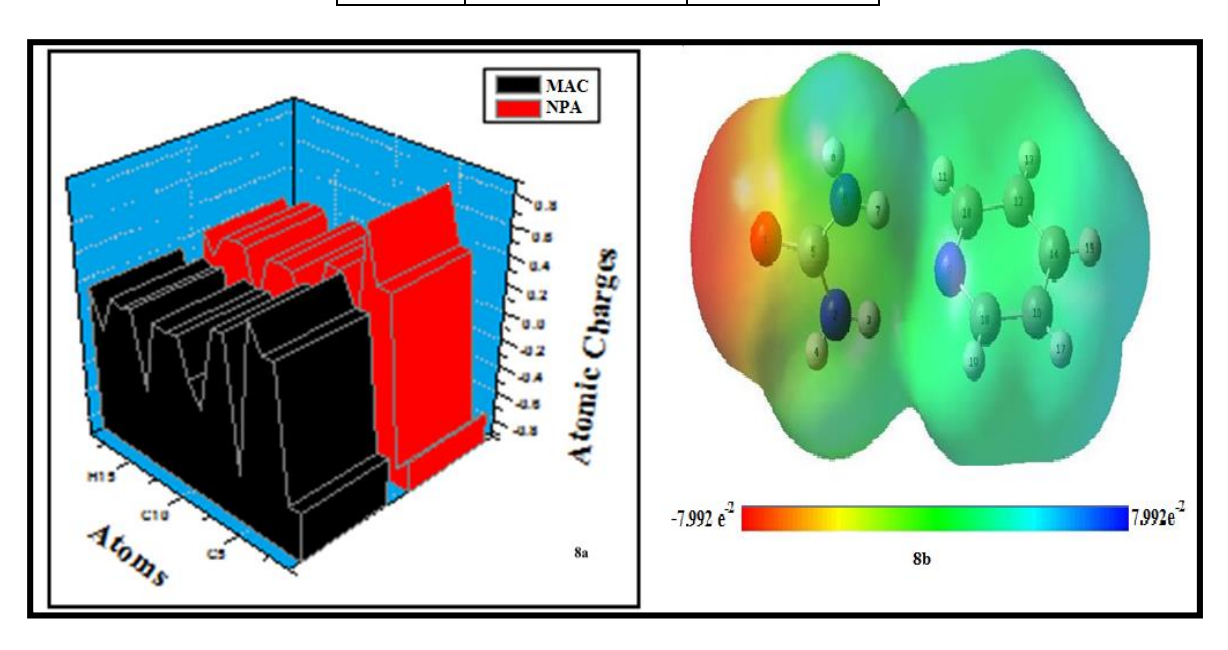


Figure 5.8 (a) The plot of Mulliken and Natural Atomic Charges of PYUA crystal (b) Molecular electrostatic potential map ranges from -7.992e<sup>-2</sup> to 7.99e<sup>-2</sup> of PYUA crystal

#### 5.8.5 Molecular electrostatic potential (MEP) map analysis

The distribution of positive and negative charges in a crystal allows us to describe its electrostatic potential. In molecular systems, the electrostatic potential is essential for understanding intermolecular interactions and locating electrophilic and nucleophilic attack sites [142]. The MEP is found from the optimized B3LYP/6-31+G (d, p) result and is illustrated in Figure 5.8(b) to evaluate reactive regions for electrophilic and nucleophilic attacks on the PYUA molecule. Different electrostatic potential values are depicted by different colours on the MEP map. The red colour represents the location of the maximum negative zone, which favours electrophilic attacks, whereas the blue colour represents the site's maximum positive zone, which favours nucleophilic attacks. The regions of negative and positive electrostatic potentials appear in red and blue, respectively, while the region of zero potential is represented by green. All these analyses revealed that the oxygencontaining region of urea is the most reactive.

# 5.8.6 NBO analysis

NBO analysis gives a consistent description of molecular and intramolecular bonding interactions in terms of electron donor and acceptor conjugative and charge carrier interactions [143, 144]. The transfer of electron density from an occupied electron orbital to an unoccupied electron orbital can be investigated using NBO analysis [145]. In accordance with the theory of second-order perturbations, the stabilization energy E(2) associated with the delocalization  $i\rightarrow j$  is determined for the donor(i) and acceptor(j) using the following equation.

$$E(2) = \triangle E_{i,j} = qi \frac{F(i,j)^2}{E_j - E_i}$$

Where qi represents the donor orbital occupancy, E(2) represents stabilization energy,  $E_i$  and  $E_i$  are diagonal factors, The diagonal is F(i,j), while the off-diagonal NBO Fock matrix

components are j and i. The NBO analysis results for the PYUA molecules are described in Table 5.5. The interactions between lone pairs are the most substantial. The lone pair of electron-donating atoms n1(N2) and n1(N6) to the antibonding orbital's  $\sigma^*(O1\text{-}C5)$  and  $\sigma^*(O1\text{-}C5)$ , have stabilization energies of 42.62 and 41.04 kcal/mol respectively. The molecule's high energy value causes intramolecular charger interactions. The interactions  $(\pi\text{-}\pi^*)$  are significant in demonstrating the presence of conjugation in the molecules under investigation. For the  $\pi(C12\text{-}C14) \to \pi^*(N9\text{-}C10)$ ,  $\pi(N9\text{-}C10) \to \pi^*(C16\text{-}C18)$ ,  $\pi(C16\text{-}C18) \to \pi^*(C12\text{-}C14)$  and  $\pi(C12\text{-}C14) \to \pi^*(C16\text{-}C18)$  transitions, the stabilization energies were found to be 29.14, 25.52, 23.34 and 18.28 kcal/mol, respectively. Finally, based on the data, it can be assumed that title molecules have directed conjugation, which facilitates intramolecular charge transfer. As a result, the strong intramolecular hyper conjugative fundamental interactions are the elementary cause of more stability in all these systems.

Table 5.5 NBO analysis of PYUA crystal

Donor(i)	Acceptor(j)	E(2) <sup>a</sup> (kcal/mol)	E(j)- $E(i)$ <sup>b</sup> $(a.u)$	$F(i, j)^{c}(a.u)$
n1 (N2)	σ*(O1-C5)	42.62	0.36	0.114
n1(N6)	σ*(O1-C5)	41.04	0.36	0.112
$\pi$ (C12-C14)	$\pi^*$ (N9-C10)	29.14	0.26	0.079
$\pi$ (N9-C10)	$\pi^*(C16-C18)$	25.52	0.33	0.083
$\pi$ (C16-C18)	$\pi^*(C12-C14)$	23.34	0.29	0.075
$\pi$ (C12-C14)	$\pi^*(C16-C18)$	18.28	0.29	0.066

<sup>&</sup>lt;sup>a</sup>F(i, j) is the Fock matrix component that associates the i and j NBO orbitals.

#### **5.8.7** Thermodynamic properties

Table 5.6 shows the thermodynamics parameters of the pyridine urea molecule, such as zero-point vibrational energy (ZPVE), rotational constants, rotational temperature,

<sup>&</sup>lt;sup>b</sup>E(2) stands for the energies of hyper conjugative interactions (kJ/mol).

<sup>&</sup>lt;sup>c</sup> the energy difference between the i and j NBO orbital of the donor and acceptor

entropy, thermal energy and heat capacity, which are calculated using theoretical harmonic frequencies. The total energy of a molecule, for example, is the sum of its rotational, vibrational and translational energies, as shown by E=Er+Ev+Et. The magnitude of heat needed to increase the temperature of a material by 1°C is known as its heat capacity. The ZPVE variation appears to be insignificant [146]. As expected, the rotational constant reduces as the rotational temperature decreases. The moment of inertia of a molecule is inversely proportional to the rotational constant [147]. As a result, a decrease in the rotational constant signifies an increase in the molecule's moment of inertia, i.e., the simplicity with which its rotating state may be adjusted in response to its environment.

Table 5.6 Theoretically computed thermodynamic parameters of PYUA

Thermodynamical parameters	DFT			
Zero-point vibrational energy (KCal/Mol)	96.2872			
Rotational constants (GHz)				
A	3.79517			
В	0.47944			
C	0.46331			
Rotational temperature (K)				
A	0.18214			
В	0.02301			
C	0.02224			
Thermal energy (KCal/Mol)				
Rotational	0.889			
Vibrational	101.303			
Translational	0.889			
Total thermal energy	103.081			
Heat capacity at constant volume (Cal/Mol-K)				
Rotational	2.981			
Vibrational	31.326			
Translational	2.981			
Total heat capacity	37.288			
Entropy(cal/mol-kelvin)				
Rotational	30.323			
Vibrational	38.924			
Translational	40.701			
Total entropy	109.948			

# 5.9 Hirshfeld surface analysis

The Hirshfeld surface analysis was considered to be substantial in determining the intermolecular interaction of the PYUA crystal using Crystal Explorer 3.1 and the associated Hirshfeld surfaces of normal view and transparent view of  $d_{norm}$ , shape index and curvedness are illustrated in Figure 5.9 (a) and 5.9 (b) respectively and are the fingerprint plots given in Figure 5. 9 (c).

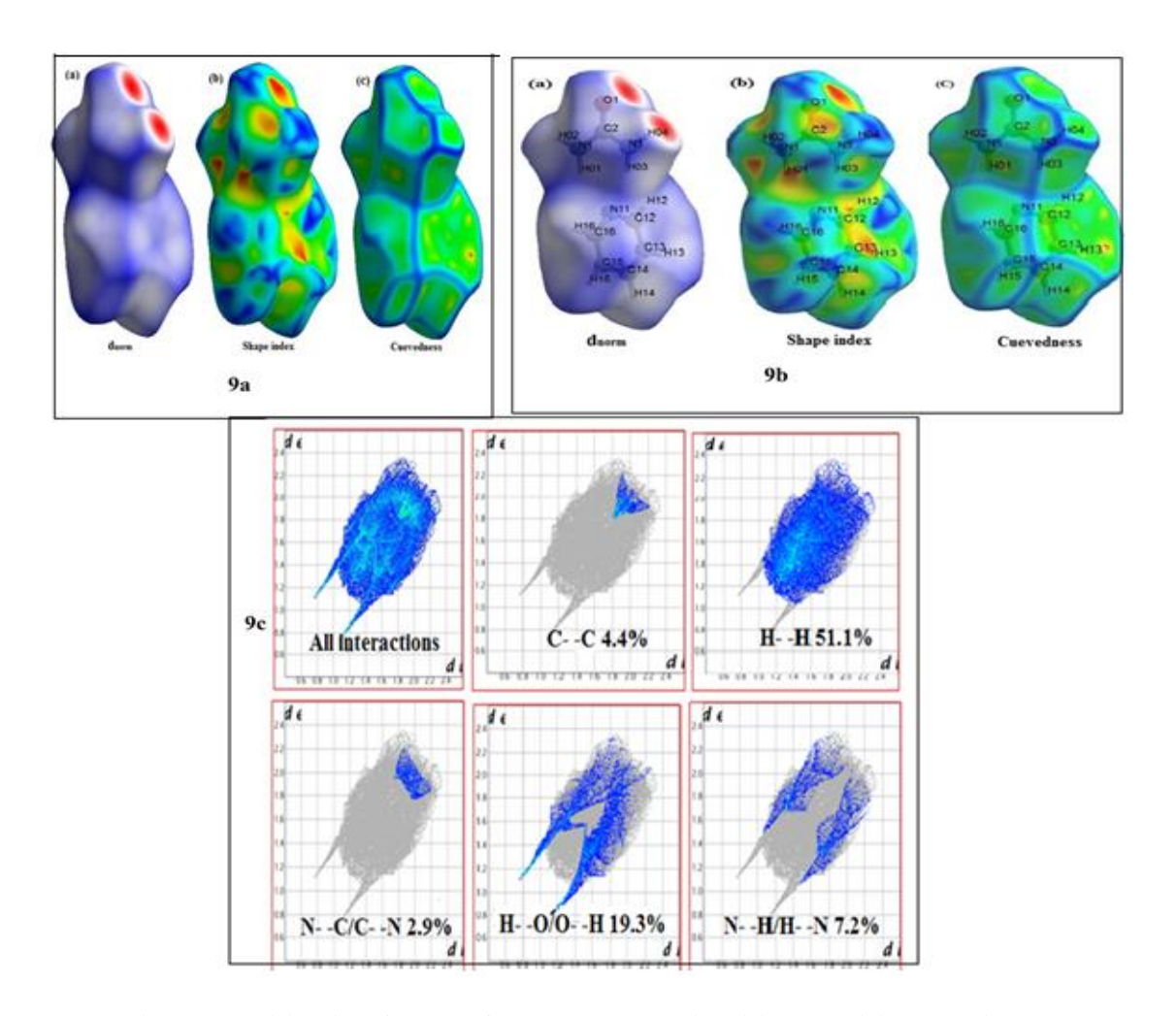


Figure 5.9 (a) Hiresfeld surfaces mapped with (a)  $d_{norm}$  (b) shape index (c) curvednesss (b) Hiresfeld surfaces mapped with transparent view (a)  $d_{norm}$  (b) shape index (c) curvednesss (c) 2D Fingerprint plots

The intermolecular interactions were investigated using crystallographic data that had been solved using single crystal XRD and the normalised contact distances ( $d_{norm}$ ) were used to map the distances between the surface point and the atoms exterior ( $d_e$ ) and interior ( $d_i$ ) Vander waals radii [148]. The  $d_{norm}$  surface illustrates intermolecular interactions in relation to the vander Waals radius using a blue and red colour scheme [149]. The  $d_{norm}$  is calculated using the mean values from  $d_i$  and  $d_e$ . The distance between the Hirshfeld area and the adjacent atom outside (blue) and inside (red) the surface is denoted by de and  $d_i$ , respectively.

The d<sub>norm</sub> can be determined using the following expression,

$$d_{norm} = \frac{d_i - r_i^{vdw}}{r_i^{vdw}} + \frac{de - re^{vdw}}{re^{vdw}}$$

Where vdw stands for Vander Walls atom radii, the red colour indicates interactions with small distances, while the blue colour represents interactions with larger distances. In addition, the white denotes a distance equivalent to the Vander Walls radii. The analyzed data shows that the PYUA molecules contain increased hydrogen-hydrogen (H- -H) interactions (51.1%) inside to outside compared to other interactions. The fraction of O- -H/H- -O contacts in all Hirshfeld surfaces is 20.4%, showing that hydrogen bonding contacts are the second most important interaction. The presence of a nitro and carboxylate group in PYUA causes the O- -H/H- -O interactions. The N- -H/H- -N connections are the third most important contributors to the overall Hirshfeld surface (7.2%). There is also the existence of  $\pi$ - -  $\pi$  (C- -C) (4.4%) and additional interactions N- -C/C- -N (2.9%). The electrostatic energy of the molecule is 3.4 kJ/mol which is obtained by Crystal Explorer.

\_\_\_\_\_\_

# SYNTHESIS, GROWTH, PHYSICOCHEMICAL CHARACTERIZATION AND COMPUTATIONAL STUDIES ON AMINOPYRIDINIUM CHLORONICOTINATE SINGLE CRYSTAL

\_\_\_\_\_

#### 6.1 Introduction

Organic nonlinear optical materials are important in fast growing industries like photonics and optoelectronics [150, 151]. Organic materials are gaining interest for optoelectronic applications and photonic because of their high frequency conversion, second-order optical nonlinearity, large optical susceptibilities, low cost, optical damage threshold and short response time [152-154]. Asymmetries in the  $\pi$ -electron conjugation systems of the electron acceptor, electron donor groups of organic molecules are extremely polarisable physical objects for nonlinear optical (NLO) applications [155, 156]. Organic optical materials have significant optical susceptibilities, ultrafast response times, high optical thresholds when compared to inorganic materials [157]. Because of their exceptional properties, such as high NLO coefficient, wide optical transparency and extended thermal stability, the pyridine groups of organic crystals play an essential role in the vicinity of nonlinear optics. Pyridinium complexes are significant in the formation of NLO materials with charge transfer systems and donor-acceptor properties that allow for modifications in physical and structural features. Because of their heterocyclic nature, pyridine derivatives have a distinct advantage in pharmaceutical applications [158, 159]. Pyridine is an aromatic heterocyclic organic molecule and structurally similar to benzene except for the substitution of a nitrogen atom in one of the CH groups. 2-aminopyridine (AP) is a chemical compound with the formula H<sub>2</sub>C<sub>5</sub>H<sub>4</sub>N. The AP molecule has two nitrogen atoms and is a heterocyclic molecule. The heterocyclic molecule 2-aminopyridine has frequently been used as a ligand in metal complexes with a second harmonic generation [160-164]. Nicotinic acid and its

biologically active derivatives have been extensively researched over the last decade [165] and 6-chloronicotinic acid (CN) is a key component of agrochemicals, animal feed enrichment, plasma cholesterol and pharmaceuticals [166]. In the present work, synthesis, growth, physicochemical characterization and computational studies on aminopyridinium chloronicotinate single crystal are discussed by employing different characterization techniques such as single crystal X-ray diffraction, powder X-ray diffraction, Fourier transforms infrared, UV-vis-NIR, TG/DTA and Vickers microhardness test. In addition to these studies, the DFT/B3LYP method was used to analyze the molecular geometry, HOMO-LUMO, Natural bond orbital, Mulliken atomic charge and molecular electrostatic potential of the molecule in the gaseous state and the results are discussed.

#### **6.2** Experimental Procedure

### **6.2.1** Synthesis and crystal growth

Aminopyridinium chloronicotinate compound was synthesized at room temperature using an AR grade. 2-aminopyridine and 6-chloronicotinic acid in 2:1 molar ratio. The required amount of 2-aminopyridine was dissolved in acetone and 6-chloronicotinic acid was slowly added into this solution and the mixture was stirred well using a magnetic stirrer. After a few seconds, white crystalline salt of aminopyridinium chloronicotinate was deposited at the bottom of the beaker. The recrystallization process enhanced the purity of the synthesized material. The chemical reaction involved in this process is represented by scheme 6.1.

Scheme 6.1 Reaction scheme of APCN crystal

The prepared APCN salt was dissolved in double distilled water and the solution was filtered into a beaker using whatmann filter sheet. The beaker is covered with a perforated aluminum foil sheet and kept for slow evaporation at room temperature. After three weeks, an optically good quality seed crystal was harvested. To grow a bulk crystal of APCN, the supersaturated solution of APCN was taken in a 100 ml beaker and one of the well-defined seed crystal was dropped into the solution. The beaker is kept in a dust-free environment in order to avoid multiple nucleations. At room temperature, the solvent was slowly evaporated, and a single crystal of size 14 x 9 x 7 mm<sup>3</sup> was obtained. Fig.1 shows a photograph of an optically transparent APCN crystal.



Figure 6.1 As grown crystals of APCN

# 6.3 Computational details

Density functional theory can be used to calculate the molecular shape, energy, and other features of aminopyridinium chloronicotinate. Using the B3LYP (Becke's three-Lee-Yang-Parr) Gaussian 09 program with 6-31+G (d, p) basis set, the DFT method was chosen to optimize the molecular geometry of the APCN. The results of HOMO-LUMO analysis, global chemical reactivity descriptors, Mulliken population analysis, molecular electrostatic potential, and thermodynamical properties are discussed.

#### 6.4 Results and Discussion

#### 6.4.1 Single and Powder X-ray diffraction analysis

The cell parameters of the APCN crystal were measured with a Bruker SMART APEXII DUO CCD system with MoK $\alpha$  radiation. The unit cell parameters and the crystal system have been identified from the single crystal X-ray diffraction analysis. The unit cell parameters of the values are a = 8.6840(4) Å, b = 10.8121(5) Å, c = 11.9241(6) Å and the cell volume is V = 1126.82(9) Å<sup>3</sup>. As a result, the crystal system is monoclinic with centrosymmetric space group P2<sub>1</sub>/c. The obtained results were found to be in good agreement with the reported values [167]. Table 6.1 shows a comparison of the obtained single X-ray diffraction values with the reported data values. Powder X-ray diffraction analysis was performed on a grown crystal APCN using an XPERT-PRO Diffractometer system with CuK $\alpha$  radiation ( $\lambda$ =1.5406 Å). The grown crystal was scanned from 10° to 80° range. The well-defined sharp intensity peaks specifying 2 $\theta$  angles confirmed the good crystalline and purity of the APCN crystals. Figure 6.2 depicts the Powder X-rd pattern of an APCN crystal.

Table 6.1 Single X-rd data of APCN crystal

Lattice parameters	Present Work	Reported Work [168]
a	8.6840(4) Å	8.6844(4) Å
b	10.8121(5) Å	10.8112(5) Å
c	11.9241(6) Å	11.9235(6) Å
α	90°	90°
β	95.2046(9)°	95.2046 (9)°
γ	90°	90°
Z	4	4
Volume	$1126.82(9)\text{Å}^3$	$1114.87(9) \text{ Å}^3$
Crystal system	Monoclinic	Monoclinic
Space group	P2 <sub>1</sub> /c	P2 <sub>1</sub> /c
R factor	-	0.019

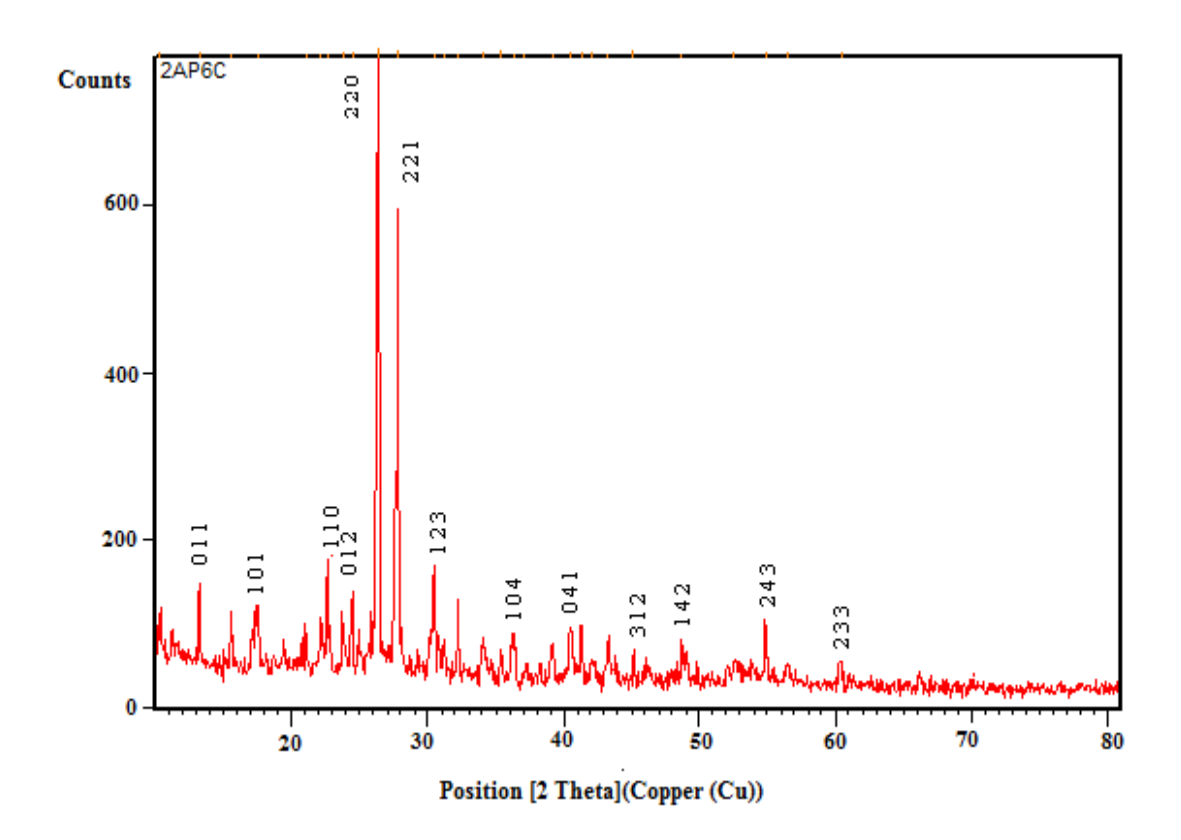


Figure 6.2 Powder XRD spectrum APCN crystal

# 6.5 FTIR spectral analysis

The FTIR spectra of the APCN crystal were recorded in the region of 4000-500 cm<sup>-1</sup> using the KBr pellet method with a Perkin-Elmer spectrometer and the various functional groups are shown in Figure 6.3. The broad band at 3383 cm<sup>-1</sup> is caused by protonated nitrogen N-H symmetric stretching vibrations in a 2-aminopyridine moiety. The band observed at wave number 2359 cm<sup>-1</sup> in the APCN crystal could be attributed to the O-H stretching of the carboxylic acid group. The NH<sub>2</sub> asymmetric stretching vibration causes a peak at 3178 cm<sup>-1</sup>. The N-H...O intramolecular hydrogen bonding affects the shift of the N-H amine group's in-plane bending vibration from 1618 cm<sup>-1</sup> to 1568 cm<sup>-1</sup> [169]. The sharp intense peak and strong absorption bands found at 1498 cm<sup>-1</sup> and 1473 cm<sup>-1</sup> were inductive of aromatic C-N stretching and C=N stretching vibrations, respectively. The weak absorption at 1243 cm<sup>-1</sup> is due to aromatic C-C stretching vibration, whereas the medium

band at 1159 cm<sup>-1</sup> is due to C=C stretching vibration. The intense peaks at 1122 cm<sup>-1</sup>, 1035 cm<sup>-1</sup> were attributed to C-H in-plane bending vibration, whereas the medium intensity peak at 685 cm<sup>-1</sup> was caused by C-H out-of-plane bending vibration. The aromatic ring's C-H bending and C-Cl stretching vibrations could be responsible for the 834 cm<sup>-1</sup> and 729 cm<sup>-1</sup> [170]. The carboxylate ion deformation vibrations are generally detected in the 700-400 cm<sup>-1</sup> range, while the COO bending vibrations are recorded at 631 cm<sup>-1</sup> and 559 cm<sup>-1</sup>. The strong band at 436 cm<sup>-1</sup> is due to the pyridine moiety's C-N-C out-of-plane bending vibration. The FTIR spectra revealed virtually all of the predicted peaks for APCN crystal, which contains amine and carboxylic acid groups. The FT-IR assignments of various functional groups of APCN crystal are shown in Table 6.2.

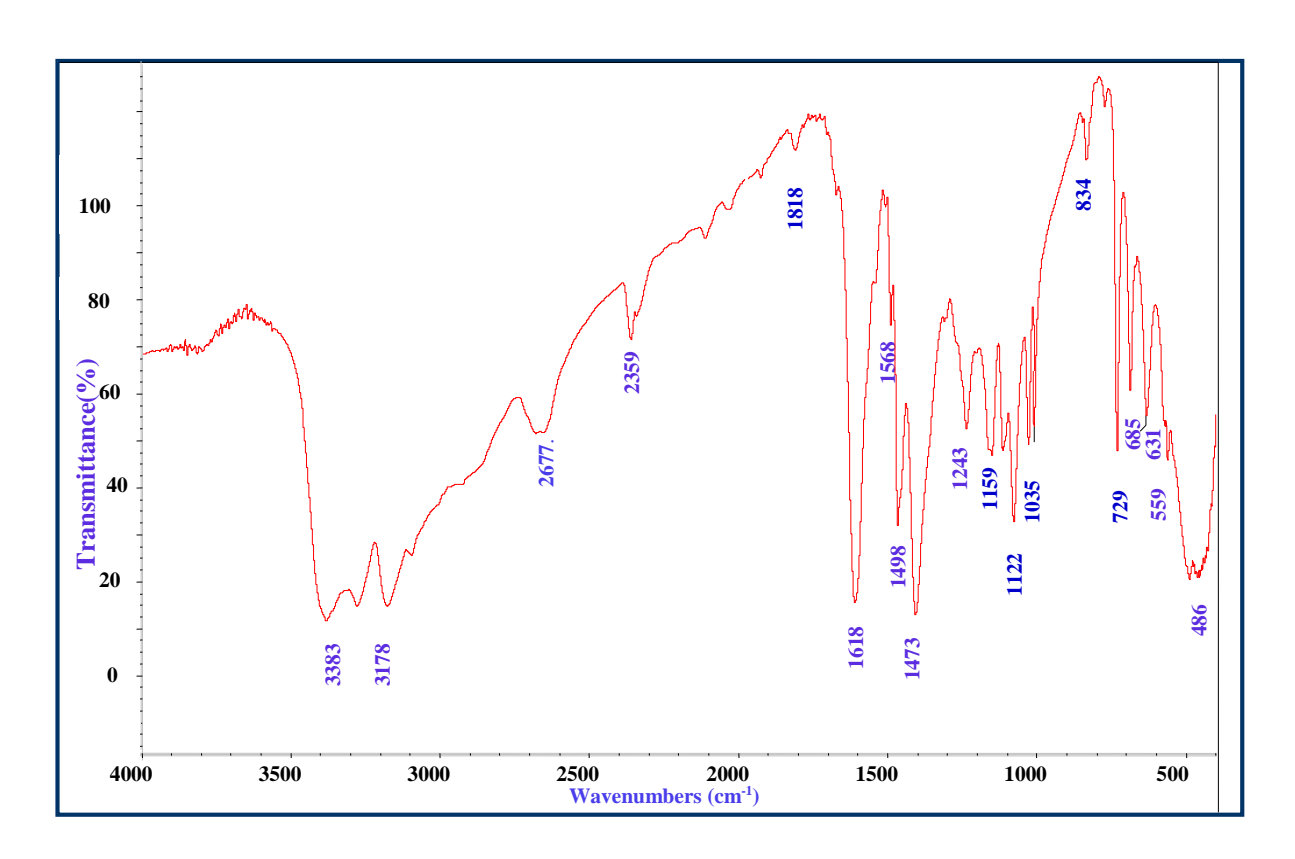


Figure 6.3 FTIR spectrum of APCN crystal

Table 6.2 Observed IR bands of APCN crystal

Wavenumber (cm <sup>-1</sup> )	Assignments
3383	NH symmetric stretching vibration
3178	NH <sub>2</sub> asymmetric stretching vibration
2677	C-H stretching vibration of pyridinium moiety
2359	OH stretching vibration in carboxylic acid group
1818	N-H in-plane bending vibration of amine group
1618	N-H in-plane bending vibration
1498	C-N stretching vibration
1473	C=N stretching vibration
1243	C-C stretching vibration
1159	C=C stretching vibration
1122	C-H in-plane bending vibration
1035	C-H bending vibration
834	C-N vibration of pyridinium moiety
729	C-Cl stretching vibration of pyridinium moiety
685	C-H out-of-plane bending vibration
631	COO bending vibration
436	C-N-C out of plane bending vibration

# 6.6 UV-vis-NIR spectral studies

Using a Lamda 35 model UV-vis-NIR spectrometer, the optical transmission spectrum of an APCN crystal was recorded from 200 nm to 800 nm as shown in Figure 6.4. The UV cut-off wavelength of the APCN crystal was determined to be 335 nm. The recorded spectrum reveals that the crystal has high transparency of more than 90% in the 470 nm - 800 nm range. The absence of visible absorption indicates that the grown crystal is suitable for optoelectronic applications [171]. For the APCN single crystal, the estimated bandgap energy is around 3.6 eV.

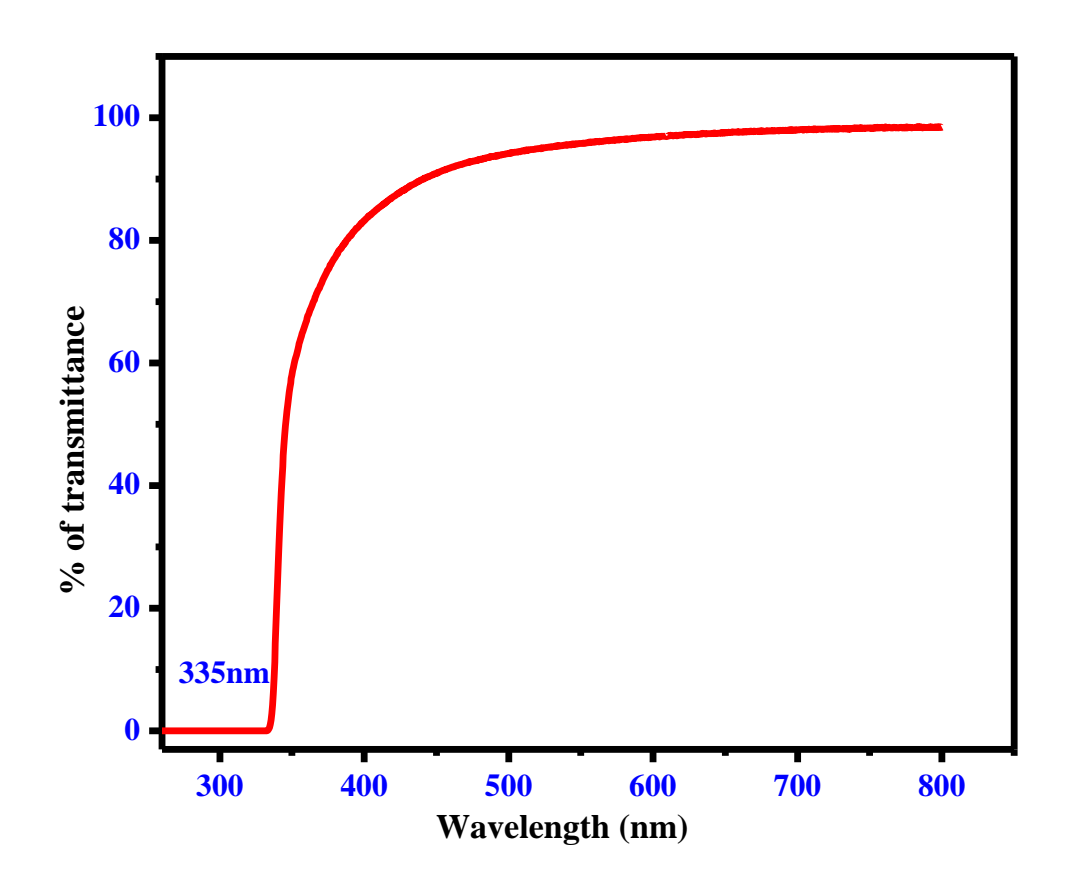


Figure 6.4 UV-vis-NIR spectrum of APCN crystal

# **6.7** Thermal Studies

The thermogravimetric (TG) and differential thermal analysis (DTA) measurements were done simultaneously by instrument SDT Q600 V20.9 Build 20 in the range of

temperatures  $25^{\circ}\text{C} - 900^{\circ}\text{C}$  under  $N_2$  atmosphere with a heating rate of  $10^{\circ}\text{C/min}$  as shown in Figure 6.5. TG/DTA analysis was used to determine the thermal stability of the grown crystal. From the TGA curve, no weight loss was observed up to  $173.1^{\circ}\text{C}$  and a major weight loss was observed between  $173.1^{\circ}\text{C}$  to  $397.4^{\circ}\text{C}$ . There are no isomorphic phase transitions in the spectra, indicating that the material is thermally stable up to  $173.1^{\circ}\text{C}$ . The DTA curve of APCN shows a sharp endothermic peak at  $193.7^{\circ}\text{C}$ , which corresponds to the materials melting point. The absence of endothermic or exothermic peaks before the material's melting point demonstrates the sample's chemical stability [172]. The sharpness of the peak demonstrates the sample's good crystallinity and purity.

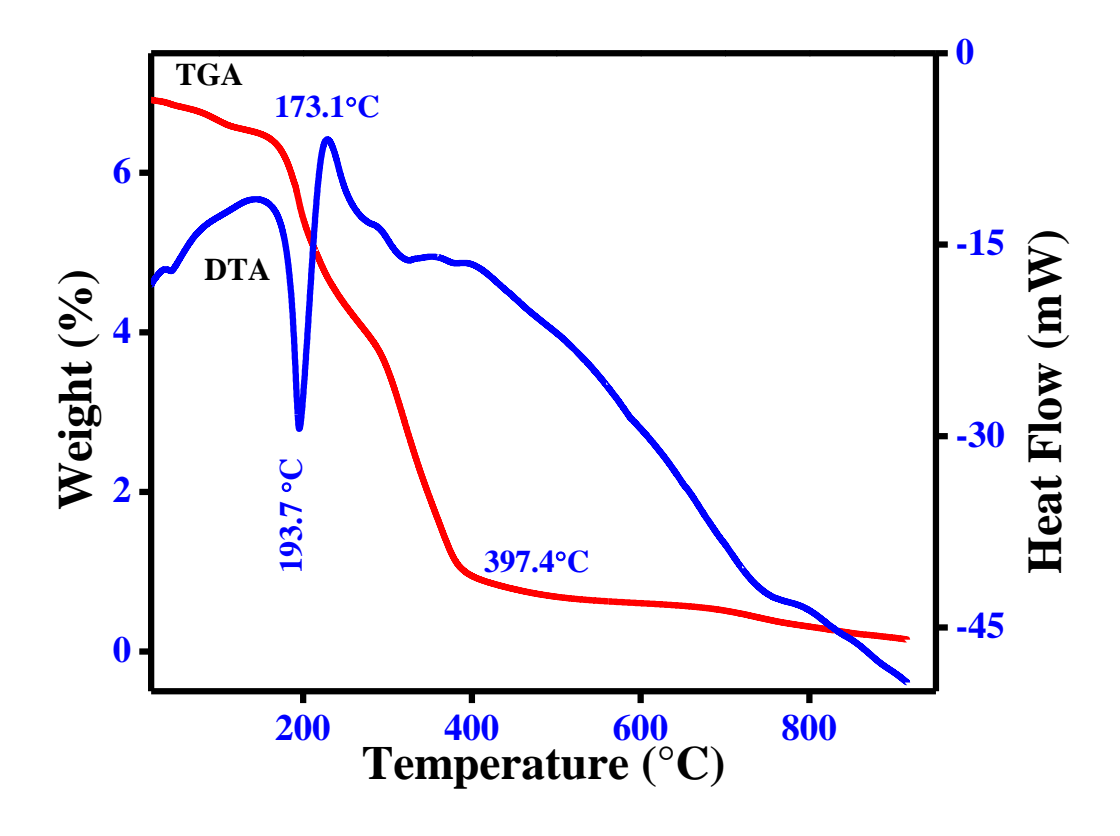


Figure 6.5 TGA/DTA curves of APCN crystal

#### 6.8 Microhardness studies

The mechanical strength was determined using the Leitz Wetzler Vickers microhardness technique. For indentation time of 10s, microhardness measurements were

taken for the various applied loads (P) varying from 25g to 100g. Several indentations were created for each weight and the diagonal length (d) of each indentation was measured. The Vickers hardness number (Hv) was calculated by the formula [173]

$$Hv=1.8544P/d^2$$
 (6.1)

Where P is the applied load on the samples and d is the diagonal length of an impression in µm. Figure 6.6 depicts a graph plotting Hv versus load P. The hardness number increases with increasing applied load, which is known as the reverse indentation size effect (RISE). The work hardening coefficient (n) was determined using the slope of a straight line between log P and log d, as shown in Figure 6.7. The values of 'n' for hard materials range between 1 and 1.6, while soft materials have values greater than 1.6. The n value of APCN was discovered to be 3.1, indicating that the grown crystal falls into the soft category of the material [174,175].

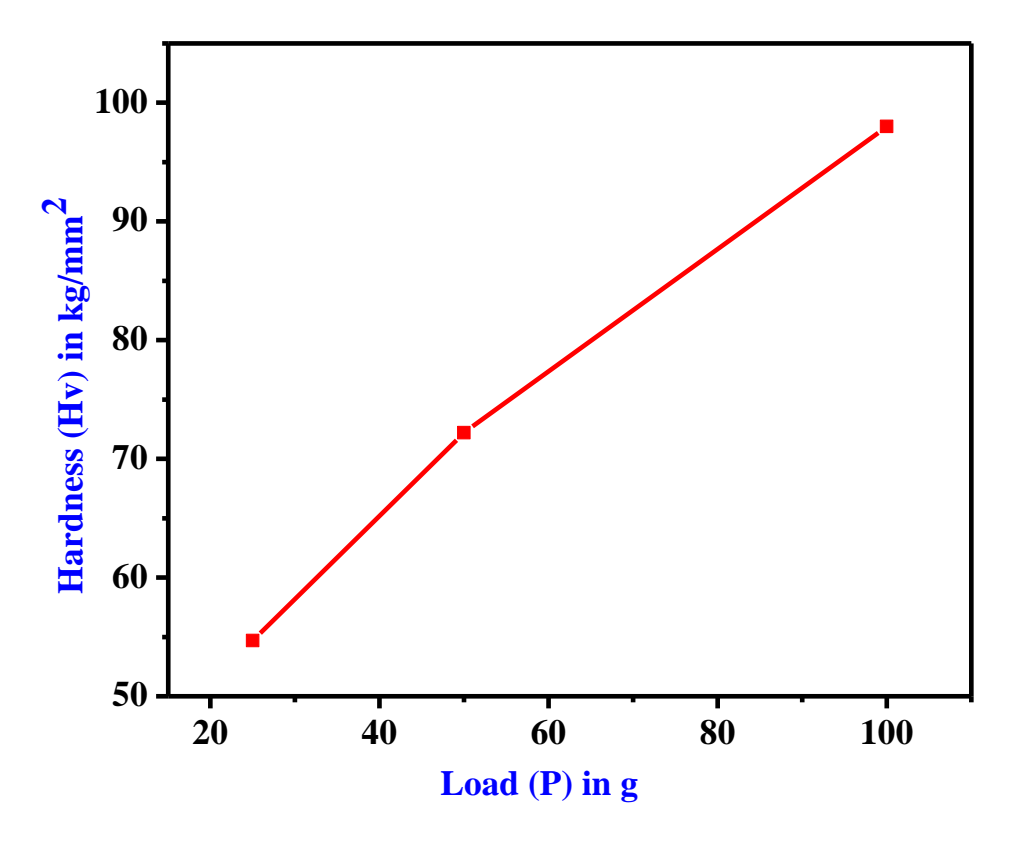


Figure 6.6 Plot of load (P) Vs Hv

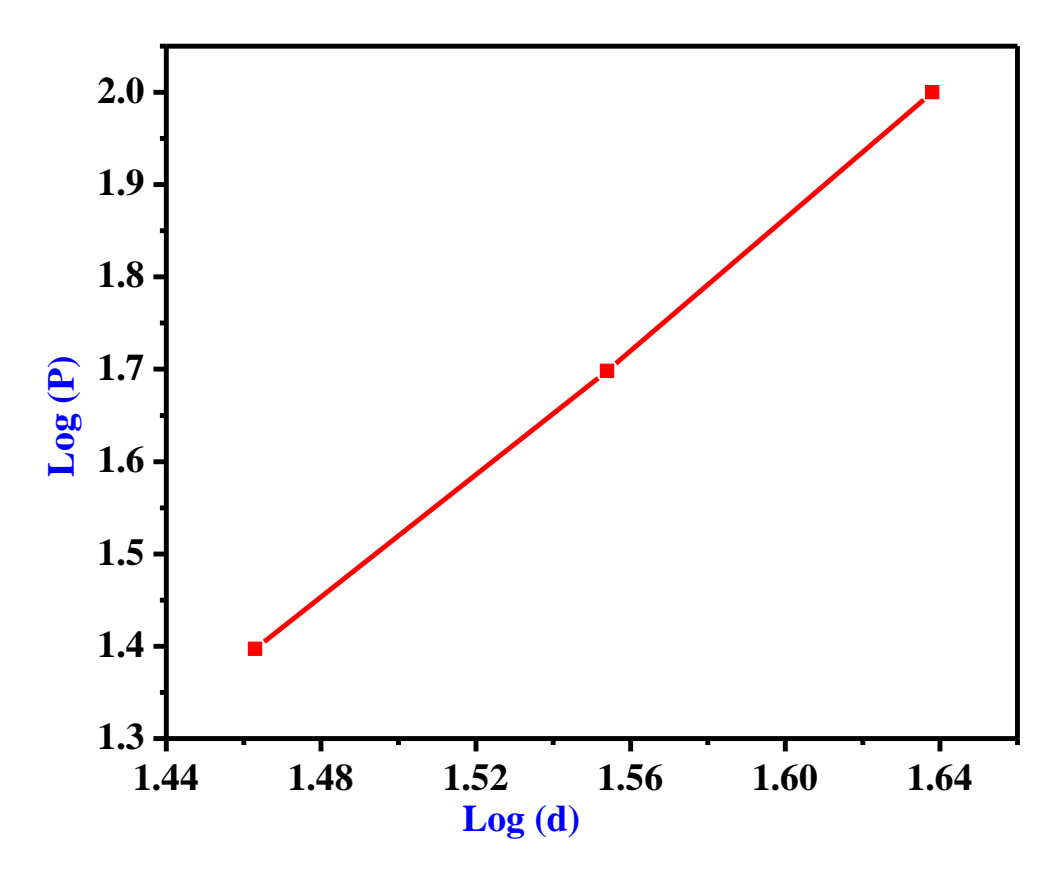


Figure 6.7 Plot of Log (d) Vs Log P

# **6.9** Theoretical investigations

# 6.9.1 Molecular geometry

DFT and B3LYP were used to optimize the molecular geometry structure of APCN using the 6-31G+(d,p) basis set. The optimized molecular structure along with the numbering of atoms is shown in Figure 6.8. Table 6.3 lists the optimized geometrical parametric quantity such as bond lengths and bond angles. Due to the presence of nitrogen in the benzene ring, the C-C bonds were not of equal length. The differences between the six C-C bond distances, on the other hand, were small. The optimized molecular structure reveals that 6-chloronictinic acid moiety is connected with 2-aminopyridine moiety via a pair of N-H...O hydrogen bonding interactions. The oxygen atom in the carboxyl group of 6-chloronictinic acid works as both a donor and an acceptor, resulting in the formation of N1-H8-O17 and N2-H9-O16 interactions, with the bond angles of 156.0° and 156.6°,

respectively. The common geometrical arrangement in 2-aminopyridine substituted heterocyclic rings [176]. It's also worth noting that the benzilate moiety has intramolecular hydrogen bonding. The optimized geometry demonstrates that intermolecular hydrogen bonding interactions have a significant influence on the molecular structure of APCN.

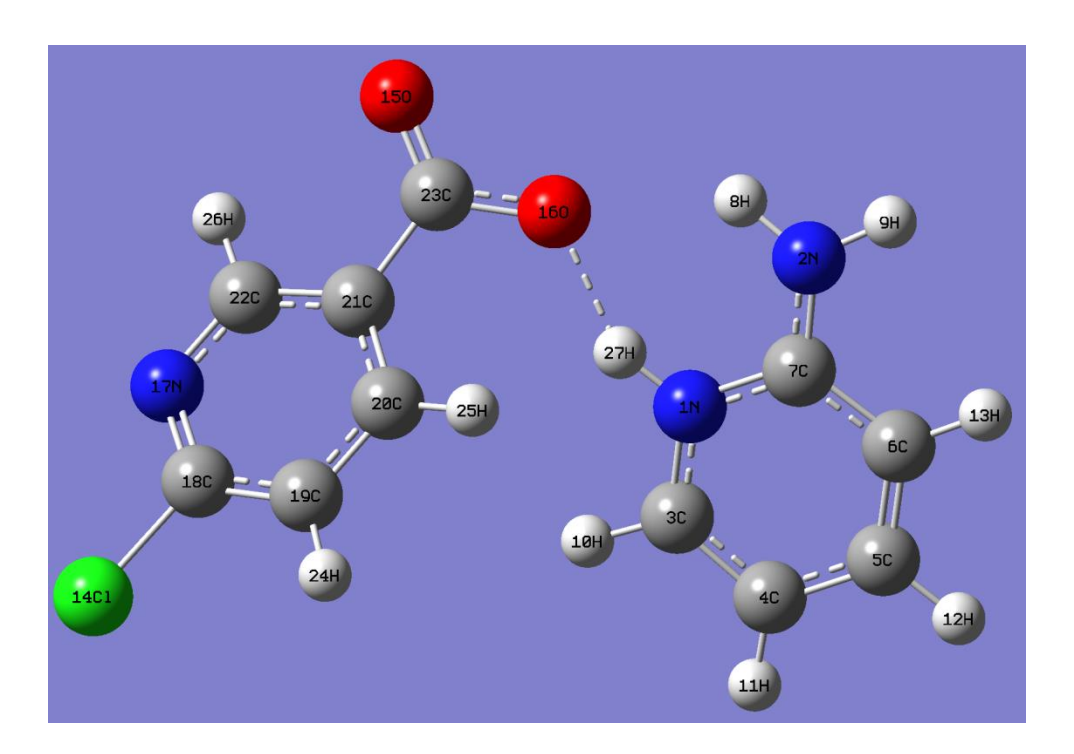


Figure 6.8 Optimized molecular structure of APCN crystal

Table 6.3 Selected bond length, bond angles of APCN crystal obtained from theoretical and experimental data

Atoms	Bond length(Å)		Atoms	Bond angles(°)	
	DFT	EXP*		DFT	EXP*
N1-C3	1.3461	1.3444	C3-N1-C7	118.7457	116.58
N1-C7	1.35	1.5556	N1-C3-C4	123.7108	123.6
N2-C7	1.3704	1.3609	C4-C3-H11	120.8066	120
N2-H9	1.0127	0.89	C3-C4-C5	117.5378	117.59
N2-H10	1.0076	0.923	C3-C4-H12	120.6695	120.00
C3-C4	1.3869	1.398	C5-C4-H12	121.7925	121
C3-H11	1.0872	0.9500	C4-C5-C6	119.7956	119.68
C4-C5	1.404	1.4129	C5-C6-C7	118.8857	118.64
C5-C6	1.384	1.3863	C5-C6-H14	121.2078	121
C5-H13	1.0861	0.95	N1-C7-N2	117.3387	118.37
C6-C7	1.4149	1.4129	N1-C7-C6	121.3217	123.6
C6-H14	1.0856	0.95	N2-C7-C6	121.315	121.16
H11-C21	3.1634	3.1	C19-N18-C23	117.4119	118.37
O16-C24	1.2142	1.2489	Cl15-C19-N18	116.6474	116.05
O17-C24	1.3432	1.2719	N18-C19-C20	124.6831	125.31
N18-C19	1.3229	1.3218	C19-C20-C21	117.3093	117.59
N18-C23	1.3389	1.3305	C19-C20-H25	120.8598	120
C19-C20	1.3986	1.398	C21-C20-H25	121.8297	121
C20-C21	1.3917	1.3917	C20-C21-C22	119.4C235	119.68
C20-H20	1.0835	0.95	C21-C22-C23	117.6C242	117.59
C21-C22	1.4017	1.4173	C23-C22-C24	118.4021	117.59
C22-C23	1.4014	1.4129	N18-C23-H27	116.7751	118.04
C22-C24	1.502	1.5075	C22-C23-H27	119.6928	119
			O16-C24-O17	121.0375	117.13
			O16-C24-C22	121.6135	125.14
			O17-C24-C22	117.34H25	117.71

Exp\* - Experimental

# 6.9.2 HOMO - LUMO analysis

The highest occupied molecular orbitals (HUMOs) are electron donors, while the lowest unoccupied molecular orbitals (LUMOs) are electron acceptors. These two types of molecular orbital are referred to as the Frontier molecular orbital's (FMOs). The energies

of HOMO and LUMO and their energy gaps are important parameters in controlling the optical properties, chemical reactivity, structural symmetry and chemical reactivity of a molecule [177]. The HOMO orbital is capable of donating an electron, whereas the LUMO orbital is capable of accepting an electron. In general, the energy gap between the HOMO and LUMO orbital indicates the molecule's stability and reactivity. Figure 6.9 depicts HUMO-LUMO and their energy of APCN energy diagram. The energy gap diagram between HOMO and LUMO was calculated to be 3.7201eV. The experimental band gap energy from the UV-vis spectrum for the APCN molecule is 3.6 eV, which is close to the theoretical value. A soft molecule is defined as a molecular structure with a low orbital energy gap; with higher energy gaps are linked with high kinetic stability and low chemical reactivity [178].

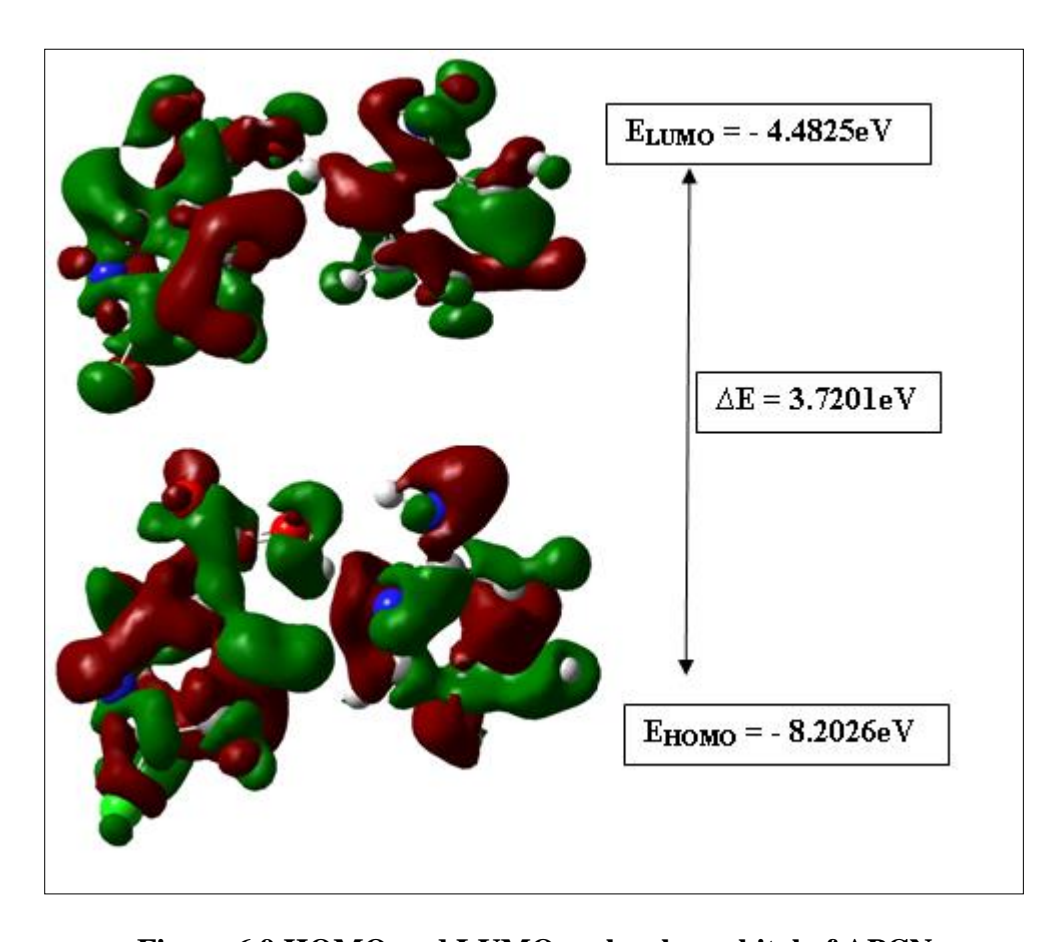


Figure 6.9 HOMO and LUMO molecular orbital of APCN

# 6.9.3 Global chemical reactivity descriptors

The values of various global chemical reactivity descriptor (GCRD) parameters such as electronegativity ( $\chi$ ), electrophilicity index ( $\omega$ ), chemical hardness ( $\eta$ ), chemical softness ( $\sigma$ ), chemical potential ( $\mu$ ), were theoretically calculated using the ionization potential (I) and electron affinity (A). According to Frontier molecular orbital (FMO) theory, the ionization potential (I) is connected to HOMO energy ( $E_{HOMO}$ ) using Koopmans's theorem [179,180] whereas electron affinity (A) is computed from LUMO energy ( $E_{LUMO}$ ) respectively, which can be expressed as,

Ionization Potential (I) = 
$$-E_{HOMO} = 8.2026eV$$
 (6.2)

Electron Affinity (A) = 
$$-E_{LUMO} = 4.4825eV$$
 (6.3)

The Electronegativity of the molecule is determined as  $(\chi) = (I+A)/2$  (6.4)

The Chemical hardness of the molecule is evaluated as  $(\eta) = (I-A)/2$  (6.5)

The Chemical potential of a molecule is calculated as,  $(\mu) = -(I+A)/2$  (6.6)

The Chemical softness of the molecule is estimated as,  $(\sigma) = 1/\eta$  (6.7)

The Electrophilicity index estimated as,  $(\omega) = \mu^2/2 \eta$  (6.8)

The calculated values of GCRD parameters such as I, A,  $\chi$ ,  $\eta$ ,  $\mu$  and  $\omega$  for APCN crystal are also represented in Table 6.4.

Table 6.4 GCRD parameters of APCN crystal

Parameters (a.u)	DFT/B3LYP
E <sub>HOMO</sub> (eV)	-8.2026
E <sub>LUMO</sub> (eV)	-4.4825
Energy gap (eV)	3.7201
Ionization Potential (I)	8.2026
Electron Affinity (A)	4.4825
Electronegativity (χ)	6.3426
Chemical hardness (η)	1.8601
Chemical potential (µ)	-6.3426
Chemical softness (σ)	0.5376
Electophilicity index (ω)	10.8136

# 6.9.4 NBO analysis

The DFT method with the B3LYP/6-31+G (d, p) basis set was used to analyze the natural bond orbital (NBO) of aminopyridinium chloronicotinate. The molecule's stabilization energies were computed using second-order perturbation theory on the Fock matrix on an NBO basis and the results are shown in Table 6.5. The formation of N-H....O is revealed by the hyper conjugate interaction between the lone pair nO and BD\*(N-H). The stabilization energies of LP(2)O16 → BD\*N1-H27, LP(1)O16 → BD\*N1-H27 and LP(1)O16 → BD\*N2-H8 intramolecular hydrogen bonding contacts between APCN molecules are 27.14, 5.60 and 3.85 kJ/mol respectively. The presence of N23-H32...O4 hydrogen bonding interactions is supported by NBO analysis [181]. The major hyper conjugate interactions LP(3)O16  $\rightarrow$  BD\*(2)O15-C23, LP(1)N2  $\rightarrow$  BD\*(2)N1-C7 and LP(2)O15 → BD\*(1)O16-C23 have high stabilization energies of 62.65, 61.09 and 28.71kJ/mol respectively, indicating  $\pi$  electron delocalization in the respective bonds in APCN. Intramolecular interactions are created by the orbital overlaps through  $\pi$ -  $\pi^*$  interactions such as  $\pi$  (C5-C6)  $\rightarrow \pi^*$ (N1-C7),  $\pi$  (N17-C22)  $\rightarrow \pi^*$ (C18-C19),  $\pi$  (C20-C21)  $\to \pi^*$ (N17-C22),  $\pi$  (N1-C7)  $\to \pi^*$ (C3-C4) and  $\pi$  (C3-C4)  $\to \pi^*$ (C5-C6) with stabilization energies of 34.65, 29.62, 27.60, 26.17 and 23.36 kcal/mol, respectively. The high stabilization energy of 188.26 kcal/mol is due to the interaction of  $\pi^*$  (N17-C22)  $\rightarrow$  $\pi^*(C20-C21)$ , resulting in the intramolecular charge transfer, which improves the optical properties of the APCN molecule.

Table 6.5 Second-order perturbation theory analysis of the APCN in NBO basis including the stabilization energies using DFT at B3LYP  $6-31+G\ (d,p)$  level

Donor(i)	Acceptor(j)	E(2)kcal/mol	E(j)-E(i)(a.u)	F( i, j)(a.u)
within unit 1	1 0/	. , ,		
BD(1)N1-C3	BD*(1)N1-C7	2.16	1.32	0.048
BD(1)N1-C3	BD*(1)N1-C7	3.62	1.31	0.061
BD(2)N1-C7	BD*(2)C3-C4	26.17	0.37	0.089
BD(2)N1-C7	BD*(2)C5-C6	5.5	0.37	0.041
BD(1)N1-H27	BD*(1)C3-C4	3.21	1.25	0.057
BD(1)N1-H27	BD*(1)C6-C7	3.88	1.2	0.061
BD(1)N2-H8	BD*(1)C6-C7	4.47	1.15	0.064
BD(1)N2-H9	BD*(1)N1-C7	5.2	1.13	0.069
BD(1)C3-C4	BD*(1)C5-H12	2.52	1.2	0.049
BD(2)C3-C4	BD*(2)N1-C7	9.92	0.23	0.045
BD(2)C3-C4	BD*(2)C5-C6	23.36	0.29	0.074
BD(1)C3-H10	BD*(2)N1-C7	4.79	1.02	0.063
BD(1)C3-H10	BD*(2)C4-C5	3.69	1.09	0.057
BD(1)C4-C5	BD*(1)C3-H10	2.45	1.17	0.048
BD(1)C4-H11	BD*(1)N1-C3	4.94	1.02	0.063
BD(1)C5-C6	BD*(1)N2-C7	3.8	1.18	0.06
BD(2)C5-C6	BD*(2)N1-C7	34.65	0.23	0.085
BD(2)C5-C6	BD*(2)C3-C4	13.53	0.28	0.056
BD(1)C5-H12	BD*(1)C3-C4	3.11	1.1	0.052
BD(1)C5-H12	BD*(1)C6-C7	3.61	1.05	0.055
BD(1)C6-C7	BD*(1)N1-H27	2.52	1.25	0.051
BD(1)C6-H13	BD*(1)N1-C7	5.5	1.01	0.067
BD(1)C6-H13	BD*(1)C4-C5	3.51	1.09	0.055
LP(1)N2	BD*(2)N1-C7	61.09	0.22	0.113
BD*(2)N1-C7	BD*(2)C3-C4	37.28	0.06	0.066
BD*(2)N1-C7	BD*(2)C5-C6	58.45	0.06	0.085
from unit 1 to uni	it 2			
BD(2)N1-C7	BD*(1)C20-H25	0.1	0.87	0.009
BD(1)N1-H27	BD*(1)O16-C23	0.17	1.2	0.013
from unit 2 to uni	it 1			
LP(1)O16	BD*(1)N1-H27	5.60	1.09	0.07
LP(1)O16	BD*(1)N2-H8	3.85	1.08	0.058
LP(2)O16	BD*(1)N1-H27	27.14	0.75	0.129

within unit 2				
BD(1)N17-C22	BD*(1)Cl14-C18	5.26	0.96	0.064
BD(2)N17-C22	BD*(2)C18-C19	29.62	0.3	3.085
BD(2)N17-C22	BD*(2)C20-C21	12.84	0.32	0.058
BD(2)C18-C19	BD*(2)N17-C22	16.65	0.29	0.062
BD(2)C18-C19	BD*(2)C20-C21	20.5	0.3	0.071
BD(1)C19-C20	BD*(1)Cl14-C18	4.61	0.85	0.057
BD(1)C19-H24	BD*(1)N17-C18	5.09	1.08	0.066
BD(1)C19-H24	BD*(1)C20-C21	3.41	1.1	0.055
BD(2)C20-C21	BD*(2)O15-C23	13.84	0.33	0.061
BD(2)C20-C21	BD*(2)N17-C22	27.60	0.26	0.077
BD(2)C20-C21	BD*(2)C18-C19	20.74	0.26	0.065
BD(1)C22-H26	BD*(1)N17-C18	4.53	1.05	0.062
BD(1)C22-H26	BD*(1)C20-C21	4.58	1.07	0.063
LP(3)Cl 14	BD*(2)C18-C19	13.07	0.31	0.062
LP(2)O15	BD*(1)O16-C23	28.71	0.66	0.125
LP(2)O15	BD*(1)C21-C23	21.67	0.65	0.107
LP(2)O16	BD*(1)O15-C23	14.33	0.94	0.106
LP(3)O16	BD*(2)O15-C23	62.65	0.28	0.12
LP(1)N17	BD*(1)C18-C19	10.91	0.88	0.089
BD*(2)N17-C22	BD*(2)C20-C21	188.36	0.02	0.087
BD*(2)C20-C21	BD*(2)O15-C23	42.62	0.04	0.069

# 6.9.5 Mulliken Atomic Charge analysis

The Mulliken atomic charge of all 27 atoms in the APCN molecule was calculated using population analysis at the B3LYP/6-31+G (d, P) level. Mulliken population analysis was used to determine the atomic charges of individual atoms and also their total value. Mulliken atomic charge calculations are important in the quantum chemical calculations such as molecular systems, dipole moments, electronic structure, molecular polarizability and many other aspects of the molecular system [182]. The plot of Mulliken atomic charges on different element atoms of the APCN molecule is shown in Figure 6.10. All of the hydrogen atoms in this molecule have positive charges, with the largest hydrogen charge being on H8 (0.409e), with the nitrogen and oxygen atoms being negatively charged. The

positive charges of the chlorine atoms Cl15 in the molecule are approximately 0.117e. Carbon atoms C6, C7, C21, C22 and C24 have positive values, while other carbon atoms have negative values of all the C atoms, C24 (0.317e) has a higher positive value and C4 (-0.009e) has a lower negative value. The sum of total Mulliken of all atoms of APCN atomic charge, but on the other hand, was calculated to be zero, preserving charge neutrality. Table 6.6 shows the obtained Mulliken atomic charge values of APCN crystal.

Table 6.6 Mulliken atomic charges of APCN crystal

Atom No.	Atomic charge	Atom No.	Atomic charge
N1	-0.236	Cl15	0.117
N2	-0.627	O16	-0.448
C3	-0.133	O17	-0.538
C4	-0.009	N18	-0.082
C5	-0.418	C19	-0.244
C6	0.163	C20	-0.084
C7	0.138	C21	0.111
Н8	0.409	C22	0.162
Н9	0.357	C23	-0.258
H10	0.302	C24	0.317
H11	0.135	H25	0.152
H12	0.135	H26	0.148
H13	0.139	H27	0.169
H14	0.124		

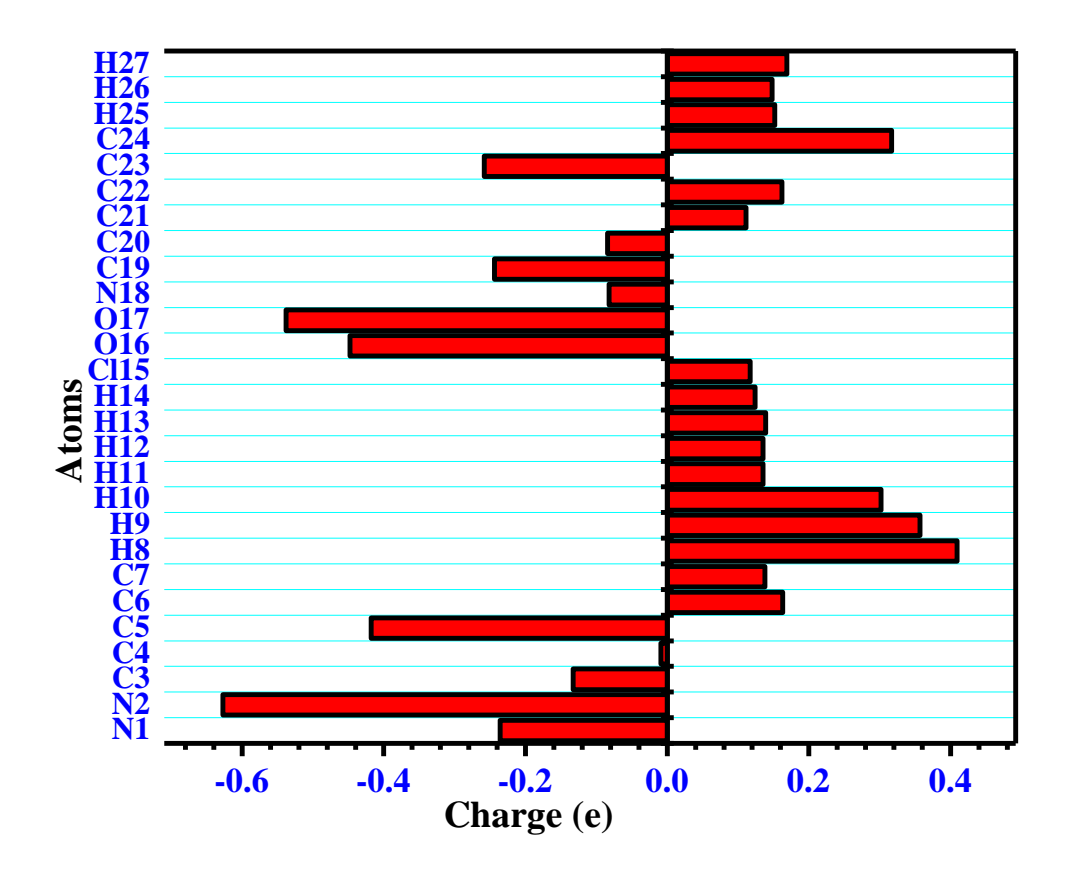


Figure 6.10 Plot of Mulliken atomic charges of APCN crystal

#### 6.9.6 Molecular electrostatic potential (MEP) map analysis

Various colours represent the electrostatic different values of potential at the surface. The MEP increases in the following order: red < orange < yellow < green < blue [183]. The highest positive region on the molecular electrostatic potential map is the favoured site for the nucleophilic attack, as indicated by the blue color. Similarly, the maximum negative region is the preferred site for an electrophilic attack, which is represented by the red surface and the zero potential regions are represented by the green surface. The colour coding for these maps ranges from  $-0.169e^0$  a.u (deepest red) to  $+0.169e^0$  a.u (deepest blue) for the APCN molecule. The negative regions are situated around the oxygen atoms O16 and O17 which are associated with electrophilic reactivity, while the majority of the C-atoms in the

APCN molecules bear the green zone in the MEP surfaces with zero potential, as shown in Figure 6.11. Positive potential zones are delocalized across all hydrogen atoms.

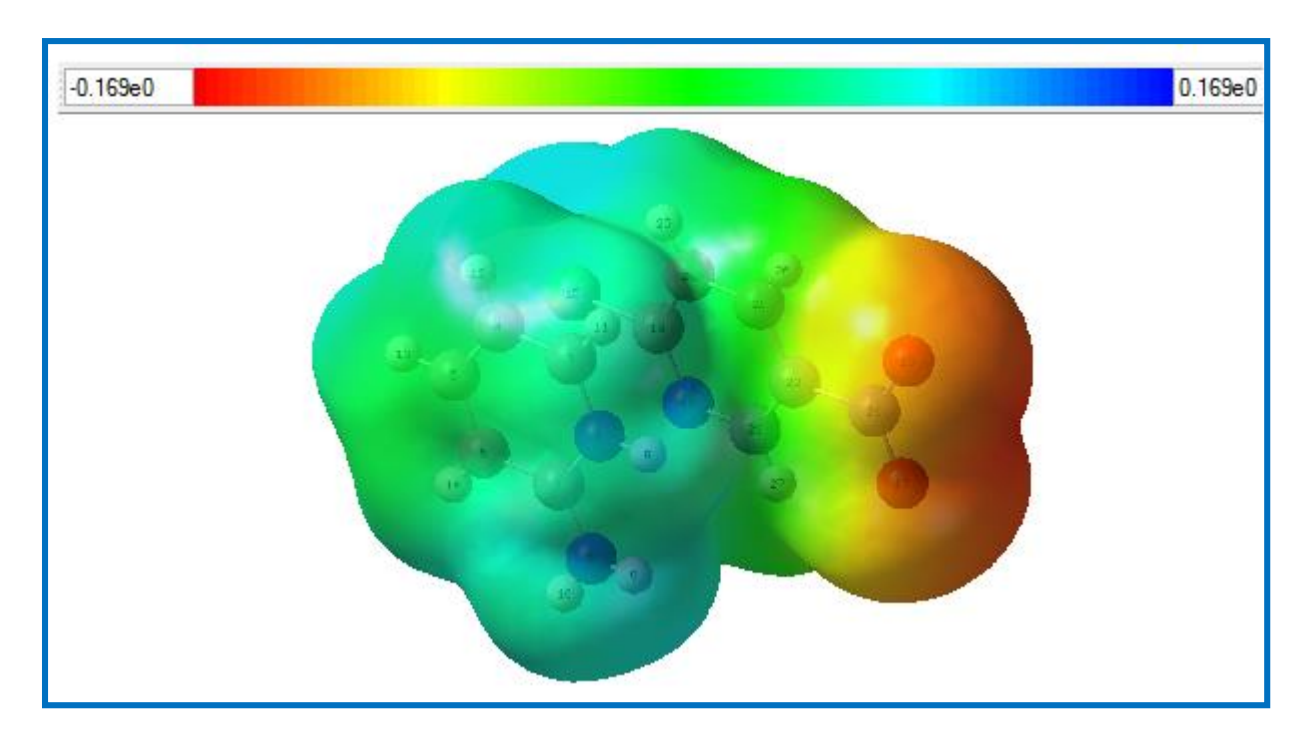


Figure 6.11 MEP surface of APCN crystal

# **6.9.7** Thermodynamical Properties

Table 6.7 shows the estimated thermo-dynamical parameters of the APCN crystal at room temperature using the B3LYP/6-31+G(d, p) basis set, including total energy, zero-point vibrational energy, rotational temperature, rotational constants, thermal energy and entropy. The thermochemistry of the grown crystal gives a moment of inertia like rotational temperature, rotational constants and so on. The zero-point vibrational energy of the APCN crystal was calculated to be 125.21896 kcal mol<sup>-1</sup>. The heat capacity (C<sub>v</sub>), entropy (S), and total thermal energy of the APCN crystal were calculated to be 116.560 cal mol<sup>-1</sup> K<sup>-1</sup>, 47.618, and 133.327 cal mol<sup>-1</sup> K<sup>-1</sup>, respectively. Furthermore, the dipole moment is a significant value for characterizing a molecule's electrical property using atomic charge distribution.

Table 6.7 Thermodynamic parameters of APCN calculated by DFT/B3LYP method

Zero point Vibrational energy (kg	cal mol <sup>-1</sup> ) 125.21896	
Rotational constants (GHz)		
A	0.60986	
В	0.32775	
C	0.27999	
Rotational temperature (K)		
A	0.02927	
В	0.01573	
С	0.01344	
Heat capacity (cal mol <sup>-1</sup> k <sup>1</sup> )		
Total heat capacity	47.618	
Translational	2.981	
Rotational	2.981	
Vibrational	41.656	
Entropy (cal mol <sup>-1</sup> k <sup>1</sup> )		
Total entropy	116.560	
Translational	42.462	
Rotational	33.018	
Vibrational	41.080	
Thermal energy (cal mol <sup>-1</sup> k <sup>1</sup> )		
Total thermal energy	133.327	
Translational	0.889	
Rotational	0.889	
Vibrational	131.550	
Dipole moment		
$\mu_{\mathrm{x}}$	-19.2099	
$\mu_{ m y}$	-5.7092	
$\mu_{z}$	1.4000	
$\mu_{tot}$	20.0892	

# SUMMARY AND SUGGESTIONS FOR FUTURE WORK

The slow evaporation solution growth method was used to grow single crystals of 4-amino-N-carbamothioylbenzene sulfonamide, pyrazolemethoxy benzaldehyde, pyridine urea and aminopyridinium chloronicotinate. The fundamental objective of this thesis is to improve the growth conditions of the materials mentioned above and to research their attributes in order to identify their applicability.

A novel NLO single crystal of 4-amino-N-carbamothioylbenzenesulfonamide was grown from aqueous solution at room temperature using a slow evaporation method. The single crystal X-ray diffraction confirms the compound formation. The sharp peaks observed in the powder X-ray diffraction spectra show the good crystallinity nature of the grown crystal. The shift in the vibrational frequency of C=S at 1471 cm<sup>-1</sup> verifies the presence of thiourea moiety inside the compound. The UV-vis - NIR studies confirm that the ACBS crystals have wider transparency in visible and UV regions and it is the lower cut-off wavelength at 344 nm that is appropriate for optoelectronic devices. The ACBS crystal contains a high melting point and its exhibits high thermal stability. The high transparency shows that ACBS crystals can be used for nonlinear optical applications. The fluorescence spectrum showed that the grown crystals emitted violet fluorescence. The chemical structure of the grown crystal was established by the <sup>1</sup>H NMR technique. The mechanical strength of ACBS single crystal measured by Vickers microhardness test allows that it belongs to the soft material category. It is concluded that the ACBS crystal is a potential candidate for the fabrication of nonlinear optical devices. The SEM images show

the layers of atoms of various sizes and also the surface of the microcrystal is ascertained to have a completely clean topography in nature.

Pyrazolemethoxy benzaldehyde (PMB) crystals were grown by the slow evaporation solution growth method. The grown crystal has a monoclinic structure with a centrosymmetric space group of C2/c, according to single crystal X-ray diffraction analysis. The sharp peak with the good crystallinity nature of the PMB crystal are confirmed by powder X-ray diffraction analysis. The vibrational modes of functional groups were analyzed using FT-IR and FT-Raman spectral analysis. The UV-vis-NIR spectrum of the grown crystal revealed the transparency in the visible region and absorption in the UV region. In the photoluminescence spectrum, the violet and blue emission peaks were analyzed for the grown crystal PMB with the excitation wavelength 250 nm. TG/DTA analysis revealed that the grown crystal is thermally stable up to 183°C. DFT theory with the B3LYP/6-311G\* method was used to optimize the geometry of the PMB crystal. The energy gap between HUMO and LUMO was calculated using theoretical calculations. The B3LYP method was used to calculate the first-order hyperpolarizability  $(24.754 \times 10^{-30} \text{ esu})$ of the grown crystal. NBO analysis of the PMB crystal revealed inter and intramolecular interactions. The bonding interactions were analyzed by Mulliken atomic charge. The electrophilic attacks in the molecule are predicted using a molecular electrostatic potential map. PMB crystal can be a suitable organic material for photonics and optoelectronic applications, according to the entire investigation.

A slow evaporation solution growth method was used to grow the crystal of pyridine urea (PYUA), at room temperature. The cell parameters calculated using the X-ray diffraction technique and the sharp peak in PXRD illustrate the crystallinity nature of the sample. The FT-IR and DFT spectra of the PYUA crystal confirmed the existence of several functional groups. Using TD-DFT and UV-vis-NIR spectrometer, the excitation energy of

the PYUA crystal was estimated to be 245.31 nm experimentally and 281.49 nm theoretically. The PYUA crystal is thermally stable up to 115°C, according to thermal analysis. The mechanical properties of the PYUA crystal imply that it is confirmed to be soft material. The energy gap between HOMO-LUMO was measured to be 4.7212 eV. The intermolecular charge transference of the PYUA crystal originates with carbon atoms, according to the Mulliken charge distribution. Negative potential areas are surrounded by electronegative atoms on the MEP map, while positive potential areas are surrounded by hydrogen atoms. These locations provide data about the area where the molecule may undergo intermolecular interactions. The NBO analysis of the Fock matrix displays second-order perturbation theory analysis. Thermodynamic properties rise as the intensity of molecular vibrations increases with temperature. According to Hirshfeld's research, the percentage of H–H interactions (51.1%) is the highest of all surfaces.

Aminopyridine chloronicotinate (APCN) was grown at room temperature by a slow evaporation method. The monoclinic crystal system of APCN crystal has the centrosymmetric space group P2<sub>1</sub>/c. The crystallographic planes and peaks are found using powder X-ray diffraction analysis. The functional groups in the grown crystal were confirmed through FT-IR spectrum analysis. The lower cut-off wavelength and optical band gap of the grown crystal were found to be 335 nm and 3.6 eV, respectively. The thermal analysis predicts that the grown crystal was thermally stable up to 173.1°C. The Vickers microhardness test reveals that the grown crystal is a soft material category. From the optimized molecular structure, it is confirmed that the 6-chloronictinic acid moiety is connected with 2-aminopyridine moiety via a pair of N-H...O hydrogen bonding interactions. The HOMO-LUMO energy gap (E) confirmed the molecules eventual charge transfer. Theoretically, an obtained value of global chemical reactivity descriptors confirms the chemical stability of the grown crystal. The Mulliken atomic charge analysis confirms the charge distributions of distinct atoms in the molecule. The active electrophilic and

nucleophilic reactive sites are identified through the MEP map. Intramolecular charge transfers due to the interaction of  $\pi^*$  (N17-C22)  $\to \pi^*$ (C20-C21) are reflected in the NBO result. The calculated dipole moment gives information about the orientation of the molecule and the dipole strength. Thus, the above mentioned studies confirmed that the grown crystal could be a suitable candidate for optical applications.

# 7.1 SUGGESTIONS FOR FUTURE WORK

The growth mechanism of all of these single crystals could be enhanced by acquiring more about their nucleation dynamics. Various crystals discussed in this work could be grown by adding suitable dopants to increase optical, thermal and mechanical properties. The slow evaporation method can be used to create more bulk crystals of these materials, allowing researchers to explore the nonlinear optical properties of single crystals. Further research into altering these systems by replacing suitable derivatives may result in materials with exceptional properties.

# \_\_\_\_\_

# REFERENCES

- [1] J. Jeyaram, K. Varadharajan, B. Singaram, R. Rajendhran, Journal of Crystal Growth 486 (2018) 96-103.
- [2] A. Priyadharshini, S. Kalainathan, Journal of Physics and Chemistry of Solids, 123 (2018) 59-69.
- [3] D. Kashchiev, "Nucleation: Basic Theory with Applications", Butterworth-Heinemann, Oxford, 2000.
- [4] I. Weissbuch, M. Lahav and L. Leiserowitz, Crystal Growth & Design, 3 (2003)125.
- [5] A. Claude., Ph.D. Thesis, Anna University, Chennai, India, 2006.
- [6] P. Santhanaraghavan, P. Ramasamy, "Crystal growth process and Method", KRU Publication, Kumbakonam, India, 2000.
- [7] J.C Brice., "The Growth of Crystals from Liquids", North-HAmsterdam, 1973.
- [8] M. Ohara, R.C Reid., "Modeling Crystal Growth Rates from Solution", Prentice-Hall, New Jersey, 1973.
- [9] H. Arend, Hulliger, J. Crystal Growth in Science and Technology, Plenum Press, London, 1987.
- [10] A. Chernov et.al., "Modern Crystallography III, Crystal Growth", Springer, Berlin, 1984.
- [11] J. Nyvlt, O. Sohnel, M. Matuchova, M. Broul, "The Kinetics of Industrial Crystallization", Elsevier, Amsterdam, 1985.
- [12] J.A. James, R.C. Kell, crystal Growth, Editor, Pamplin B.R. Pergamon Press, New York 1975.
- [13] W. Blau, Phys. Technol. 18 (1987) 250.
- [14] F. Zernike, J. Midwinter, "Applied Nonlinear Optics", Wiley, New York, 1973.
- [15] P.N. Prasad, D.J. Williams, "Introduction to Nonlinear Optical Effects in Molecules and Polymers", Wiley, New York, 1990.
- [16] K.D. Singer, J.E. John, L.A. king, H.M. Gordon, H.E. Katz, C.W. Dirk, J. Opt. Soc. Am. B 6 (1989) 1339.
- [17] L. Arizmendi, Phys. Stat. Solid A., 201 (2004) 253-283.

- [18] X.Q. Wang, D. Xu, M. K. Lu, D.R. Yuan, S.Y. Guo, J. Cryst. Growth, 224, (2001) 284-293
- [19] Y.X. Fan, R.C. Eckardt, R.L. Byer, R.K. Rout, R.S. Feigelson, Appl. Phys. Lett. 45 (1984) 313.
- [20] V. Venkataramanan, S. Maheswaran, J.N. Sherwood, H.L. Bhat, J. Crystal Growth, 179 (1997) 605.
- [21] W. F. Smith, J. Hashemi, R. Prakash, Material science and engineering, Fourth edition, New York, 2008.
- [22] G. M. Sheldrick, SHELXL97, University of Gottingen, Germany, 1997.
- [23] G. M. Sheldrick, Acta Cryst. A 46 (1990) 467 473.
- [24] G. M. Sheldrick, TOPAZ-R, version 3, University of Gottingen, Germany, 1997.
- [25] W.F. Smith. J.Hashemi, R. Prakash, Material science and engineering, Fourth edition, New York, 2008.
- [26] M. Silverstein, X. Webster, J. Kiemle, Spectrometric identification of organic compounds, seventh edition, State University of New York, 1963.
- [27] P.L. Soni, Fundamental organic chemistry, Sultan Chand, 1981.
- [28] R.L. Smith, G. Sandland, Proc. Inst. Mech. Engrs. 1 (1923) 623.
- [29] F.L. Balta Calleja, D.R. Rueda, R.S. Roster, W.T. Mead, J. Materials Science, 15 (1980) 765.
- [30] K. Kishan Rao, V. Surender and B. Saritha Rani, Bull. Mater. Sci., 25 (2002) 641.
- [31] N. Saba, M.T.H. Sultan, Lignocellulosic Fibre and Biom. Based Composite Materials, 2017.
- [32] Willard H.H., Merritt, L.L., dean, JR. J.A., Settle, JR.F.A. "Instrumental Methods of analysis", Wadsworth Pub.Co,1986.
- [33] M. I. Pope, M.D. Judd, "Differential Thermal Analysis", Heyden, Philadelphia, 1997.
- [34] R.M. Silverstein, F.X. Webster, D.J. Kiemle, Chapter 2 infrared spectrometry, Spectrom. Identify. Org. Compd. 7th Ed., John Wiley Sons, Inc., Hobeken, NJ, 2005.
- [35] P.L. Soni, Fundamental organic chemistry, Sultan Chand, 1981.
- [36] M. Karabacaka, Z. Cinar, M. Kurt, S. Sudha, N. Sundaraganesan, Spectrochimica Acta Part A 85 (2012) 179–189.
- [37] R.S. Mulliken J. Chem. Phys. 23 (1955) 1833.

- [38] R. Thirumurugan, B. Babu, K. Anitha, J. Chandrasekaran, Journal of molecular structure, 1149 (2017) 48-57.
- [39] A. Mark, Spackman, Dylan Jayatilaga, Cryst Eng Comm, 11 (2009) 19-32.
- [40] R. Mohanakumar, D. Rajan babu, G. Ravi, R. Jayavel, J. Cryst. Growth, 250 (2003), 113 117.
- [41] D. S. Chemla, J. Zyss, Nonlinear Optical Properties of organic molecular and crystals, Academic Press, New York, 1987.
- [42] P. Srinivasan, T. Kanagasekaran, R. Gopalakrishnan, Crystal. Growth Des. 8 (2008) 2340 2345.
- [43] P.N. Prasad, D.J. Williams, Non-linear Optical effects in molecules and polymers, Wiley, USA, 1991.
- [44] J. Basset et al., Vogels Text Book of Practical Organic Chemistry, Fourth edition, English Language book society, 1987.
- [45] M.P. Cifuentes, J. Driver, Mark G. Humphery, I. Asselberghs, A. Persoons, M. Samoc, B. Luther-Davies, J. Organoment. Chem. 607 (2000) 72-77.
- [46] P. S. Patil, M. S. Bannur, D. B, Badigannavar and S. M. Dharmaprakash, Optics & Laser Technology 55 (2014) 37-41.
- [47] M. Prakash, M. Lydia Caroline and D. Geetha, Spectrochim. Acta part A 108 (2013) 32-37.
- [48] K.P. Bhuvana, S.J. Robinson and T. Balasubramanian, Mater. Lett 61 (2007) 1489-1491.
- [49] R.W.G. Wyckoff, R.B. Corey, The crystal Structure of Thiourea, Zeitschrift Fur Krist. 81 (1932) 386 -395.
- [50] G. Thilakavathi, R. Arun Kumar, A. Kumaresh and N. Ravi Kumar, Materials Research Innovations, 20 (2016) 254-258.
- [51] P. Saritha, Synthesis, Growth, International journal of physics and research. 1 (2019) 21-30.
- [52] M.M. Kumari, P.J. Ramchandra, C. Ravikumar, I.H. Joe, I. Numa, J. Raman Spectrose. 42 (2011) 1462 1469.
- [53] R. Q. Brewster and W.E. Mcewen, "Organic chemistry; 3<sup>rd</sup> ed.", Prentice-Hall of india: New Delhi, 862 (2001).
- [54] John N. Low and Christopher Guidewell, Acta Cryst, C 58 (2002) 209.
- [55] P. Mythili, T. Kanagasekaran and R. Gopalakrishnan, Cryst. Res. Technol.42, 8 (2007) 791 -799.

- [56] A. Maghraby and E. Tarek, Radiat. Measurem. 41 (2006) 170-176.
- [57] P. N. Prasad, D.J. Williams, Introduction to Nonlinear Optical Effects in Organic Molecules And Polymers, Wiley, New York, 1991.
- [58] A. Rita, Gharde, T. Divakar, A. Chunarkar international Journal of scientifical technology research volume 2 (2013) 109-111.
- [59] P. Kalsi, 'Spectroscopy of organic compounds', Wiley Eastern Publishers, New Delhi (1985).
- [60] B. Lal, K.K. Bamzai, P.N. Kotru, Mechanical strength of melt growth doped KMgF3 crystals, Mater. Chem. Phys. 78 (2003) 202-207.
- [61] A. Ruby and S. Alfredcecil Raj, International journal of scientific Research Publications. 3 (2013) 1-5.
- [62] M. Hanneman, Metall, Manch. 23 (1941) 135-139.
- [63] E.M. Onitsch, Mikroscopia 2 (1947) 131-151.
- [64] H.C. Gates, Thirty years of progress in surface science, in: Crystal Growth and Characterization, Edi. North Holland, 1975.
- [65] R. Archana, S. Sudhahar, S. Sagadevan, et al., Appl. Phys. A 126 (2020) 188.
- [66] Preeti Singh, M.M. Abdullah, Suresh Sagadevan, Saiqa Ikram, J. Mater Sci: Mater Electron 29 (2018) 7904–7916.
- [67] Archana Rajendran, S. Sudhahar, K. Sadayandi, M. Vidhya, S. Sagadevan, F. Mohammad, J. Podder, Chinese J. Phys. 67 (2020) 283–292.
- [68] S. Suresh, J. Elec. Mater. 45 (2016) 5904–5909.
- [69] R. Archana, S. Sagadevan, et al., Chemical Physics Letters 764 (8) (2021) 138269.
- [70] A. Nataraj, V. Bala Chandran, J. Karthick, J. Mol. Struct. 1006 (2011) 104–112.
- [71] K. Karrouchi, S. Radi, Y. Ramli, J. Taoufik, Y. Mabkhot, F. Alaizari, M. Ansar, Synthesis and pharmacological activities of pyrazole derivaties: a review, Molecules 23 (2018) 134.
- [72] F.E. Bennani, L. Doudach, Y. Cherrah, Y. Ramli, K. Karrouchi, M. Ansar, M.E.A. Faouzi, Overview of recent developments of pyrazole derivaties as an anticancer agent in different cell line, Bioorg, Chem (2019) 103470.
- [73] K. Karrouchi, S. Fettach, S. Radi, J. Taoufik, Y.N. Mabkhot, S. Alterary, My E... Faouzi, M. Ansar, Lett. Drug. Des. Discov. 16 (2019) 712–720.
- [74] M. Messal. A.Titi, B.A. Alqurashy, R. Touzani, T. Shiga, H. Oshio, T.B. Hadda, J. Mol. Struct. 1205 (2020) 127625.

- [75] K. Karrochi, E.B. Yousfi, N.K. Sebbar, Y. Ramli, J. Taouufik, Y. Quzidan, Y.N. Mabkhot, H.A. Ghabbour, S. Radi, Int. J. Mol. Sci. 18 (2017) 2215.
- [76] L.R.S. Dias, R.R.S. Salvador, Pyrazole carbohydrazide derivatives of pharmaceutical interest, Pharmaceuticals 5 (2012) 317–324.
- [77] B. Ballesteros, L. Santos, Spectrochimica Acta Part A: Molecular and Biomolecular Spectroscopy 58 (2002) 1069–1081.
- [78] W.B. Tzeng, K. Narayanan, J.L. Lin, C.C. Tung, Spectrochim. Acta 55A (1998) 153–162.
- [79] M. Salim, M.A. Munawar, M.N. Tahir, M. Shahid, K.I. Malik, Acta Cryst. E 71 (2015) 0414–0415.
- [80] O. Noureddine, S. gatfaoui, S.A. Brandan, H. Marouani, N. Issaoui, J. Mol. Struct. 1202 (2020) 127351.
- [81] S. Gatfaoui, N. Issaoui, S.A. Brandan, T. Roisnel, H. Marouani, J. Mol. Struct. 1151 (2018) 152–168.
- [82] K. Karrouchi, S.A. Brandan, Y. Sert, H. El-marzouqi, S. Radi, M. Ferbin-teanu, M.E.A. Faouzi, Y.Garcia, M. Ansar, J. Mol. Struct. 128541 (2020).
- [83] C. Shruthi, V. Ravindrachary, B. Guruswamy, D. Jagadeesh Prasad, Janet Goveas, N.K. Karthik Kumara, J. Mol. Struct. (2020) 129739.
- [84] S. Kalaiyarasi, I. Md Zahid, S. Reena Devi, R. Maoan Kumar, J. Cryst. Growth 460 (2017) 105–111.
- [85] A. Krishna, N. Vijavan, C. Bagdia, k. Thukral, D. Haranat. Sonia, K.K. Maurya, G. Bhagavannaravana, Cryst Eng. Comm 18 (2016) 4844–4850.
- [86] K. Senthil, S. Kalainathan, F. Hamada, Y. Kondo, RSC Adv 5 (2015) 79298–79308.
- [87] G. Parvathy, R. Kaliammal, K. Sankaranarayanan, M. Arivanandhan, M. Krishnakumar, S. Sudhahar, J. Mol. Struct 1217 (2020) 128406.
- [88] H.J. Ravindra, W.T.A. Harrision, M.R. Suresh kumar, S.M. Dharmaprakash, J. Cry. Growth 311 (2009) 310–315.
- [89] S. Mugeshini, et al., Chinese Journal of Physics, 72 (2021) 229–239.
- [90] M. Buvaneswari, R. Santhakumari, R. Jayasree, et al., Appl. Phys. A 127 (2021) 544.
- [91] R. Vasanthakumari, W. Nirmala, et al., Journal of Molecular Structure, 1239 (2021) 130449.

- [92] Shivaraj R. Maidur, Parutagouda Shankaragouda Patil, Anusha Ekbote, Tze Shyang Chia, Ching Kheng Quah, Spectrochimica Acta Part A: Molecular and Biomolecular Spectroscopy 184 (2017) 342-354.
- [93] P. Dhamodharan, K. Sathya, M. Dhandapani, J. Mol. Structure 1146 (15) (2017) 782–792.
- [94] Rajesh Kumar, Amit Kumar, Vipin Deval, Archana Gupta, Poonam Tandon, P. S.Patil, Prathmesh Deshmukh, Deepika Chaturvedi, J.G. Watve, J. Mol. Structure 1129 (2017) 292–304.
- [95] F. J, Nye Physical properties of Crystal, Clarendon Press, Oxford, 1960.
- [96] Shivaraj R. Maidur, Parutagouda Shankaragouda Patil, Optical Materials, 84 (2018) 28–37.
- [97] V. Krishnakumar, R. Nagalakshmi, Physica B 403 (2008) 1863–1869.
- [98] J.V. Ramaclus, T. Thomas, S. Ramesh, P. Sagayaraj, E.A. Michael, Cryst. Eng. Comm. 16 (2014) 6889–6895.
- [99] P. Muthuraja, T. Joselin Beaula, T. Shanmugavadivu, V. Bena Jothy, M. Dhandapani, J. Mol. Structure 1137 (5) (2017) 649–662.
- [100] Basak Kosar, Cigdem Albayrak, Spectrochimica Acta Part A, 78 (2011) 160–167.
- [101] V. Balachandran, K. Parimala, Spectrochimica Acta Part A: Molecular and Biomolecular Spectroscopy, 102 (2013) 30–51.
- [102] D.A. Kteinman, Nonlinear Dielectric Polarization in Optical Media, Phys. Rev 126 (1962) 1977–1979.
- [103] S.K. Seth, Cryst. Eng. Comm. 15 (2013) 1772-1781.
- [104] Shivaraj R. Maidur, Parutagouda Shankaragouda Patil, Optical Materials 84 (2018) 28–37.
- [105] K. Muthu, V. Meenatchi, M. Rajasekar, A. Aditya Prasad, K. Meena, R. Agilanaeshwari, V. Kanagarajan, S.P. Meenakshisundaram, J. Mol. Str. 1091 (2015) 210–221.
- [106] A. Aditya Prasad, S.P. Meenashisundram, Cryst. Res. Technol. (2015) 1–10.
- [107] E.D. Glendening, A.E. Reed, J.E. Carpenter, F. Weinhold, NBO version 3.1, Pitts burg, Theoretical chemistry Institute and Department of chemistry, University of Wisconsin, Madison, 1988.
- [108] J. Chocholousova, V. Vladimir, Spirko, Hobza first local minimum of thformic acid dimer Exhibits Simultaneously red shifted O-H....O and Improper blueshifted C-H...O hydrogen bonds, P. Phys. Chem.Phys. 6 (2004) 37–41.

- [109] R.S. Mulliken, Electronic Population Analysis on LCAO-MO Molecular Wave Functions. The Journal of Chemical Physics 23 (10) (1955) 1833–1840.
- [110] C.S. Karthik, K. Kumara, S. Naveen, L. Mallesha, P. Mallu, M.V. Deepa Urs, N.K. Lokanath, J, Mol. Struct. 1224 (2021) 129077.
- [111] J.H. Zhou, L.W. Zheng, M.C. Yan, M.J. Shi, J. Liu, G.Q. Shangguan, J. Chem. 2017.
- [112] S. Mugeshini, R. Santhakumari, N. Rajeshwari, G. Amudha, D. Chandrika, S. Sagadevan, Chin. J. Phys. 76 (2022) 14-23.
- [113] G. Amudha, R. Santhakumari, D. Chandrika, S. Mugeshini, N. Rajeswari, S. Sagadevan, Chin. J. Phys. 76 (2022) 44-58.
- [114] C. Usha, R. Santhakumari, R. Jayasree, M. Bhuvaneswari, S. Sagadevan, J. Mol. Struct. 1249 (2022) 131570.
- [115] N. Rajeswari, R. Santhakumari, S. Mugeshini, D. Chandrika, S. Sagadevan, Chin. J. Phys. 73 (2021) 746-755.
- [116] S. Mugeshini, R. Santhakumari, N. Rajeshwari, G. Amudha, D. Chandrika, S. Sagadevan, J. Mol. Struct. 1249 (2022) 131600.
- [117] A. Ayman, M.H. Zaki, Nagi, R.E.R. Nagi, Synthesis and optical properties of new alkylated pyridinium halides, Optik 139 (2017) 95-103.
- [118] V. Chithambaram, S. J. Das, R. Arivudai Nambi, S. Krishnan, Solid State Sci. 14 (2012) 216-218.
- [119] S. Krishnan, C. Justin Raj, S. Jerome Das, J. Cryst. Grow. 310 (2008) 3313-3317.
- [120] P. Li, M.R. Ryder, J. F. Stoddart, Acc. Mater. Res. Acc. Mater. Res. 1 (2020) 77-87.
- [121] B. Wang, R. B. Lin, Z. Zhang, S. Xiang, B. Chen, J. Am. Chem. SOC 142 (2020) 14399-14416.
- [122] M. Strey, P.G. Jones, Pyridine 1:1 adducts of urea (Z'=1) and thiourea (Z'=8) Acta Cryst. C 74 (2018) 406-410.
- [123] S. Gatfaoui, N. Issaoui, S.A. Brandan, T. Roisnel, H. Marouani, J. Mol. Struct. 1151 (2018) 152-168.
- [124] O. Noureddine, S. gatfaoui, S. A. Brandan, A. Sagaama, H. Marouani, N. Issaoui, J Mol. Struct. 1207 (2020) 127762.
- [125] Ghiasuddin et. al., J. Mol. Struct. 1160 (2018) 129-141.
- [126] D. Sathiyanaryanan, Vibrational Spectroscopy Theory and Application, New Age International Publishers, New Delhi, 2004.
- [127] I.M. Ibrahim, S. Yunus, M.A. Hashim, Int. J. Eng. Res. 4 (2) 2014 1-12.

- [128] G. Madharambal, M. Mariappan, S.C. Mojumdar, J. Therm. Anal. Calorim. 100 (2010) 763-768.
- [129] A. Aditya Prasad, K. Muthu, M. Rajesekar, V. Meenatchi, S.P.Meenakshisundaram, Spectrochem. Acta Part A Mol. Biomol. Spectros. 135 (2015) 805-813.
- [130] K. Sathya, P. Dhamodharan, M. Dhandapani, Opt. Laser Technol. 101 (2018) 328-340.
- [131] P. Jayaprakash, P. Sangeetha, M. Peer Mohamed, G. Vinitha, S. Muthu, M. Prakash, M. L. Caroline, J. Mol. Struct.1148 (2017) 314-321.
- [132] S. Panchapakesan, K. Subramani, B. Srinivasan, Optics and Laser Technology113 (2019) 246-260.
- [133] Y. Matveychuk, E. Bartashevich, V. G. Tsirelso, Cryst. Growth Des. 18 (6) (2018) 3366-3375.
- [134] S.K. Wolff, D.J. Grimwood, J.J. McKinnon, M.J. Turner, D. Jayatilaka, M.A. Spackman, CrystalExplorer Version 3.1, University of Western Australia, (2012).
- [135] S. Saravanan, V. Balachandran, K. Viswanathan, Spectrochim, Acta Part A 12 (2014) 685-697.
- [136] I. Fleming, Frontier Orbitals, Organic Chemical Reactions, Wiley, London, 1976.
- [137] S. Muthu, G. Ramachandran, Spectrochim, Acta Part A 121 (2014) 394-403.
- [138] S. Muthu, S. Renga, Spectrochim. Acta 132 (2014) 313-325.
- [139] A. Karthik Kumara, A. Dileep Kumar, S. Naveen, K. Ajay kumar, N. K. Lokanath, J. Mol. Struct., 1161 (2018) 285-320.
- [140] T. A. Koopmans, Physica 1 (1934) 104-113.
- [141] R.S. Mulliken, Electronic population analysis on LCAO-MO molecular wave functions, J. Chem. Phys. 23 (1955) 1833-1840.
- [142] N. B. RachidaRahmani, A. Chouaih, S.G.S FodilHamzaoui, J. Mol. Struc.1155 (2018) 484-495.
- [143] M. Adeel, A.A. Braga, M.N. Tahir, F. Hag, M. Khalid, M.A. Halim, J. Mol. Struct. 1131 (2017) 136-148.
- [144] S. Naseem, M. Khalid, M.N. Tahir, M.A. Halim, A.A. Braga, M.M. Naseer, Z. Shafiq, J. Mol. Struct. 1143 (2017) 235-244.
- [145] M.A. Ghiasuddin, M. Adeel, M. Khalid, T. M. Nawaz, M. U. Khan, M. A. Asghar, M. A. Ullah, M. Iqbal, J. Mol. Struct. 1131 (2017) 136-148.

- [146] V. Balachandran, A. Lakshmi, J. Mol. Struct. 1006 (2011) 395-401.
- [147] K. Rastogi, M. A. Palafox, R. P. Tanwar, L. Mittal, Spectrochim. Acta A 58 (2002) 1989-2004.
- [148] S. Karthicka, K. Thirupugalmani, M. Krishnakumar, V. Kannane, G. Vinitha, S. Brahadeeswaranan, Optics and Laser Technology 122 (2020)105849.
- [149] K. Sathya, P. Dhamodharan, M. Dhandapani, Opt. Laser Technol. 101 (2018) 328-340.
- [150] S. Mugeshini, R. Santhakumari, N. Rajeswari, G. Amudha, D. Chandrika, Suresh Sagadevan, Chinese Journal of Physics, 72 (2021) 229-239
- [151] M.Buvaneswari, R. Santhakumari, R. Jayasree, R. et al. Appl. Phys. A 127(2021). 544
- [152] R. Archana, S. Suresh, J Anita Lett, Gobi Saravanan Kaliaraj, Is Fatimah, Faruq Mohammad, Hamad A Al-Lohedan, Solhe F Alshahateet, Jiban Podder, Chemical Physics Letters, 764, (2021), 138269
- [153] S. Mugeshini, R. Santhakumari, N. Rajeswari, G. Amudha, D. Chandrika, Suresh Sagadevan, Journal of Molecular Structure, 1249, (2022), 131600
- [154] Preeti Singh, M.M. Abdullah, Suresh Sagadevan, Saiqa Ikram, J Mater Sci: Mater Electron, 29 (2018) 7904-7916
- [155] M. Buvaneswari, R. Santhakumari, C. Usha, R. Jayasree, Suresh Sagadevan, Journal of Molecular Structure, 1243 (2021)130856
- [156] N. Rajeswari, R. Santhakumari, S. Mugeshini, D. Chandrika, Chinese Journal of Physics, 30 (2021)746-755
- [157] G. Amudha, R. Santhakumari, D. Chandrika, S. Mugeshini, N. Rajeswari, Suresh Sagadevan, Chinese Journal of Physics, 76, (2022) 44-58
- [158] P. Sujin Jose, S. Mohan, Spectrochimica Acta Part A 64 (2006) 240–245
- [159] E. Kose et al. Spectrochimica Acta Part A: Molecular and Biomolecular Spectroscopy 97 (2012) 435–448
- [160] R. Srineevasan, R. Rajasekaran, Elixir Crystal Growth 66 (2014) 20551-20555.
- [161] S. Brahadeeswaran, Y. Takahashi, M. Yoshimura, M. Tani, S. Okada, S. Nashima, Y. Mori, M. Hangyo, H. Ito, T. Sasaki, Crys. Growth Des. (2013) 415-421.
- [162] R. Srineevasan, D. Sivavishnu, K. Arunadevi, R. Tamilselvi, J. Johnson, S. Ravi Kumar, Mech. Mater. Sci. Eng. 7 (2016) 39-51.
- [163] M. Sethuram, G. Bhargavi, M.V. Rajasekaran, M. Dhandapania, G. Amirthaganesan, Optik, 125 (2014) 55.

- [164] K. P. Bhuvana, S. Robinson. T. Balasubramanian, Cryst. Res. Technology 45 (2010) 299-302.
- [165] Varun, B.V., Vaithegi, K., Yi, S. et al. Nat Commun 11, (2020) 6308.
- [166] W. C. J. Ross, Biochem, Pharmacol.16 (1967) 675-680.
- [167] N. Jeeva Jasmine, A. Rajam, P. Thomas Muthiah, N. Stanley, I. Abdul Razak and M. Mustaqim Rosli, Acta Cryst. E71, (2015) 0655-0656.
- [168] R.M.Silverstein, F.X. Webster, Spectroscopic Investigations of Organic Compounds, John Wiley and Sons, New York, 2003.
- [169] G. Shanmugam, S. Brahadeeswaran, Spectrochim, Acta A 95 (2012) 177-183.
- [170] Archana, S., Sagadevan, S. et al. Chemical Physics Letters, 764(8), (2021) 138269
- [171] H.J. Ravindra, W. T.A. Harrision, M.R. Suresh Kumar, S.M. Dharmaprakash, J. Cry. Growth 311 (2009) 310-315,
- [172] P. Karuppusamy, V. Sivasubramani, M. Senthil Pandian, P. Ramasamy, RSC Adv. 6 (2016) 109105-109123.
- [173] M. Hanneman, Metall, March 23 (1941) 135.
- [174] E. M. Onitch Mikroscopia 2 (1947) 131-151.
- [175] T. Muthuraja, T. Joselin Beaula, V. Shanmugavadivu, M. Bena Jothy, J. Dhandapani, J. Mol. Struct. 1137 (2017) 649-662.
- [176] P. Muthuraja, T. Joselin Beaula, S. Balachandar, V. Bena Jothy, M. Dhandapani, J. Mol. Struct. 1146 (2017) 723 -734,
- [177] M. Govindarajan, M. Karaback, Spectrochim. Acta A 96 (2012) 421-435.
- [178] B. Kosar, C. Albayrak, Spectrochim Acta A 78 (2011) 160-167.
- [179] S. M. Zain, S.W. Ng, Acta Cryst, E63 (2007) 03303.
- [180] C. A. Mebi, J. Chem, Sci 123 (2011) 727-731.
- [181] P. Muthuraja, T. Joselin Beaula, M. Sethuram, V. Bena Jothiy, M. Dhandapani, Curr. Appl. Phys.18 (2018) 774-784.
- [182] V.K. Rastogi, M.A. Palafox, L. Mittal, N. Peica, W.Kiefer, K. Lang, P. Ohja, J. Raman Spectras. 38 (2007) 1227-1241.
- [183] M. Karabacak, Z. Cinara, M. Kurt, S. Sudha, N. Sundaraganesan, Spectrohim. Acta A 85 (2012) 179-189.

# LIST OF PUBLICATIONS IN INTERNATIONAL JOURNALS

- [1] Growth and characterization of 4-amino-N-carbamothioylbenzene sulfonamide: A nonlinear optical single crystal. G. Amudha, R. Santhakumari, D. Chandrika, S. Mugeshini, N.Rajeswari, International Journal of Mechanical and Production Engineering Research and Development (IJMPERD), 3 (2020) 7291-7302. (Scopus indexed journal)
- [2] Synthesis, growth, DFT and HOMO-LUMO studies on pyrazolemethoxy benzaldehyde single crystals. G. Amudha, R. Santhakumari, D. Chandrika, S. Mugeshini, N.Rajeswari, Suresh Sagadevan, Chinese Journal of Physics 76 (2022) 44-58. (Elsevier journal)
- [3] Growth, spectroscopic and Hirshfeld surface analysis on pyridine urea single Crystal. G. Amudha, R. Santhakumari, D. Chandrika, S. Mugeshini, N.Rajeswari, Suresh Sagadevan, Journal of Molecular Structure, 1257 (2022) 132606. (Elsevier journal)
- [4] Synthesis, growth, physicochemical characterization and computational studies on aminopyridinium chloronicotinate single crystal. G. Amudha, R. Santhakumari, D. Chandrika, S. Mugeshini, N.Rajeswari, Suresh Sagadevan, Crystal Research & Technology. (Wiley Online Library)

\_\_\_\_\_

# LIST OF CONFERENCES/SEMINAR PARTICIPATED

- 1. "Synthesis & Characterization of 1,1-Di-isopropyl thiourea single crystal", National Conference on recent trends in nano and bulk superconducting & magnetic materials, Srimad Andavan Arts and Science College (Autonomous), Tiruchirappalli, December 20-21, 2018.
- 2. "Growth and characterization of 4-amino-N-carbamothioylbenzene sulfonamide: A nonlinear optical single crystal", Theivanai Ammal College for Women (Autonomous), Villupuram, 10 <sup>th</sup> December 2021.
- 3. National seminar on specific industrial and environmental applications of Physics, Srimad Andavan Arts and Science College (Autonomous), Tiruchirappalli, 10<sup>th</sup> December, 2019.
- 4. International Conference on Advances in Materials Science (ICAMS 2017), Holy Cross College (Autonomous), Tiruchirappalli, 6<sup>th</sup> & 7<sup>th</sup> January 2017.

International Journal of Mechanical and Production Engineering Research and Development (IJMPERD) ISSN (P): 2249–6890; ISSN (E): 2249–8001 Vol. 10, Issue 3, Jun 2020, 7291-7302 © TJPR Pyt. Ltd.



# GROWTH AND CHARACTERIZATION OF 4-AMINO-N-CARBAMOTHIOYLBENZENESULFONAMIDE: A NONLINEAR OPTICAL SINGLE CRYSTAL

# G. AMUDHA, R. SANTHAKUMARI, D. CHANDRIKA, S. MUGESHINI & N. RAJESWARI

Department of Physics, Government Arts College for Women (Autonomous), Pudukkottai, Tamil Nadu, India

# ABSTRACT

Single crystals of 4-amino-N-carbamothioylbenzenesulfonamide (ACBS) have been grown at room temperature using slow evaporation solution growth method. The cell parameters of the grown crystals were calculated through X-ray diffraction analysis. The ACBS crystal belongs to monoclinic crystal system with P21 space group. The crystalline planes were identified by powder X-ray diffraction analysis. The presents of various functional groups in the grown crystal was obtained by Fourier Transform Infrared (FTIR) spectral analysis. UV-Vis-NIR, thermal analysis, fluorescence analysis, spectral analysis were carried out in order to study the optical properties of the grown crystal. The molecular structure, mechanical strength and the surface morphology were analyzed through <sup>1</sup>H NMR, Vickers microhardness and SEM techniques respectively.

KEYWORDS: Crystal growth, Non linear optical material, X-ray diffraction & Thermal analysis

Received: May 25, 2020; Accepted: Jun 27, 2020; Published: Aug 07, 2020; Paper Id.: IJMPERDJUN2020689

# 1. INTRODUCTION

Non Linear Optical (NLO) materials are scientifically important class of materials which find applications in the area of fiber optic communication, laser technology, optical switching and optical signal Processing [1]. Organic materials are exquisite interest within the synthesis of materials with NLO properties and they additionally provide a chance to use theoretical modeling [2, 3]. In the past decades, considerable research work has shown that the organic materials can exhibit NLO efficiencies which can be two orders of value more than the counterpart inorganic crystals [4, 5]. From the device factor of view, the NLO materials are usually used within the shape single crystals and that they must satisfy kind of material necessities for optical usage [6]. The organic crystals exhibit excellent non linear properties due to their electronic structure Π conjugated structures among donors and accepters [7, 8]. This is because of non - centrosymmetry nature which leading to large NLO performance, showed by way of organic crystals of the order of 10 to 100 times of large than that of inorganic crystals through the macroscopic second order non linear reaction [9]. Thiourea (TU) is an organosulfur compound with the chemical formula CH<sub>4</sub>N<sub>2</sub>S which belongs to an orthorhombic crystal system, with centrosymmetric, Pnma space group with the capability of forming extensive network of hydrogen bonds because of its big dipole moment [10-13]. Sulphanilic acid (SA) is an interesting and important compound with the formula of (NH<sub>3</sub><sup>+</sup>C<sub>6</sub>H<sub>4</sub>SO<sub>3</sub><sup>-</sup>), which find variety of applications including non linear optics and crystallized in orthorhombic crystal system with Pca2<sub>1</sub> space group [14-16]. The inductive zwitterionic structure of sulphanilic acid has dosimetric part and anionic part [17]. With these literature survey attempt has been made to grow new NLO crystal 4-amino-N-carbamothioylbenzenesulfonamide from the aqueous solution by slow evaporation method and the physical and chemical properties were discussed.

#### 2. EXPERIMENTAL PROCEDURE

### 2.1 Synthesis

Thiourea and Sulphanilic acid were separately taken in 2:1 molar ratio. The estimated amount of thiourea was dissolved in triple distilled water at room temperature. The sulphanilic acid was then slowly added to the solution with constant stirring. The resultant solution was continuously stirred for 3 hours. The reaction mechanism for the growth of 4-amino-N-carbamothioylbenzenesulfonamide is depicted in scheme 1.

Scheme 1: Reaction mechanism of 4-amino-N-carbamothioylbenzenesulfonamide.

# 2.2 Crystal Growth

The fully dissolved solution was filtered using a whatmann filter paper. Then the solution was optimally tightly closed by using a perforated polythene paper and stored in undisturbed situations. The resultant final solution was allowed to dry at room temperature. After three weeks, good quality of ACBS crystal of size 13 x 8 x 7 mm<sup>3</sup> was obtained and is shown in Fig 1.



Figure 1: As grown single crystal of ACBS.

#### 2.3 Instrumentation

The single crystal X-ray diffraction (XRD) analysis on ACBS was executed employing Bruker Apex CCD diffractometer the usage of Mo K $\alpha$  monochromated radiation ( $\lambda$ =0.7107 Å) device. The powder X-ray diffraction study of the grown crystal was performed using Rigaku X-ray diffractometer using CuK $\alpha$  radiation ( $\lambda$  = 1.5406 Å). The sample was scanned in the 2 $\theta$  range starting from 10° to 70°. The FT-IR spectrum was recorded by using KBr pellet technique ranging from 400 cm<sup>-1</sup> and 4000 cm<sup>-1</sup>. Optical transmission spectrum also has been recorded in the range of 200 nm - 800 nm using Perkin Elmer Lambda 35 Model UV-Vis-NIR spectrophotometer. Thermo gravimetric and differential thermal analysis (DTA) were carried out by using a SDT Q600 V20.9 alumina thermal analyzer within the temperature vary from 20 °C to 650 °C at a heating rate of 20 °C within the nitrogen atmosphere. The Photoluminescence (PL) spectrum was recorded using a Varian Carry Eclipse Fluorescence spectrometer. The proton <sup>1</sup>H NMR spectra experiments were performed for the ACBS crystal and spectral data were recorded in a magnetic field of 11.75 tesla using Bruker AVANCE III 500 MHz (AV 500) Fourier Transform NMR spectrometer (For 500 MHz <sup>1</sup>H NMR) for analyzing the molecular structure. The microhardness studies of the ACBS crystal have been characterized by Leitz wetzler Vickers microhardness technique. The surface analysis of the grown crystal was performed with CAREL ZEISS EVO 18 High resolution scanning electron

microscope.

# 3. RESULTS AND DISCUSSIONS

## 3.1 Single Crystal X-Ray Diffraction Analysis

The crystalline nature and the lattice parameters have been determined using X-ray diffraction studies. It is observed that the ACBS crystal crystallizes in monoclinic system of P2<sub>1</sub> space group. The determined values of the lattice parameters are a=6.45Å, b=18.32 Å, c=6.78Å,  $\alpha$ = $\gamma$ =90°,  $\beta$ =93° with the cell volume of V=801Å<sup>3</sup>. The single crystal data of ACBS is compared with the reported value [11, 16] and are depicted in Table 1.

Lattice Parameters	TU Reported work[11]	SA Reported work[16]	ACBS Present Work		
a(Å)	7.8585	7.5113	6.45		
b(Å)	8.4850	7.2791	18.32		
c(Å)	5.485	13.898	6.78		
α=β= γ(°)	90	90	$\alpha = \gamma = 90; \beta = 93$		
Volume(Å <sup>3</sup> )	380.8926	-	801		
System	Orthorhombic	Orthorhombic	Monoclinic		
Space group	Pnma	Pca2 <sub>1</sub>	P2 <sub>1</sub>		

Table 1: Comparison of Crystal Data of ACBS Crystal

From the table, it was found that the structure of ACBS crystal belongs to the monoclinic system differs from those of thiourea and sulphanilic acid system of reported values with changes in a, b and c cell parameters values.

# 3.2 Powder X-Ray Diffraction Analysis

The indexed powder x-ray diffraction pattern of ACBS single crystal is shown in Fig. 2. Due to large difference in intensity of the peaks, the diffraction pattern is splitted into two part and the indexed patterns are shown in inset. It is found that a sharp high intense present at  $19.94^{\circ}$ . The XRD pattern also indicates many different peaks and the presence of sharp peaks shows that the material is in good crystalline nature. The properly described Bragg's peaks at specified  $2\theta$  angles suggest the high crystalinity of the grown crystals.

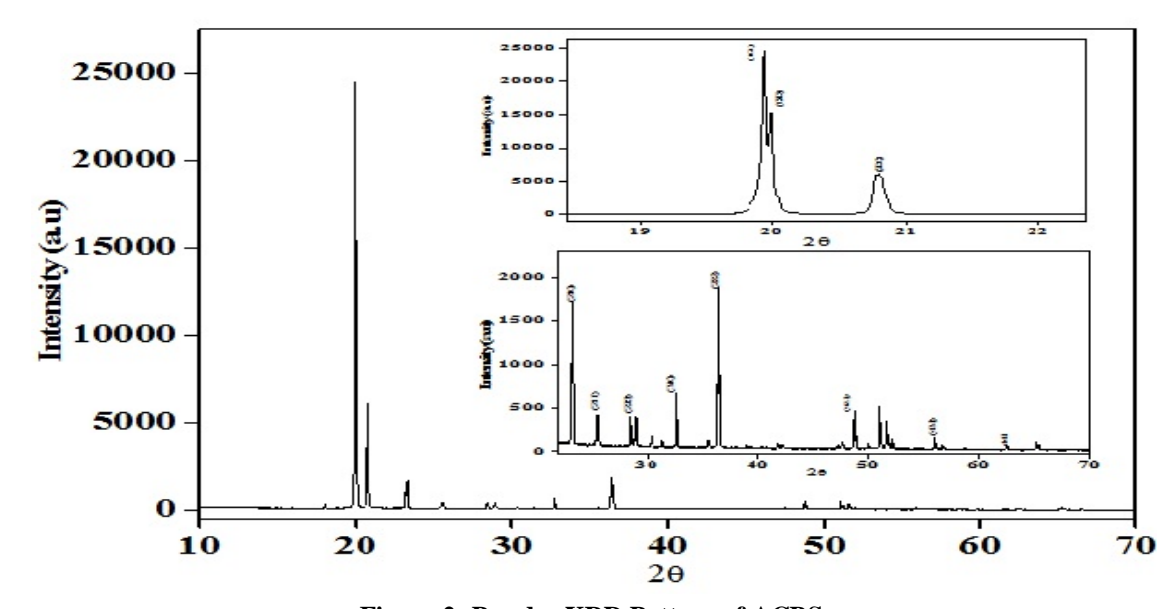
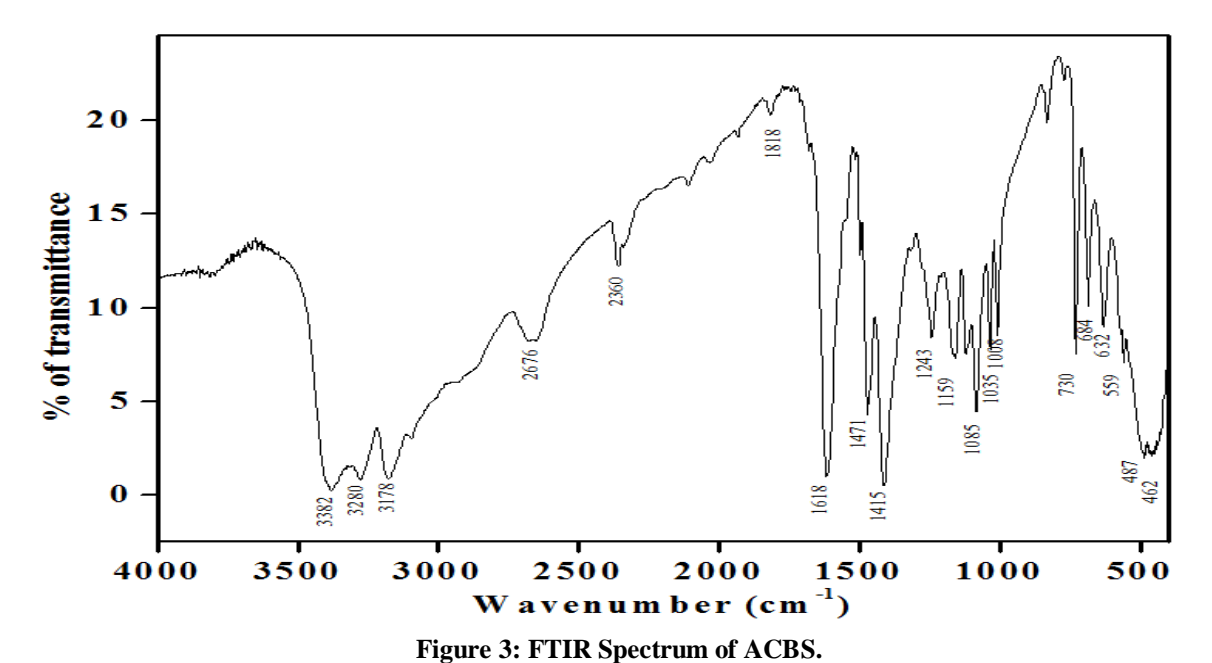


Figure 2: Powder XRD Pattern of ACBS.

# 3.3 Vibrational Analysis

The FTIR spectra of grown ACBS single crystal are shown in Fig. 3. The functional groups present in the ACBS crystals are identified and compared with thiourea (TU), Sulphanilic acid (SA) as stacked in Table 2. In the present work, the sharp high intense peaks at 3382 cm<sup>-1</sup> and 3178 cm<sup>-1</sup> are attributed to asymmetric and symmetric stretching modes of NH<sub>2</sub> group. The C=S asymmetric and symmetric stretching frequencies show a shift towards higher wave number when compared to thiourea and sulphanilic acid [11,16]. The metal – sulfur bond is assumed to be responsible for the shifting of vibration at 1471cm<sup>-1</sup> and 834 cm<sup>-1</sup> to high wavenumber in each material. The peak observed at 1415 cm<sup>-1</sup> and 1008 cm<sup>-1</sup> are the symmetric and asymmetric frequency of SO<sub>2</sub> group respectively. The stretching and bending vibrations of N-C-N and C-N-C were positioned at 684 cm<sup>-1</sup> and 487 cm<sup>-1</sup> respectively.



.

			,
Wavenumber(cm <sup>-1</sup> )			
TU[11]	SA[16]	<b>ACBS Present work</b>	Assignments
3347	3371	3382	NH <sub>2</sub> asymmetric stretching
3167	3051	3178	NH <sub>2</sub> symmetric stretching
2350	2400	2360	C-H stretching
1464	1431	1471	C=S asymmetric stretching
1387	1349	1415	asymmetric SO <sub>2</sub> vibration
1091	1271	1085	C-N symmetric stretching
-	1025	1008	symmetric SO <sub>2</sub> vibration
731	782	834	C=S symmetric stretching
627	694	684	N-C-N symmetric stretching
491	511	487	C-N-C bending

Table 2: Assignments of Vibrational Wave Number (cm<sup>-1</sup>) of TU, SA and ACBS Single Crystals

# 3.4 UV-Vis-NIR Spectral Analysis

The UV spectra of ACBS single crystal is shown in Fig. 4. From the UV spectra it is seen that the UV transparency cut off wavelength for ACBS crystal happens at 344 nm and transparency ~95% in the visible regions 416 nm - 800 nm which makes the ACBS crystal is potential candidate for second harmonic generations (SHG) Since it is seen that the absence of absorption in the visible region, the grown crystal is an appropriate candidate for optoelectronic applications [18]. The

Tauc's plot variation of  $(\alpha h v)^2$  vs. the photon energy (h v) is estimated as proven in Fig. 5. The optical band gap  $(E_g)$  for the ACBS crystal was predicted using the relation,

$$A (hv - E_g)^2$$

$$\alpha = \frac{}{(hv)}$$

Where  $\alpha$  is the absorption coefficient and A is the proportional constant. The  $E_g$  is measured by using the extrapolation of the linear part and the band gap of the ACBS crystal was become found to be 2.69 eV.

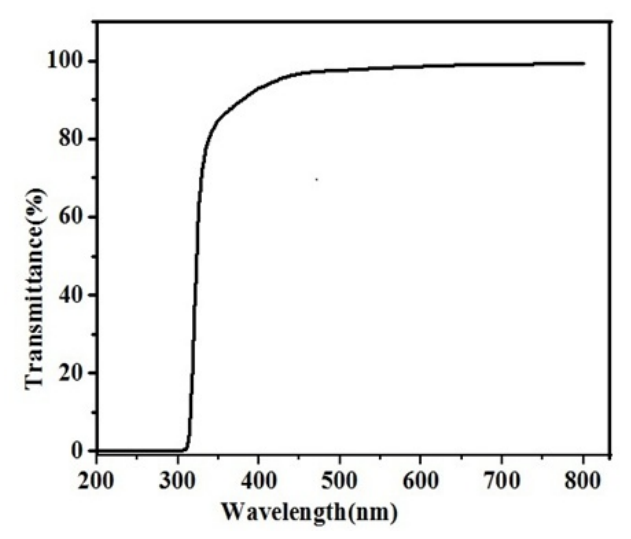


Figure 4: UV - Vis - NIR Transmission Spectrum of ACBS.

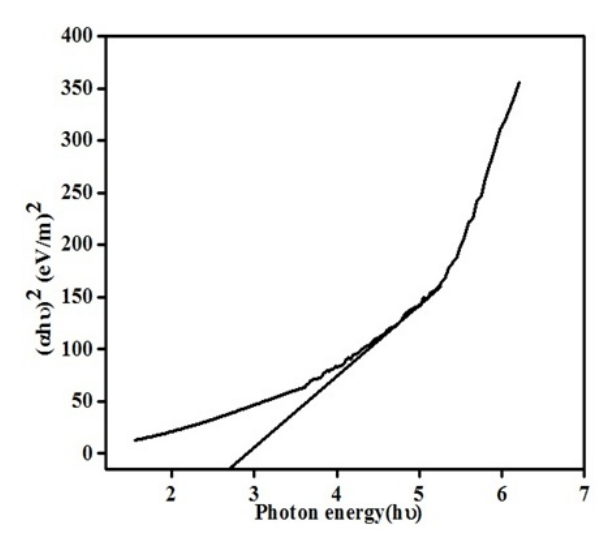


Figure 5: Plot of (αhv) 2 vs. hv of ACBS Crystal.

# 3.5 Thermal Analysis

Thermal stability, melting point, endothermic or exothermic reactions have been analyzed using thermal studies. The thermal analysis curves are shown in fig. 6. Because, there is no endothermic or exothermic transition below 175 °C and as a result of the material is strong up to this temperature. Within the differential thermal analysis curve, endothermic

reactions are found at 184 °C and 253 °C. The endothermic peak placed at 184 °C suggests the begin of decomposition and the material is completely decomposed at 253 °C and consequently the trace in TGA at 175°C in TGA shows the melting point of the crystal. The sharp endothermic peak indicates the good crystalline of the ACBS crystal. On the same time the melting point of ACBS crystal is determined to be more than that of reported value 173°C of pure sulphanilic acid crystal [19].

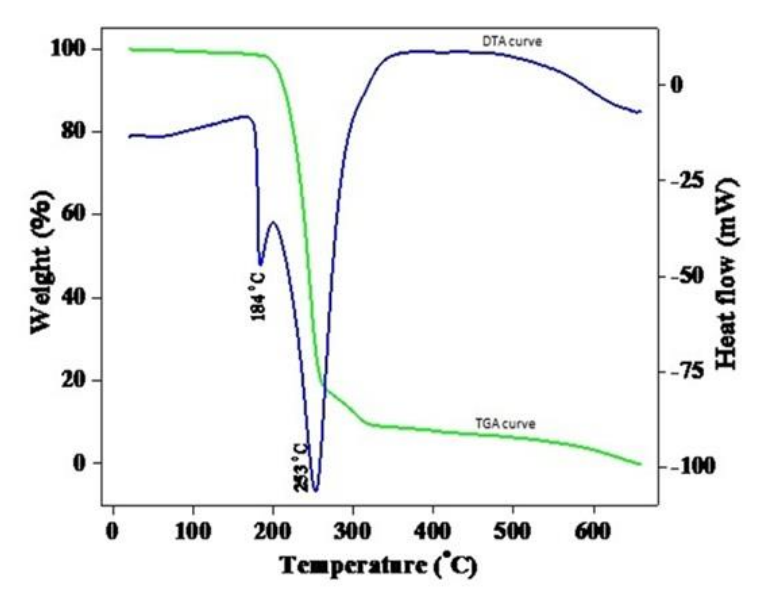


Figure 6: TGA / DTA Curve of ACBS Crystal.

# 3.6 Fluorescence Studies

The fluorescence spectra of ACBS single crystal is shown in Fig. 7. The photoluminescence spectrum of ACBS crystal gives information of various energy states available among valance band and conduction band answerable for radiative recombination. The ACBS was excited at 297.8 nm and the spectra were recorded in the range from 200 nm to 800 nm. From the figure is observed the high intense peak at 416.2 nm. The usage of the conversion wavelength to energy relation  $E_g = (1.24 / \lambda)$  eV, the band gap value calculated and  $\lambda$  is the wavelength of fluorescence. The fluorescence band gap of the ACBS single crystal is  $E_g$  located to be 2.97 eV. This indicates that the ACBS crystal is a violet light emitting material. Either different low intensity peaks can be intrinsic defects of the crystal.

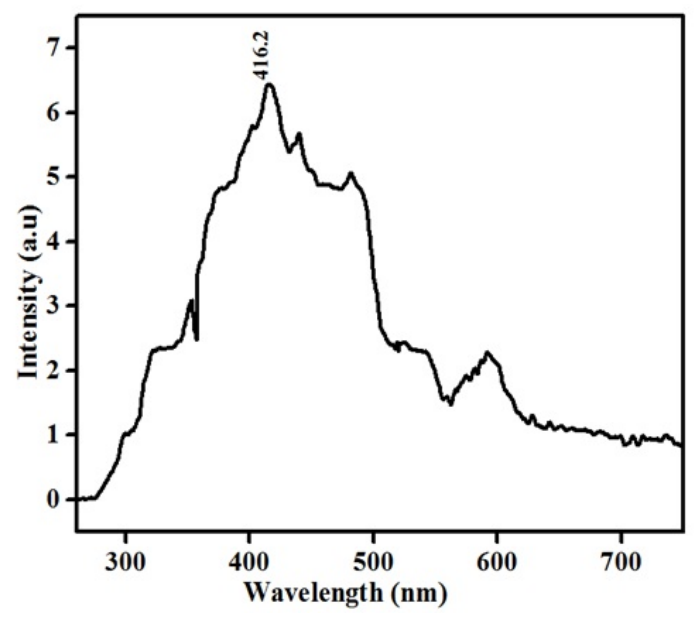


Figure 7: Fluorescence Spectrum of ACBS Single Crystal.

# 3.7 <sup>1</sup>H NMR Spectral Analysis

The Proton NMR spectrum of ACBS single crystal is shown in Fig. 8. It is seen that the  $^1H$  Proton NMR spectra affirms the nearness of eleven protons in ACBS compound which incorporate interchangeable protons also. In the spectrum, a singlet signal appearing at  $\delta = 2.110$  ppm is due to the protons of carboxylic acid connected sulphanilic acid moiety. The doublet signals appearing at  $\delta = 3.404$  and  $\delta = 3.389$  ppm attributed to the presence of –CH group of sulphanilic acid. The solvent  $D_2O$  sharp peak  $\delta = 4.69$  ppm is merged with the protons of –NH $_2$  and HSO $_3$  groups. Due to that the peak intensity is very high [20]. The doublet signal at  $\delta = 6.761$  and  $\delta = 6.734$  are assigned to phenyl protons which are present in ortho position group. The doublet peaks observed at  $\delta = 7.483$  and  $\delta = 7.455$  are assigned to the proton of NH $_2$  group of thiourea.

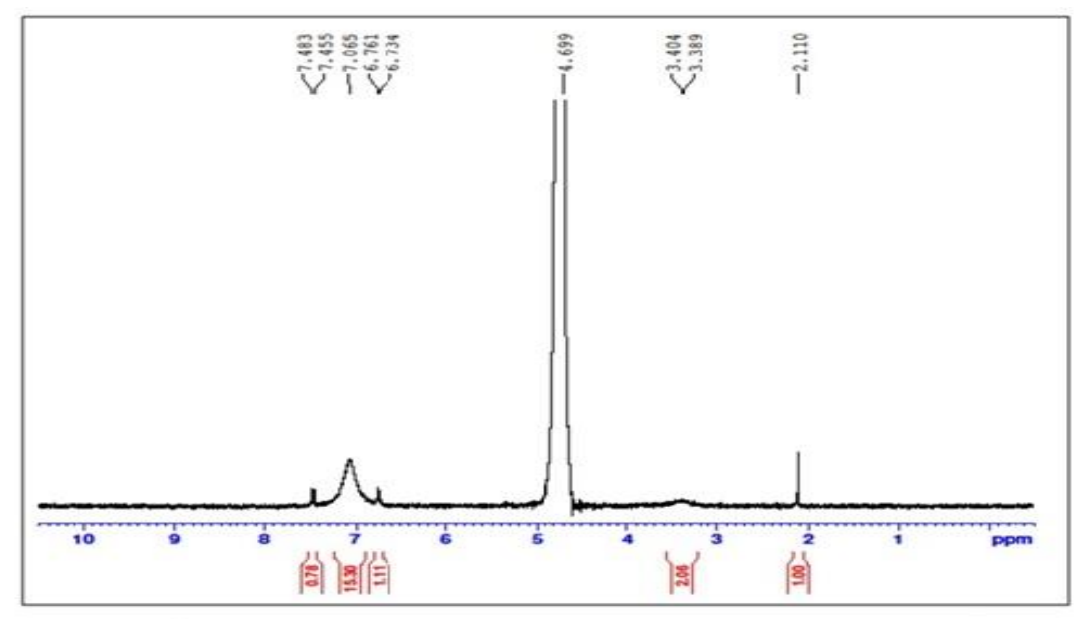


Figure 8: <sup>1</sup>H NMR Spectrum of ACBS Single Crystal.

#### 3.8 Microhardness Analysis

The microhardness analysis of the ACBS crystal was carried out by a Leitz Wetzler tester with a Vickers diamond pyramidal indenter. Hardness is a measure of a materials resistance to the nearby deformation resulting from indentation. It plays a key role in device fabrication [21]. The indentation hardness is generally defined as the ratio of the implemented load to the surface area of the indentation. The time of indentation became stored constituent at 10s for all trials and therefore the microhardness activity became taken between the implemented load (P) varying from 25 g to 100 g. The micro hardness number (Hv) was calculated using the formula [22]. Hv = 1.8544 P / d² (kg / mm²), where P is the applied load in kg and d is the average diagonal length of the indentation in mm. The hardness value H<sub>v</sub> with load P for ACBS as shown in Fig. 9. It is concluded that Hv increases with increases in P which is known as reverse indentation size effect. For an indentation load of 100g, cracks had been located on the crystal surface across the indent and it is far because of the discharge of internal pressure domestically initiated through indentation. The index number 'n' is predicted as 2.81 from the graph drawn between log P versus log d from Fig. 10. According to Hanneman [23] and Onitsch [24] the values of 'n' lies between 1 and 1.6 for difficult materials and it is more than 1.6 for soft materials. For this reason from Mayer's index number it is far clean that ACBS belongs to soft material category.

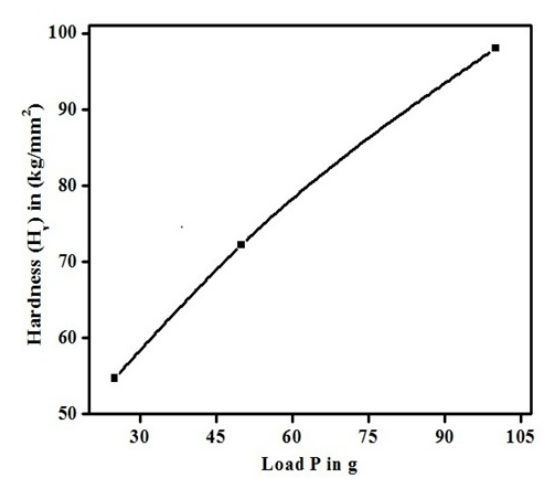


Figure 9: Hardness H<sub>v</sub> Verses Load (P) for ACBS Crystal.

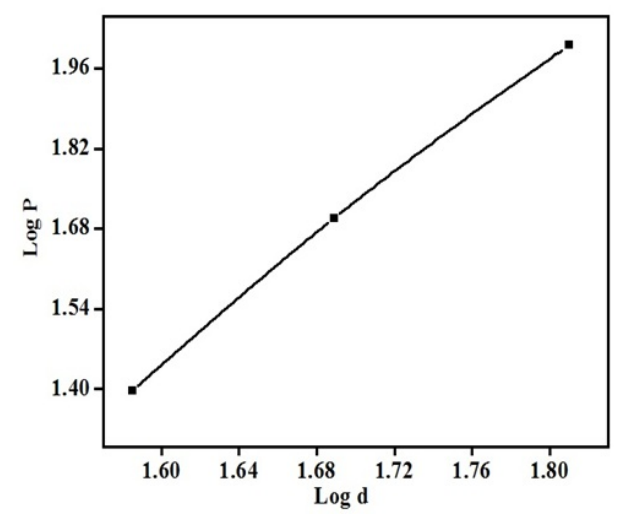


Figure 10: Log P and Log d for ACBS Crystal.

#### 3.9 SEM Analysis

Surface morphology of ACBS crystal was carried out using high resolution scanning electron microscope. Fig.11 (a) and (b) show the SEM pictures of ACBS crystal surface with magnification of 10 µm and 20 µm respectively. The scanning electron microscope studies give the information regarding the nature, morphology, composition variations and also it is mainly used to check surface imperfections. Because the organic materials are non-conducting in nature, gold carbon coating ought to be done before subjecting the crystal surface to electron beam. It is observed from the SEM image it is clear that the surface of the crystal appears smooth through it has pots and microcrystal on the surface. Overall the surface was very smooth, fine grain boundaries and few vale regions are determined [25].

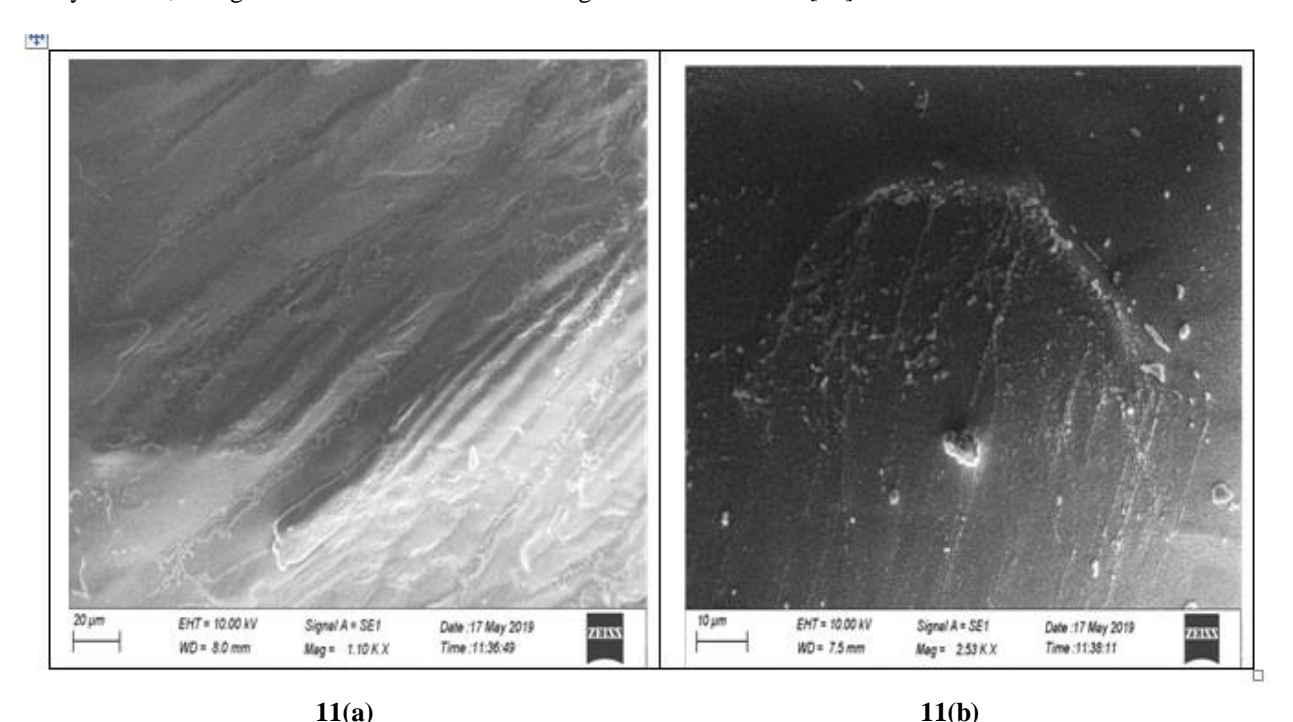


Figure 11: (a) and (b) SEM Pictures of ACBS Crystal

# 4. CONCLUSIONS

A novel NLO single crystal of 4-amino-N-carbamothioylbenzenesulfonamide was grown from aqueous solution at room temperature using a slow evaporation method. The single crystal X-ray diffraction confirms the compound formation. The sharp peaks observed in the powder x-ray diffraction spectra shows the good crystalinity nature of the grown crystal. The shift in the vibrational frequency of C=S at 1471cm<sup>-1</sup> verify the presence of thiourea moiety inside the compound. The UV-Vis - NIR studies confirm that the ACBS crystals have wider transparency in visible and UV regions and it is lower cut-off wavelength at 344 nm that is appropriate for optoelectronic devices. The ACBS crystal contains a high melting point and its exhibits high thermal stability. The high transparency shows that ACBS crystals can be used for nonlinear optical applications. The fluorescence spectrum showed that the grown crystals emitted violet fluorescence. The chemical structure of the grown crystal was established by <sup>1</sup>H NMR technique. The mechanical strength of ACBS single crystal measured by Vickers microhardness test allows that it belongs to soft material category. It is concluded that the ACBS crystal is a potential candidate for the fabrication of nonlinear optical devices. The SEM images show the layers of atoms of various sizes and also the surface of the microcrystal are ascertained to have a completely clean topography in nature.

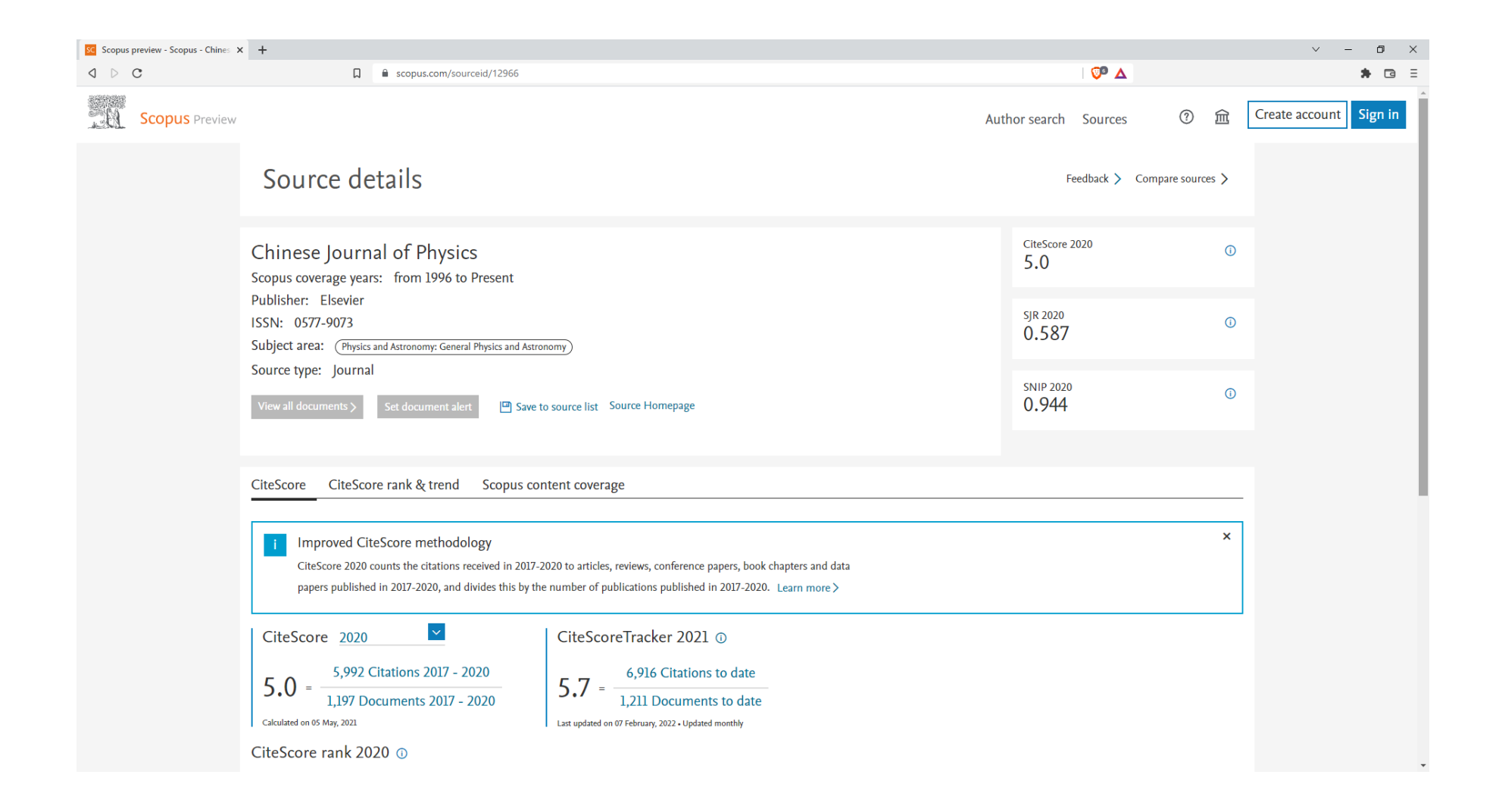
# ACKNOWLEDGEMENTS

One of the authors (RS) thank the Tamil Nadu State Council for Higher Education for the financial support [File No. D.O.Rc.No.744/2017 A]. The authors thank IIT Madras, Alagappa University, Karaikudi, St. Joseph's college, Tiruchirappalli and SASTRA University, Thanjavur for extending the lab facilities to record the Single crystal, XRD, FTIR, Microhardness and NMR, TGA/DTA spectrum respectively.

#### REFERENCES

- 1. R. Mohanakumar, D. Rajan babu, G. Ravi, R. Jayavel, Growth and characterization of 4- Dimethylamino-N-methyl-4-stilbazoliumtosylate (DAST) single crystals, J. Cryst. Growth 250 (2003) 113 117.
- 2. D. S. Chemla, J. Zyss, Non linear Optical Properties of organic molecular and crystals, Academic Press, New York, 1987.
- 3. P. Srinivasan, T. Kanagasekaran, R. Gopalakrishnan, A highly efficient organic nonlinear donor –accepter single crystal: L-Valinium Picrate, Crystal. Growth Des. 8 (2008) 2340 2345.
- 4. P. N. Prasad, D. J. Williams, Non-linear Optical effects in molecules and polymers, Wiley, USA, 1991.
- 5. J. Basset et al., Vogels Text Book of Practical Organic Chemistry, Fourth edition, English language book society, 1987.
- 6. M. P. Cifuentes, J. Driver, Mark G. Humphery, I. Asselberghs, A. Persoons, M. Samoc, B. Luther- Davies, J. Organoment. Chem. 607 (2000) 72-77.
- 7. P. S. Patil, M. S. Bannur, D. B, Badigannavar and S. M. Dharmaprakash, "Study on nonlinear optical properties of 2,4,5-trimethaxy-4-bromochalcone single cerystal", Optics & Laser Technology 55 (2014) 37-41.
- 8. M. Prakash, M. Lydia Caroline, and D. Geetha, "Growth, structural, spectral, optical and thermal studies acid based new NLO single crystal: L-phenylalanine-4-nitrophenol", Spectrochim. Acta part A 108 (2013) 32-37.
- 9. K. P. Bhuvana, S. J. Robinson, and T. Balasubramanian, "Synthesis and spectral studies of 2-aminopyridinium paranitrobenzoate: A novel optoelecronic crystal", Mater. Lett 61 (2007) 1489-1491.
- 10. R. W. G. Wyckoff, R. B. Corey, The crystal Structure of Thiourea, Zeitschrift Fur Krist. 81(1932) 386-395.
- 11. G. Thilakavathi, R. Arun Kumar, A. Kumaresh and N. Ravi Kumar, Materials Research innovations 20 (2016) 254-258.
- 12. P. Saritha, Synthesis, Growth, Structural, Spectral, Optical and Thermal properties of lithium nitrate doped thiourea crystal: International journal of physics and research.1(2019) 21-30.
- 13. M. M. Kumari, P. J. Ramchandra, C. Ravikumar, I. H. Joe, I. Numa, J. Raman Spectrose. 42 (2011) 1462 1469.
- 14. R. Q. Brewster and W. E. Mcewen, "Organic chemistry; 3<sup>rd</sup> ed.", Prentice-Hall of india: New Delhi, 862(2001).
- 15. John N. Low and Chris topher Guidewell, Acta Cryst, C 58 (2002) 209.
- 16. P. Mythili, T. Kanagasekaran, and R. Gopalakrishnan, Investigations on nucleation kinetics, growth and characterization of sulphanilic acid single crystas, Cryst. Res. Technol.42, 8 (2007) 791 -799.
- 17. A. Maghraby and E. Tarek, Radiat. Measurem. 41 (2006) 170.
- 18. P. N. Prasad, D. J. Williams, Introduction to Nonlinear Optical Effects in Organic Molecules and Polymers, Wiley, New York, 1991.
- 19. A. Rita, Gharde, T. Divakar, A. Chunarkar international Journal of scientifical technology research volume 2(2013)109-111.
- 20. P. Kalsi, 'Spectroscopy of organic compounds'. Wiley Eastern Publishers, New Delhi (1985).

- 21. B. Lal, K. K. Bamzai, P. N. Kotru, Mechanical strength of melt growth doped KMgF3 crystals, Mater. Chem. Phys. 78(2003) 202-207
- 22. A. Ruby and S. Alfredcecil Raj, 'Growth, Spectral, Optical, thermal and mechanical properties of thiourea doped tri glycine zinc chloride non linear optical crystal, International journal of scientific Research Publications. 3(2013) 1-5.
- 23. M. Hanneman, Metall, Manch. 23(1941) 135.
- 24. E. M. Onitsch, Mikroscopia 2(1947)131-151.
- 25. H. C. Gates, Thirty years of progress in surface science, in: Crystal Growth and Characyerization, Edi. North Holland, 1975.



FISEVIER

Contents lists available at ScienceDirect

# Chinese Journal of Physics

journal homepage: www.sciencedirect.com/journal/chinese-journal-of-physics





# Synthesis, growth, DFT, and HOMO-LUMO studies on pyrazolemethoxy benzaldehyde single crystals

G. Amudha <sup>a</sup>, R. Santhakumari <sup>a</sup>, <sup>\*</sup>, D. Chandrika <sup>a</sup>, S. Mugeshini <sup>a</sup>, N. Rajeswari <sup>a</sup>, Suresh Sagadevan <sup>b</sup>

- <sup>a</sup> Department of Physics, Government Arts College for Women (Autonomous), Pudukkottai, 622 001 (Affiliated to Bharathidasan University, Tiruchirappalli-620 024) Tamil Nadu, India
- <sup>b</sup> Nanotechnology& Catalysis Research Centre, University of Malaya, Kuala Lumpur 50603, Malaysia

#### ARTICLE INFO

Keywords: Nonlinear optical crystal optical properties DFT HUMO-LUMO

#### ABSTRACT

Pyrazolemethoxy benzaldehyde (PMB) was synthesized and crystals were grown by slow evaporation solution growth method. PMB was crystallized in a monoclinic crystal system with a centrosymmetric C2/c space group, according to single-crystal X-ray diffraction analysis. The crystalline planes were identified using powder X-ray diffraction analysis. FTIR - FT-Raman spectroscopic techniques were performed to determine the vibrational modes of functional groups for the grown crystal. UV-visible spectral analysis and photoluminescence studies were taken to investigate the linear optical properties of the grown crystal. Thermogravimetric and differential thermal analysis (TG/DTA) were used to determine the thermal stability of the PMB crystal. In addition to this density functional theory (DFT) calculations such as frontier molecular orbital's (FMOs), global chemical reactivity parameters, hyperpolarizability, natural bond orbital (NBO) analysis, Mullikan atomic charge distribution, and molecular electrostatic potential map analysis were carried out in gaseous phase using B3LYP/6-311G\* basis set.

# 1. Introduction

Organic material has been sought for the variety of applications in recent years, particularly photonics, electro-optic systems, color display optical switching, optoelectronics and frequency doubling [1–3]. As a result, several research groups are interested in developing new organic crystals with strong nonlinear optical properties. Organic crystals usually outperform inorganic and semi-organic materials, with substantial optical nonlinearity due to  $\pi$ -electron delocalization, low dielectric constant at higher frequencies, and a high damage threshold value [4–5]. 2-Methoxybenzaldehyde is an organic material containing a benzene ring that has been replaced with an aldehyde and a methoxy group. It appears in three varieties, ortho, Meta and Para in which the two functional groups (methoxy and aldehyde) are alpha, beta and gamma to each other. Benzaldehyde and its derivatives have vibrational spectra which can be used to study biological processes and analyze comparatively complex structures. It is used to make pharmaceuticals, plastic cleaners, agrochemicals and dyes among other things. It is very important in the intermediate processing of performs and flavoring elements [6]. Pyrazole is an aromatic organic material. A five-membered lactam ring structure of three carbon atoms and two nitrogen atoms in adjacent locations distinguishes it from other heterocyclic sequences. Antifungal and pesticide properties are found in Pyrazole derivatives, and crystals with the hydrazine moiety are a common class of organic molecules in medicinal and

E-mail addresses: santhasrinithi@yahoo.co.in (R. Santhakumari), drsureshnano@gmail.com (S. Sagadevan).

Corresponding author.

pharmaceutical chemistry [7–12]. The methyl and amino groups are frequently referred to as electron donation substituents in aromatic ring structures. Hyper conjugation of the methyl group with the adjacent  $\pi$ -system causes electronic delocalization, which the molecular orbital technique takes into consideration [13, 14]. In the present study, experimental and theoretical investigations of Pyrazolemethoxy benzaldehyde (PMB) are reported. The PMB crystals were investigated by powder X-ray diffraction, Fourier transforms infrared analysis, FT-Raman, UV-vis-NIR studies, photoluminescence, and thermogravimetric differential thermal analysis. Computational studies such as optimized molecular structure, Frontier molecular orbital, Global chemical reactivity descriptors, natural bond orbital, Mullikan atomic charge, and molecular electrostatic potential analysis are performed and discussed its results.

#### 2. Material and Methods

### 2.1. Synthesis and crystal growth

The PMB compound was synthesized using commercially available AR grade 4-acetyl-3-methyl-1-phenyl-5-hydroxy pyrazole (4A5P) and 2-methoxybenzaldehyde (2MB) in a 1: 1 molar ratio in acetone. The prepared solution was continually stirred with a magnetic stirrer, and the solution becomes turbid, Hence, ethanol was added and gradually warmed until a clear solution was obtained. The clear homogeneous solution was filtered using Whattman filter paper to eliminate impurities. The prepared homogeneous solution was transferred to a beaker and covered with a perforated sheet to manipulate the evaporation. It was kept in an undisturbed condition. Yellow-colored PMB powder was obtained according to the chemical reaction process depicted in Fig. 1.

As a first step towards the crystal growth process, the solubility of PMB compounds in different solvents like ethanol and methanol is performed at various temperatures. From Fig. 2 it is concluded that the PMB has a high solubility in ethanol compared to methanol. Hence ethanol has been taken as a solvent to grow PMB crystals. The synthesized material was further purified by repeating the recrystallization process two times in ethanol. The purified salt dissolved in ethanol solution provides a high-quality PMB crystal, which was collected over 4 weeks. The photographs of as-grown PMB crystals are shown in Fig. 3.

#### 3. Results and discussions

#### 3.1. Single and Powder X-ray diffraction studies

The single-crystal X-ray diffraction studies revealed that PMB crystal belongs to the monoclinic system with centrosymmetric space group C2/c, with lattice parameters of a = 28.179 Å, b = 4.71108 Å and C = 23.819 Å, and a cell volume of 3157.7 Å<sup>3</sup>. The lattice parameters are in good agreement with the reported values [15].

#### 3.2. Powder X-ray diffraction Analysis

The powder X-ray diffraction pattern of the grown crystal was recorded using a powder X-ray diffractometer with ( $\lambda=1.5408$ ) CuK $\alpha$  radiation. The grown crystal was scanned at  $2\theta$  values ranging from  $10^\circ$ - $80^\circ$ . The indexed powder X-ray diffractogram of the PMB crystal is shown in Fig. 4. The XRD results also show a variety of peaks and the presence of sharp peaks suggests that the material is in good crystalline nature. The clearly defined Bragg's peaks at  $2\theta$  angles indicate that the grown crystal has high crystallinity.

# 3.3. FT-IR, FT-Raman spectral analysis

The FT-IR spectrum was obtained on a JASCO FTIR 460 plus spectrometer in the wavelength range of  $4000-400 \text{ cm}^{-1}$  at room temperature (300K) using the KBr pellet technique with a scanning speed of 2 mm s<sup>-1</sup>. A Bruker RFS 100/s spectrometer was analyzed to examine the FT-Raman spectrum at room temperature (300K). Fig. 5(a-b) and Fig. 6(a-b) show the experimental, theoretical FT-IR and FT-Raman spectrum respectively. The various frequencies of functional groups in PMB crystal were calculated by the DFT/B3LYP method using 6-311G\* level and compared with the experimental values. The vibrational frequency assignments are listed in Table 1. Aromatic ring C-H stretching vibrations are assigned in the range of 3200-3000 cm<sup>-1</sup> [16–18]. The C-H stretching vibrations are

Fig. 1. Reaction scheme of PMB crystal

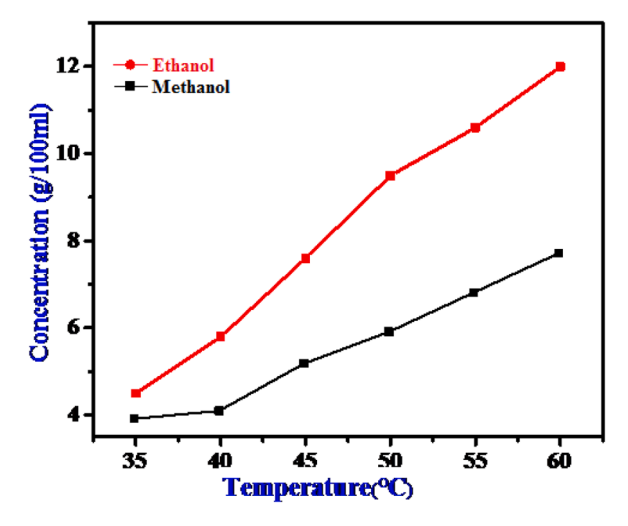


Fig. 2. Solubility curve of PMB

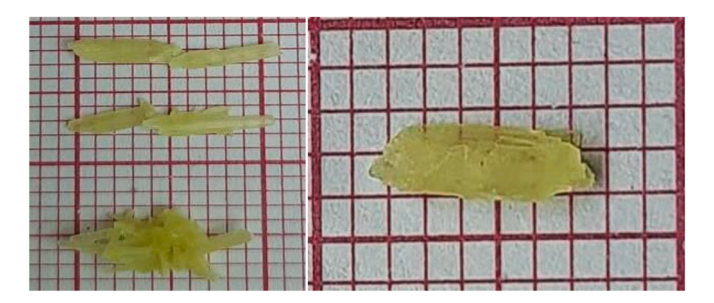


Fig. 3. As a grown crystal of PMB crystal

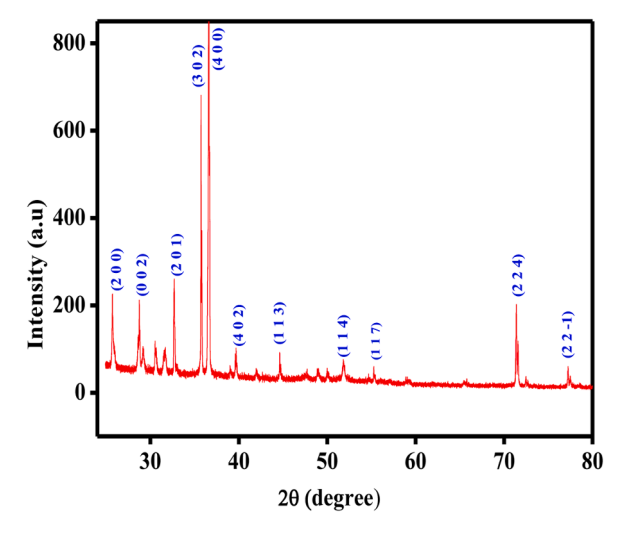


Fig. 4. Powder XRD spectrum of PMB crystal

observed experimentally at  $3167~\rm cm^{-1}$  in the FT-IR spectrum and  $3053~\rm cm^{-1}$  in the FT-Raman spectrum in the present work. The asymmetric stretching modes of  $\rm CH_3$  groups belonging to methoxy groups are assigned to the absorption bands at  $3092~\rm cm^{-1}$  in FT-IR and  $2968~\rm cm^{-1}$  in FT-Raman. In particular, the bands at  $1616~\rm cm^{-1}$  and  $1590~\rm cm^{-1}$  observed in FT-IR and FT-Raman spectra corresponds to C=O stretching vibrations in the methyl group with the pyrazole ring. In the crystal, the phenyl ring C=C stretching band is observed experimentally at  $1416~\rm cm^{-1}$  in the FT-IR spectrum and  $1450~\rm cm^{-1}$  in the FT-Raman spectrum. The N-N stretching mode is

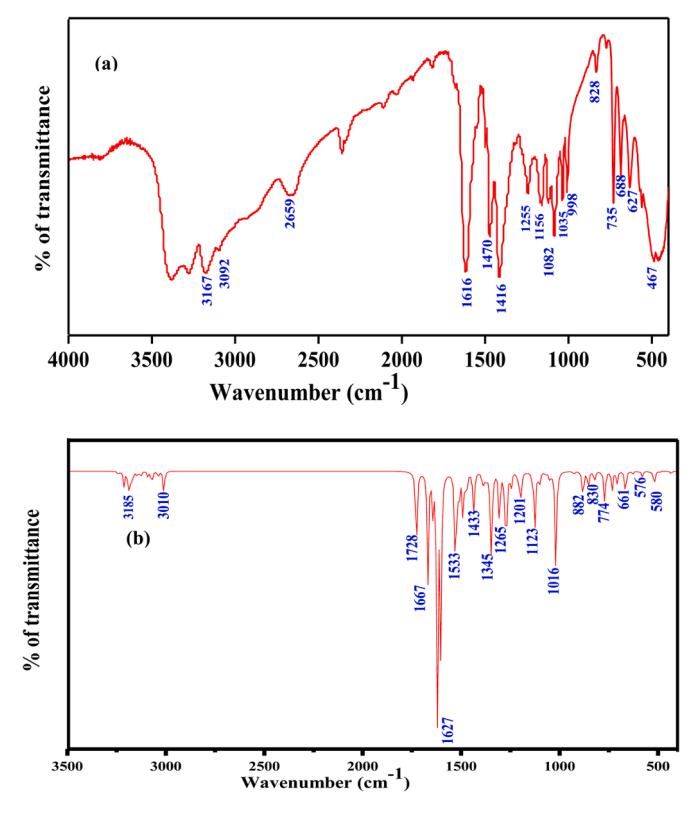
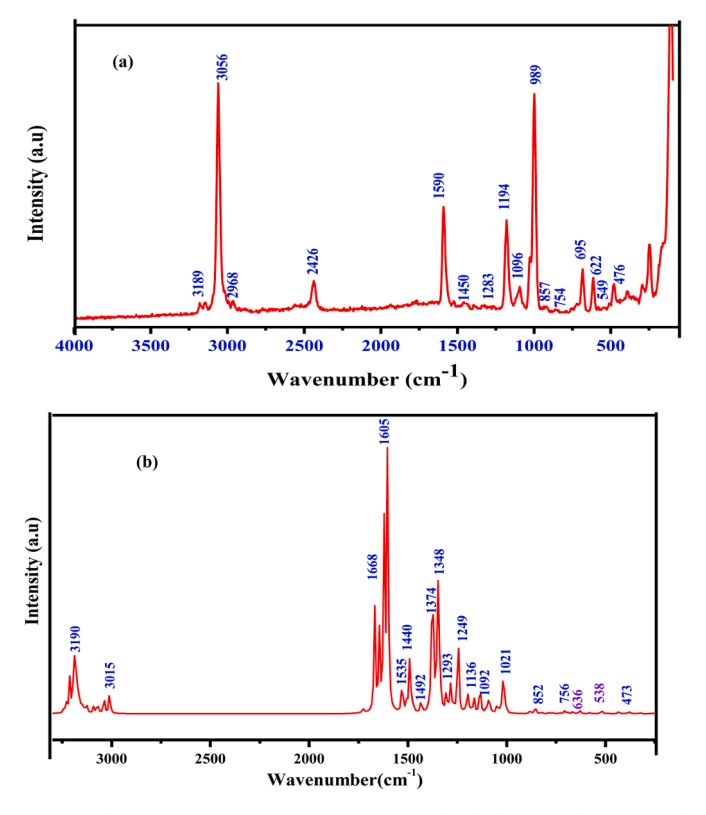


Fig. 5. (a-b) FT-IR spectrum of experimental and theoretical PMB crystal



 $\textbf{Fig. 6.} \ \, \text{(a-b) FT-Raman spectrum of experimental and theoretical PMB crystal}$ 

Table 1
FT-IR, FT-Raman and DFT frequencies with their assignments of PMB crystal

Experimental	FT-IR Theoretical	FT-Raman Experimental	Theoretical	Assignments
3167	3185	3056	3190	C-H stretching
3092	3010	2968	2968	CH3 asymmetric stretching
1616	1627	1590	1605	C=O stretching
1416	1433	1450	1440	C=C stretching
1255	1265	1283	1249	C-H stretching
1156	1123	1194	1136	C-N stretching
1082	1016	1096	1092	N-N stretching
828	882	857	852	C-H bending
735	744	695	756	C-H twisting
627	661	622	636	Skeleton deformation
467	465	476	473	C=O out of plane bending

 $1082~{\rm cm}^{-1}$  and  $1096~{\rm cm}^{-1}$  observed by IR and Raman spectrum, respectively. In the IR and Raman spectra, the benzene ring exhibits C-H out-of-plane bending, with peaks at  $467~{\rm cm}^{-1}$  and  $476~{\rm cm}^{-1}$  respectively.

#### 3.4. UV-vis NIR spectral analysis

The UV-visible absorbance spectrum of the grown crystal was recorded using a PerkinElmer Lamda 35 UV-vis-NIR spectrometer in the range of 200nm-1100 nm and is given in Fig. 7. The optical absorption spectrum of PMB crystal shows low absorption across the visible range, with no absorbance from 290 nm to 1100 nm. The cut-off wavelength of the grown crystal was discovered to be 235 nm. Excitation in the aromatic ring and the C=O group would be responsible for the observed absorption. The advantages of this method for NLO applications are the high transparency of the grown crystal in the UV-visible region [19].

#### 3.5. Photoluminescence studies

The photoluminescence (PL) emission spectrum of PMB crystal was analyzed on a Varian Cary Eclipse fluorescence spectrometer from 200 nm to 800 nm, as shown in Fig. 8. The PL emission spectrum is a mechanism that emits light when photons are excited from their ground state, and it provides information about molecular electronic transitions, defects, and some imperfections in the grown crystal [20, 21]. The grown crystal was excited at 250 nm and the emission was measured from 250 nm to 800 nm. The two emission peaks are shown in the same figure at 415 nm and 484 nm. The violet light emission was visible in the first emission peak at 415 nm. The second blue emission at 484 nm was caused by the  $\pi$ - $\pi$ \* transition [22]. These results demonstrated that the PMB crystal had violet and blue emission properties, making it suitable for usage in light-emitting devices [23].

#### 3.6. Thermal analysis

The thermal analysis was performed on the PMB crystal using SDT Q600 V20.9 Build 20 in the temperature range of 30°C – 700°C

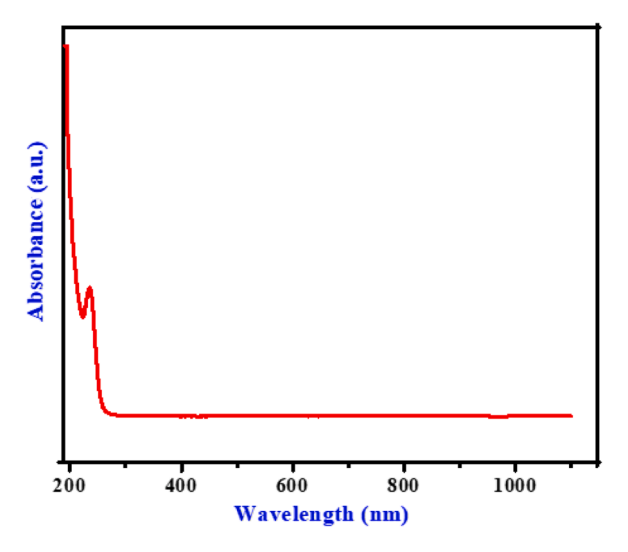


Fig. 7. UV-visible absorption spectrum PMB crystal

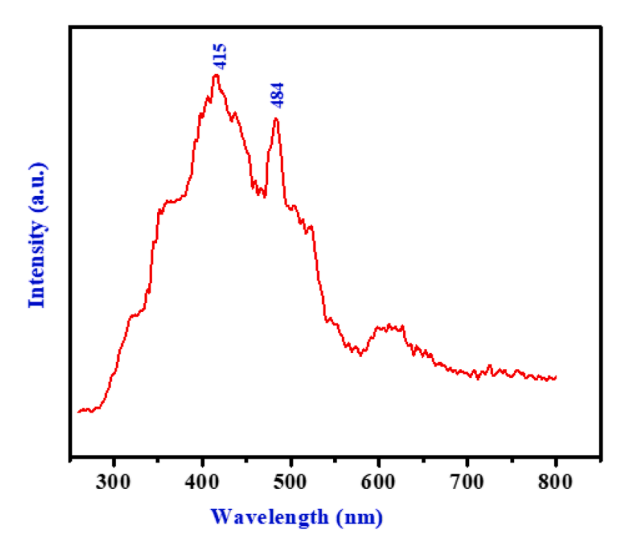


Fig. 8. Photoluminescence of the PMB crystal

under an N2 atmosphere at a rate of 10°C/min. Thermogravimetric (TG) and differential thermal analysis (DTA) were used to measure the thermal stability of the grown crystal. Fig. 9 shows the TG/DTA thermogram of the grown crystal. Two transitions can be seen in the TGA curve. The first and second transitions occur between 185°C to 263°C and 263°C to 315°C, respectively, due to the melting point of the substance. The TGA curve shows that the material is stable up to 183°C. Two endothermic peaks were found on the DTA curve. The sharp endothermic peak suggests that the material has good crystallinity and purity. The DTA curve indicates that the PMB crystal has a first endothermic peak at 184°C, which is attributed to the material's melting point. The second endothermic peak was recorded at 250°C, equivalent to significant material weight loss. At a temperature of 183°C, the material starts to decompose slowly, with the majority of the material evaporating and the substance becoming volatile. The absence of endothermic or exothermic peaks before the melting point of a substance indicates thermal stability [24].

#### 3.7. Computational Details

The molecular structure, energies, and other properties of a crystal can be calculated using DFT analysis through *ab initio* computational calculation. The geometry of PMB has been optimized at the B3LYP level of theory and the 6-311G\* basis set was utilized to describe the atoms of the molecule. Vibrational frequency calculations are performed on the optimized structure to confirm their stationary points. Natural bond orbital (NBO) is estimated using the same level of theory and basis sets. Quantum chemical computational calculations through DFT have been effective in predicting the vibrational spectra of chemical crystals. All these computational procedures have been used as per the Gaussian-09 package [25–29] guidelines. The molecular structure, electronic

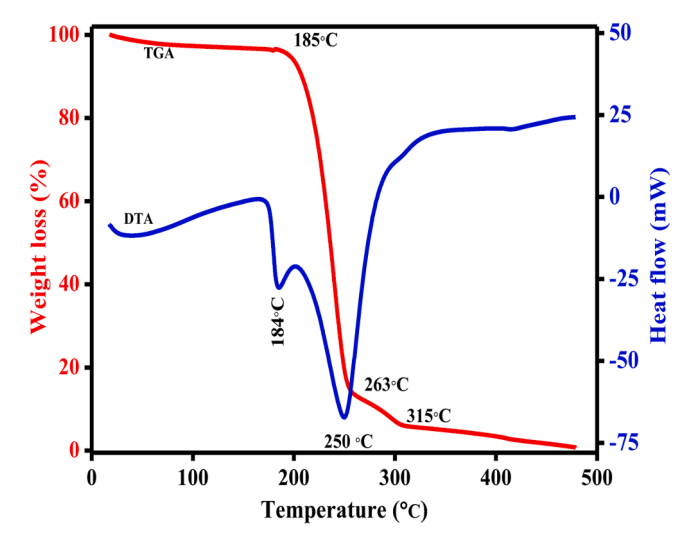


Fig. 9. TGA/DTA thermogram of PMB crystal

properties, and vibrational spectra were visualized and rendered from the output data of DFT calculations.

#### 3.7.1. Molecular geometry optimization

The structure of PMB was optimized to produce a precise molecular geometry of the molecule, as shown in Fig. 10. PMB contains 41 atoms, 174 electrons and is neutral in charge with spin at singlet. From the calculation, the global minimum energy or self-consistent field (SCF) energy of PMB at B3LYP level with the basis set of 6-311G is -1107.1823 a.u; with a dipole moment of 8.8811 Debye. The single and double bonds are highlighted and the van Der Walls radii of each atom are represented in the same figure.

The Optimized geometrical parameters derived by the B3LYP (Becke three-parameter Lee-yang-parr) method using 6-311G\* basis sets are more similar to the experimental values listed in Table 2. The C-C bond lengths vary from 1.367Å to1.493Å for XRDs values and from1.353 Å to1.495 Å for B3LYP values. The C-H bond length was measured in the range of 0.930 Å - 0.960 Å in XRD and 1.080 Å-1.095 Å in B3LYP and found to be similar. The experimental bond distances of C17-C18, C18-C-19, N5-C19, N4-N5 and N4-C1 atoms in the pyrazolone ring, XRD values of 1.462, 1.438, 1.305, 1.405 and 1.389 respectively, were found to be similar to theoretical DFT values of 1.477, 1.448, 1.299, 1.392 and 1.397 Å. The bond lengths in X-ray data were much shorter than observed theoretical values, which might be explained by packing interactions in the solid-state molecule, whereas estimated bond distances for free molecules in the gaseous state were achieved. The O3-C38 (1.424 Å) bond length is longer than the other C-O bond lengths, due to oxygen atom commitment in carbon bond interactions, while the O1-C17 (1.230 Å) bond length is shorter. The calculated N-C bond length value in B3LYP was between 1.299Å - 1.416Å with the equivalent XRD value between 1.305 Å – 1.419 Å. The N-N bond length is 1.392 Å for the B3LYP/6-311G\* method and 1.392 Å for XRD. The DFT-B3LYP/6-311G\* estimated bond angles of PMB were found to be in extremely good agreement with the XRD values, with a few small deviations. Because of the presence of the methyl group, the bond angles of C6-N4-C17 are greater than other bond angles, with a value of 129.2°.

#### 3.7.2. Frontier molecular orbital property

The quantum chemical properties  $E_{HOMO}$ ,  $E_{LUMO}$ ,  $\Delta E$  and related parameters provide valuable information about the reactivity of chemical crystals. The reactivity zone of a molecule is shown by the electron density at the molecule's frontier. The calculation of Frontier electron density can be calculated in many ways. The difference between a neutral system's highest occupied molecular orbital (HOMO) and its lowest unoccupied molecular orbital (LUMO) gives excitation energies. This is also referred to energy gap that reveals molecular stability. LUMO represents an electron acceptor containing a region and HOMO represents an electron donator containing the region of a molecule. The relative energy of the molecular orbital has been calculated and graphical representations of HOMO and LUMO of PMB are given in Fig. 11. HOMO<sup>+</sup>, HOMO<sup>2+</sup>, LUMO<sup>-</sup> and LUMO<sup>2-</sup> are also rendered in the same figure. The atoms 6C, 7C, 9C, 11C, 13C, 15C, 4N, 5N, 17C, 18C, and 19C of the molecules largely contributed to the HOMO energy. The HOMO+ energy of the molecule is contributed by most of the atoms of the PMB molecule. HOMO2<sup>+</sup> energy is primarily derived from the 7C, 9C, 13C and 15C atoms of the molecule. The LUMO energy of PMB was from 5N, 17C, 18C, 19C, 24C, 25C, 27C, 37C, 30C, 32C, 34C, and 36C atoms. The LUMO energy of the molecule was from almost the same atoms except a few in the region. LUMO2 energy exhibited from 29C, 30C, 32C, 34C, 36C, and 37C atoms of the molecule. The HOMO-LUMO energies were: -5.38839 eV; and -2.5788 eV respectively, while the energy gap,  $\Delta E$  was 2.80959 eV; ( $\Delta E$  reveals the molecule's chemical activity). The energy gap conveys the molecule's small excitation energies. The energy gap of PMB discloses that the molecules possess low reactivity and high kinetic stability. But, adding a reactive molecular region to this base molecule would be valuable to make highly reactive crystals from this molecule. The calculated values of E<sub>HOMO</sub>. E<sub>LUMO</sub> and energy gap are listed in Table 3.

#### 3.7.3. Global Chemical Reactivity Analysis

The energy gap values obtained from the DFT method have been used to measure the material's total electrochemical reactivity and structural stability [30]. The theorem of Koopmans says HOMO – LUMO energy gap values can determine ionization potential and

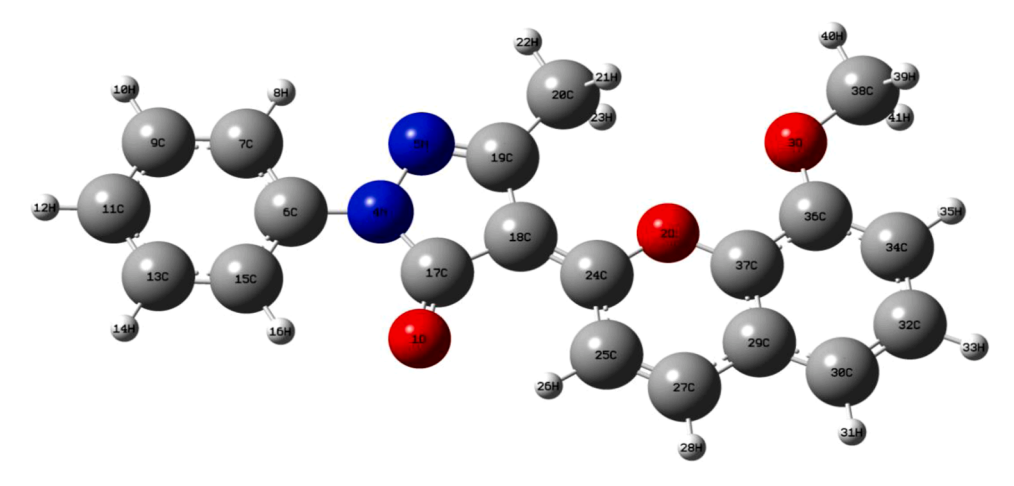


Fig. 10. Optimized molecular structure of PMB crystal

**Table 2** Experimental and optimized geometry parameters of PMB crystal computed by B3LYP/6311G\* basis set

Bond length(Å)			Bond angles (°)		
Parameters	EXP*	B3LYP/ 6311G*	Parameters	EXP*	B3LYP/ 6-311G
O1-C17	1.230	1.226	C24-O2-C37	121.4	121.9
O2-C24	1.358	1.364	C36-O3-C38	117.1	118.3
O2-C37	1.377	1.365	N5-N4-C6	118.4	118.9
O3-C36	1.358	1.355	N5-N4-C17	112.4	112.2
O3-C38	1.424	1.424	C6-N4-C17	129.2	128.9
N4-N5	1.405	1.392	N4-C6-C7	119.6	119.1
N4-C6	1.419	1.416	N4-C6-C15	121.6	121.3
N4-C17	1.389	1.397	C6-C7-H8	119.4	119.0
N5-C19	1.305	1.299	C6-C7-C9	119.2	119.9
C6-C7	1.401	1.402	C7-C9-C11	120.9	120.8
C6-C15	1.404	1.402	C9-C11-H12	120.5	120.5
C7-H8	0.930	1.080	C9-C11-C13	119.2	119.0
C7-C9	1.390	1.390	H12-C11-C13	120.5	120.5
C9-H10	0.960	1.085	C11-C13-H14	120.0	120.0
C9-C11	1.390	1.393	C11-C13-C15	121.2	121.2
C13-C15	1.391	1.392	C6-C15-H16	119.6	119.6
C17-C18	1.462	1.477	O1-C17-N4	125.9	126.7
C18-C19	1.438	1.448	O1-C17-C18	130.8	130.0
C18-C24	1.372	1.373	N4-C17-C18	103.7	103.2
C19-C20	1.493	1.495	C17-C18-C19	105.5	105.3
C20-H21	0.960	1.093	C17-C18-C24	125.0	124.5
C24-C25	1.438	1.436	C19-C18-C24	129.6	130.2
C25-C27	1.367	1.353	N5-C19-C18	111.9	111.1
C27-C29	1.433	1.442	N5-C19-C20	119.6	120.3
C29-C30	1.404	1.407	C18-C19-C20	128.5	128.6
C29-C37	1.390	1.399	C19-C20-H21	109.5	111.3
C30-C32	1.382	1.382	C19-C20-H22	109.5	109.0
C32-C34	1.404	1.402	H21-C20-H22	109.5	109.4
C34-C36	1.391	1.393	O2-C24-C18	116.3	116.8
C36-C37	1.404	1.408	O2-C24-C15	118.1	118.3
C38-H39	0.960	1.095	C18-C24-C25	124.5	124.9
C50-1157	0.500	1.055	C24-C25-C27	120.6	120.4
			C25-C27-H28	120.5	120.4
			C25-C27-C29	120.9	120.9
			C25-C27-C29	124.5	124.1
			C27-C29-C30 C27-C29-C37	118.3	116.8
			C27-C29-C37 C30-C29-C37	119.2	119.1
			O3-C36-C34	125.9	125.8
					116.1
			O3-C36-C37	116.1	
			C34-C36-C37	119.0	118.1
			O2-C37-C29	121.6	121.6
			C29-C37-C36	121.3	121.6

electron affinity [31]. The Ionization Potential of the PMB was estimated using the HOMO orbital energy value.

$$Ionization Potential(I) = -E_{HOMO}$$
 (1)

The LUMO orbital energy was utilized to compute electron affinity because it is determined as the ability to require one electron from a donor.

$$Electronaffinity(A) = -E_{LUMO}$$
 (2)

The chemical reactivity descriptors provided by the electron affinity and ionization potential required by using energy values help in the computation of specific chemical quantities and the characterization of molecular properties [32]. The electronegativity ( $\chi$ ) and global hardness ( $\eta$ ) of PMB were computed using the formulas shown below [33].

The Electronegativity of PMB is calculated as 
$$(\chi) = (I+A)/2$$
 (3)

The global hardness is calculated as, 
$$(\eta) = (I - A)/2$$
 (4)

The chemical potential is computed as 
$$(\mu) = -(I+A)/2$$
 (5)

The softness of the molecule is measured as, 
$$(\sigma) = 1/\eta$$
 (6)

The global electrophilicity index of a material is estimated as, 
$$(\omega) = \mu^2/2\eta$$
 (7)

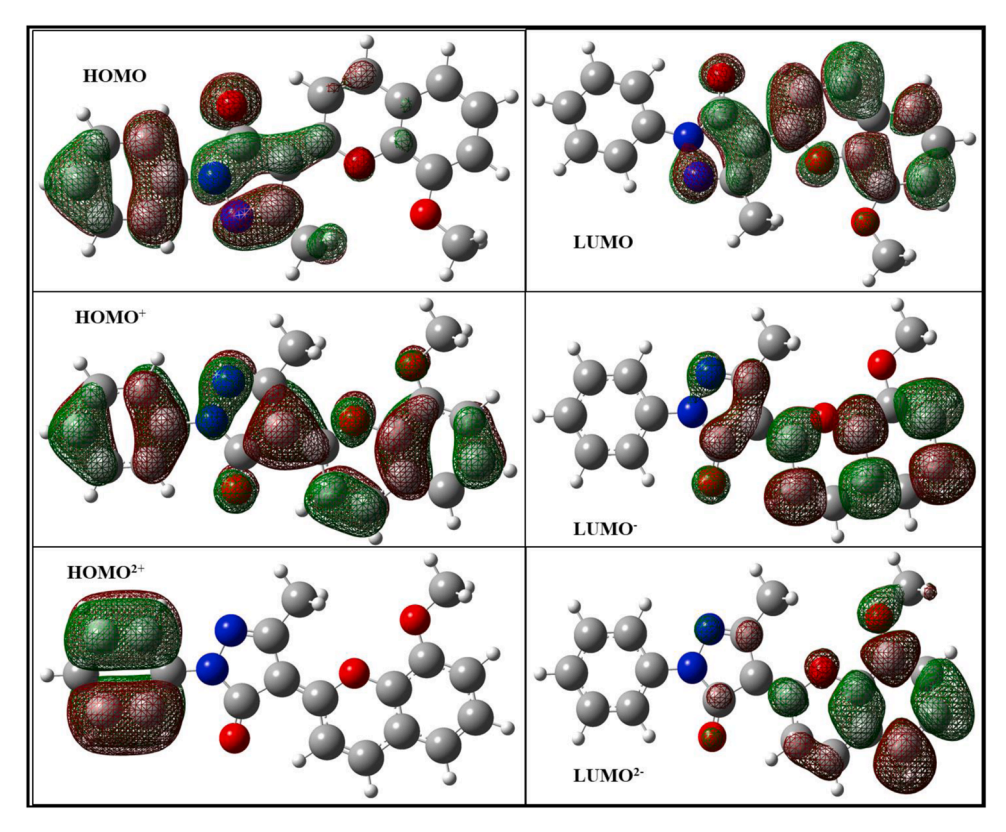


Fig. 11. Frontier molecular orbital of PMB crystal

$$\label{eq:control_equation} \begin{split} \textbf{Table 3} \\ E_{HOMO,} \ E_{LUMO} \ \text{and energy gap values of PMB crystal} \end{split}$$

,		
S. No	Property	Value
1	E (method)	-1107.18233229 a.u.
2	Dipole Moment	8.8811 Debye
3	$E_{\text{HOMO}}$	-5.38839 eV
4	$E_{LUMO}$	-2.5788 eV
5	Energy gap (ΔE)	2.80959 eV

The chemical reactivity descriptors evaluated using HOMO – LUMO energy values display that the crystals have high stability [34], with a hardness value of 1.40475 eV. The PMB molecule's chemical potential is negative, indicating strong stability. In the present study, PMB confirmed the material's great chemical potential and good stability, indicating its suitability for optoelectronic applications. Table 4 displays the calculated values for  $E_{HOMO}$ ,  $E_{LUMO}$ , energy gap, and other global descriptor parameters.

#### 3.7.4. Hyperpolarizability studies

The dipole moment  $(\mu)$ , polarizability  $(\alpha)$  and first hyperpolarizability  $(\beta)$  values each have a significant impact on optical properties [35–39] and are derived from the nonlinear properties of a PMB crystal using x, y, and z components are given as follows.

The total electrostatic dipole moment is

$$\mu_{tot} = \left(\mu_{x}^{2} + \mu_{Y}^{2} + \mu_{Z}^{2}\right)^{1/2} \tag{8}$$

Where  $\mu_{X_1}\,\mu_{Y}$  and  $\mu_{Z}$  are diagonal moments along  $x,\,y$  and z directions The isotropic polarizability is

$$\alpha_{tot} = \frac{1}{3} \left( \alpha_{xx} + \alpha_{yy} + \alpha_{zz} \right) \tag{9}$$

Where,  $\alpha_{xx}$ ,  $\alpha_{yy}$ , and  $\alpha_{zz}$  are the diagonal components of polarizability tesnor The mean hyperpolarizability

**Table 4**Calculated quantum parameters and electronic properties of PMB crystal

S. No	Property	B3LYP/6-311G*
1	E <sub>HOMO (</sub> eV)	-5.38839
2	E <sub>LUMO</sub> (eV)	-2.5788
3	Energy gap (eV)	2.80959
4	Ionization potential	5.38839
5	Electron affinity	2.5788
6	Global hardness	1.40475
7	Electronegativity 3.983	
8	Global softness 0.711	
9	Chemical potential	-3.98355
10	Global Electrophilicity	5.81288
	Index	

$$\beta_{tot=} \left(\beta_{x}^{2} + \beta_{y}^{2} + \beta_{z}^{2}\right)^{1/2} \tag{10}$$

Where,

$$\beta_{x=}\beta_{xxx+}\beta_{xyy}+\beta_{xzz}$$

$$\beta_{y=}\beta_{yyy+}\beta_{yzz}+\beta_{yxx}$$

$$\beta_{z=}\beta_{zzz+}\beta_{zxx}+\beta_{zyy}$$

The first hyperpolarizability could also be a 3rd rank tensor which can be characterized as a  $3\times3\times3$  matrix, with Kleinman symmetry reducing the 27 elements of the 3D matrix to 10 elements [40]. Since polarizability and hyperpolarizability are measured in atomic units, they are converted to electrostatic units using 1 a.u =  $0.1482\times10^{-24}$  esu and the values using 1 a.u =  $8.6393\times10^{-33}$  esu, [41, 42]. The theoretically predicted values of  $\mu$ ,  $\alpha$  and  $\beta$  are found to be 8.881D,  $19.683\times10^{-24}$ esu, and  $24.754\times10^{-30}$ esu respectively, for the present molecule. As a result, many molecules start to align in the direction of the supplied electric field. Because of their large dipole moment, organic molecules have large nonlinearities [43, 44]. Table 5 displays the tensor values for polarizability and hyperpolarizability.

#### 3.7.5. NBO analysis

A natural bond orbital (NBO) is a computed bonding orbital having the highest electron density in quantum theory. Computational chemistry calculates bond order, donor and acceptor interactions, and hence the electron density between the atoms. The donor-acceptor interactions in NBO analysis are evaluated using the version of the NBO 3.1 program as implemented within the Gaussian 09 package at the DFT/B3LYP method using the second-order perturbation theory of Fock matrix [45–46] with 6-311G\* basis set for each donor (i) and acceptor (j), the stabilization energy (E2) associates with the delocalization i-j are estimated as,

$$E(2) = \Delta Ei = qi = \frac{(Fi, j)}{Ei - Ei}$$

Where,  $F_{(i,\ j)}$  is the off-diagonal Fock matrix element,  $E_i$ ,  $E_j$  are diagonal elements (orbital energy) and  $q_i$  is the donor orbital occupancy. The different interactions with PMB stabilization energies are listed in Table 6. The highest E (2) value provides important information about the donor and acceptor group's relationship. In the present work, the electron-donating from the BD (C11-C13), BD (C6-C15), BD (C18-C24), LP(2)O3, and LP(1) N4 to the antibonding acceptor BD\*(C7-C9), BD\*(C11- C13), BD\*(O1-C17), BD\*(C34 – C36), BD\*((O1 – C17), orbitals and their corresponding energy values are 21.61, 21.70, 22.45, 31.72, and 58.34 KJ/ mol, with the highest stabilization energies of electron delocalization because of the replacement of the molecule.

**Table 5** The dipole moment  $(\mu)$ , polarizability  $(\alpha)$  hyperpolarizability  $(\beta)$  of the PMB crystal

Parameters	Value	Parameter	Value
$\alpha_{xx}$	-118.0839	$\beta_{xxx}$	195.5831
$\alpha_{xy}$	2.6418	$\beta_{xxy}$	37.1705
$\alpha_{yy}$	-130.7497	$\beta_{xyy}$	69.6588
$\alpha_{xz}$	-0.0021	$\beta_{yyy}$	17.5852
$\alpha_{yz}$	-0.0007	$\beta_{xxz}$	-0.0353
$\alpha_{zz}$	-149.616	$\beta_{xyz}$	0.0117
$\alpha_{totol}$	$-19.683 \times 10^{-24}$ esu	$\beta_{yyz}$	-0.003
$\mu_{\mathbf{x}}$	8.8219	$\beta_{xzz}$	14.2906
$\mu_{y}$	1.0235	$\beta_{yzz}$	8.1743
$\mu_z$	-0.0006	$\beta_{zzz}$	0.0104
$\mu_{tot}$	8.881D	$eta_{ m total}$	$24.754 \times 10^{-30}$ esu

**Table 6**The significant second order perturbation theory analysis of the PMB crystal

Donor(i)	Acceptor(j)	E(2)(kcal/mol)	E(j)-E(i) (a.u)	F(i, j) (a.u)
BD(1) N4-N5	BD*(1) C19-C20	4.99	1.23	0.07
BD(1) C36-C37	BD*(1) C29-C37	4.75	1.26	0.069
BD(2) N5-C19	BD*(2) C18-C24	10.94	0.33	0.057
BD(2) C6-C15	BD*(2) C7-C9	18.98	0.29	0.066
BD(2) C6-C15	BD*(2) C11-C13	21.70	0.29	0.071
BD(2) C7-C9	BD*(2) C6-C15	20.94	0.28	0.07
BD(2) C7-C9	BD*(2) C11-C13	18.83	0.28	0.066
BD(2) C11-C13	BD*(2) C6-C15	19.33	0.28	0.067
BD(2) C11-C13	BD*(2) C7-C9	21.61	0.28	0.070
BD(2) C18-C24	BD*(2) O1-C17	22.45	0.30	0.076
BD(2) C18-C24	BD*(2) N5-C19	20.81	0.31	0.072
BD(2) C25-C27	BD*(2) C18-C24	20.06	0.31	0.073
BD(2) C25-C27	BD*(2) C29-C37	13.22	0.29	0.059
BD(2) C29-C37	BD*(2) C25-C27	13.65	0.31	0.061
BD(2) C29-C37	BD*(2) C30-C32	16.60	0.30	0.064
BD(2) C30-C32	BD*(2) C29-C37	20.00	0.28	0.069
BD(2) C30-C32	BD*(2) C34-C36	17.88	0.28	0.064
BD(2) C34-C36	BD*(2) C29-C37	18.26	0.29	0.067
BD(2) C34-C36	BD*(2) C30-C32	19.75	0.30	0.069
LP(2)O1	BD*(2) N4-C17	26.75	0.67	0.121
LP(2)O1	BD*(2) C17-C18	17.88	0.69	0.101
LP(2)O2	BD*(2) C18-C24	30.47	0.38	0.098
LP(2)O2	BD*(2) C29-C37	26.78	0.36	0.092
LP(2)O3	BD*(2) C34-C36	31.72	0.34	0.098
LP(1)N4	BD*(2) O1-C17	58.34	0.27	0.112
LP(1)N4	BD*(2) N5-C19	22.42	0.28	0.073
LP(1)N4	BD*(2) C6-C15	33.09	0.3	0.089

## 3.7.6. Mulliken atomic charges

Mulliken population analysis revealed the atomic electronic charges of PMB crystal. The atomic charges have an impact on electronic structure, properties of molecular systems, dipole moment, and molecular polarizability. Furthermore, a molecule's bonding ability is determined by the electronic charge of the chelating atoms. Mulliken population analysis was used to determine the atomic charge values [47]. The Mulliken population analysis of PMB was calculated using the B3LYP/6311G\* basis set to confirm the reliability of our results. The calculated Mulliken atomic charge values of PMB crystal values are given in Table 7. The Mulliken charges of each atom of the molecule are shown in Fig. 12. Fig. 13 shows the plot of Mulliken atomic charges on several element atoms of the PMB crystal. The Mulliken atomic charge of all hydrogen carries a positive charge. The atoms C17, C24 and C37 have more positive charges (0.554, 0.208 and 0.238) and these atoms may donate electrons during interactions and atoms 4N, 5N, 1O, 2O and 3O (-0.429, -0,225, -0.403, -0.317, and -0.335) have a more negative charge and these atoms may act as electron acceptors.

**Table 7**Mulliken Atomic Charges PMB crystal

S. No	Atom. No	Charges	S. No	Atom. No	Charges
1	01	-0.403	22	H22	0.118
2	O2	-0.317	23	H23	0.120
3	O3	-0.335	24	C24	0.208
4	N4	-0.429	25	C25	-0.111
5	N5	-0.225	26	H26	0.154
6	C6	0.227	27	C27	0.047
7	C7	-0.096	28	H28	0.107
8	Н8	0.114	29	C29	-0.135
9	C9	-0.101	30	C30	-0.050
10	H10	0.089	31	H31	0.094
11	C11	-0.090	32	C32	-0.098
12	H12	0.085	33	H33	0.108
13	C13	-0.103	34	C34	-0.112
14	H14	0.089	35	H35	0.116
15	C15	-0.118	36	C36	0.143
16	H16	0.135	37	C37	0.238
17	C17	0.554	38	38C	0.135
18	C18	-0.441	39	39H	0.117
19	C19	0.287	40	40H	0.140
20	C20	-0.233	41	41H	0.117

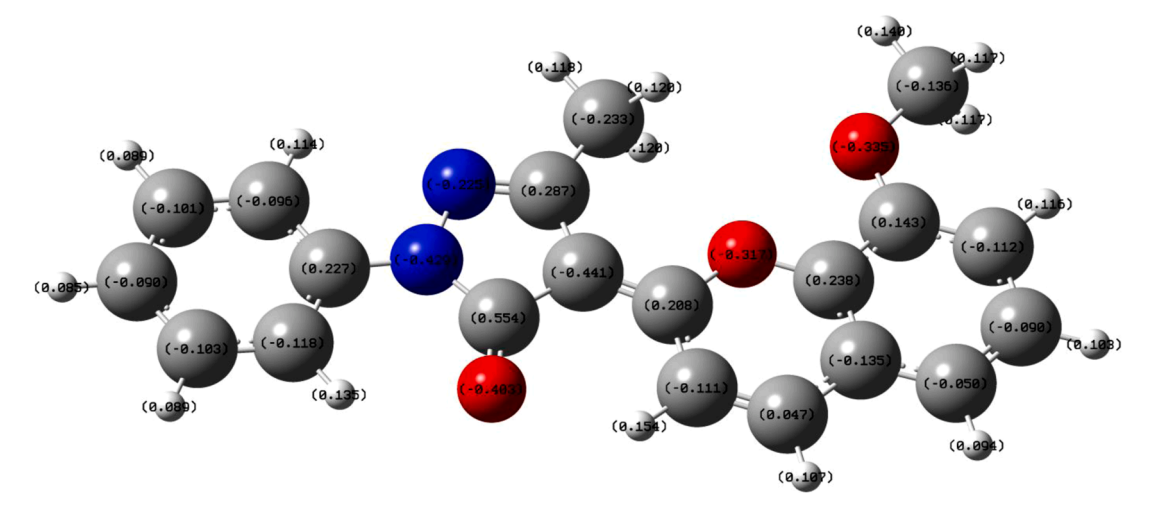


Fig. 12. The Mulliken atomic charge distribution of PMB crystal

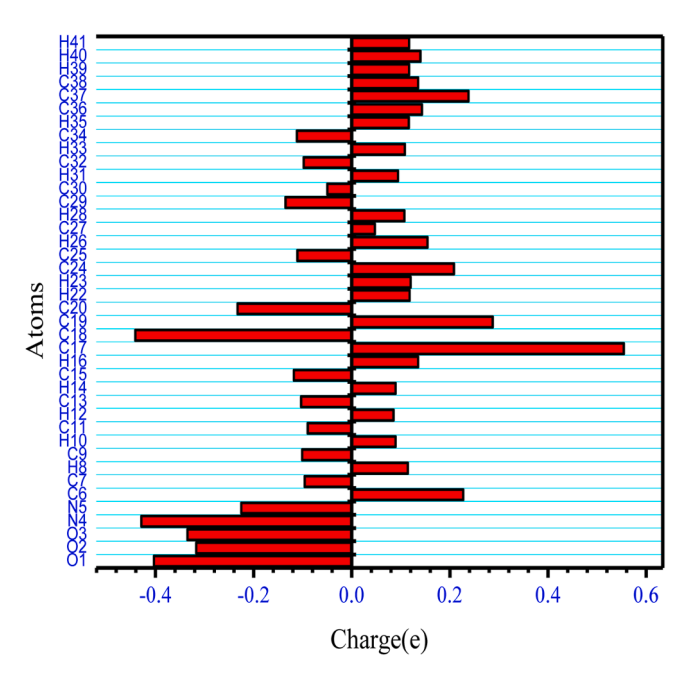


Fig. 13. Plot of Mulliken atomic charges of PMB crystal

#### 3.7.7. Molecular Electrostatic Potential analysis

A molecular electrostatic potential is a useful tool for predicting the reactivity of a variety of chemical systems in electrophilic and nucleophilic reactive sites. Fig. 14 shows a map of molecular electrostatic potential (MEP). For the PMB material the electrostatic potential map colour coding ranges from -5.098e-2 (red) to +5.098e-2 (blue). The values are most often represented by different colours, with the magnitude increasing as red < orange < yellow < green < blue [48, 49]. The regions of negative electrostatic potential are represented by red, the regions of positive electrostatic potential are represented by green. The negative portions are connected with electrophilic reactivity, whereas the positive portions are connected with nucleophilic reactivity. In the present work, the hydrogen atoms bound to the methyl group represent an electron-deficient, partially positive charge in blue colours with a nucleophilic nature. The red colour in oxygen (O1) atoms indicates the negative potential of electrophilic activity, whereas the green colour indicates zero potential.

#### 4. Conclusions

Pyrazolemethoxy benzaldehyde (PMB) crystals were grown by the slow evaporation solution growth method. The grown crystal

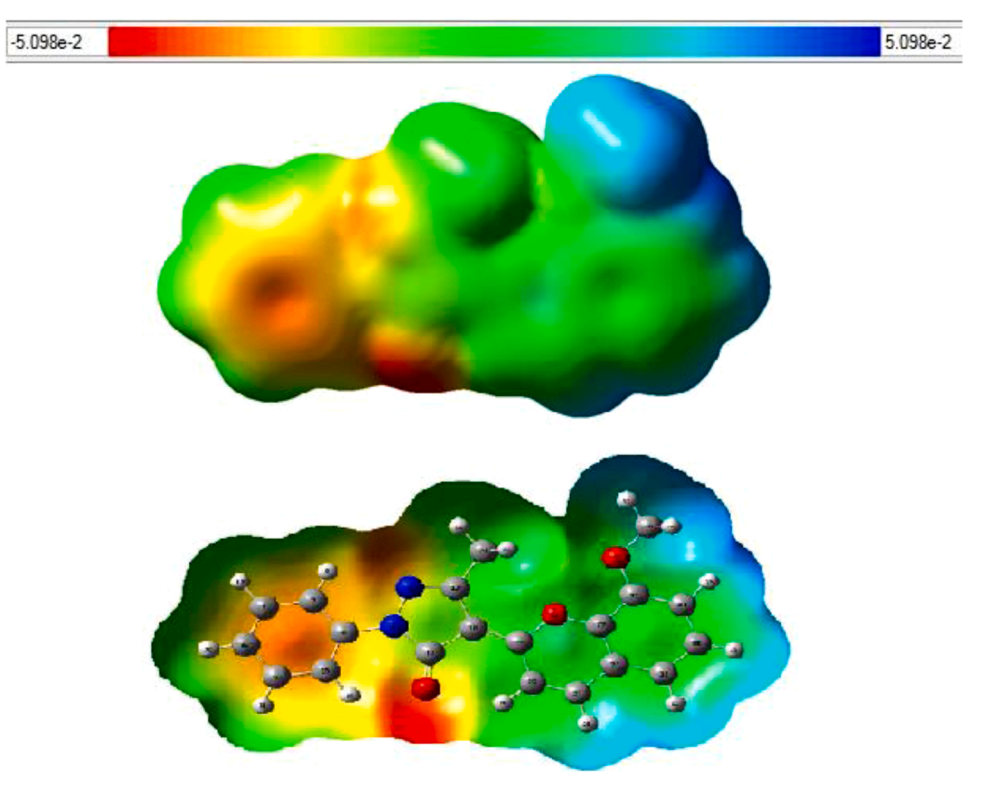


Fig. 14. Molecular electrostatic potential (MEP) map of PMB crystal

has a monoclinic structure with a centrosymmetric space group of C2/c, according to single-crystal X-ray diffraction analysis. The sharp peaks with the good crystallinity nature of the PMB crystal were confirmed by powder X-ray diffraction analysis. The vibrational modes of functional groups were analyzed using FT-IR and FT-Raman spectral analysis. The UV-vis-NIR spectrum of the grown crystal revealed the transparency in the visible region and absorption in the UV region. In the photoluminescence spectrum, the violet and blue emission peaks were analyzed for the grown crystal PMB with the excitation wavelength 250 nm . TG/DTA analysis revealed that the grown crystal was thermally stable up to  $183^{\circ}$ C. DFT theory with the B3LYP/6-311G\* method was used to optimize the geometry of the PMB crystal. The energy gap between HUMO and LUMO was calculated using theoretical calculations. The B3LYP method was used to calculate the first-order hyperpolarizability (24.754  $\times$  10<sup>-30</sup> esu) of the grown crystal. NBO analysis of the PMB crystal revealed inter and intramolecular interactions. The bonding interactions were analyzed by Mulliken atomic charge. The electrophilic attacks in the molecule are predicted using a molecular electrostatic potential map. PNB crystal can be a suitable organic material for photonics and optoelectronic applications, according to the entire investigation.

#### **Declaration of Competing Interest**

The authors declare no conflict of interest with this work.

## Acknowledgments

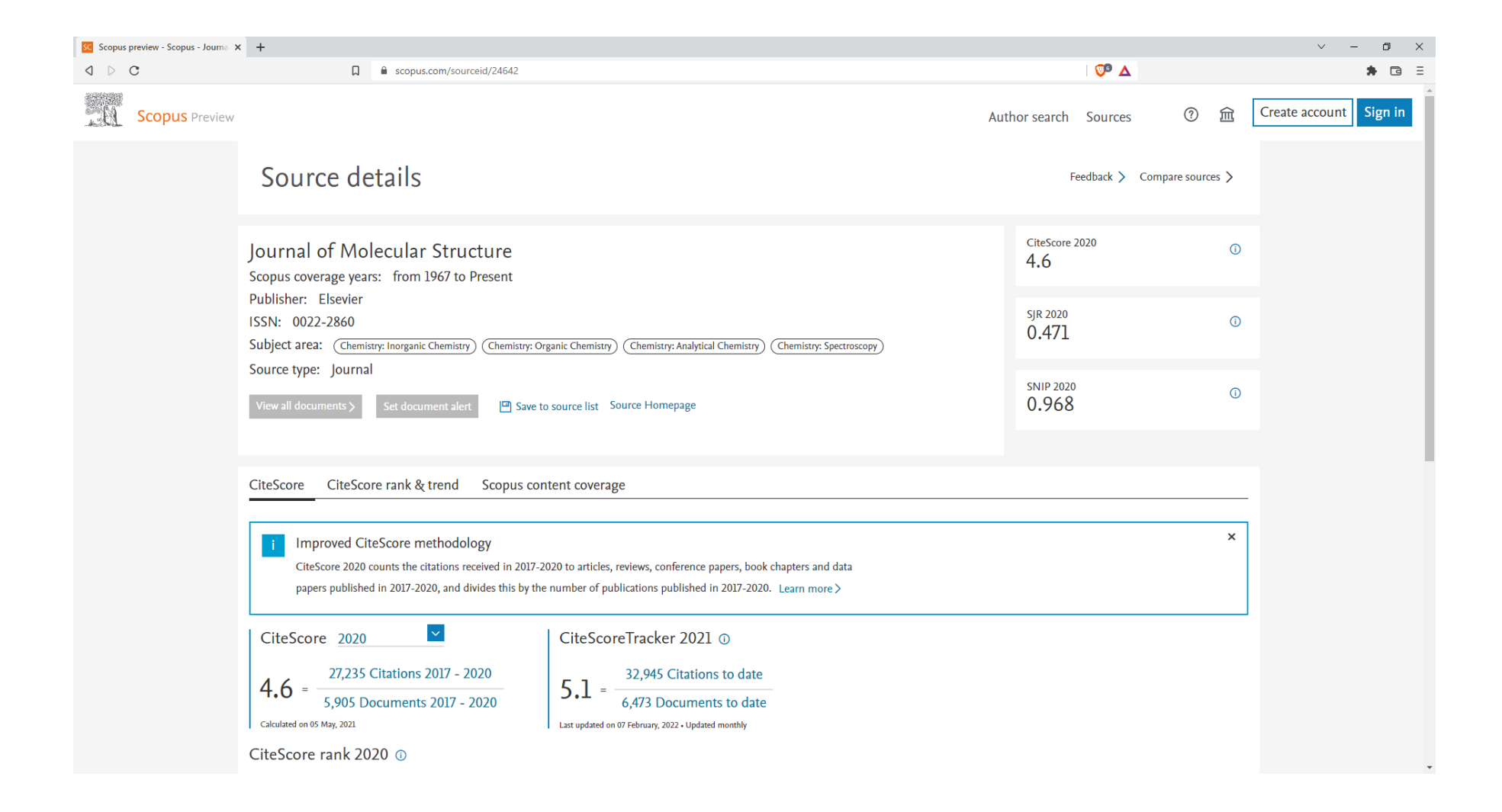
One of the (RS) thanks the Tamil Nadu State Council for Higher Education for the financial support [File No. D.O. Rc. No. 744/2017 A]. The authors thank Alagappa University, Karaikudi, St. Joseph's college, Thiuchirappalli, Sastra University, Thanjavur for extending the lab facilities to record the powder XRD, FTIR, UV, Photoluminescence and TG/DTA spectrum respectively.

#### References

- R. Archana, S. Sudhahar, S. Sagadevan, et al., Synthesis, growth and physicochemical characterization of 8-hydroxyquinolinium 3,4 dimethoxybenzoate, a novel
  organic nonlinear optical single crystal, Appl. Phys. A 126 (2020) 188.
- [2] Preeti Singh, MM Abdullah, Suresh Sagadevan, Saiqa Ikram, Enhancement of electro-optic and structural properties of TGS single crystals on doping with l-glutamic acid, J Mater Sci: Mater Electron 29 (2018) 7904–7916.
- [3] Archana Rajendran, S. Sudhahar, K. Sadayandi, M. Vidhya, S. Sagadevan, F. Mohammad, J. Podder, Investigation of the optical, photoluminescence, and dielectric properties of P-Toludinium picrate single crystals, Chinese J. Phys. 67 (2020) 283–292.
- [4] S. Suresh, Growth, Optical, Dielectric and Ferroelectric Properties of Non-Linear Optical Single Crystal: Glycine-Phthalic Acid, J. Elec. Mater. 45 (2016) 5904–5909.

- [5] R. Archana, S. Sagadevan, et al., Synthesis, growth, supramolecularity and antibacterial efficacy of 3,4-dimethoxybenzoic acid single crystals, Chemical Physics Letters 764 (8) (2021), 138269.
- [6] A. Nataraj, V. Bala Chandran, J. Karthick, Density functional study on the structural conformations, intramolecular charge transfer and vibrational spectra of 4-hydroxy-3-methoxy-5-nitrobenzaldehyde, J. Mol. Struct. 1006 (2011) 104–112.
- [7] K. Karrouchi, S. Radi, Y. Ramli, J. Taoufik, Y. Mabkhot, F. Alaizari, M. Ansar, Synthesis and pharmacological activities of pyrazole derivaties: a review, Molecules 23 (2018) 134.
- [8] F.E. Bennani, L. Doudach, Y. Cherrah, Y. Ramli, K. Karrouchi, M. Ansar, M.E.A. Faouzi, Overview of recent developments of pyrazole derivaties as an anticancer agent in different cell line, Bioorg, Chem 97 (2019), 103470.
- [9] K. Karrouchi, S. Fettach, S. Radi, J. Taoufik, Y.N. Mabkhot, S. Alterary, My E.A Faouzi, M. Ansar, synthesis, characterization, free-radical scavenging ca-pacity and antioxidant activity of novel series of hydrazone, 1, 3, 4-oxadiazole and 1, 2, 4-triazole derived from 3, 5-dimethyl-1H- pyrazole, Lett. Drug. Des. Discov. 16 (2019) 712–720.
- [10] M.Messali A.Titi, B.A. Alqurashy, R. Touzani, T. Shiga, H. Oshio, T.B. Hadda, Synthesis, Characterization, X-Ray crystal study and bioactivities of pyrazole derivaties: identification of Antitumor, antifungal and antibacterial pharma-cophore sites, J. Mol. Struct. 1205 (2020), 127625.
- [11] K. Karrochi, E.B. Yousfi, N.K. Sebbar, Y. Ramli, J. Taouufik, Y. Quzidan, Y.N. Mabkhot, H.A. Ghabbour, S. Radi, New pyrazole-hydrazone derivaties: X-ray analysis, molecular structure Investigation via density functional theory (DFT) and their high in-situ catecholase activity, Int. J. Mol. Sci. 18 (2017) 2215.
- [12] L.R.S. Dias, R.R.S. Salvador, Pyrazole carbohydrazide derivatives of pharmaceutical interest, Pharmaceuticals 5 (2012) 317-324.
- [13] B. Ballesteros, L. Santos, A reinvestigation of the molecular structures, vibrations and rotation of methyl group in o-methylaniline in S0 and S1 states studied by laser induced fluorescence spectroscopy and ab initio calculations, Spectrochimica Acta Part A: Molecular and Biomolecular Spectroscopy 58 (2002) 1069–1081
- [14] W.B. Tzeng, K. Narayanan, J.L. Lin, C.C. Tung, Structures and vibrations of o-methylaniline in the S0 and S1 states studied by ab initio calculations and resonant two-photon ionization spectroscopy, Spectrochim. Acta 55A (1998) 153–162.
- [15] M. Salim, M.A. Munawar, M.N. Tahir, M. Shahid, K.I. Malik, Crystal structure of (4E)-4-(8-meth-oxy-2H-chromen-2-yl-idene)-3-methyl-1-phenyl-1H-pyrazol-5 (4H)-one, Acta Cryst E71 (2015) 0414–0415.
- [16] O. Noureddine, S. gatfaoui, S.A. Brandan, H. Marouani, N. Issaoui, Structural, docking and spectroscopic studies of a new piperazine derivative, 1-Phenylpiperazine, 1,4diim-bis(hydrogen sulfate, J. Mol. Struct. 1202 (2020), 127351.
- [17] S. Gatfaoui, N. Issaoui, S.A. Brandan, T. Roisnel, H. Marouani, Synthesis and characterization of p-xylyenediaminiumbis(nitrate). Effects of the coordination modes of nitrate groups on their structural and vibrational properties, J. Mol. Struct. 1151 (2018) 152–168.
- [18] K. Karrouchi, S.A. Brandan, Y. Sert, H. El-marzouqi, S. Radi, M. Ferbin-teanu, M.E.A. Faouzi, Y. Garcia, M. Ansar, Synthesis, X-ray structure, vibrational spectroscopy, DFT investigation and biological evaluation studies of (E)- N' (4-(dimethylamino)benzylidene) 5-methyl- 1H -pyrazole-3-carbohydrazide, J. Mol. Struct. 128541 (2020).
- [19] C. Shruthi, V. Ravindrachary, B. Guruswamy, D. Jagadeesh Prasad, Janet Goveas, N.K. Karthik Kumara, Hiresfeld Surface and density Lokanath, Molecular structure Functional Theoretical Analysis of a NLO active Chalone Derivative Single Crystal – A Quantum Chemical Approach, J. Mol. Struct. (2020), 129739.
- [20] S. Kalaiyarasi, I. Md Zahid, S. Reena Devi, R. Maoan Kumar, Studies on the growth aspects, structural and third-order nonlinear optical properties of piperdinum 3-carboxy-4-hyaroxy benzensulfonate single crystal, J. Cryst. Growth 460 (2017) 105–111.
- [21] A. Krishna, N. Vijavan, C. Bagdia, k. Thukral, D.Haranath Sonia, K.K. Maurya, G. Bhagavannaravana, Effect of ampoule support on the growth of organic benzimidazole single crystal by vertical Bridgeman technique for nonlinear optical applications, Cryst Eng Comm 18 (2016) 4844–4850.
- [22] K. Senthil, S. Kalainathan, F. Hamada, Y. Kondo, Bulk crystal growth and nonlinear optical characterization of a stilbazolium derivative crystal: 4-[2-(3,4-dimetoxyphenyl)ethenyl]1 methylpyridiniumtetraphenylborate (DSTPB) for NLO device fabrication, RSC Adv 5 (2015) 79298–79308.
- [23] G. Parvathy, R. Kaliammal, K. Sankaranarayanan, m. Arivanandhan, M. Krishnakumar, S. Sudhahar, Growth, experimental and theoteical investications on 4-hydroxy-3-methoxybenzaldehyde 5-chloro-2-hydroxybenzoic acid: A new high second order nonlinear optical material, J. Mol. Struct 1217 (2020), 128406.
- [24] H.J. Ravindra, W.T.A. Harrision, M.R. Suresh kumar, S.M. Dharmaprakash, Synthesis, Crystal growth, characterization and structure-NLO property relationship in 1,3-bis(4-methoxyphenyl)prop-2-en-1-one single crystal, J. Cry. Growth 311 (2009) 310–315.
- [25] S. Mugeshini, et al., Growth and computational studies on vanillin isoniazid single crystals, Chinese Journal of Physics 72 (2021) 229-239.
- [26] M. Buvaneswari, R. Santhakumari, R. Jayasree, et al., Synthesis, growth and computational studies on vanillin nicotinamide single crystals, Appl. Phys. A 127 (2021) 544.
- [27] R. Vasanthakumari, W. Nirmala, et al., Synthesis, growth, crystal structure, vibrational, DFT and HOMO, LUMO analysis on protonated molecule-4-aminopyridinium nicotinate, Journal of Molecular Structure 1239 (2021), 130449.
- [28] M. Buvaneswari, R. Santhakumari, C. Usha, R. Jayasree, Suresh Sagadevan, Synthesis, growth, structural, spectroscopic, optical, thermal, DFT, HOMO-LUMO, MEP, NBO analysis and thermodynamic properties of vanillin isonicotinic hydrazide single crystal, Journal of Molecular Structure 1243 (2021), 130856.
- [29] N. Rajeswari, R. Santhakumari, S. Mugeshini, D. Chandrika, Suresh Sagadevan, Synthesis, growth, spectral and computational studies on aminomethylpyridinium trichloroacetate single crystal, Chinese Journal of Physics 30 (2021) 746–755.
- [30] Shivaraj R. Maidur, Parutagouda Shankaragouda Patil, Anusha Ekbote, Tze Shyang Chia, Ching Kheng Quah, "Molecular structure, second- and third-order nonlinear optical properties and DFT studies of a novel non- centrosymmetric chalcone derivative: (2E)-3-(4- fluorophenyl)-1-(4-{[(1E)-(4-fluorophenyl) methylene]amino}phenyl)prop-2-en-1-one", Spectrochimica Acta Part A: Molecular and Biomolecular Spectroscopy 184 (2017) 342–354.
- [31] P. Dhamodharan, K. Sathya, M. Dhandapani, Physico-chemical characterization density Functional theory (DFT) studies and Hirshfeld surface analysis of a new organic optical material:1H-benzo[d]imidazol-3- ium-2,4,6-trinitrobenzene-1 bis(olate), J. Mol. Structure 1146 (15) (2017) 782–792.
- [32] Rajesh Kumar, Amit Kumar, Vipin Deval, Archana Gupta, Poonam Tandon, P. S.Patil, Prathmesh Deshmukh, Deepika Chaturvedi, J.G. Watve, "Molecular structure, spectroscopic (FT-IR, FT Raman, UV, NMR and THz) investigation and hyperpolarizability studies of 3-(2-Chloro-6-fluorophenyl)-1-(2-thienyl) prop-2-en-1-one", J.Mol. Structure 1129 (2017) 292–304.
- [33] F J, Nye Physical properties of Crystal, Clarendon press, Oxford, 1960.
- [34] Shivaraj R. Maidur, Parutagouda Shankaragouda Patil, Z-scan studies of third-order nonlinear optical and optical limiting properties of chalcones doped Poly (methy methacrylate) thin films for visible laser protection, Optical Materials 84 (2018) 28–37.
- [35] V. Krishnakumar, R. Nagalakshmi, Studies on the first-order hyperpolarizability and Terahertz generation in 3-nitroaniline, Physica B 403 (2008) 1863-1869.
- [36] J.V. Ramaclus, T. Thomas, S. Ramesh, P. Sagayaraj, E.A. Michael, Growth, linear and nonlinear optical properties of a DSSS crystal, Cryst. Eng. Comm. 16 (2014) 6889–6895.
- [37] P. Muthuraja, T. Joselin Beaula, T. Shanmugavadivu, V. Bena Jothy, M. Dhandapani, "Hydrogen bonded R2(8) graph set in inducing charge transfer mechanism in guanidinium- 3, 5-dinitrobenzote: A combined experimental, theoretical and Hirshfeld surface study", J. Mol. Structure 1137 (5) (2017) 649–662.
- [38] Basak Kosar, Cigdem Albayrak, Spestoscopic investigations and quantum chemical Computational study of (E)-4-methoxy-2-[(p-tolylimino)methyl]phenol, Spectrochimica Acta Part A 78 (2011) 160–167.
- [39] V. Balachandran, K. Parimala, Molecular structures, FT-IR and FT-Raman spectra, NBO analysis, NLO properties, reactive sites and quantum chemical calculations of keto-enol tautomerism (2- amino-4-pyrimidinol and 2-amino-pyrimical-4(1H)-one), Spectrochimica Acta Part A: Molecular and Biomolecular Spectroscopy 102 (2013) 30–51.
- [40] D.A. Kteinman, Nonlinear Dielectric Polarization in Optical Media, Phys.Rev 126 (1962) 1977–1979.
- [41] S.K. Seth, Tunning the information of MOFs by pH influence: Xray structural variations And Hiresfeld surface analysis of 2-amino-5-nitropyridine with cadmium chloride, Cryst. Eng. Comm. 15 (2013) 1772–1781.
- [42] Shivaraj R. Maidur, Parutagouda Shankaragouda Patil, Z-scan studies of third-order Nonlinear optical and optical limiting properties of chalcones doped Poly (methyl methacrylate) thin films for visible laser protection, Optical Materials 84 (2018) 28–37.

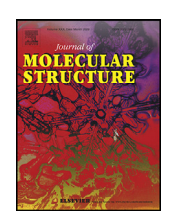
- [43] K. Muthu, V. Meenatchi, M. Rajasekar, A. Aditya Prasad, K. Meena, R. Agilanaeshwari, V. Kanagarajan, S.P. Meenakshisundaram, Combined theoretical and experimental studies on the molecular structure, spectral and Hirshfeld surface studies on the molecular structure, spectral and Hirshfeld surface studies of NLO tris(thiourea)zinc(II) sulfate crystal, J. Mol. Str. 1091 (2015) 210–221.
- [44] A. Aditya Prasad, S.P. Meenashisundram, Crystal growth, characterization and Density functional theory computations of supramolecular N-carbamothioyl acetamide, Cryst. Res. Technol. 50 (5) (2015) 1–10. /DOI 10.1002 / crat.201500031.
- [45] E.D. Glendening, A.E. Reed, J.E. Carpenter, F. Weinhold, NBO version 3.1, pitts burg, Theoretical chemistry Institute and Department of chemistry, University of Wisconsin, Madison (1988).
- [46] J. Chocholousova, V. Vladimir, Spirko, Hobza first local minimum of thformic acid dimer exhibits Simultaneously red shifted O-H....O and Improper blue-shifted C-H....O hydrogen bonds, P. Phys. Chem. Phys. 6 (2004) 37–41.
- [47] R.S. Mulliken, Electronic Population Analysis on LCAO-MO Molecular Wave Functions. I, The Journal of Chemical Physics 23 (10) (1955) 1833-1840.
- [48] C.S. Karthik, K. Kumara, S. Naveen, L. Mallesha, P. Mallu, M.V. Deepa Urs, N.K. Lokanath, Thermal, optical, etching, structural studies and theoretical calculations of [1-(2, 5-Dichloro-benzenesulfonyl)-piperidin-4-yl]-(2,4-difluoro-phenyl)-methanone oxime, J, Mol.Struct. 1224 (2021), 129077.
- [49] J.H. Zhou, L.W. Zheng, M.C. Yan, M.J. Shi, J. Liu, G.Q. Shangguan, Synthesis, Crystal Structure, and DFT Study of Ethyl 1-(2-(Hydroxyimino)-2-phenylethyl)-3-phenyl-1H-pyrazole-5-carboxylate, J. Chem. 22 (2017) 1–9, https://doi.org/10.1155/2017/6537402. Article ID 6537402.



Contents lists available at ScienceDirect

## Journal of Molecular Structure

journal homepage: www.elsevier.com/locate/molstr



# Growth, spectroscopic and Hirshfeld surface analysis on pyridine urea single crystal



G. Amudha<sup>a</sup>, R. Santhakumari<sup>a</sup>, D. Chandrika<sup>a</sup>, S. Mugeshini<sup>a</sup>, N. Rajeswari<sup>a</sup>, Suresh Sagadevan b,\*

- <sup>a</sup> Department of Physics, Government Arts College for Women (Autonomous), Pudukkottai-622 001 (Affiliated to Bharathidasan University, Tiruchirappalli-620 024) Tamil Nadu, India
- <sup>b</sup> Nanotechnology and Catalysis Research Centre, University of Malaya, Kuala Lumpur 50603, Malaysia

## ARTICLE INFO

Article history: Received 13 December 2021 Revised 5 February 2022 Accepted 7 February 2022 Available online 8 February 2022

Keywords: Pyridine urea X-ray diffraction Thermal analysis DFT Hirshfeld surface analysis

#### ABSTRACT

Organic single crystal pyridine urea (PYUA) was synthesized using the slow evaporation solution growth method at room temperature. Structural characteristics of the crystal were studied through crystal X-ray diffraction, Fourier transform infrared (FT-IR), and UV-vis-NIR spectral analyses. The thermogravimetric analysis (TGA) and differential thermal analysis (DTA) techniques was used to investigate the thermal stability of the PYUA crystal. The Vickers hardness study confirmed the PYUA as a soft crystal constructed by H-bonds and  $\pi...\pi$  interactions of average strength. The DFT calculations with the B3LYP method and Gaussian 09 software were used to perform computational analyses in a gaseous state. Hirshfeld investigations reveal H-H interactions demonstrating the largest contribution in the molecular packing.

© 2022 Elsevier B.V. All rights reserved.

#### 1. Introduction

Owing to the recent advances in crystal growth technology, several innovative nonlinear optical (NLO) materials have been developed for various applications like frequency conversion, electronic switching, and modification of electro-optical signals [1-3]. An organic compound having nonlinear optical characteristics has stimulated the interest of researchers due to its extensive range of applications, including optical modulation, optical data storage, medical applications, and laser remote sensing. Desirable materials are highly sought owing to their strong nonlinear optical susceptibilities, high laser damage thresholds, and ultrafast nonlinear reaction times [4-7]. High-quality crystals with greater efficiency in nonlinear optical materials are still desired [8]. Organic nonlinear optical devices have faster response times and stronger second-order nonlinear susceptibilities than inorganic NLO crystals [9]. Organic molecules have been proven to be more effective in material tailoring than inorganic molecules [10]. Pyridine and its derived functions are excellent nonlinear materials having a variety of technological and industrial uses, including optical telecommunication,

E-mail addresses: santhasrinithi@yahoo.co.in (R. Santhakumari), drsureshnano@ gmail.com (S. Sagadevan).

image processing, and data processing [11,12]. The chemical formula for the organic molecule urea, also known as carbamide, is CO(NH<sub>2</sub>)<sub>2</sub>. There are few hydrogen bonds sources and acceptors in urea. In this amide, a carbonyl (C=O) functional group connects two -NH2 groups. Urea based crystals are with high optical nonlinear absorption coefficients, birefringence, but they have hygroscopic qualities, making it difficult to generate laser-sized crystals for various applications [13]. Hydrogen-bonded organic frameworks (HOFs) are a type of porous molecular material that uses hydrogen-bonding interactions to assemble organic building blocks into two-dimensional (2D) and three-dimensional (3D) crystalline networks. The role of H-bonds and  $\pi...\pi$  interactions in the assembly and stabilisation of contemporary soft materials such as hydrogen-bonded organic frameworks (HOFs) [14,15].

In this study, a crystal of pyridine urea was grown using slow evaporation solution growth method. The PYUA crystal was characterized using XRD, FT-IR, UV-vis-NIR, (TGA/DTA), microhardness tests, and theoretical calculations. The DFT analysis was carried out by Frontier molecular orbital, Global chemical reactivity descriptors analysis, Mulliken atomic charge, molecular electrostatic potential analysis, NBO analysis, thermodynamic parameters, and the results are discussed. In addition to these studies, the intermolecular interaction within the PYUA was obtained from Hirshfeld analysis, and the theoretical discussion based on the results have been presented.

Corresponding authors.

Scheme 1. The reaction scheme of pyridine urea.



Fig. 1. The photograph of PYUA crystal.

#### 2. Experimental procedure

## 2.1. Crystal growth

Pyridine urea (PYUA) single crystal was synthesized in the 2:1 molar ratio of pyridine (Purity: 99.8% -Aldrich) and urea (Purity 99.5%- Aldrich) and dissolved in acetone and deionized water mixed solvents at room temperature. The synthesized chemical solution was continuously stirred for approximately 7 h to achieve homogeneity, and the resulting solution was filtered using Petri dish paper to eliminate the impurities. The saturated solution was poured into a beaker and a clear polythene paper was used to cover the mouth of the beaker to protect the solution from dust and other impurities. Within two weeks, an optically good, transparent, colourless crystal was obtained. Scheme 1 depicts the chemical reaction of the pyridine urea crystal. Fig. 1 is an image of an as grown crystal of pyridine urea.

#### 3. Results and discussion

#### 3.1. Single crystal and powder X-ray diffraction studies

To determine lattice parameter values, the XRD data of the PYUA crystal was obtained using the BRUKER KAPPA II CCD X-ray diffractometer with MoK $\alpha$  ( $\lambda$ =0.70173 Å) radiation. The PYUA crystal has the centrosymmetric space group P2 $_1$ /c and is a monoclinic crystal system. The cell parameters obtained are a=9.6052(3) Å, b=10.7195 (2) Å, c=7.4485(2) Å,  $\alpha=\gamma=90^\circ$ ,  $\beta=110.615(3)^\circ$  and cell volume V=724.57(4) Å $^3$ . The observed unit cell parameters are good in agreement with the reported values [16]. Powder XRD (PXRD) of pyridine urea crystal was measured with an XPERT-PRO diffractometer using CuK $_\alpha$  ( $\lambda$ =1.54056 Å) radiation in the  $2\theta$ 

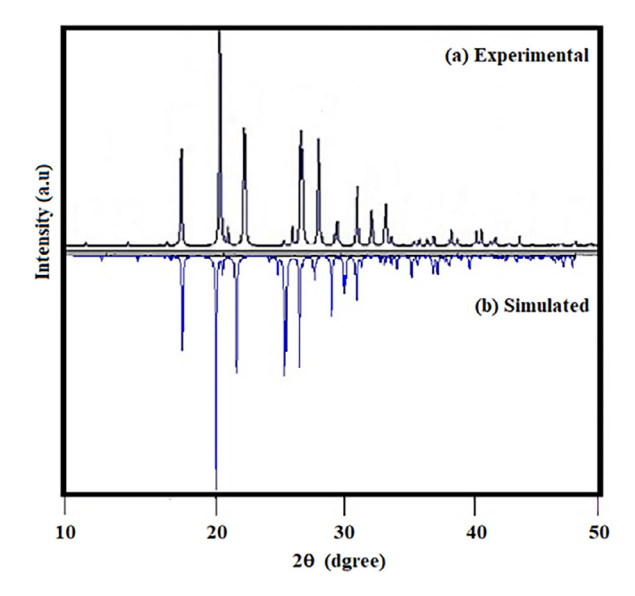


Fig. 2. (a) Experimental and (b) Simulated Powder XRD spectrum of PYUA crystal.

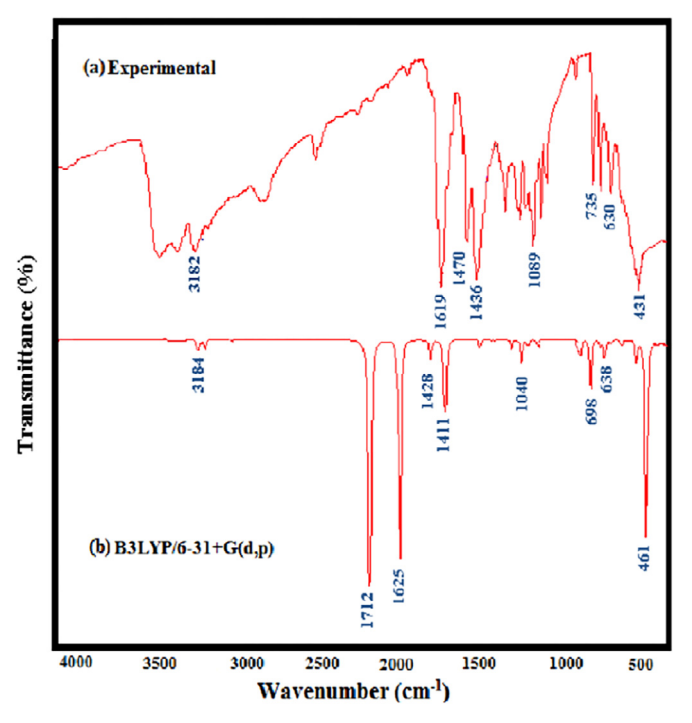


Fig. 3. FT-IR spectra of PYUA (a) Experimental (b) Simulated.

range from 10° to 50°, and compared with the PXRD stimulated spectrum using MERCURY software. The experimental and simulated XRD patterns of the PYUA crystal are compared in Fig. 2(a) and (b). The experimental PXRD pattern matches the simulated PXRD pattern very closely. The intensity of sharp peaks defining  $2\theta$  angles indicates the good crystalline and purity of PYUA crystal.

## 3.4. FT-IR spectral analysis

FT-IR analysis was performed on an FT-IR 8000 spectrometer in the range of 4000–400 cm<sup>-1</sup> using the KBr pellet method. Fig. 3(a) and (b) shows the experimental and simulated FT-IR spectra, respectively. Stretching vibrations of the aromatic ring C-H appear in the range of 3200–3000 cm<sup>-1</sup>[17,18]. The DFT/B3LYP method

**Table 1**Experimental and simulated (DFT) FT-IR spectral assignments of PYUA crystal.

		Observed Wavenun	Observed Wavenumbers (cm <sup>-1</sup> )			
Pyridine [21]	Urea [22]	Experimental	DFT/6-31+G(d,p)	Assignments		
-	3196	3182	3184	C-H stretching		
1632	1625	1619	1625	C=O stretching		
1462	1453	1470, 1436	1428, 1411	C-C stretching		
1162	1162	1185	1172	N-C-N stretching		
1078	1053	1089, 1035	1096, 1040	C-H in-plane bending		
929	-	925	957	NH <sub>2</sub> rocking		
746	785	735	764	NH <sub>2</sub> wagging		
725	-	688	698	C-C in-plane bending		
699	587	630	638	N-H out-of plane bending		
464	-	491	461	C-C out-of plane bending		

was used to compute the various frequencies of functional groups in PYUA crystal using the 6-31+G(d,p) level, and the results were compared to experimental and reported values. Table 1 shows the vibrational frequency assignments. Experimentally at 3182 cm<sup>-1</sup>, and in DFT at 3184 cm<sup>-1</sup>, C-H stretching vibrations were identified. The stretching mode of vibration C=O assigned band at 1619 cm<sup>-1</sup> in experimental and 1625 cm<sup>-1</sup> in DFT. In pyridine derivatives, the C-C stretching vibrations range from 1650 to  $1400~\text{cm}^{-1}$ [19,20] are getting match for the crystal PYUA in the experimental spectra at 1470 cm<sup>-1</sup>, 1436 cm<sup>-1</sup>, and in the DFT spectra at 1428 cm<sup>-1</sup>, 1411 cm<sup>-1</sup>, respectively. Experimental and DFT spectra show the N-C-N stretching vibration of the pyridinium ring in the PYUA crystal at 1185 cm<sup>-1</sup> and 1172 cm<sup>-1</sup>. In the experimental and DFT spectra, the C-H in-plane bending modes of vibrations in the PYUA molecule are shown at 1089 cm<sup>-1</sup>, 1035 cm<sup>-1</sup>, and 1096 cm<sup>-1</sup>,1040 cm<sup>-1</sup>, respectively. The intense peaks found at 925 cm<sup>-1</sup> and 957 cm<sup>-1</sup>, shows the presence of NH<sub>2</sub> vibration rocking in both the experimental and DFT, respectively. Peaks at 735 cm<sup>-1</sup> in the experimental spectrum and 764 cm<sup>-1</sup> in the DFT spectrum were recognised as NH2 vibration of wagging. In the experimental and DFT spectrum of the PYUA crystal, NH out-of-plane bending modes of vibration are recorded at 630 cm<sup>-1</sup> and 638 cm<sup>-1</sup>. In the experimental and DFT spectrum of PYUA, which contain amine and carboxylic acid groups, nearly all of the predicted peaks were detected.

#### 3.4. UV-vis-NIR spectral analysis

Fig. 4(a) depicts the ultraviolet spectrum of pyridine urea measured with a Perkin Elmer Lambda-35 UV spectrometer from 200 to 800 nm. It specifies the wavelength of absorption in the visible region. Fig. 4(b) illustrates the theoretical absorption spectra of PYUA crystal produced using TD-DFT. The oscillator strengths and theoretical electronic excitation energies were estimated using the TD-DFT method with the basis set at 6–31+G(d,p) to support experimental data [23]. The excitation energy in TD-DFT is 281.49 nm, while the oscillator strength f is  $\sim\!0.0047$  experimentally at a wavelength of 245.31 nm. The TD-DFT (gaseous) method predicts a value of 281.49 nm and the experimental excitation wavelength is 245.31 nm, which is quite similar to the experimental value.

## 3.5. Thermal studies

The thermal investigation was carried out in a nitrogen atmosphere, using an SDT Q600 V20.9 alumina thermal analyser maintaining a temperature of 10 °C/min. Thermogravimetric and differential thermal analyses were done on the PYUA crystal and the results are shown in Fig. 5. The crystal was stable upto 150 °C. which confirms the melting point of the PYUA crystal, since the melting point of the pyridine is found to be 115 °C. and urea is 133 °C . The

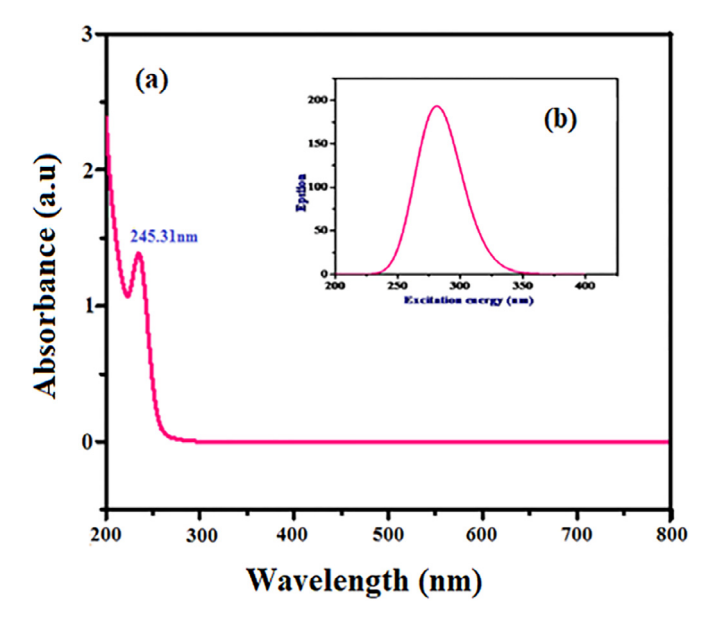


Fig. 4. (a) Experimental UV-vis -NIR spectrum of PYUA crystal, Fig. 4.(b) Theoretical UV-vis spectrum of PYUA.

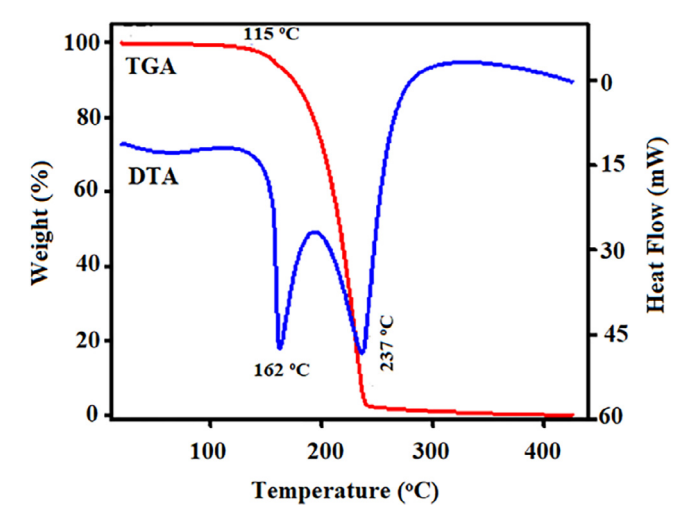


Fig. 5. TGA/DTA plot of PYUA crystal.

first strong endothermic peak was found in the DTA plot at 162 °C . The second strong endothermic peak accompanied by a substantial weight loss was detected at 237 °C , indicating the decomposition point of the PYUA crystal. The sharpness of the endothermic peak shows the crystalline nature and purity of the material [24]. There were no endothermic or exothermic peaks absorbed before

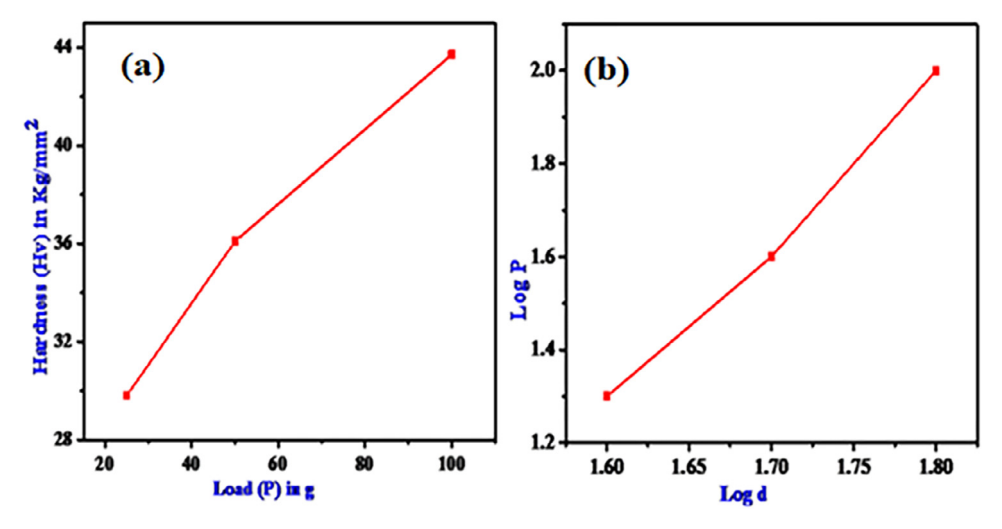


Fig. 6. (a) Plot of load (P) versus hardness (Hv) of PYUA crystal (b). Plot of log d versus of log P of PYUA crystal.

this melting point. This suggests that there is no isomorphic transition.

#### 3.6. Microhardness studies

Vickers microhardness testing was performed on the PYUA crystal with a diamond pyramidal indenter on a SHIMADZU HMV microhardness tester. Using a Vickers microhardness tester, the grown crystal's mechanical strength was tested. Microhardness is an important mechanical property of the material that plays a significant part in the fabrication of devices. Fig. 6(a) depicts a graph of Vickers hardness (Hv) versus load P. The reverse indentation size effect (RISE) is seen to rise when the hardness number  $(H_v)$  increases [25]. For microhardness measurements, a transparent polished crystal with no crakes and a smooth surface was chosen. For indentation durations of 10 s, hardness values were obtained for various applied loads (P) ranging from 25 to 100 g. There was a crack initiated by indentation with a 100 g indentation load. By means of the following equation, the Vickers micro hardness number Hv was determined.

$$Hv = \frac{1.8544P}{d^2} (Kg/mm^2) \tag{1}$$

Where P is the applied load in kg, d is the indentation's diagonal length in mm and  $H_V$  is the Vicker's hardness number. The work hardening coefficient (n) was determined by finding the slope of the straight line between log P and log d, as illustrated in Fig. 6(b). It's PYUA has a work hardening coefficient of 3.2, showing that its PYUA crystal has a work hardening coefficient greater than 1.6, indicating that it is in the soft material group [26,27].

## 3.7. Computational analyses

The DFT method was also applied at B3LYP, with a 6–31+G (d, p) basis set and the Gaussian 09 programme. The NBO 3.1 programme was used to perform the natural bond orbital study. Crystal Explorer 3.1 was used for the Hirshfeld surface analysis and display of the 2D fingerprint plot [28].

#### 3.7.1. Molecular geometry optimization

PYUA is composed of 19 atoms, 74 electrons, and has a singlet spin and is neutral in charge. The global minimum energy of PYUA at B3LYP level with the basis set of 6-31+G(d,P) is -473.6057a.u, with a dipole moment of 8.3704 Debye, according to the calculations. Table 2 compares the geometrical parameters of the PYUA

molecule, such as bond lengths, bond angles, and dihedral angles, to experimental values. These values have a good agreement between our experimental and calculated results.

#### 3.7.2. HOMO-LOMO analysis

The ability to donate and accept electrons is represented by the highest occupied molecular orbital (HOMO) and the lowest unoccupied molecular orbital (LUMO). These orbitals are known as frontier molecular orbital's (FMOs). The FMOs are instrumental in determining optical and electrical characteristics, and also in evaluating molecular properties [29,30]. There are 235 molecular orbitals in the PYUA molecule, 37 of which are occupied and 198 of which are unoccupied. The energy band gap value between the PYUA compound's HOMO-LUMO has been estimated at the Becke-3-Lee-Yang-Parr (B3LYP) level by means of the Gaussian 09 W computer software program basis set [31]. The molecule's energy value between HOMO (-9.2268 eV) and LUMO (-4.5056 eV) is roughly 4.7212 eV. The charge carrier interactions inside the molecule are described by the HOMO and LUMO energy gaps. Fig. 7 depicts the HOMO-LUMO energy levels. The LUMO is located over C-C bond of pyridine and HOMO is located over N-H group of urea.

#### 3.7.3. Global reactivity descriptors

The outer-most orbital of HOMO has a nucleophilic feature that is primarily caused by electron donation and is directly associated with the ionization potential. However, LUMO is an electrophilic property of the inner-most orbital hypothesis that functions as an electron acceptance centre and is closely linked to electron affinity [32]. The energy difference between HOMO and LUMO could be a significant characteristic in defining a molecular system's nonlinear optical properties. The global chemical reactivity characteristics of pyridine urea molecules like electronegativity ( $\chi$ ), electrophilicity index ( $\omega$ ), and chemical potential ( $\mu$ ), softness (s), hardness  $(\eta)$ , of the molecule can be evaluated using HOMO and LUMO energy values for a PYUA molecule [33]. The ionization potential (I) and electron affinity (A) for closed-shell molecules could be stated using Koopmans's theorem [34]  $I = -E_{HOMO}$  and A= -E<sub>LUMO</sub>. The DFT B3LYP/6-31+G (d, p) technique was calculated using the ionization potential and electron affinity of pyridine urea. The molecule's electronegativity is  $(\chi) = (I + A) / 2$ ; its chemical hardness  $(\eta) = (I-A) / 2$ ; its chemical potential  $(\mu) = (I-A) / 2$ ; its softness (S) = 1/2; its electrophilicity index ( $\omega$ ) =  $\mu^2/2\eta$ ; and its energy gap  $(E_g) = E_{LUMO}-E_{HOMO}$ . Table 3 presents the estimated values of the global reactivity descriptors parameters.

**Table 2** Experimental and geometrical parameters of PYUA crystal calculated by B3LYP/6-31+G(d,p) basis set.

Bond length	n(Å)		Bond angle (°)			Dihedral angle		
Atoms	DFT	EXP*	Atoms	DFT	EXP*	Atoms	DFT	EXP*
01-C5	1.229	1.250	01-C5-N2	122.9	122.0	C18-N9-C10-C12	-0.002	0.160
N2-H3	1.013	0.875	01-C5-N6	122.9	121.9	C10-N9-C18-C16	-0.001	0.210
N2-H4	1.008	0.872	N2-C5-N6	114.1	116.1	N9-C10-C12-C14	0.002	0.040
N2-C5	1.380	1.336	C5-N6-H7	119.4	118.4	C10-C12-C14-C16	-0.001	-0.590
C5-N6	1.380	1.347	C5-N6-H8	115.4	118.0	C12-C14-C16-C18	-0.001	0.920
N6-H7	1.013	0.866	H7-N6-H8	118.7	120.8	C14-C16-C18-N9	0.002	-0.760
N6-H8	1.008	0.875	C10-N9-C18	117.7	116.1			
N9-C10	1.343	1.345	N9-C10-H11	116.0	118.4			
N9-C18	1.343	1.336	N9-C10-C12	123.3	123.4			
C10-H11	1.088	0.950	C10-C12-H13	120.1	120.6			
C10-C12	1.396	1.385	C10-C12-C14	118.5	118.6			
C12-H13	1.085	0.950	C12-C14-H15	120.7	120.7			
C12-C14	1.396	1.385	C12-C14-C16	118.7	118.8			
C14-H15	1.086	0.950	C14-C16-H17	121.4	120.7			
C14-C16	1.396	1.377	C14-C16-C18	118.5	118.6			
C16-H17	1.085	0.950	N9-C18-C16	123.3	123.4			
C16-C18	1.396	1.379	N9-C18-H19	116.1	118.3			
C18-H19	1.088	0.950	C16-C18-H19	120.6	120.6			

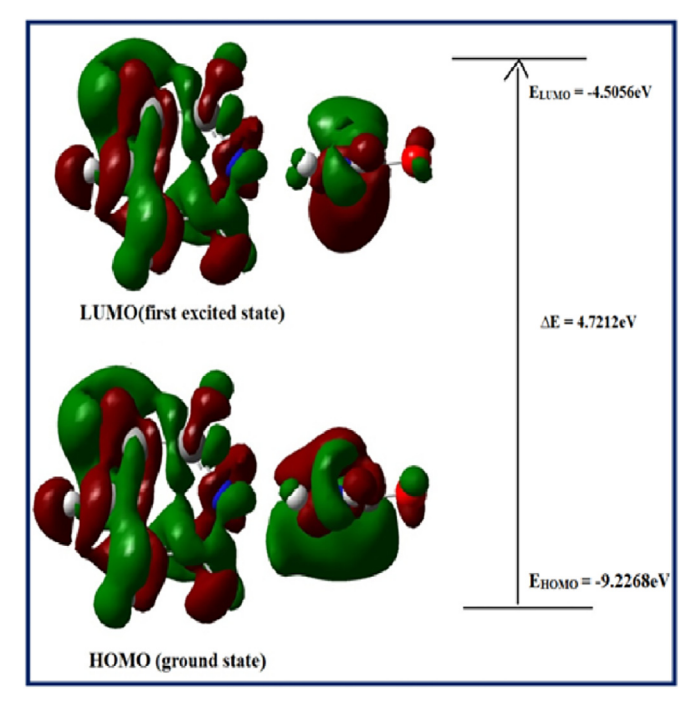


Fig. 7. HOMO-LUMO energy gap of PYUA.

The molecule was stabilized by N-H-N, N-H-O and C-H-O hydrogen bonding and characterized by its chemical potential (-6.8662 eV). The molecule's hardness (2.3606 eV) made it soft, allowing for faster electron transport. The pyridine urea compound had a high electrical attraction power based on electronegativity and electrophilicity values.

## 3.7.4. Mulliken and natural population analysis

Mulliken atomic charges (MAC) and natural population analysis (NPA) could be a great tool for population analysis and determining the charge distribution in each atom of a PYUA molecule. The plot of Mulliken and natural atomic charges on various PYUA molecule element atoms is shown in Fig. 8(a). Because they influence the electronic structure, molecular polarizability, dipole moment along with other system features, Mulliken atomic charges are significant in the usage of molecular systems for quantum chemical processing [35]. Both negative and positive charges are

**Table 3**Global chemical reactivity descriptors parameters of PYUA.

Parameters	DFT/B3LYP (e.V)
E <sub>HOMO</sub>	-9.2268
E <sub>LUMO</sub>	-4.5056
Energy gap $(E_g)$	4.7212
Ionization potential	9.2268
Electron affinity	4.5056
Electronegativity	6.8662
Chemical hardness	2.3606
Chemical potential	-6.8662
Electrophilicity index	9.9857
Dipole moment (Debye)	11.4991

 Table 4

 Mullikan atomic charges and Natural population analysis.

		=
Atom No	MAC	NPA
01	-0.58216	-0.71093
N2	-0.5994	-0.80724
Н3	0.330892	0.38457
H4	0.310982	0.38729
C5	0.512015	0.77528
N6	-0.59931	-0.80807
H7	0.330847	0.37901
H8	0.310954	0.38974
N9	-0.28757	-0.50375
C10	-0.12778	0.04905
H11	0.147413	0.20256
C12	0.111184	0.23882
H13	0.140861	0.21892
C14	-0.39361	-0.16027
H15	0.143793	0.21439
C16	0.112921	0.24143
H17	0.139929	0.21923
C18	-0.14103	0.04941
H19	0.139067	0.20108

found on distinct atoms in the PYUA molecule and are given in Table 4. According to the charge distribution molecule, all the hydrogen atoms are positively charged. Positive charges were applied to carbon atoms C5, C12, and C16, while negative charges were applied to the other carbon atoms. C5 has the biggest positive charge (0.512015 e) and C14 has the most negative charge (-0.39361 e). The nitrogen atoms in N2 (-0.5994 e), N6 (-0.59931 e), and N9 (-0.28757 e) are all negative. According to the charge distribution, carbon (C10 and C18) atoms coupled to nitrogen atoms possess negative charges, while carbon (C5) atoms connected to oxygen atoms possess positive charges. As a result, negatively charged

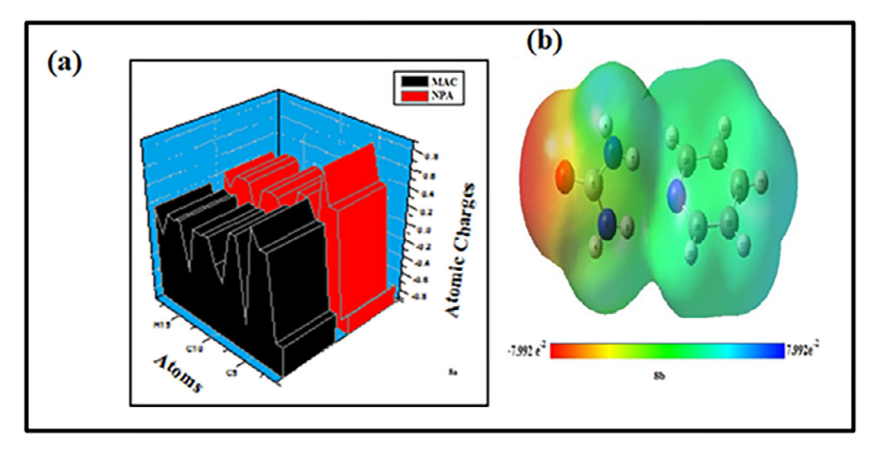


Fig. 8. (a). The plot of Mulliken and Natural Atomic Charges of PYUA crystal (b). Molecular electrostatic potential map ranges from -7.992e<sup>-2</sup> to 7.99e<sup>-2</sup> of PYUA crystal.

carbon atoms are linked to nitrogen atoms, whereas positively charged hydrogen atoms are attached to carbon atoms.

#### 3.7.5. Molecular electrostatic potential (MEP) map analysis

The distribution of positive and negative charges in a crystal allows us to describe its electrostatic potential. In molecular systems, the electrostatic potential is essential for understanding intermolecular interactions and locating electrophilic and nucleophilic attack sites [36]. The MEP is found from the optimized B3LYP/6-31+G (d, p) result and is illustrated in Fig. 8(b) to evaluate reactive regions for electrophilic and nucleophilic attacks on the PYUA molecule. Different electrostatic potential values are depicted by different colours on the MEP map. The red colour represents the location of the maximum negative zone, which favours electrophilic attacks, whereas the blue colour represents the site's maximum positive zone, which favours nucleophilic attacks. The regions of negative and positive electrostatic potentials appear in red and blue, respectively, while the region of zero potential is represented by green. All these analyses revealed that the oxygencontaining region of urea is the most reactive.

#### 3.7.6. NBO analysis

NBO analysis gives a consistent description of molecular and intramolecular bonding interactions in terms of electron donor and acceptor conjugative and charge carrier interactions [37,38]. The transfer of electron density from an occupied electron orbital to an unoccupied electron orbital can be investigated using NBO analysis [39]. In accordance with the theory of second-order perturbations, the stabilization energy E(2) associated with the delocalization  $i \rightarrow j$  is determined for the donor(i) and acceptor(j) using the following equation.

$$E(2) = \Delta E_{i,j} = qi \frac{F(i,j)^2}{E_i - E_i} \tag{2} \label{eq:2}$$

Where qi represents the donor orbital occupancy, E(2) represents stabilization energy,  $E_i$ , and  $E_j$  are the diagonal factors, The diagonal is F(i,j), while the off-diagonal NBO Fock matrix components are j and i. The NBO analysis results for the PYUA molecules are described in Table 5. The interactions between lone pairs are the most substantial. The lone pair of electron-donating atoms n1(N2) and n1(N6) to the antibonding orbital's  $\sigma^*(O1\text{-}C5)$  and  $\sigma^*(O1\text{-}C5)$ , have stabilization energies of 42.62 and 41.04 kcal/mol respectively. The molecule's high energy value causes intramolecular charger interactions. The interactions  $(\pi$ -  $\pi^*)$  are significant in demonstrating the presence of conjugation in the molecules under investigation. For the  $\pi(C12\text{-}C14) \to \pi^*(N9\text{-}C10)$ ,  $\pi(N9\text{-}C10) \to \pi^*(C16\text{-}C18)$ ,  $\pi(C16\text{-}C18) \to \pi^*(C12\text{-}C14)$  and  $\pi(C12\text{-}C14) \to \pi^*(C16\text{-}C18)$  transitions, the stabilization energies were found to be 29.14, 25.52,

**Table 5**NBO analysis of PYUA crystal.

Donor(i)	Acceptor(j)	E(2)a(kcal/mol)	$E(j)-E(i)^b(a.u)$	$F(i, j)^{c}(a.u)$
n1 (N2)	σ*(01-C5)	42.62	0.36	0.114
n1(N6)	$\sigma^*(01-C5)$	41.04	0.36	0.112
$\pi$ (C12-C14)	$\pi^*(N9-C10)$	29.14	0.26	0.079
$\pi$ (N9-C10)	$\pi^*(C16-C18)$	25.52	0.33	0.083
$\pi$ (C16-C18)	$\pi^*(C12-C14)$	23.34	0.29	0.075
$\pi$ (C12-C14)	$\pi^*(C16-C18)$	18.28	0.29	0.066

- <sup>a</sup> F(i, j) is the Fock matrix component that associates the i and j NBO orbital's.
- <sup>b</sup> E(2) stands for the energies of hyper conjugative interactions (kJ/mol).
- <sup>c</sup> The energy difference between the i and j NBO orbital of the donor and acceptor.

**Table 6**Theoretically computed thermodynamic parameters of PYUA.

Thermodynamical parameters	DFT	
Zero-point vibrational energy (KCal/Mol)	96.2872	
Rotational constants (GHz)		
A	3.79517	
В	0.47944	
С	0.46331	
Rotational temperature (K)		
A	0.18214	
В	0.02301	
C	0.02224	
Thermal energy (KCal/Mol)		
Rotational	0.889	
Vibrational	101.303	
Translational	0.889	
Total thermal energy	103.081	
Heat capacity at constant volume (Cal/Mol-K)		
Rotational	2.981	
Vibrational	31.326	
Translational	2.981	
Total heat capacity	37.288	
Entropy(cal/mol-kelvin)		
Rotational	30.323	
Vibrational	38.924	
Translational	40.701	
Total entropy	109.948	

23.34 and 18.28 kcal/mol, respectively. Finally, based on the data, it can be assumed that title molecules have directed conjugation, which facilitates intramolecular charge transfer. As a result, the strong intramolecular hyper conjugative fundamental interactions are the elementary cause of more stability in all these systems.

## 3.7.7. Thermodynamic properties

Table 6 shows the thermodynamics parameters of the pyridine urea molecule, such as zero-point vibrational energy (ZPVE), rotational constants, rotational temperature, entropy, thermal en-

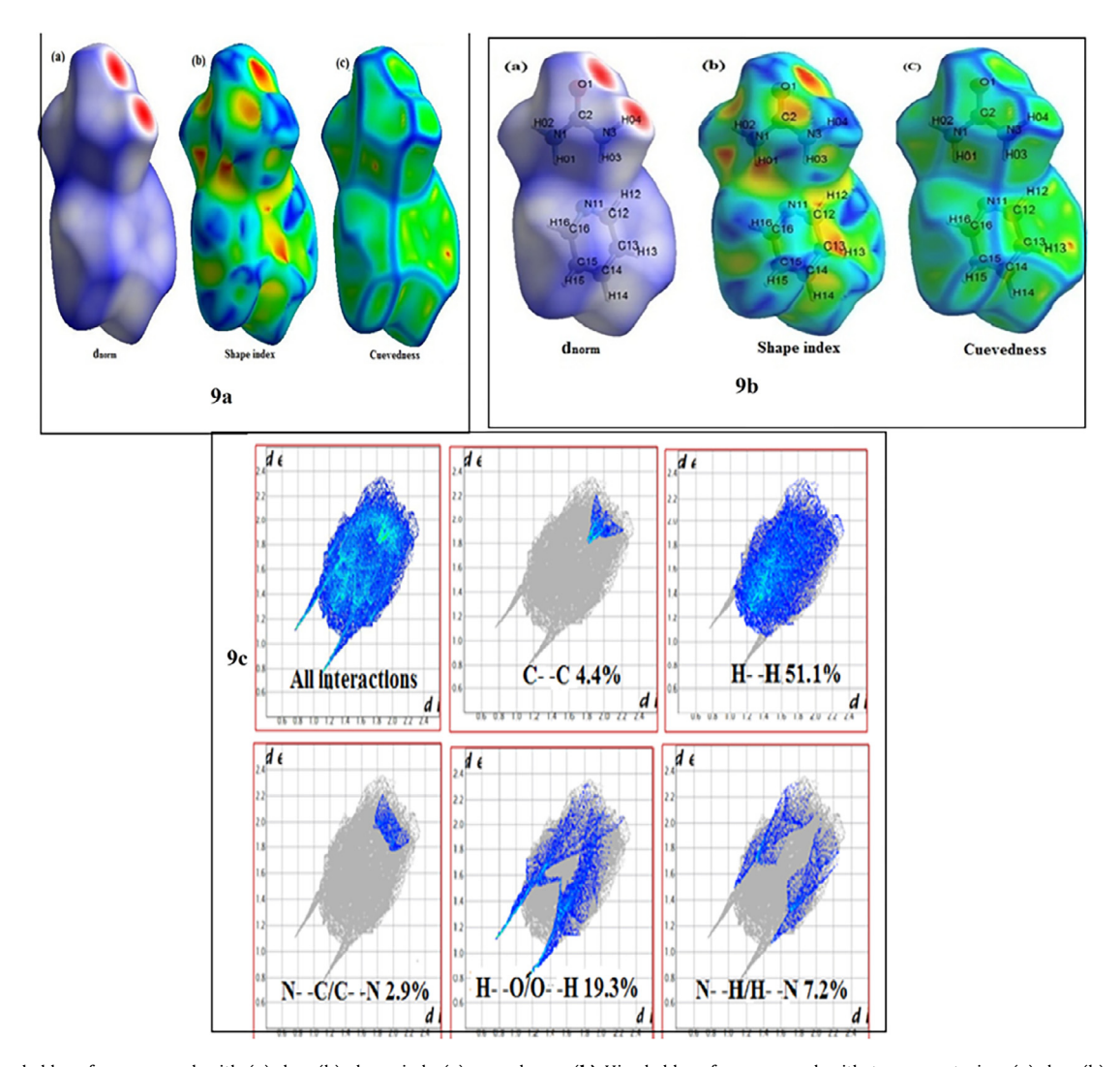


Fig. 9. (a) Hiresheld surfaces mapped with (a) d<sub>norm</sub>(b) shape index(c) curvednesss (b) Hiresheld surfaces mapped with transparent view (a) d<sub>norm</sub>(b) shape index (c) curvednesss (c)2D Fingerprint plots.

ergy, and heat capacity, which are calculated using theoretical harmonic frequencies. The total energy of a molecule, for example, is the sum of its rotational, vibrational, and translational energies, as shown by E=Er+Ev+Et. The magnitude of heat needed to increase the temperature of a material by 1 °C is known as its heat capacity. The ZPVE variation appears to be insignificant [40]. As expected, the rotational constant reduces as the rotational temperature decreases. The moment of inertia of a molecule is inversely proportional to the rotational constant [41]. As a result, a decrease in the rotational constant signifies an increase in the molecule's moment of inertia, i.e. the simplicity with which its rotating state may be adjusted in response to its environment.

## 3.7.8. Hirshfeld surface analysis

The Hirshfeld surface analysis was considered to be substantial in determining the intermolecular interaction of the PYUA crystal using Crystal Explorer 3.1, and the associated Hirshfeld surfaces of normal view and transparent view of  $d_{norm}$ , shape index, and curvedness are illustrated in Fig. 9(a) and 9 (b) respectively, and are the fingerprint plots given in Fig. 9(c). The intermolecular interactions were investigated using crystallographic data that had been solved using single-crystal XRD and the normalised contact distances ( $d_{norm}$ ) were used to map the distances between the surface point and the atoms exterior ( $d_e$ ), and interior ( $d_i$ ) Vander Waals

radii [42]. The  $d_{norm}$  surface illustrates intermolecular interactions in relation to the vander Waals radius using a blue and red colour scheme [43]. The  $d_{norm}$  is calculated using the mean values from  $d_i$  and  $d_e$ . The distance between the Hirshfeld area and the adjacent atom outside (blue) inside (red) the surface is denoted by de and  $d_i$ , respectively.

The d<sub>norm</sub> can be determined using the following expression,

$$d_{norm} = \frac{d_i - r_i^{vdw}}{r_i^{vdw}} + \frac{de - re^{vdw}}{re^{vdw}} \tag{3} \label{eq:dnorm}$$

Where vdw stands for Vander Waals atom radii, the red colour indicates the interactions with small distances, while the blue colour represents the interactions with larger distances. In addition, the white denotes a distance equivalent to the Vander Waals radii. The analysed data shows that the PYUA molecules contain increased hydrogen-hydrogen (H- -H) interactions (51.1%) inside to outside compared to other interactions. The fraction of O- -H/H- -O contacts in all Hirshfeld surfaces is 20.4%, showing that hydrogen bonding contacts are the second most important interaction. The presence of a nitro and carboxylate group in PYUA causes the O-H/H- -O interactions. The N- -H/H- -N connections are the third most important contributors to the overall Hirshfeld surface (7.2%). There is also the existence of  $\pi$ - -  $\pi$  (C- -C) (4.4%) and addi-

tional interactions N--C/C--N (2.9%). The electrostatic energy of the molecule is 3.4 kJ/mo which is obtained by Crystal Explorer.

#### 4. Conclusion

A slow evaporation solution growth method was used to grow the crystal of pyridine urea (PYUA), at room temperature. The cell parameters calculated using the X-ray diffraction technique and the sharp peak in PXRD illustrates the crystallinity nature of the sample. The FT-IR and DFT spectra of the PYUA crystal confirmed the existence of several functional groups. Using TD-DFT and UV-vis-NIR spectrophotometer, the excitation energy of the PYUA crystal was estimated to be 245.31 nm experimentally and 281.49 nm theoretically. The PYUA crystal is thermally stable up to 115 °C, according to thermal analysis. The mechanical properties of the PYUA crystal imply that it is confirmed to be soft material. The energy gap between HOMO-LUMO was measured to be 4.7212 eV. The intermolecular charge transference of the PYUA crystal originates with carbon atoms, according to the Mulliken charge distribution. Negative potential areas are surrounded by electronegative atoms on the MEP map, while positive potential areas are surrounded by hydrogen atoms. These locations provide data about the area where the molecule may undergo intermolecular interactions. The NBO analysis of the Fock matrix displays second-order perturbation theory analysis. Thermodynamic properties rise as the intensity of molecular vibrations increases with temperature. According to Hirshfeld's research, the percentage of H-H interactions (51.1%) is the highest of all surfaces.

#### **Declaration of Competing Interest**

The authors declare that they have no known competing financial interests or personal relationships that could have appeared to influence the work reported in this paper.

## **CRediT authorship contribution statement**

**G. Amudha:** Conceptualization, Methodology, Formal analysis. **R. Santhakumari:** Supervision, Formal analysis, Methodology, Data curation, Validation. **D. Chandrika:** Data curation, Visualization, Validation. **S. Mugeshini:** Formal analysis, Validation, Data curation. **N. Rajeswari:** Data curation, Visualization, Validation. **Suresh Sagadevan:** Formal analysis, Data curation, Validation, Writing – review & editing.

## Acknowledgement

One of the authors (RS) expresses gratitude to the Tamil Nadu State Council for Higher Education and the Tamil Nadu State Council for Science and Technology for financial support [File No. D.O.Rc.No.744/2017A and TNSCST/STP/AR/PS/2014–15, Date: 11.04.2017]. The authors would also like to thank IIT Madras, Chennai, CECRI, Karaikudi, Sastra University, Thanjavur, and Bharathidasan University, Tiruchirappalli for providing laboratory facilities for the SXRD, Powder XRD, FT-IR, UV-vis-NIR, and TGA spectra, as well as the Microhardness studies.

#### Supplementary materials

Supplementary material associated with this article can be found, in the online version, at doi:10.1016/j.molstruc.2022.132606.

#### References

[1] S. Mugeshini, R. Santhakumari, N. Rajeshwari, G. Amudha, D. Chandrika, S. Sagadevan, Synthesis, growth, experimental, and theoretical characterization of 6-amino-1H-pyrimidine-2,4-dione dimethylacetamide single crystal, Chin. J. Phys. 76 (2022) 14–23.

- [2] G. Amudha, R. Santhakumari, D. Chandrika, S. Mugeshini, N. Rajeswari, S. Sagadevan, Synthesis, growth, DFT, and HOMO-LUMO studies onpyrazolemethoxy benzaldehyde single crystals, Chin. J. Phys. 76 (2022) 44–58.
- [3] C. Ushaa, R. Santhakumari, R. Jayasree, M. Bhuvaneswari, S. Sagadevan, Growth, NBO, and vibrational studies combined with intramolecular hydrogen bond interaction of L-Valine lead (II) nitrate complex: DFT, J. Mol. Struct. 1249 (2022) 131570.
- [4] N. Rajeswari, R. Santhakumari, S. Mugeshini, D. Chandrika, S. Sagadevan, Synthesis, growth, spectral and computational studies on aminomethylpyridinium trichloroacetate single crystal, Chin. J. Phys. 73 (2021) 746–755.
- [5] S. Mugeshini, R. Santhakumari, N. Rajeswari, G. Amudhaa, D. Chandrika, S. Sagadevan, Growth, computational studies, and docking analysis on  $\alpha$ -pyrrolidinopentiophenone hydrochloride monohydrate single crystal, J. Mol. Struct. 1249 (2022) 131600.
- [6] R. Vasanthakumari, W. Nirmala, S. Suresh Sagadevan, N. Mugeshini d, R. Rajeswari, R. Balu, SanthakumariSynthesis, growth, crystal structure, vibrational, DFT and HOMO, LUMO analysis on protonated molecule-4-aminopyridinium nicotinate, J. Mol. Struct. 1239 (2021) 130449.
- [7] M. Buvaneswari, R. Santhakumari, R. Jayasree, S. Sagadevan, Synthesis, growth and computational studies on vanillin nicotinamide single crystals, Appl. Phys. A 127 (2021) 544.
- [8] S. Archana, S. Sagadevan, et al., Synthesis, growth, supramolecularity and antibacterial efficacy of 3,4-dimethoxybenzoic acid single crystals, Chem. Phys.s Lett. 764 (8) (2021) 138269 2021.
- [9] M. Buvaneswari, R. Santhakumari, C. Usha, R. Jayasree, S. Sagadevan, Synthesis, growth, structural, spectroscopic, optical, thermal, DFT, HOMO-LUMO, MEP, NBO analysis and thermodynamic properties of vanillin isonicotinic hydrazide single crystal, J. Mol. Struct. 1243 (2021) 130856.
- [10] S. Mugeshini, R. Santhakumari, N. Rajeswari, G. Amudha, D. Chandrika, S. Sagadevan, Growth and computational studies on vanillin isoniazid single crystals, Chin. J. Phys. 72 (2021) 229–239.
- [11] A. Ayman, M.H. Zaki, R.E.R Nagi, Synthesis and optical properties of new alkylated pyridinium halides, Optik 139 (2017) 95–103 Stuttg.
- [12] V. Chithambaram, S.J Das, R. ArivudaiNambi, S. Krishnan, Synthesis, growth and characterization of nonlinear optical urea-ammonium chloride crystals, Solid State Sci. 14 (2012) 216–218.
- [13] S. Krishnan, C. Justin Raj, S. Jerome Das, Growth and characterization of novel ferroelectric urea succinic acid single crystals, J. Cryst. Growth 310 (2008) 3313–3317.
- [14] P. Li, MR. Ryder, J.F Stoddart, Hydrogen-bonded organic frameworks: a rising class of porous molecular materials, Acc. Mater. Res. Acc. Mater. Res. 1 (2020) 77–87.
- [15] B. Wang, R.B. Lin, Z. Zhang, S. Xiang, B. Chen, Hydrogen-bonded organic frameworks as a tunable platform for functional materials, J. Am. Chem. SOC 142 (2020) 14399–14416.
- [16] M. Strey, P.G. Jones, Pyridine 1:1 adducts of urea (Z'=1) and thio-urea (Z'=8), Acta Cryst. C74 (2018) 406–410.
- [17] S. Gatfaoui, N. Issaoui, S.A. Brandan, T. Roisnel, H. Marouani, Effects of the coordination modes of nitrate groups on their structural and vibrational properties, J. Mol. Struct. 1151 (2018) 152–168.
- [18] O. Noureddine, S. gatfaoui, S.A. Brandan, a. sagaama, H. Marouani, N. Issaoui, Experimental and DFT studies on the molecular structure, spectroscopic properties and molecular docking of 4-phenylpiperazine-1-ium dihydrogen phosphate, J. Mol. Struct. 1207 (2020) 127762.
- [19] Ghiasuddin, et al., A combined experimental and computational study of 3-bromo-5-(2,5- difluorophenyl) pyridine and 3,5-bis(naphthalen-1-yl)pyridine: insight into the synthesis, spectroscopic, single crystal XRD, electronic, nonlinear optical and biological properties, J. Mol. Struct. 1160 (2018) 129–141.
- [20] D. Sathiyanaryanan, Vibrational Spectroscopy Theory and Application, New Age Inernational Publishers, New Delhi, 2004.
- [21] I.M. Ibrahim, S. Yunus, M.A. Hashim, Relative performance of isopropylamine, pyrrole and pyridine as corrosion inhibitors for carbon steels in saline water at mildly elevated temperatures, Int. J. Sci. Eng. Res. 4 (2) (2013) 1–12.
- [22] G. Madharambal, M. Mariappan, S.C. Mojumdar, Thermal, UV and FTIR spectral studies of urea- thiourea zinc chloride single crystal, J. Therm. Anal. Calorim. 100 (2010) 763–768.
- [23] A. Aditya Prasad, K. Muthu, M. Rajasekar, V. Meenatchi, S. P.Meenakshisundaram, Crystal growth, characterization and theoretical studies of 4-aminopyridinium picrate, Spectrochem. Acta Part A Mol. Biomol. Spectrosc. 135 (2015) 805–813.
- [24] K. Sathya, P. Dhamodharan, M. Dhandapani, Structural characterization and DFT study of a optical crystal: 2-amino-3-methylpyridinium-3,5-dinitrobenzote, Opt. Laser Technol. 101 (2018) 328–340.
- [25] P. Jayaprakash, P. Sangeetha, M. Peer Mohamed, G. Vinitha, S. Muthu, M. Prakash, M.L Caroline, Figure shows molecular electrostatic potential and HOMO-LUMO energy of DLMA. Growth and characterization of DL-Mandelic acid single crystal for third order nonlinear optical applications, J. Mol. Struct. 1148 (2017) 314–321.
- [26] S. Panchapakesan, K. Subramani, B. Srinivasan, Investigations on the quantum chemical studies and physico-chemical properties of an optoelectronic material 1-Allyl-2-Aminopyridine-1-ium bromide, Opt. Laser Technol. 113 (2019) 246–260
- [27] Y. Matveychuk, E. Bartashevich, V.G. Tsirelso, How the H-bond layout determines mechanical properties of crystalline amino acid hydrogen maleates, Cryst. Growth Des. 18 (6) (2018) 3366–3375.

- [28] S.K. Wolff, D.J. Grimwood, J.J. McKinnon, M.J. Turner, D. Jayatilaka, M.A. Spack-man, CrystalExplorer Version 3.1, University of Western Australia, (2012).
- [29] S. Saravanan, V. Balachandran, K. Viswanathan, Spectroscopic investigation of 4-nitro-3-(trifluoromethyl) aniline, NBO analysis with 4-nitro-3-(trichloromethyl) aniline and 4-nitro-3-(tribromomethyl) aniline, Spectrochim, Acta Part A 12 (2014) 685–697.
- [30] I. Fleming, Frontier Orbitals, Organic Chemical Reactions, Wiley, London, 1976.
- [31] S. Muthu, G. Ramachandran, Spectroscopic studies (FT-IR, FT-Raman and UV-Visible), normal coordinate analysis, NBO analysis of (IR)-N-(Prop-2-yn-1yl)-2,3-dihydro-1Hinden-1- amine molecule by ab initio HF and density functional methods, Spectrom. Acta Part A 121 (2014) 394-403.
- [32] S. Muthu, S. Renga, vibrational spectra and normal coordinate analysis of 2-hydroxy-3-(2-methoxyphenoxy) propyl carbamate, Spectrochim. Acta 132 (2014) 313–325.
- [33] A. Karthik Kumara, A. Dileep Kumar, S. Naveen, K. Ajay kumar, N. K.Lokanath, Synthesis, spectral characterization and X-ray crystal structure studies of 3-(benzo[d][1,3]dioxol-5-yl)-5-(3-methylthiophen-2-yl)-4,5-dihydro-1H-pyrazol e-1-carboxamide: hirshfeld surface, DFT and thermal analysis, J. Mol. Struct. 1161 (2018) 285–320.
- [34] T.A. Koopmans, Über die zuordnung von wellenfunktionen und eigenwerten zu den einzelnen elektronen eines atoms, Physica 1 (1934) 104–113.
- [35] R.S. Mulliken, Electronic population analysis on LCAO-MO molecular wave functions, J. Chem. Phys. 23 (1955) 1833–1840.
- [36] N.B. RachidaRahmani, A. Chouaih, S.G.S. FodilHamzaoui, On the molecular structure, vibrational spectra, HOMO-LUMO, molecular electrostatic potential, UV-Vis, first order hyperpolarizability, and thermodynamic investigations

- of 3-(4-chlorophenyl)-1-(pyridine-3-yl) prop-2-en-1-one byquantum chemistry calculations, J. Mol. Struct. 1155 (2018) 484–495.
- [37] M. Adeel, A.A. Braga, M.N. Tahir, F. Hag, M. Khalid, M.A. Halim, Synthesis, X-ray crystallographic, spectroscopic and computational studies of amino-thiazolederivaties, J. Mol. Struct. 1131 (2017) 136–148.
- [38] S. Naseem, M. Khalid, M.N. Tahir, M.A. Halim, A.A. Braga, M.M. Naseer, Z. Shafiq, Synthesis, structural, DFT studies, docking and antibacterial activity of a xanthenesbased hydrazone ligand, J. Mol. Struct. 1143 (2017) 235–244.
- [39] M.A. Ghiasuddin, M. Adeel, M. Khalid, T.M. Nawaz, M.U. Khan, M.A. Asghar, M.A. Ullah, M. Iqbal, A combined experimental and computational study of 3-broma-5-(2,5-difluorophenyl) pyridine and 3,5-bis(naphthalen1-yl)pyridine: insight into the synthesis, spectroscopic, single crystal XRD, electronic nonlinear optical and biological properties, J Mol. Struct. 1131 (2017) 136–148.
- [40] V. Balachandran, A. Lakshmi, Ab initio, DFT, HOMO-LUMO and natural bond orbital analyses of the electronic structure of 2-mercapto-1-methylimidazole, J. Mol. Struct. 1006 (2011) 395–401.
- [41] K. Rastogi, M.A. Palafox, R.P. Tanwar, L. Mittal, 3,5-Difluorobenzonitrile: ab initio calculations, FTIR and Raman spectra, Spectrochim. Acta A 58 (2002) 1987–2004.
- [42] S. Karthicka, K. Thirupugalmani, M. Krishnakumar, V. Kannane, G. Vinitha, S. Brahadeeswaranan, Synthesis, structural, dielectric, laser damage threshold, third order linear optical quantum chemical investigations on a novel organic crystalline material: pyrrolidin-1-ium 2chloro-4-electronic applications, Opt. Laser Technol. 122 (2020) 105849.
- [43] K. Sathya, P. Dhamodharan, M. Dhandapani, Structural characterization and DFT study of a new optical crystal: 2-amino-3-methylpyridinium-3,5-dinitrobenzoatek, Opt. Laser Technol. 101 (2018) 328–340.